Mesoporous molecular sieve catalysts

Højholt, Karen Thrane

Publication date:
2011

Document Version
Publisher's PDF, also known as Version of record

Citation (APA):
Højholt, K. T. (2011). *Mesoporous molecular sieve catalysts*. Technical University of Denmark.

Mesoporous molecular sieve catalysts

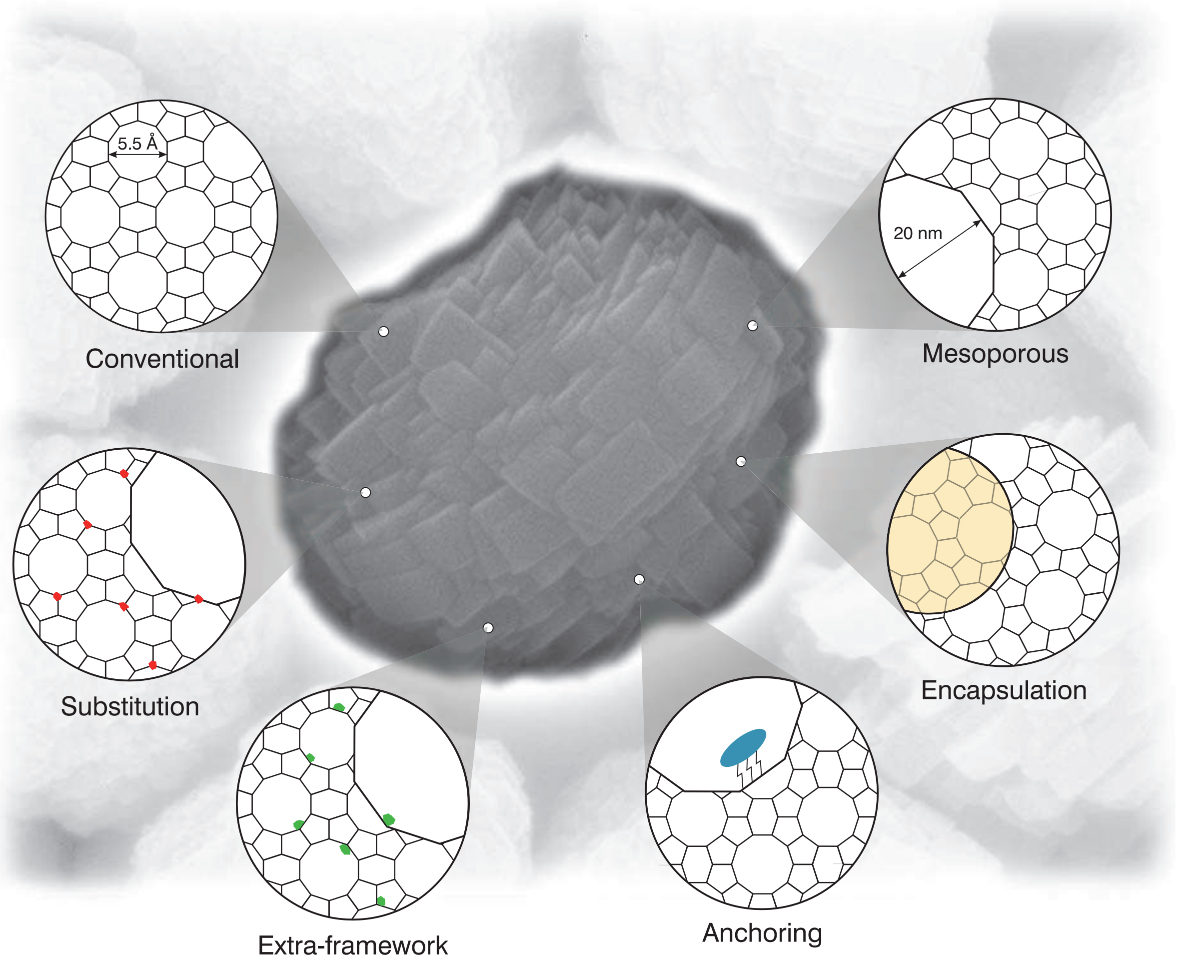

Karen Thrane Højholt

PhD Thesis
Department of Chemistry
Technical University of Denmark
August 2011

Centre for Catalysis and Sustainable Chemistry

DTU

Mesoporous molecular sieve catalysts

Karen Thrane Højholt

PhD Thesis
Department of Chemistry
Technical University of Denmark
August 2011

HALDOR TOPSØE
CATALYSING YOUR BUSINESS

Preface

The present thesis is submitted in candidacy for the PhD degree from the Technical University of Denmark (DTU). It is based on work carried out at Haldor Topsøe A/S and the Centre for Catalysis and Sustainable Chemistry (CSC), Department of Chemistry from August 2007 to August 2011. From August 2007 to July 2008 the supervision at DTU was performed by Professor Claus Hviid Christensen and continued to the end by Docent Rasmus Fehrmann. In the entire period the supervision at Haldor Topsøe A/S was conducted by Dr. Michael Brorson. The PhD project was funded by Haldor Topsøe A/S, the Danish National Research Foundation and the Technical University of Denmark.

The objective of this thesis is the development of new zeolite and zeotype materials for catalytic applications. The focus of the experimental work is synthesis and characterisation of modified zeolite and zeotype materials. Along with the thesis, 6 publications in international journals were prepared and are included as appendices.

First of all, I am grateful to my main supervisor Dr. Michael Brorson at Haldor Topsøe A/S for his inspiration and willingness to share his immense knowledge in all aspect of chemistry and at the same time allowing me to work on several different and highly diverse projects during my time as a PhD student. This has given me the opportunity to work closely with several students and employees at Haldor Topsøe A/S. In particular, my thanks go to Dr. Pablo Beato for fruitful collaboration and for always answering my never-ending questions. I thank Professor Claus Hviid Christensen for his innovative spirit and for challenging me to do the PhD project. I also thank Docent Rasmus Fehrmann for stepping in as a supervisor.

Most of the work presented in this thesis has been done in close collaboration with other students and/or scientists. I would like to thank PhD student Peter N. R. Vennestrøm, PhD Uffe V. Mentzel and PhD Søren Kegnæs for testing some of the prepared materials and PhD students Pia K. Nielsen and Anders B. Laursen for great collaborations on synthesising hybrid zeolite materials and MOFs. Thanks to Dr. Jørgen Skibsted (University of Århus) for NMR measurements and PhD Katia Barbera (University of Turin) for IR investigations. Thanks also goes to the staff at the Analytical and Characterisation department at Haldor Topsøe A/S, especially research technician Aino Nielsen for doing an endless number of SEM investigations and PhD Søren B. Simonsen and PhD Lars F. Lundegaard for TEM investigations. Furthermore, I thank all my colleagues at CSC and Haldor Topsøe A/S for fruitful discussions and collaborations and at the same time providing a great working environment, especially PhD Frank B. Johansson for providing a nice atmosphere in the office and to Dr. Konrad Herbst for my thesis proof-reading. Additionally, I would like to thank my husband Per Thrane Højholt for his unlimited support and patience.

Karen Thrane Højholt
Kgs. Lyngby, August 2011

Abstract

This thesis deals with a very specific class of molecular sieves known as zeolites. Zeolites are a class of crystalline aluminosilicates characterised by pores or cavities of molecular dimensions as part of their crystal structure. In this work zeolites were modified for the use and understanding of different catalytic applications. Primarily the zeolites were modified regarding the porosity and the introduction of metals to the framework. The obtained materials were used as solid acid catalysts, as an inert matrix for stabilising metal nanoparticles and as an anchoring material for molecular metal oxide species.

Nanosized and mesoporous zeolites were prepared to investigate the effect of inter- or intracrystalline mesopores on the catalytic lifetime in the conversion of methanol to hydrocarbons (MTH). It was found that the mesoporous zeolite with intracrystalline mesopores displayed the significantly longest catalytic lifetime compared to the nanosized zeolites and the conventional counterpart.

Even though the introduction of mesopores improved the catalytic lifetime in the MTH reaction it was concluded that the normal benefits from desilication, *e.g.* mesoporosity and repairing of defects, became masked by the generation of extra-framework aluminum and that the catalytic lifetime was severely dependent on the amount of extra-framework aluminum.

Conventional and mesoporous ZSM-5 zeolites were prepared together with the Ga-MFI zeotype analogues to investigate the differences in activity, selectivity and mode of deactivation. The differences in selectivity were primarily ascribed to the difference in the lower acidity of the individual active sites of the Ga-MFI zeotypes compared to the zeolites. In general, the Ga-MFI zeotypes deactivated faster than the ZSM-5 zeolites. Further investigations of the mode of deactivation revealed that the zeolites deactivated due to coke formation and that the Ga-MFI zeotypes deactivated due to loss of the catalytically active Brønsted acid sites caused by hydrolysis of Ga-O bonds leading to formation of inactive extra-framework gallium.

Zeolites can not only be used as solid acid catalysts but can also be used as a size-selective matrix. It was shown that it is possible to encapsulate 1-2 nm sized gold nanoparticles by silicalite-1 or ZSM-5 zeolite crystals thereby forming a sintering-stable and substrate size-selective oxidation catalyst. After carrying out calcination experiments, both *in situ* and *ex situ* indicated that the gold nanoparticles embedded in the crystals were highly stable towards sintering. The catalytic tests proved that the embedded gold nanoparticles were active in selective aldehyde oxidation and were only accessible through the micropores.

Furthermore, preliminary work was done using mesoporous ZSM-5 zeolites as support material for anchoring molecular $CoMo_6$ species for the application as potential bi-functional catalyst in simultaneous hydrodesulfurisation (HDS) and hydrocracking. HDS activity tests revealed that the anchoring improved the activity compared to an impregnated counterpart.

Resume

Denne afhandling omhandler en specifik klasse af molekylesier, nemlig zeolitter. Zeolitter, der er en klasse af krystallinske aluminosilikater, er kendetegnet ved, at deres krystalstruktur indeholder kanaler og hulrum i samme størrelsesorden som små molekyler. I dette projekt er zeolitter blevet modificeret til brug i udvalgte katalytiske reaktioner, hvorved der også er opnået en dybere forståelse af reaktionerne. Zeolitter er hovedsageligt blevet modificeret med hensyn til porøsitet. Desuden er forskellige metaller blevet integreret både i og på krystalstrukturen. De fremstillede materialer er blevet brugt som fast sur katalysator, som inert matrix for at stabilisere metal nanopartikler og som forankringsmateriale for molekylære metaloxid specier.

Mesoporøse zeolitter og zeolitter i nanostørrelse er blevet fremstillet for at undersøge effekten af tilstedeværelsen af intra- eller interkrystallinske mesoporer på den katalytiske levetid i omdannelsen af methanol til hydrocarboner (MTH). Mesoporøse zeolitter med intrakrystallinske mesoporer viste sig at have den signifikant længste levetid sammenlignet med en konventionel zeolit og zeolitter i nanostørrelse.

Selvom introduktionen af mesoporer i zeolitter forbedrede den katalytiske levetid i MTH, er det bevist, at de normale positive konsekvenser af desilicering, så som mesoporøsitet og reparation af krystaldefekter, kan blive maskeret af tilstedeværelsen af extra-framework aluminium, og at den katalytiske levetid er stærkt afhængig af dette.

Konventionel og mesoporøs ZSM-5 zeolitter er blevet fremstillet sammen med analoge Ga-MFI zeotyper for at undersøge forskellen i aktivitet, selektivitet og form for deaktivering. Forskellen i aktivitet og selektivitet kan hovedsagelig tilskrives den lavere surhed af de individuelle sure sites i Ga-MFI zeotyperne sammenlignet med ZSM-5 zeolitterne. Generelt deaktiverede Ga-MFI zeotyperne hurtigere end ZSM-5 zeolitterne. Det blev konstateret, at ZSM-5 zeolitterne deaktiverede på grund af kuldannelsen, hvorimod Ga-MFI zeotyperne deaktiverede på grund af tab af de katalytisk aktive Brønsted sure sites ved hydrolyse af Ga-O bindinger, som førte til dannelse af inaktiv extra-framework gallium.

Zeolitter kan ikke kun bruges som en fast sur katalysator, men kan også bruges som en størrelses-selektiv matrix. Det er blevet påvist, at det er muligt at indkapsle 1-2 nm store guld nanopartikler i silicalite-1 eller ZSM-5 krystaller og derved danne en sinterings-stabil og reaktant størrelses-selektiv oxidations katalysator. Kalcinerings eksperimenter både *in situ* og *ex situ* indikerede, at guld nanopartikler, som er indkapslet i krystallerne, er yderst sinteringsstabile. De katalytiske test beviste, at de indkapslede guld nanopartikler er katalytisk aktive i selektiv aldehyd oxidation og er kun tilgængelig gennem mikroporerne.

Sluttelig er der udført et indledende arbejde med henblik på at fremstille en bifunktionel katalysator til samtidig brug i hydrodesulfurisation (HDS) og hydrokrakning ved at forankre aktive $CoMo_6$ nanopartikler på mesoporøs ZSM-5 zeolit. HDS aktivitetstest viste, at forankring af molekylære $CoMo_6$ specier forbedrede den katalytiske aktivitet sammenlignet med en imprægneret reference af samme.

List of publications and conference contributions during the PhD project

Scientific publications in international peer-reviewed journals

S. Sørensen, K.T. Højholt, P.N. R. Vennestrøm, K. Barbera, F. Bonino, S. Bordiga, H. Fordsmand, P. Beato, J. Skibsted *"Characterization of mesoporous H-ZSM-5 zeolites after desilication and dealumination by FTIR and solid-state NMR spectroscopy"*, to be submitted in J. Catal.

U.V. Mentzel, K.T. Højholt, M.S. Holm, R. Fehrmann, P. Beato *"Conversion of methanol to hydrocarbons over conventional and mesoporous H-ZSM-5 and H-Ga-MFI: Differences in deactivation behaviour"*, to be submitted in Appl. Catal. A., General (**2011**)

K.T. Højholt, P.N.R. Vennestrøm, P. Beato, *"Tight bifunctional hierarchical catalyst"*, submitted in Chem. Commun. (**2011**)

K.T. Højholt, A.B. Laursen, S. Kegnæs, C.H. Christensen, *"Size-selective oxidation of aldehydes with zeolite encapsulated gold nanoparticles"*, accepted in Top. Catal. (**2011**) DOI 10.1007/s11244-011-9722-x

A.B. Laursen, K.T. Højholt, L.F. Lundegaard, S.B. Simonsen, S. Helveg, F. Schüth, M. Paul, J.-D. Grunwaldt, S. Kegnæs, C.H. Christensen, K. Egeblad, *"Substrate size-selective catalysis with zeolite-encapsulated gold nanoparticles"*, Angew. Chem. Int. Ed. 49 3504-3507 (**2010**)

K.T. Leth, A.K. Rovik, M.S. Holm, M. Brorson, H.J. Jakobsen, J. Skibsted, C.H. Christensen, *"Synthesis and characterization of conventional and mesoporous Ga-MFI for ethane dehydrogenation"*, Appl. Catal. A., General 348 (**2008**) 257-265

Oral presentations at international conferences

K.T. Højholt, A.B. Laursen, S.B. Simonsen, L.F. Lundegaard, S. Helveg, S. Kegnæs, K. Egeblad og C.H. Christensen, *Size-selective Oxidation with Au nanoparticles embedded in Zeolite Crystals*, 16th International Zeolite Conference joint with the 7th International Mesostructured Materials Symposium, Sorrento (Italy), July 4-9 (**2010**)

K.T. Højholt, P. Beato, *Surface modification of ZSM-5 zeolite for the MTH reaction*, inGAP Summer School, Trondheim (Norway), June 21-26 (**2009**)

B.S. Clausen, K.T. Leth, A.K. Rovik, K. Egeblad, C.H. Christensen, C.H. Christensen, *Hierarchical Zeolite Catalysts: Larger Molecules Welcome*, 14th International Conference on Catalysis, Seoul, (Korea), July 13th-18th (**2008**)

Poster presentations at international conferences

K. T. Leth, P. Beato, *"Enhanced conversion capacity for the MTH Reaction through Surface modification of MFI zeolite"*, The XXXIInd Annual British Zeolite Association Conference, Ambleside (UK), August 23-28 (**2009**)

K.T. Højholt, P. Beato, *"A new, one-step synthesis method for hierarchical zeolites by carbon templating"*, IX EuropaCat, Salamanca (Spain) August 30-September 4 (**2009**)

K.T. Højholt, P. Beato, *"Surface modification of ZSM-5 zeolite for the MTH reaction"*, inGAP-NANOCAT Summer School, Trondheim (Norway), June 21-26 (**2009**)

K.T. Leth, A.K. Rovik, M. Brorson, J. Skibsted, C.H. Christensen, *"Impact of Morphology on the Catalytic Properties of Gallium-Substituted Molecular Sieves in Ethane Dehydrogenation"*, 14th International Conference on Catalysis, Seoul (Korea) July 13-18 (**2008**)

K.T. Leth, A.K. Rovik, C.H. Christensen, M. Brorson, J. Skibsted, *"Valorisation of ethane by catalytic dehydrogenation over hierarchically porous materials"*, 3rd International Conference on Green and Sustainable Chemistry, Delft (Holland) July 1-5 (**2007**)

Table of Contents

Chapter 6

Introduction

In 1932 J.W. McBain defined the term "molecular sieve" to be a material that is able to separate components of a mixture on the basis of molecular size and shape.[1] No requirements on elemental composition or structure, *i.e.* crystalline or amorphous exist, the only pre-condition being that the molecular sieve is a porous solid material which has the property of acting as a sieve on a molecular scale. Zeolites are one of the most known classes of molecular sieves. Zeolites are crystalline aluminosilicates featuring pores and/or cavities in the range of 3-12 Å, which according to the IUPAC classification of porous materials[2] classifies zeolites as microporous. Zeolites are often highly thermally stable materials with remarkably high surface areas and due to the inherent micropore system of molecular dimensions zeolites are often used for shape-selective catalysis.[3] The catalytic activity of the zeolites is mostly determined by the Brønsted acidity and/or by the active metal species that may be deposited within the zeolite framework. Today there exist around 190 different zeolite structures[4] which can be tuned in terms of acidity and/or redox properties. Zeolites are among the most frequently used industrial catalysts at the beginning of the 21st century. Their catalytic applications range from oil refining, *i.e.* FCC (Fluid Catalytic Cracking), petrochemistry and the synthesis of special chemicals to environmental catalysis.[5] It should be stated that zeolites are also used within several other areas due to their molecular sieving properties, adsorption affinities or ion exchange abilities. Depending on the hydrophobicity/hydrophilicity of the zeolite framework drying or purification by *i.e.* moisture adsorption or removal of organics by selective adsorption can be done. In non-catalytic applications zeolites are mostly used as laundry detergent.[6]

Even though zeolites are remarkable materials, the sole presence of micropores in zeolites may in some cases limit the catalytic performance of zeolite catalysts, particular when diffusion in the micropores becomes significantly slower than the catalytic reaction.[7] To overcome this limitation one possibility is the introduction of mesopores (2-50 nm). Mesoporous zeolites are zeolites featuring an auxiliary system of mesopores in addition to the intrinsic micropore system of zeolites. Since mesoporous zeolites contain pores in two different ranges, they are considered to be hierarchically porous materials and are therefore also termed hierarchical zeolites. Mesoporous zeolites are today primarily used in industry for cracking large hydrocarbons into the gasoline range.

This thesis covers the synthesis and characterization of modified zeolites with application potential for various catalytic processes. Zeolites are in this work used as solid acid catalysts, as an inert matrix for stabilising metal nanoparticles and as an anchoring material for active metal oxides. Furthermore zeolites have been modified regarding the porosity and type of incorporated metal in the zeolite framework.

The thesis is divided into 6 chapters.

In Chapter 1, the basic concepts of zeolites are introduced together with applications and pitfalls of the used characterisation techniques.

Recently, it was shown[8-10] that hierarchical zeolites can enhance the catalytic lifetime compared to solely microporous zeolites due to an improved mass transport. In Chapter 2 nanosized and mesoporous ZSM-5 zeolites are synthesised and compared with a conventional ZSM-5 zeolite for the catalytic lifetime in the conversion of methanol to hydrocarbons (MTH). It is shown that especially the presence of intracrystalline mesopores improves the catalytic lifetime. It is also observed that several factors influence the catalytic lifetime and in particular the presence of extra-framework aluminum has a severe effect.

In Chapter 3, a more detailed and in-depth investigation of the effect of extra-framework aluminum on the catalytic lifetime in the MTH reaction is provided. It is shown that a mesoporous zeolite containing extra-framework aluminum has a significant lower catalytic lifetime compared to the conventional counterpart. Upon removing the extra-framework aluminum the catalytic lifetime is considerably improved and the catalyst has an even longer catalytic lifetime than the conventional zeolite.

In Chapter 4 conventional and mesoporous Ga-MFI zeotypes are synthesised and tested together with the ZSM-5 analogues in the MTH reaction to investigate the catalytic lifetime and type of deactivation. It is shown that the ZSM-5 zeolites deactivate due to coke formation while the Ga-MFI zeotype deactivates due to extraction of gallium from the framework and thereby loss of the catalytically active Brønsted acidity.

In heterogeneous catalysis, metal nanoparticles supported on high surface area carriers play a crucial role as active and selective catalysis for numerous chemical reactions.[11] Particularly for high temperature applications, inevitable problems with nanoparticle sintering arise. In Chapter 5 the preparation of new substrate-size selective oxidation catalysts is described. They are prepared by encapsulating gold nanoparticles in MFI type zeolites making the active gold nanoparticles only accessible though the zeolite micropores.

Catalytically active species can not only be a part of the zeolite framework or encapsulated in the zeolite crystals but it is also possible to ion exchange, impregnate or to anchor them onto the zeolite surface. In Chapter 6 is described the synthesis of anchoring molecular $CoMo_6$ species on mesoporous ZSM-5 zeolite for hydrodesulfurisation reactions. The prepared material is compared to an impregnated counterpart to observe if the anchoring improves the catalytic activity. It is shown that the catalytic activity is improved due to a better dispersion of the active species.

Chapter 1

Basic concepts

This chapter gives an introduction to zeolites concerning their structure, properties, diffusion effects and implementation of mesoporosity. Furthermore a discussion is presented of applications and pitfalls of the characterisation techniques used in this work.

1.1. Zeolites

1.1.1. Structure and properties

Zeolites are extremely attractive materials due to their unique physico-chemical properties and structures. Zeolites are crystalline microporous aluminosilicates featuring well-defined pores and/or cavities smaller than 2 nm as a part of their crystal structure. Structurally, zeolites are built from tetrahedral TO_4 units (T = Si or Al) that are organised into three-dimensional networks by sharing of the oxygen corner-atoms in the TO_4 units. The microporous system entails that zeolites are solids with very high surface areas and pore volume.[1]

In general, zeolites contain silicon, oxygen and aluminum, but it is possible to synthesise materials of the same structure as zeolites, but with different elements such as gallium, phosphorous, germanium or others. These materials are known as zeotypes. The only requirements are that the element has to have a tetrahedral oxygen configuration and an appropriate size.[12] Zeolites are normally found to obey what is known as Löwenstein's rule[13], which states that an Al-O-Al linkage is forbidden, implying that the majority of T atoms must be silicon. Consequently, zeolites can be regarded as silicates with a certain portion of the silicon being substituted with aluminum atoms and as a result the Si/Al ratio in the zeolite framework cannot be smaller than unity.

All known zeolite frameworks can be thought to consist of a relatively small numbers of finite or infinite (i.e. chain- or layer-like) component units. These finite units are known as secondary building units (SBUs)* and consist of a n-ring structure which can contain as many as 16 T-atoms and as little as 3. Selected ones are shown in Figure 1.1 where each corner in the SBU represents the centre of a tetrahedral. It should be noted that SBUs are invariable non-chiral.[4]

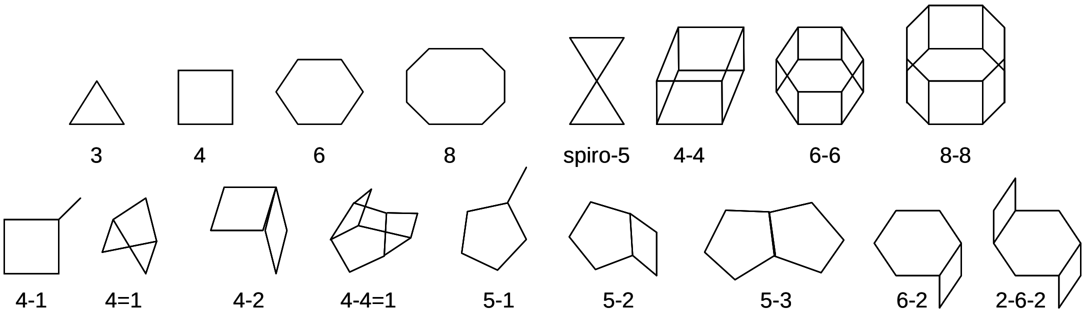

Figure 1.1: Selected Secondary building units and their symbols. Modified from [4]

---

* The primary building units are single TO_4 tetrahedra.

The zeolite frameworks may furthermore be described in terms of large polyhedral building blocks forming *e.g.* characteristic cages. For example, sodalite (SOD), Linde Type A (LTA) and Faujasite (FAU) can all be generated by the truncated octahedron known as the β-cage, Figure 1.2.

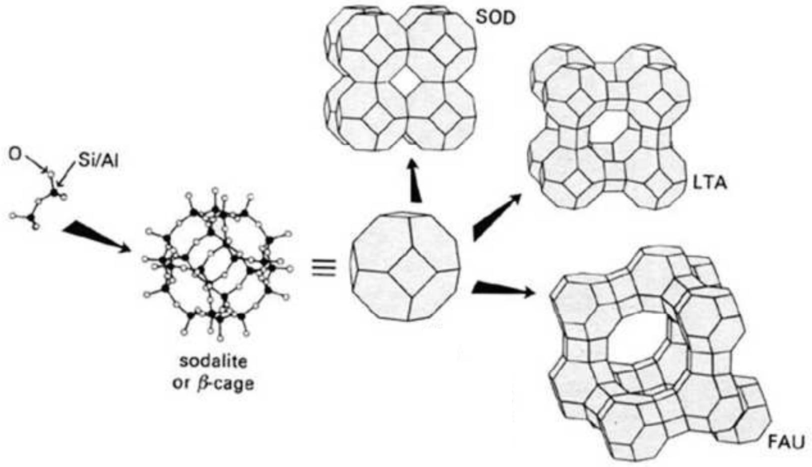

Figure 1.2: Possible zeolite structures from β-cages

The β-cage has both four and six-membered rings (SBU 4 and 6) in its structure. The cage formed has an internal diameter of approximately 6 Å. By fusing together the four-membered rings, SOD is formed, by bridging the four-membered rings LTA is formed and by bridging the six-membered rings FAU is formed. Especially, the LTA structure is interesting since the structure besides the β-cages contains supercages (α-cages); the void between the interlinked β-cages with an opening of 12 T-atoms. The diameter of these α-cages is approximately 12 Å. All the zeolite structures in Figure 1.2 contain channels beside cages. The SOD has only channels formed by six-membered rings, while the LTA has channels with eight-membered rings leading to a diameter of 4.1 Å. The FAU has channels formed by twelve-membered rings and with a diameter around 7.4 Å.[4] This example shows that it is possible to obtain many different zeolite structures by combining a rather simple cage structure in different ways.

To distinguish between the more than 190 different zeolites structures known today the International Zeolite Association (IZA) has introduced a three-letter code which classifies each framework type *e.g.* MFI, MEL and BEA, Figure 1.3.[4]

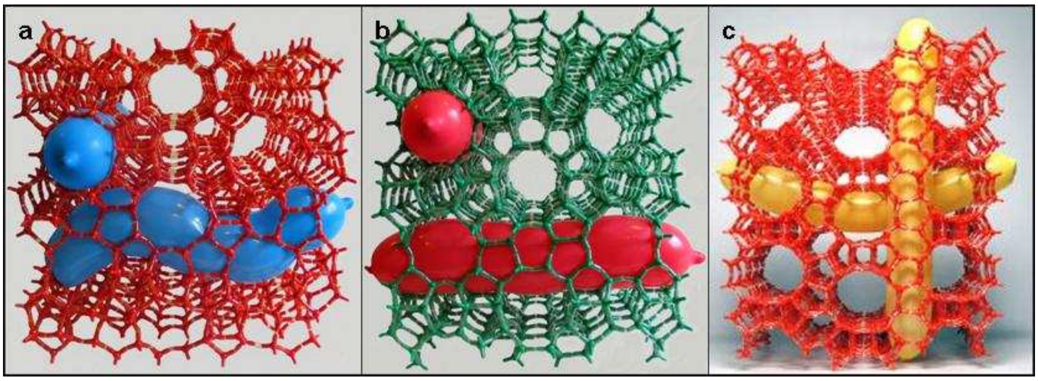

Figure 1.3: Structures of a) MFI, b) MEL and c) BEA

The IZA classification does not take into account the chemical composition of the framework, which has to be provided as side information. For example, ZSM-5 and silicalite-1 have the same MFI type framework While ZSM-5 is a true zeolite, silicalite-1 consists only of silica and oxygen. Other ways to classify zeolites are either by the number of T-atoms in the pore mouth or by the Si/Al ratios. Pores containing 8, 10, 12 or more than 12 T-atoms between the bridging oxygen atoms are defined as small, medium, large and ultralarge pores respectively depending on the number of T-atoms that limit the pore aperture of their largest channels. The diameter of the pores varies between 5 and 20 Å.[14] According to Flanigen's notation[15] low silica zeolites are defined as having $1 \leq Si/Al < 2$, while intermediate zeolites contain $2 \leq Si/Al \geq 5$ and high-silica zeolites contain $Si/Al > 5$.

1.1.2. Catalysis with zeolites

The size and shape of the micropore system induce one of the unique features of zeolite catalysts, namely the shape selectivity. There exist four types of shape selectivity: i) reactant, ii) product, iii) transition-state and iv) molecular traffic control.[3] Reactant selectivity is present when only molecules with the right size and shape will penetrate into the catalytically active micropore system of the zeolite and be converted to products. Product selectivity occurs when a reaction takes place in which several products are possible, but only those who can diffuse out of the microporous system are detected. Bulkier products, if formed, are either converted to less bulky ones or will eventually deactivate the catalyst by blocking the pores. The transition-state selectivity refers to reactions where certain possible transition states are too bulky to fit the channels or cavities of the zeolite and thus can not be formed during the course of the reaction. Molecular traffic control can occur in a zeolite which has at least two different pore systems. The reactants may circulate preferentially in one pore system, while the products will tend to diffuse though another, which will lead to improved diffusion of these species. The shape selectivity can be illustrated by the use of different zeolite structures in the conversion of methanol to hydrocarbons (MTH-reaction), Figure 1.4. Three microporous structures are relevant: CHA (SAPO-34), MFI (ZSM-5) and BEA (Beta), which are small, medium and large pore zeolites, respectively. It should be mentioned that SAPO-34 is a zeotype containing silicon, aluminum, phosphor and oxygen.

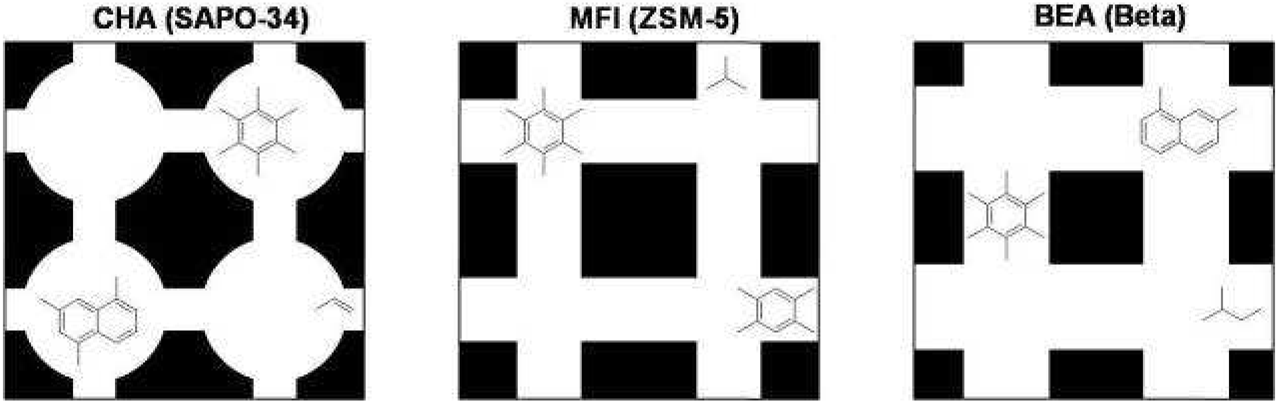

Figure 1.4: Illustration of the pore and cage sizes of CHA, MFI and BEA. Adapted from [16]

SAPO-34 has small channels of 3.8 Å and at the intersection it contains large cavities of around 10 Å which are able to house larger compounds. However, due to the narrow pores, only small compounds are able to leave the cages. ZSM-5 has interconnected straight and sinusoidal channels of 5.3-5.6 Å. In contrast to the SAPO-34 the micropore system of ZSM-5 allows aromatic compounds to leave the catalyst interior expanding the product selectivity. The largest compound able to leave the ZSM-5 catalyst pores is durene (1,2,4,5-tetramethylbenzene).[17] At the pore intersection larger compounds such as pentamethylbenzene and hexamethylbenzene can be formed, but they are not able to diffuse through the pore system.[18, 19] Due to the large pores of zeolite Beta (7.7 Å), the product selectivity is shifted even further towards larger products and even hexamethylbenzene is able to diffuse through the pore system to leave the catalyst.

Zeolites are not only capable of separating molecules by their molecular size but also by their polarity.[14] Since aluminum has a lower number of valence electrons than silicon, the presence of tetrahedrally coordinated aluminum in the zeolite framework leads to an overall negatively charge inside the zeolite framework. The environment inside the channels and cavities becomes therefore increasingly polar and the need for charge-compensating cations arises to balance the overall negative charge of the aluminosilicate framework. Aluminum-rich zeolites have a polar interior which makes them hydrophilic and therefore capable of adsorbing polar molecules such as water. Conversely, zeolites with a low aluminum-content are less polar and therefore more hydrophobic, which makes zeolites capable of adsorbing large amounts of hydrocarbons. During synthesis alkali or alkali earth metals are usually trapped inside the inorganic framework and compensate the negative charge by an ionic bond. In principle all cations which are small enough to physically fit in the zeolite channels can function as charge-compensating cations and can be exchanged by ion-exchange. The type of charge-compensating cations determines some of the properties of the zeolite. If the charge-compensating cation is Cs^+, the zeolite becomes slightly alkaline, while when the framework is balanced by protons, Figure 1.5a, the zeolite becomes acidic. Such sites, Al-O(H)-Si linkages, are known as Brønsted acid sites. Not only Brønsted acid sites may occur in zeolites, but also Lewis acid sites can be present due to defects in the zeolite structure, Figure 1.5b.

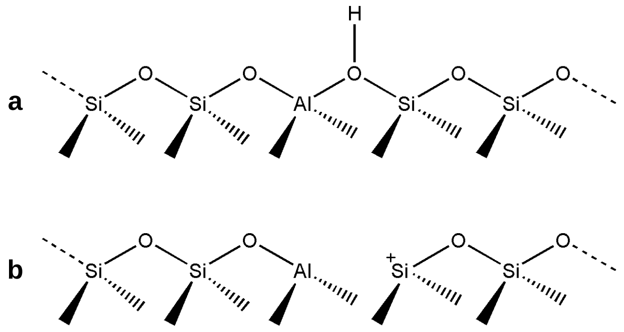

Figure 1.5: Schematic illustration of zeolite acid-sites: a) Brønsted acid site and b) Lewis acid site

By using protons as the charge-compensating cations, zeolites are solid acid materials. The number of Brønsted acid sites is generally determined by the degree of aluminum substitution and denoted as the ratio between silicon and aluminum in the structure. Assuming only Brønsted acid sites are present, a low value of Si/Al corresponds to a high overall acidity and vice versa a high value corresponds to a low overall acidity. The strength of the single acid site is dependent on the Si/Al ratio as the acid strength of a proton at the bridging Al-O-Si group depends on the number of next-neighbouring aluminum atoms.[20] When the distance between two aluminum atoms increases, the strength of each acid site increases meaning, the higher Si/Al the stronger is the individual acid site. Maximum acidity is obtained for Si/Al ratios above 10.[21, 22] As recapitulation, Table 1.1 summarises the trends in the properties of the zeolite as a function of the Si/Al ratio. In zeotypes the strength of each acid site dependent on which type of element is incorporated in the framework in the following order: Al > Ga > Fe > B.[23]

Table 1.1: Trends in the properties of zeolites as a function of the Si/Al ratio. Modified from [24]

Si/Al decreases		Si/Al increases
↑	**Number of cations**	↓
↓	**Stability in acidic solutions**	↑
↓	**Acid strength zeolite proton**	↑
↓	**Thermal Stability**	↑
↑	**Hydrophilic character**	↓
↓	**Hydrophobic character**	↑
↑	**Affinity for polar molecules**	↓
↓	**Affinity for apolar molecule**	↑

By tuning the Si/Al ratio in a certain zeolite, it is therefore possible to control the adsorption properties and the strength and concentration of the acid sites. These material properties, together with the intrinsic micropore system which can direct a given catalytic reaction to a desired product, make zeolites to one of the preferred choices for many catalytic applications. Examples for these industrial applications are found in catalytic fuel-upgrading in refineries and in the production of various petrochemicals.[5, 25, 26]

1.1.3. Zeolite synthesis

Zeolites are normally prepared under hydrothermal conditions, *i.e.* in an aqueous solution at elevated temperature and autogenous pressure. The crystallisation temperatures are usually 80-110 °C for low-silica zeolites and 110-200 °C for high-silica zeolites. These conditions enable complete crystallisation within a few hours to several weeks, depending on the zeolite type and gel composition.[25] A typical crystallisation procedure involves the use of water, sources of silicon and aluminum, a mineralizing agent and a structure-directing agent (SDA).[27] Usually the sources of silicon and aluminum are dissolved or suspended in water along with the SDA together with the mineralizing agent. The homogenised synthesis gel is afterwards transferred to an autoclave and heated for the required time. The density of the gels formed might vary significantly from almost solid-like to low-viscous depending on the composition. After the crystallisation the product is filtered off and washed with water. After drying the product calcination is necessary to remove the organic template by thermal composition and by burning off the decomposition products. The mineralizing agent is added to catalyse the breaking and formation of T-O-T bonds. The most commonly used mineralizing agent is the hydroxide ion which entails that zeolite synthesis is often conducted at high pH. The fluoride ion has also proven suitable as mineralizing agent which makes it possible to synthesise zeolites at neutral pH conditions. The fluoride route is very useful when elements are to be incorporated in the zeolites framework which would form insoluble precipitate at high pH. SDAs can be soluble organic species such as quaternary ammonium ions and/or alkali metal ions such as Na^+ or K^+. Organic SDA molecules added to the synthesis gel are often referred to as templates because they direct formation of a certain type of zeolite.

Ever since the discovery that zeolites may be artificially synthesised in the laboratory, researches have been trying to understand how these microporous materials crystallise from complex mixtures. The difficulty in trying to understand the precise details of the mechanism and processes occurring during the formation of a zeolitic material is due to the extreme complexity of hydrothermal crystallisations. The reactions occur in multi-component systems in which there are a plethora of interactions, chemical reactions, equilibria and crystal nucleation and growth processes taking place throughout a heterogeneous reaction mixture. Further to complicate matters, many of these processes are interrelated and change with time over the course of the crystallisation.[1] Nevertheless, several authors have proposed mechanism for the synthesis of zeolites. In general the crystallisation can be considered to follow an idealised process involving three states, as illustrated in Figure 1.6.

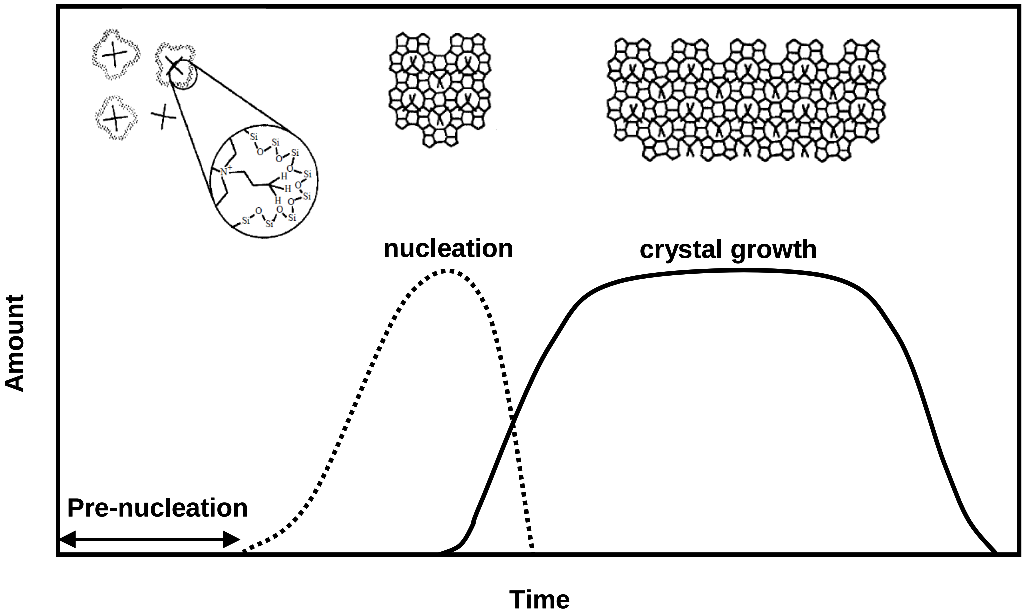

Figure 1.6: Schematic illustration of nucleation and growth curves for a hydrothermal zeolite synthesis. Modified from [1]

Initial is the dissolution of the solid starting reagent by the solvent water to form a randomly distributed array of reaction components in the form of active monomer or oligomer species. In the first step no crystalline material is though detected yet. The second step is nucleation. Here the precursor species organise into simple ordered structures that form countless seeds within the gel. Last is the growth period, where the nuclei increase in size to form the final material in which long range order is observed. The crystal growth phase continues until all the amorphous material is transformed into the crystalline zeolite structure. If the synthesis is not stopped timely the zeolite product may transform into a denser phase such as quartz owing its metastable property. When the different stages occur depends on the reaction conditions like composition, temperature, pH, pressure and reaction cell volume.[28]

A very common practice is to add a small amount of the desired product phase, called seeds, to encourage the nucleation and growth of that phase. Seeds can be generated *in situ* using a procedure called aging. Aging a gel, by allowing it to stand either at room temperature or at elevated temperatures which are below the normal crystallisation temperature for the zeolite phase of interest, allows the system to equilibrate and generate seed nuclei which, when the gel is heated, will increase the rate of crystallisation. With up to 5 wt% based on silicon, relatively large amounts of seeds may be used in zeolite synthesis.

1.1.4. Diffusion effects

Even though conventional zeolites are remarkable materials with tuneable properties, high surface area and high thermal stability the presence of the micropore system may in some cases also limit the catalytic performance of zeolite catalysts. In some hydrocarbon reactions the size of a molecule closely matches the pore size of a zeolite and therefore is almost in physical contact. This will inevitably slow down the reaction rate since the mass transfer of reactants, intermediates and products to and from the active sites inside the micropores will be severely restricted. The intracrystalline migration in theses systems is termed configurational diffusion and is characterised by diffusivities in the range of 10^{-8} to 10^{-20} m^2/s, (see Figure 1.7). It is strongly dependent on the size and nature of the reactant, the type of molecular sieve and temperature.[14] In comparison, diffusivities in the Knudsen regime, which is the dominant mechanism for mesoporous materials, are in the range of 10^{-5} to 10^{-8} m^2/s. Concerning the pore diameter of zeolites one should bear in mind that due to lattice vibrations the effective pore size is somewhat larger than the crystallographic one. Still, in zeolite micropores the diffusivities are often so low that the overall rate-limiting factor is in fact configurational diffusion and the reaction is said to be in a diffusion-controlled or limited regime.[14]

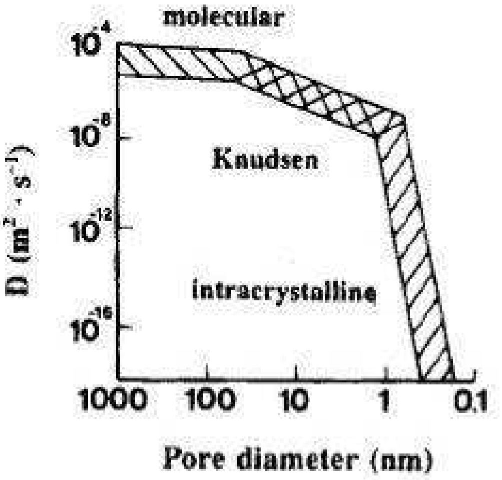

Figure 1.7: Relation between pore diameter and typical diffusitivites illustrating three types of diffusion regimes: Molecular, Knudsen and intracrystalline. Adapted from [14]

Diffusion limitation in zeolite catalysis can entail that the reaction will not operate at its full potential since the observed rate of a given reaction will be lower than the intrinsic rate. Another issue is that the zeolite crystal is not used efficiently for catalysis, since only the outer-most part of the zeolite crystals is utilised in the chemical reaction, as illustrated in Figure 1.8 as the green zone. The concentration of reactant molecules in the bulk of the zeolite crystal will rapidly drop as the distance to the exterior surfaces increases (Figure 1.8) since it is not possible for the molecules to diffuse into the core of the zeolite crystals and be converted.[29]

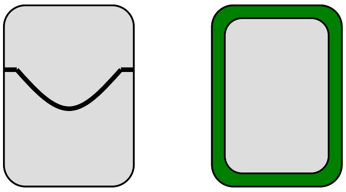

Figure 1.8: Schematic illustration of the concentration profile cross-section of a zeolite crystal (left) and the corresponding utilised reaction zone shaded in green (right)

Several strategies have been proposed to enhance the diffusion of reactants, intermediates or products. One way is to increase the pore diameter of the zeolite, but this will necessarily influence the molecular sieve effect and the shape selective properties of the zeolite. Generally, the challenge is to improve the accessibility to the active sites without altering the zeolite nature *i.e.* affect the shape selectivity. By reducing the zeolite crystal size the mean diffusion path is unquestionable decreased, Figure 1.9a and 1.9b, and it is possible to utilise a larger part of the zeolite crystal and still maintain the zeolite properties. However, zeolite crystals are often in the range of 0.5-10 µm[1, 29] and to decrease the size and still be able to separate the small zeolite crystals from the reaction mixture by filtration is often difficult owing to the colloidal properties of such materials. The mean diffusion path length can also be decrease by introducing an auxiliary pore system consisting of larger pores that intersect the micropores, Figure 1.9c. The additional larger pore system is used for molecular transport to and from the active sites in the micropore deep within the structure without altering the zeolite properties.

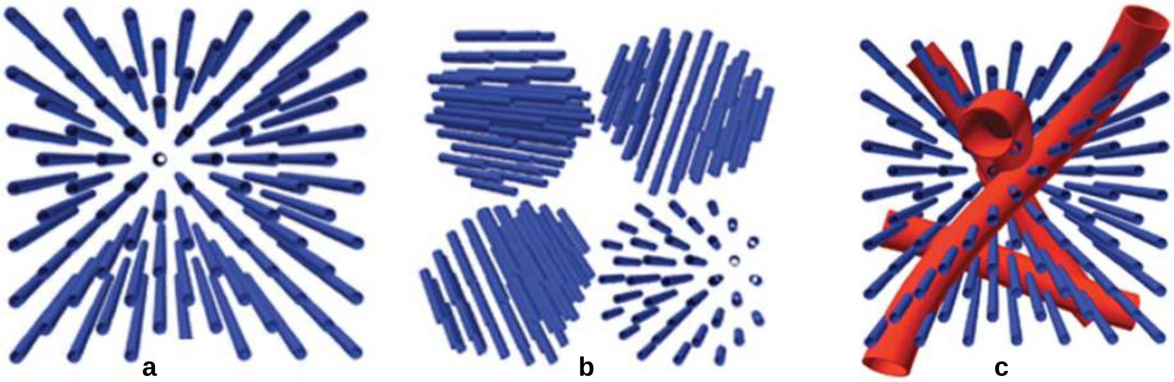

Figure 1.9: Illustration on how to decrease the mean diffusion path length from conventional zeolite (a) by decreasing the zeolite crystals (b) and introducing an auxiliary pore system (c). Micropores are illustrated by blue tubes and the larger pores that intersect the micropores are red tubes. Adapted from [30]

When a material features porosity in at least two different size ranges in the micropore (less than 2 nm), mesopore (2-50 nm) or macropore (larger than 50 nm) region the resulting material is often termed hierarchical.[30] Zeolites containing both micropores and mesopores combine the shape selectivity, hydrothermal stability and possibility for high acidity typical of conventional zeolites with highly efficient transport of reactants and products due to mesopores. Therefore the combination of micropores and mesopores in hierarchical zeolite crystals renders some highly beneficial effects with respect to catalytic applications.[31]

1.1.5. Mesoporous zeolites

Mesopores can be present in hierarchical zeolite either inter- or intracrystalline. If the auxiliary porosity of the zeolite crystals is classified as intercrystalline the mesopores are due to pores or voids between the crystals. On the other hand, if the auxiliary porosity is intracrystalline the mesopores are present in each zeolite crystal connecting the micropores with larger non-crystallographic mesopores. This means that there are three kinds of mesoporous zeolites, Figure 1.10; nanosized zeolite crystals, supported zeolite crystals on a mesoporous support material or mesoporous single zeolite crystals.[30]

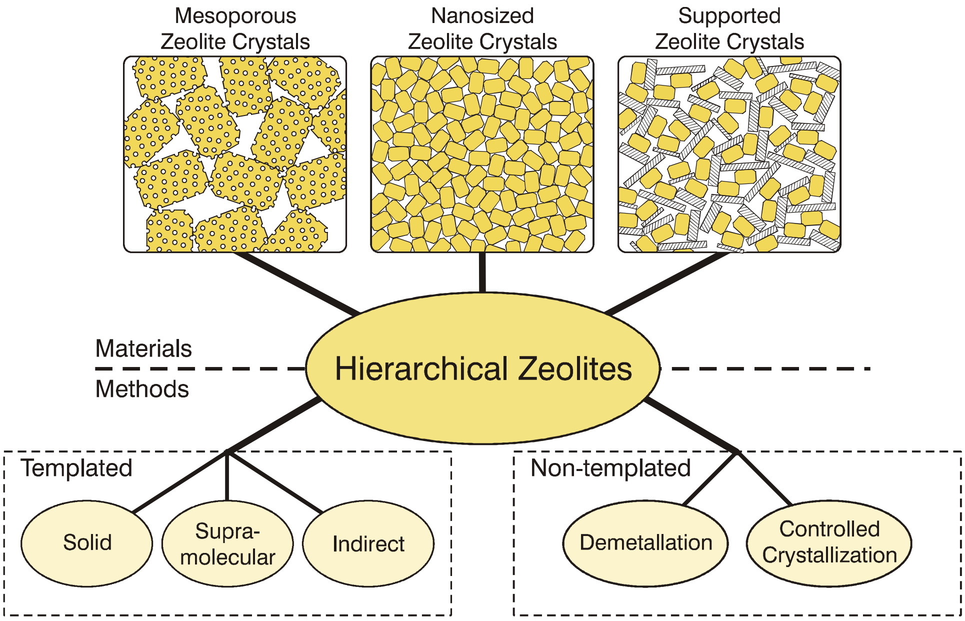

Figure 1.10: Categorisation of classes of hierarchical zeolites materials. Adapted from [30]

As a consequence of the packing of nanosized zeolite crystallites, typical smaller than 100 nm, intercrystalline pores or voids can be present in the material. The pore size and geometries of these pores are determined by the size, shape and packing of the zeolite crystals which can obviously be packed more or less loosely. The supported zeolite crystals are characterised being dispersed or supported in the pore system of another material. This creates a material which is not a purely zeolitic material but instead a composite material. In this case the support material provides the pore required for improving mass transport to and from the zeolite crystals. The mesoporous zeolite crystals include ordinary zeolite crystals having additional porosity present in each individual zeolite crystal.[32]

The preparation of mesoporous zeolite crystals can be conceived in two conceptually different ways. The mesopores are either introduced directly during the crystallisation of the zeolite or they are introduced by a post-synthetic treatment step, also referred to as templating or non-templating methods, Figure 1.10. Templating is divided into three groups: solid templating, supramolecular templating or indirect templating. In solid and supramolecular templating, the zeolite crystals is grown in the presence of either a solid material or a supramolecular assembly of organised surfactant molecules which is eventually removed to generate porosity. Typically the template is removed by combustion but in principle it might also be removed by dissolution, sublimation or extraction.[32] A variety of solids have been applied to control the mesopores formation during zeolite crystallisation. Especially the use of different types of porous carbons[33-38] seems to be a versatile approach but also other solid templates have been investigated such as organic resins[39], aerogels[40, 41], polymers[42, 43], biological templates such as bacteria[44], plants[45, 46] and starch[47] as well as purely inorganic compound such as $Mg(OH)_2$[48] and $CaCO_3$[48, 49]. In supramolecular approaches several molecules have been investigated. One type of applied template are tuneable organosilanes such as $[(CH_3O)_3SiC_3H_6N(CH_3)_2C_nH_{2n+1}]Cl$[50,51] which is used as both a silica source and supramolecular template and by varying the alkyl chain length it is possible to obtain mesoporous materials with controlled mesopore diameter up to 20 nm. The third templating method is the indirect templating which consists of two steps: A templated mesoporous nonzeolitic material is first formed and in a separate step the mesoporous nonzeolitic material is more or less completely transformed into the mesoporous zeolite, or the zeolite is deposited onto the templated mesoporous material. Both cases result in a composite material comprising zeolite crystals embedded in or deposited onto a mesoporous material.[32, 52, 53] The templating effect is considered to be indirect because the template is not present when the zeolite crystallises. However, the resulting mesoporous zeolite material can still maintain some of the order or structure of the original template if only limited reorganisation of solid material occurs during zeolite crystallisation.[30] Most reports on indirect templating are concerned with the partial crystallisation of mesoporous materials into zeolite structures.[54-57] Using this methology, highly mesoporous and relatively stable zeolite materials have been prepared, particular when the thick-walled SBA-15 have been used as the starting material.[54, 55]

The non-templating methods fall under two general headings: controlled crystallisation and demetallation. In the controlled crystallisation [58, 59] the crystallisation conditions are regulated to favour nucleation over crystal growth so that predominant nanosized zeolite crystals are formed. In many ways this is a very desirable way to improve the accessibility of the active sites in zeolite catalysts since it does not require discovery of an entirely new structure type but merely the development of a modified synthesis procedure that favours nucleation over growth for the desired zeolite material. One drawback is that nanocrystals typically possess a relatively low internal surface area due to the decrease in microporosity with decreasing crystal size.[59] In the demetallation method, intracrystalline mesopores are introduced by extracting one constituent from the framework of a conventionally prepared zeolite material, Figure 1.11.

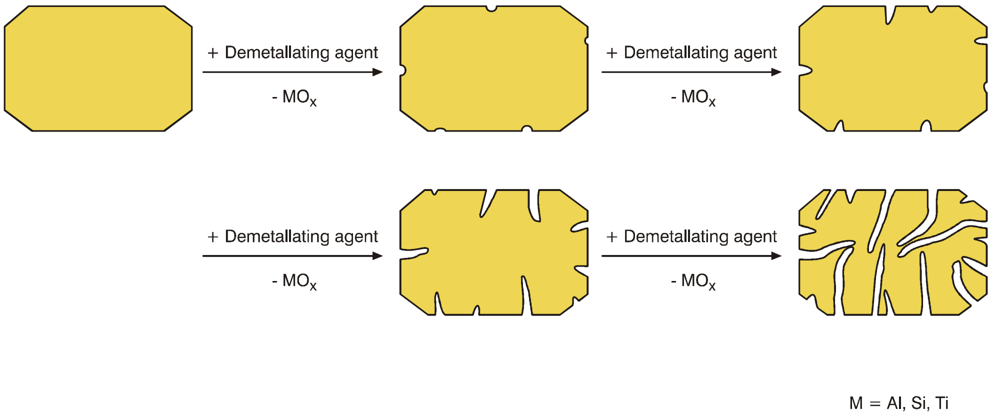

Figure 1.11: Schematic illustration of the demetallation method used for the introduction of intracrystalline mesopores by more or less selective dissolution of part of the zeolite crystal. Adapted from [29]

The selective extraction leads to removal of some of the metallic or semimetallic components of the zeolite typically in the form of soluble oxoanions but it can also be in the form of complexed species.[29] The traditional method is dealumination which involves preferential extraction of framework aluminum by hydrolysis of the Al-O-Si bond through calcinations, steaming, acid leaching or chemical treatment.[7, 60, 61] Even though steaming is used industrially to produce mesoporous zeolites[30] dealumination is often not a viable route to create mesoporosity since it will simultaneously lead to a dramatic lowering of the number of acid sites that are typically desirable for catalysis. Instead selective removal of silicon, the so-called desilication, is an attractive method to create intracrystalline mesoporosity by the use of a strong base like NaOH, $NaAlO_2$, Na_2CO_3, LiOH and KOH.[61-63] Most zeolites have high concentration of silicon and relatively high mesoporosities can be achieved. Several factors such as time, temperature, type of base, base concentration and material related parameters like framework Si/Al, crystal size and different framework types determine the degree of mesoporosity of the resulting zeolite materials.[62, 64, 65] Especially, the zeolite framework Si/Al influences the degree of mesoporosity as illustrated in Figure 1.12.

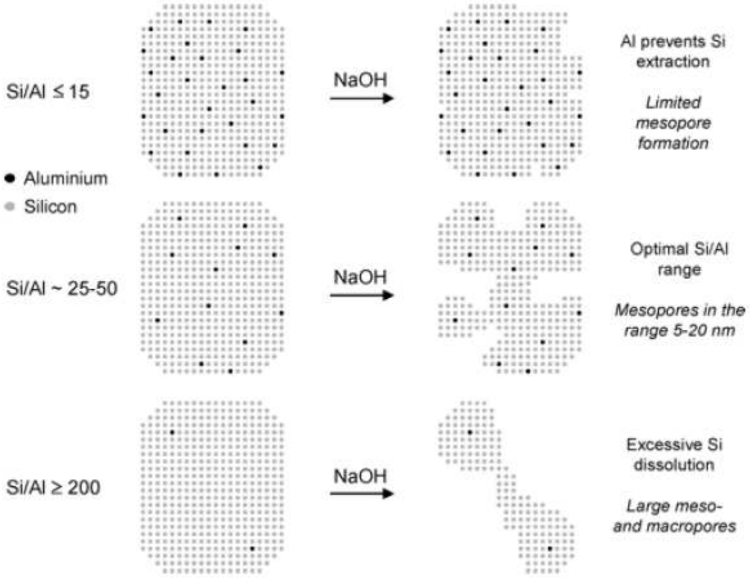

Figure 1.12: Effect of Si/Al on the type of mesopores generated in zeolite crystals by alkaline treatment. Adapted from [63]

As a result of the negatively charged AlO_4^- tetrahedra, aluminum in framework positions suppresses the extraction of neighbouring silicon species. The hydrolysis of the Si-O-Al bond in the presence of OH^- is hindered compared to the relatively easy cleavage of the Si-O-Si bond in the absence of neighbouring aluminum tetrahedral. Materials with relatively high density of framework aluminum (low Si/Al) are relatively inert to silicon extraction whereas relatively low aluminum content (high Si/Al) induces the opposite effect. An intermediate framework aluminum content of Si/Al 25-50 appropriately regulates the extent of silicon extraction leading to controlled porosity development. However, operating in the optimal Si/Al window is not the only condition for treatments success, since the type of zeolite framework also plays a quite decisive role in the outcome of the desilication.[63]

Even though the desilication procedure seems to be a useful, simple and quite versatile method for introducing intracrystalline mesoporosity in zeolite crystals it still has some drawbacks: i) Loss of zeolite material as the generation of mesopores occurs by partial dissolution, ii) difficult control of the Si/Al ratio in the resulting zeolite, iii) almost no direct control of the size and geometry of the created mesopores, iv) appearance of extra-framework aluminum species by which the type of acid sites is changed from Brønsted to Lewis acidic sites which can be very important for the catalytic activity, v) the effectiveness depends on Si/Al ratio and type of framework, vi) chance of partial amorphization of the zeolite framework which can lead to a partial blockage of pores and/or active sites and vii) typically quite harsh desilication conditions as zeolites are quite stable materials.

It is possible to introduce a very high degree of intracrystalline mesoporosity in zeolite crystals in a much more controlled manner by using a templating method. Such mesoporous zeolite single crystals are prepared by nucleating the zeolite crystals inside an inert carbon matrix so the zeolite crystals grow and partially encapsulate the carbon. After complete crystallisation the carbon is removed by combustion, Figure 1.13.[35]

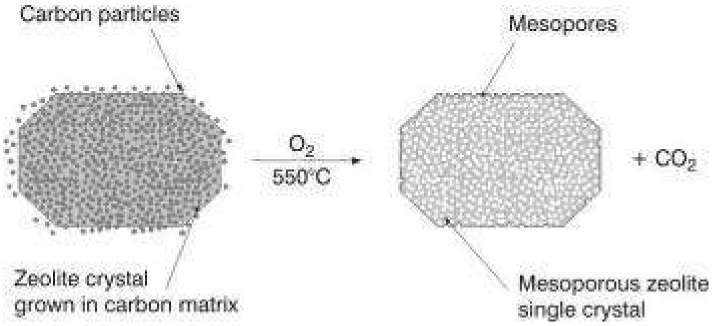

Figure 1.13: Schematic illustration of preparation of a mesoporous single zeolite by combustion of carbon particles encapsulated in zeolite crystals during crystallisation. Adapted from [35]

The carbon-templating approach seems to have several advantages for introducing mesopores into zeolites compared to the demetallation. Firstly, it does not lead to the partial destruction of the zeolite crystals and the method is in principle applicable to all zeolites irrespective of their structure and chemical composition and therefore also to zeotype materials that do not necessarily contain silicon or aluminum. Second, it provides some opportunities for tailoring the pore system to the desired application by choosing suitable carbon templates. Importantly, the introduction of mesopores does not alter the Si/Al ratio but allows independent control of the mesoporosity and the acidity. Industrially the use of the method might be hampered by the fact that suitable carbon templates can be quite expensive and because efficient introduction of the zeolite gel into the carbon can require more elaborate synthesis steps.[30] From a safety point of view, it is very difficult to apply the removal of a high amount of carbon by combustion on a large industrial scale under controlled conditions.[61] Recently the hurdle regarding price was alleviated to some extent by the so-called *in-situ* carbon templating method in which the carbon template is generated by decomposing sugar inside the pores of the silica source used for zeolite crystallisation.[66]

No matter which type of synthesis strategy is used to prepare mesoporous zeolites, there are several examples that the improved transport properties of the mesoporous zeolite catalyst do indeed result in an increased catalytic activity and/or selectivity and/or catalyst lifetime.[67-70] With the necessity for the refining industry to treat heavier feedstocks, the optimisation of the accessibility of zeolite-based catalysts for large reactant molecules is of paramount importance and the preparation of mesoporous zeolites are therefore anticipated to attract significant attention in the forthcoming years.

1.1.6. Summary

Zeolites are among the most studied families of heterogeneous catalysts and they have been shown to be useful catalysts for an overwhelming range of important catalytic reactions. This success can be attributed to the possibilities for tailoring the intrinsic catalytic properties of zeolites by carefully controlling the strength and number of acid sites, the pore size and pore geometry and the redox properties. However, in many cases the sole presence of micropores in zeolite catalyst results in too low diffusion of reactants, intermediates and products inside the zeolite. One approach to improve mass transport without altering the microporous structure is by the introduction of mesopores into each zeolite crystal. Different strategies can be used to prepare zeolites with intracrystalline mesopores. Roughly, it can be divided into two categories either directly during the crystallisation of the zeolite by the use of different types of templates or by a post-crystallisation treatment step like demetallation. Industrially the destructive dealumination pathway is used where intracrystalline mesopores are introduced by extracting aluminum from the framework of a conventionally prepared zeolite material by steaming. This is a simple and valid route but it still has drawbacks *i.e.* partial amorphisation of the zeolite framework and lowering of active sites. Even though over the years enormous progress has been monitored in the domains of synthesis and characterization of mesoporous zeolites their application in industry is still limited.

1.2. Characterization techniques

In general, the characterization of a catalyst has to provide information about (i) its structure and morphology, (ii) its chemical composition, (iii) its ability to sorb and retain molecules and (iv) its ability to chemically convert molecules.

1.2.1. Structural properties

X-ray powder diffraction (XRPD) is by far the most important technique for structural characterization of crystalline materials.[71] Each crystalline phase has a characteristic powder pattern and beside information about the crystal structure several features about the sample can be extracted from a powder diffraction pattern using the peak positions, their relative intensities, their width and the background, Figure 1.14.[72]

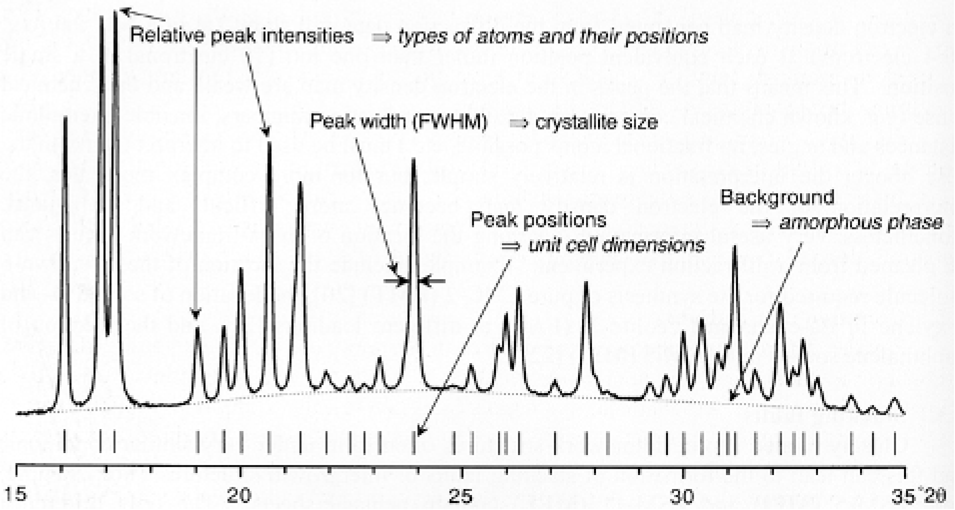

Figure 1.14. The relevant features of a powder diffraction pattern and their origin. Adapted from [72]

There are two main factors that determine powder patterns: i) the size and shape of the unit cell and ii) the atomic number and position of the atoms in the cell. The peak positions in a powder pattern (usually measured as 2θ degrees) are determined only by the size and shape of the unit cell. The relative intensity of the peaks depends on which atoms are present and where they are located in the unit cell. The intensity of each reflection is not only affected by the position of all atoms in the unit cell, but can also be influenced if the crystallites in the powder lie in a preferred orientation. The width of the peaks gives an indication of the crystalline quality and the crystal size, the latter can be determined by the Debye-Scherrer Equation.[71] The background indicates whether or not an amorphous material is present in the sample.[72, 73]

Even though diffraction is the single most powerful experimental technique for determining the crystal structure of zeolites[73] care must be taken when evaluating the crystal size of single crystal mesoporous zeolites. According to Egeblad *et al.*[29] peaks obtained for large mesoporous zeolite single crystals can be as broad as the peaks obtained for a nanosized zeolite sample, Figure 1.15. The crystal size determined by the Debye-Scherrer equation would consequently suggest the crystal size of the mesoporous zeolite to be in the nanosized range. Assuming the mesoporous zeolite is a single crystal Egeblad *et al.* explain that it can be due to the disturbance of the longer-range ordering by the presence of non-crystallographic voids or mesopores and thus, XRPD cannot be applied to determine whether the mesopores in mesoporous zeolite materials are intercrystalline or intracrystalline, *i.e.* whether the individual crystals are nanosized or large but mesoporous. Furthermore they suggest to use more indirect imaging techniques such as electron microscopy when determining the size of individual crystal of mesoporous zeolites.

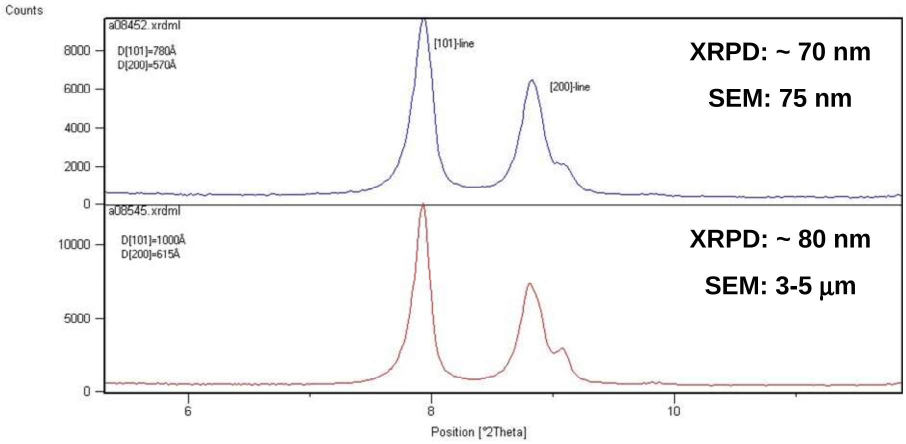

Figure 1.15: Close-up on the [101] and the [200]-reflections in XRPD patterns of a) nanosized zeolite crystals and carbon-templated mesoporous zeolite crystals. Adapted from [29]

In this work XRPD patterns are used to identify the crystal structure of the synthesised materials, to estimate the crystal size using the Debye-Scherrer equation, to evaluate whether or not a post-synthesis treatment has induced structural changes and to establish whether or not impurities, amorphous or crystalline, are present in the sample. All synthesised materials were characterised by XRPD at Haldor Topsøe A/S. The XRPD patterns were recorded using Cu-Kα radiation in the 2θ interval 5-70° using a Philips X'pert powder diffractometer.

1.2.2. Textural properties

In catalysis an accurate assessment of the porous characteristics is essential since pore size and topology play a significant role. N_2 physisorption measurements at 77 K is one of the most widely used technique providing information on both surface area and pore size distribution in the micro-, meso- and macroporosity range (~0.5-200 nm). [74-76]

Most N_2 physisorption isotherms for solid materials can be classified as one of Types I-VI according to the IUPAC classification system[2], shown in Figure 1.16.

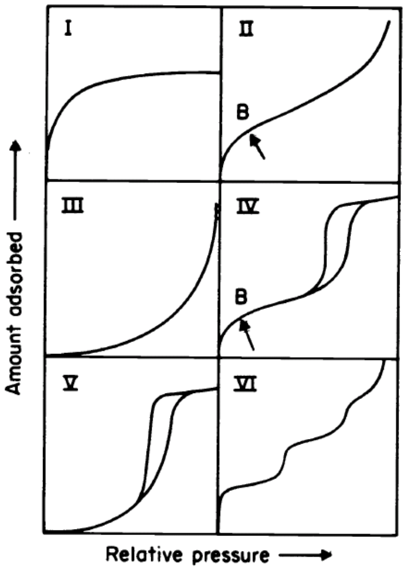

Figure 1.16: The five types of isotherms as classified by IUPAC. Adapted from [2]

For all isotherms the amount of adsorbed N_2 gradually increases as its partial pressure is increased. At some point adsorption becomes equivalent to a monolayer, which eventually become equivalent to a multilayer and finally merges into a condensed phase.

The Type I isotherms are typical for conventional zeolites and other microporous solids. The micropores are filled and emptied at similar low relative pressures, resulting in a reversible ad- and desorption isotherm with the limiting uptake being governed by the accessible micropore volume. Type IV isotherms are obtained for mesoporous materials. The most characteristic feature is the hysteresis loop between the adsorption and desorption branches, which is due to capillary condensation of the adsorbate. The hysteresis is observed since mesopores of a specific size are emptied at a pressure lower than the pressure at which they are filled. The initial part of the isotherm can be attributed to monolayer adsorption and the limiting uptake at relatively high P/P_0 indicates complete pore filling.

Type II, III, V and VI are not commonly observed for zeolite materials, since they are typical for non-porous, macroporous or materials with weak forces of adsorption.[2, 77] Information about the shape of the mesopores can be deduces from the shape of the hysteresis loop.[76] However, since most mesoporous zeolites have a broad variation in pore shapes and sizes, cautions should be taken when evaluating the shape of the isotherms.

Microporous ZSM-5 can in some cases display a hysteresis loop, Figure 1.17 even though it does not contain any intracrystalline mesopores. In most cases the hysteresis loop is associated with pore condensation in mesopores between the crystals (interparticle voids).[76]

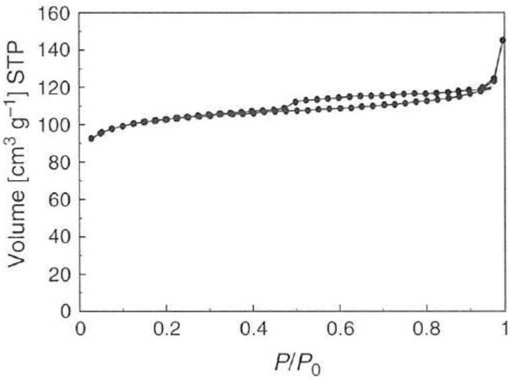

Figure 1.17: Nitrogen Physisorption on a ZSM-5 zeolite with Si/Al=23. Adapted from [76]

Using the Brunauer-Emmett-Teller method (BET)[79] it is possible to estimate the surface area from physisorption measurements. The BET method is in a strict sense not applicable in case of microporous materials.[76, 77] In the BET equation it is necessary to know the volume equivalent of an adsorbed monolayer. Since it is difficult to separate the process of mono-multilayer adsorption from micropore filling the surface area obtained by the BET method on microporous solids does not reflect the true surface area but should instead be considered as a fingerprint.

To acquire information about the micropore volume the t-plot method proposed by Lippens and de Boer[79] can be used. Besides estimating the micropore volume the method can provide the specific surface area of mesopores and the external specific surface area.[80] If a detailed study is wanted on the micropore size distribution another adsorption technique is required because the usual adsorption technique starts at P/P_0 around 0.01 and as a consequence the micropores are already filled to a large extent.[76]
A widely used method for mesopore analysis is the Barett-Joyner-Halenda method (BJH)[81]. Using the BJH model the mesopore volume and mesopore size distribution can be performed on both the adsorption or desorption branch of the isotherm. Even though various authors[74, 82, 83] have shown that the BJH model in general underestimates the “real” mesopore size with approximately 25 % the ready accessibility of the model in commercial software means that this model is still very widely used. Therefore the derived pore size distribution must only be used as a fingerprint of the resulting pore structure. Depending on the material and the use of either the adsorption or desorption branch the BJH method can result in artefacts in the pore size distribution at diameters around 2 and 4 nm.[74-76] The artefacts at diameter around 2 nm and 4 nm are not reflecting the porous properties of the material but are associated with properties of the adsorbed nitrogen, Figure 1.18.

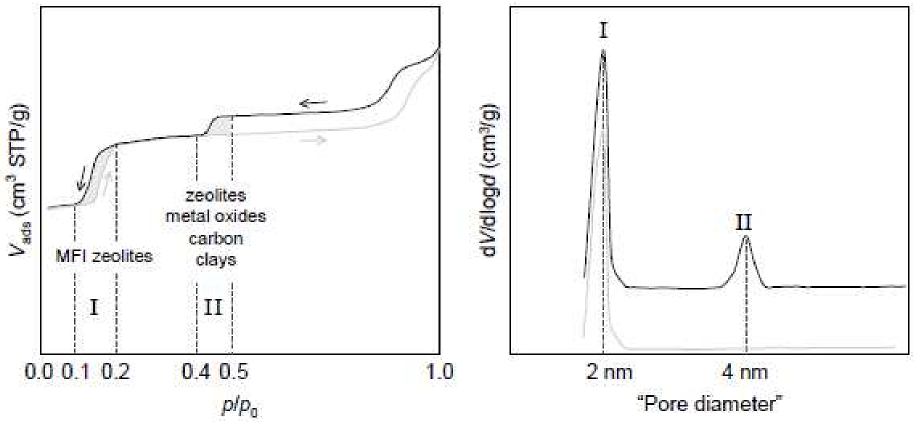

Figure 1.18: N_2 adsorption and desorption isotherms at 77 K of silicalite-1 and corresponding pore size distribution derived from BJH model. Region I: Fluid-to-crystalline like phase transition; region II: lower closure point of the hysteresis loop. Adapted from [74]

The artefact around 2 nm, which can occur from both the adsorption and desorption branch, is only observed for MFI type zeolites with high Si/Al ratios and depends also on the presence of defects.[74] For this type of materials adsorbed N_2 can make a phase transition from a disordered "fluid-like" phase to a more ordered "crystalline" phase which will result in a hysteresis loop between P/P_0=0.1-0.2 and consequently does not indicate mesoporosity.[75, 84] The artefact around 4 nm is only observed using the desorption branch to calculate the pore size distribution and is common for zeolites especially in the cases of broad pore size distribution, pore network and cage-like structures. The artefact arises from the forced closure of the hysteresis loop around P/P_0 = 0.42 in the case of using N_2 at 77 K.[82, 85, 86] The adsorption branch is not sensitive towards this forced closure and will not show any pore around 4 nm.

As artefacts disturb the pore size distribution, especially when using the desorption branch, it is recommended to compare the pore size distribution from both the adsorption and desorption branch and also to investigate the isotherm since it can provide information about the pore network.[74]

All materials presented in this work were characterised by N_2 physisorption measurements performed at liquid nitrogen temperature (77K) on a Quantachrome Autosorb 3B instrument. The zeolite samples were outgassed in vacuum at 300 °C for 16 h prior to measurement. Total surface areas were calculated according to the BET method. Micro- and mesopore volumes and mesopore size distribution were determined by the t-plot method and the BJH method, respectively.

1.2.3. Acidic properties

Acidity is one of the most important properties of zeolites in relation to catalysis. As solid acids zeolites are characterised by the type (Brønsted or Lewis), the concentration and the strength of the acid sites. As stated previously, the type and concentration of acid sites are primarily controlled by the presence of aluminum atoms in framework (tetrahedral positions) and non-framework positions[87], while the strength of each site is especially controlled by the chemical composition and hence the polarity of the lattice[20]. The strongest Brønsted acid sites are formed with isolated Al-O tetrahedra and the strength of each Brønsted acid site gradually decreases with increasing aluminum content in the framework due to the overall increase in polarity.[89]

It is commonly accepted that the Lewis sites in zeolites are associated with both framework and extra-framework aluminum species. The exact structure of the extra-framework species is, however not known with certainty but the neutral species AlOOH and $Al(OH)_3$, $(Al(OH)_3)_2$ and oxoaluminum cations such as AlO^+, $Al(OH)_2^+$ and $Al(OH)^{2+}$ have been proposed.[90]

Several techniques can be used to investigate the acidic properties of zeolites. In this work Temperature-Programmed Desorption of Ammonia (NH_3-TPD) is used as a relatively fast technique to estimate the concentration (mmol/g) and the corresponding Si/Al ratio. Infrared spectroscopy and ^{27}Aluminum Magic-Angle Spinning Nuclear Magnetic Resonance spectroscopy (^{27}Al MAS NMR) is primarily used to investigate the type of acid sites including the presence of extra-framework aluminum.

1.2.3.1. Temperature Programmed Desorption of Ammonia

Temperature Programmed Desorption of Ammonia (NH_3-TPD) has for a long time been used to characterise acid sites of zeolites.[91-93] Since ammonia is a strong base and a relatively small molecule (kinetic diameter 2.62 Å) with a lone pair of electrons, it can reach practically all acid sites. In NH_3-TPD it is assumed that the intracrystalline zeolite surface is homogeneous without interactions among adsorbed NH_3 molecules and the amount of adsorbed NH_3 is less than that required for monolayer coverage. Furthermore it is assumed that no re-adsorption of ammonia takes places during desorption.[92]

In the NH_3-TPD curves of H-zeolites peaks are generally observed in two temperature regions. The regions below and above 673 K are referred to as low-temperature (LT) and high-temperature (HT) region, respectively.[94, 95] The peaks in the HT region can be attributed to desorption of NH_3 from strong Brønsted and Lewis sites. The assignment of the LT region seems more controversial. According to Hidalgo *et al.*[93] the concentration of Brønsted sites is proportional to the intensity of the HT TPD peak and to that of the LT peak, suggesting that the appearance of the LT peak was also connected somehow with the presence of strongly acidic hydroxyls as sorption sites. Several authors[91, 92, 96-98] believe that for H-ZSM-5 the LT peak is ascribed to desorption from weakly acidic silanol groups, possible weak Lewis acid sites, extra-framework alumina species or the release of NH_3 hydrogen bonded to NH_4^+ cations.

It is difficult to compare NH_3-TPD results since much depends on the experimental conditions such as rate of temperature increase and evacuating temperature. In Figure 1.19 NH_3-TPD curves are shown for the same H-ZSM-5 sample at different evacuating temperatures (T_{ev}) prior to desorption of NH_3 and they clearly have significantly different appearances.

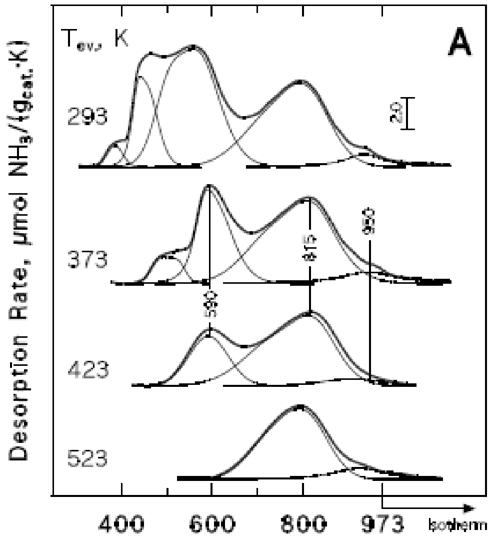

Figure 1.19: NH_3-TPD curves obtained for H-ZSM-5 after evacuating the NH_3-loaded samples at the indicated temperature T_{ev}. The thin lines under the curves give the best-fit component peaks. Adapted from [98]

Even though Christensen *et al.*[68] have shown that there exists a good correlation for determining the amount of framework aluminum using NH_3-TPD, Infrared spectroscopy and ^{27}Al MAS NMR for conventional and mesoporous H-ZSM-5 care must be taken using NH_3-TPD. Among the limitation of NH_3-TPD is that it can distinguish sites by sorption strength only, but Lewis and Brønsted sites are indistinguishable. Moreover, desorption may proceed simultaneously from sites of different types resulting in more or less overlapping TPD peaks. [98]

The acidity was determined by NH_3-TPD, using the following procedure: 40 mg of the sample was pre-treated by heating the sample to 500°C in a flow of nitrogen (75 ml/min, heating ramp 20 °C). The temperature was kept for 120 min before cooling to 150 °C. At this temperature the NH_3 gas was adsorbed by switching to 2% NH_3/He (75ml/min) for 30 min. To remove physically adsorbed ammonia the sample was flushed with N_2 (75 ml/min) at 150 °C for 4 hours prior to desorption measurements. Subsequently, the sample was heated to 600 °C (heating ramp 10 °C/min). The rate of NH_3 desorption was monitored by measuring the weight loss of the sample with thermogravimetric analysis. The total amount of desorbed NH_3 was calculated from the area under the TPD curve assuming one NH_3 molecule per acid site. All NH_3-TPD measurements were performed at Haldor Topsøe A/S.

1.2.3.2 Infrared spectroscopy

One way to distinguish between Brønsted and Lewis acid sites is by using Fourier Transform Infrared spectroscopy (FT IR). Acidity regarding strength, location and accessibility cannot be assessed by investigations of the solid alone but must be measured indirectly by assessing the interaction strength between an adsorbed basic probe molecule and the solid.[99] Several basic probe molecules are frequently used depending on the type of sites probed and the type of solid. CO is usually used for acid sites characterisation of zeolites since it is a relative small molecule (minimum kinetic diameter 0.073 nm) and will probe the maximum concentration of acid sites. CO is a weakly base which is adsorbed end-on through the carbon on polarizing sites.[90, 100] For acid sites characterization in mesoporous zeolites the use of molecular probes of different sizes has been used to provide information regarding the location of the catalytically active acid sites in various zeolites.[101]

Even if no probe molecule is used FTIR spectra of dehydrated samples are still valuable for following major changes in surface OH groups resulting from different treatments. If no probe molecules are used silanol and bridging hydroxyl groups are seen as isolated bands in the 3000-3800 cm^{-1} region while framework Si-O vibrations are located at lower wavenumbers of typically 600-1200 cm^{-1}. In Table 1.2 is listed the wavenumber (cm^{-1}) and the corresponding assignment for different types of bonds between atoms in zeolites and in Figure 1.20 is shown where some of the bonds are located in ZSM-5.

Table 1.2: Wavenumber and corresponding bonds in zeolites [90,100,102-105]

Wavenumber [cm^{-1}]	Corresponding bonds
3780	Partly connected framework aluminum
3745	Terminal Si-OH groups which is virtually isolated and located on the external surface. 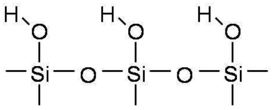
3720 3690	Perturbed Si-OH sites predominantly located inside the zeolite structure. So-called silanol nests involved in relatively strong hydrogen bonds. 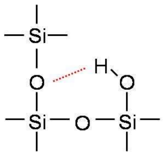
3660	Extra-framework aluminum.
3610	Strong Brønsted acid sites. 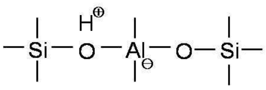
3460	Internally silanol nests. 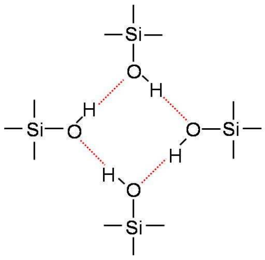

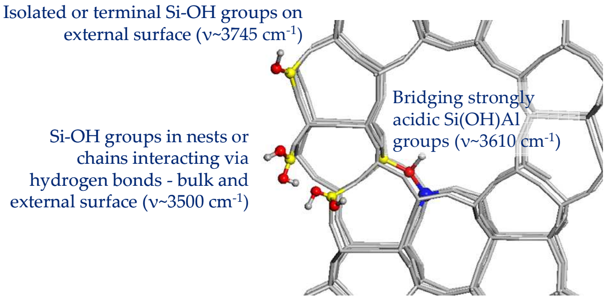

Figure 1.20: Location of bonds in ZSM-5

If a zeolite is completely free from defects in the crystal lattice there will only be observed a Si-OH contribution from the external surface where the lattice is terminated giving a sharp adsorption peak at 3745 cm^{-1}. Si-OH components located at lower frequencies represent various imperfections in the zeolite framework.[90] The limitation of FTIR is, however, the complete lack of information concerning possible changes in the acid strength, generation of Lewis acidity, the site localization (internal vs. external) and accessibility.[90] To acquire information of this CO- FTIR has to be performed. Not only information about the acid sites in zeolites can be extracted from a CO-FTIR spectrum but also extra-framework aluminum and structural defects can be investigated.
A crucial point during the determination of the acid site concentration with FTIR is to ensure the complete coverage of all sites and the absence of physisorbed molecules. This is typically achieved by out-gassing the sample in vacuum.

In this work CO-FTIR at 77 K has been performed at Department of Inorganic, Physical and Materials Chemistry, NIS Centre of Excellence and Centro di Riferimento INSTM, University of Turin. The CO-FTIR at the University of Turin were performed on self supporting pellets pre-activated in vacuo and heated up to 150, 350 and 500 °C for 1 h respectively. CO adsorption at low temperature has been performed on samples pre-activated at 350 and 500 °C. The spectra have been registered at decreasing pressure of CO in the cell, using a Nicolet 6700 spectrometer operating in transmission mode with a resolution of 2 cm^{-1} and a MCT detector. Additionally, FTIR has been performed at Haldor Topsøe A/S on self supporting pellets pre-activated in vacuo and heated up to 350 °C or 450 °C for 12 h with a heating ramp of 3 °C/min. After pre-activation the samples were cooled to room temperature and the spectra have been registered using a FTS 575C spectrometer operating in transmission mode with a resolution of 2 cm^{-1} and a MCT detector.

1.2.3.3. ^{27}Aluminum Magic-Angle Spinning Nuclear Magnetic Resonance

^{27}Al MAS NMR is a powerful tool for analysing the coordination of aluminum atoms in zeolites. Since NMR is sensitive to the local surrounding of the nuclei under study it is not necessary to have samples with long-range order as is required when using XRPD.[106]
From a ^{27}Al MAS NMR spectrum it is possible to distinguish between different coordinated aluminum.[107] Framework aluminum is only tetra-coordinated and will exhibit a resonance with a

center of gravity around 53 ppm.[108, 109] In the ^{27}Al MAS NMR spectrum shown in Figure 1.21 it is the dominant signal. In Figure 1.21 is furthermore present a broader and less intense resonance at 0 ppm which is due to the presence of octahedrally coordinated aluminum and ascribed to the occurrence of extra-framework aluminum.[110, 111]

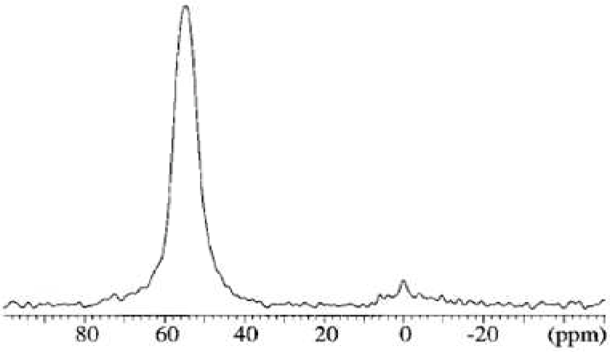

Figure 1.21: ^{27}Al-MAS NMR spectra recorded for ZSM-5. Adapted from [112]

Besides information about the coordination of aluminum, ^{27}Al MAS NMR can also provide information about the Si/Al ratio. From the line width it is also possible to get an idea of the crystallinity since a smaller line width may reflect a higher degree of crystallinity and a higher degree of local ordering around the individual aluminum sites is expected for crystals that are larger than the nm size.[112]

In this work ^{27}Al MAS NMR has been performed at Instrument Centre for Solid-State NMR Spectroscopy and Interdisciplinary Nanoscience Center (iNANO) at Department of Chemistry, University of Aarhus. The ^{27}Al MAS NMR spectra were recorded on a Varian Direct Drive VNMRS-600 spectrometer (14.1 T, ^{1}H decoupling) using a home-built CP/MAS probe for 4 mm o.d. rotors and a spinning speed of ν_R = 13.0 kHz. This single-pulse spectra employed a 0.5 µs excitation pulse for an rf field strength of $\gamma B_1/2\pi$ = 60 kHz, a 2-s repetition delay, and ^{1}H decoupling ($\gamma B_2/2\ \pi \approx 60$ kHz) during acquisition.

In addition, ^{29}Si MAS NMR is used to analyse the coordination of silicon in zeolites and to estimate the Si/Al ratios of selected zeolite samples. The ^{29}Si MAS NMR spectra were conducted at Instrument Centre for Solid-State NMR Spectroscopy and Interdisciplinary Nanoscience Center (iNANO) at Department of Chemistry, University of Aarhus. The spectra were recorded on a Varian INOVA-400 Spectrometer (9.4T) using a home-built CP/MAS probe for 5 mm o.d. rotors, a spinning speed of ν_R = 10.0 kHz, a 2.5 µs excitation pulse (~ 45 °flip angle for $\gamma B_1/2\pi$ = 50 kHz) and a recycle delay of 30 s.

1.2.4. Morphology

Electron microscopy is frequently used for investigating the morphology, chemical composition and homogeneity of a zeolite sample. Scanning Electron Microscopy (SEM) is particular frequently used to determine the size and morphology of the individual zeolite crystals as it is often directly observable whether the sample consists of agglomerates of nanosized crystals or contains larger crystals.[1] In Figure 1.22 typical SEM images of a conventional zeolite with the MFI structure are shown.

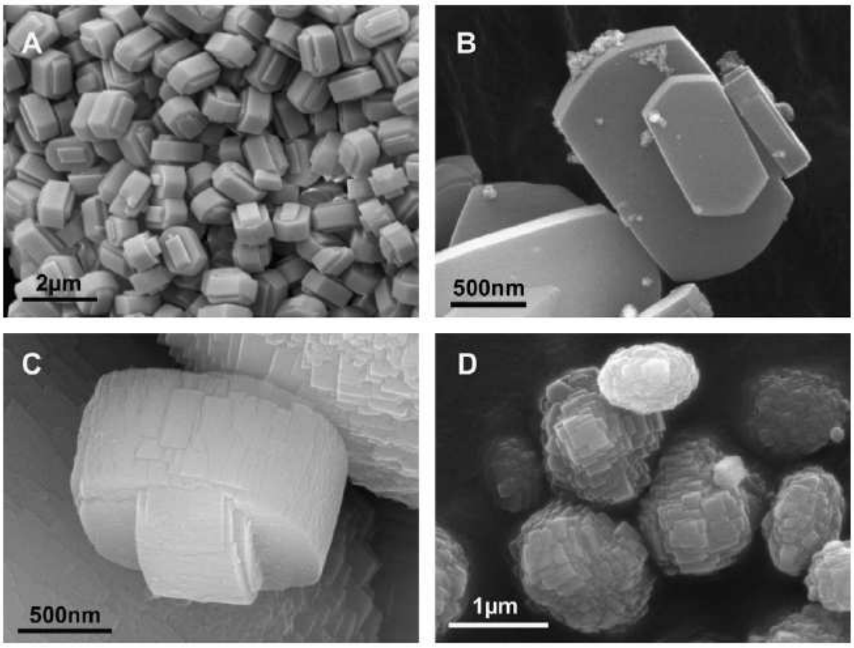

Figure 1.22: SEM image of a conventional and mesoporous ZSM-5. Adapted from [113]

As seen in Figure 1.22 it is possible to obtain MFI crystals with quite different morphologies. In Figure 1.22a is an example of the archetype MFI morphology referred to as twinned prisms and the particles shown in Figure 1.22b are often described as coffin-shaped. The particles in Figure 1.22c and d appear to have surface roughness and seem to be formed of smaller subunits. Mesoporous zeolites have a different morphology than the conventional counterpart as seen in Figure 1.23.

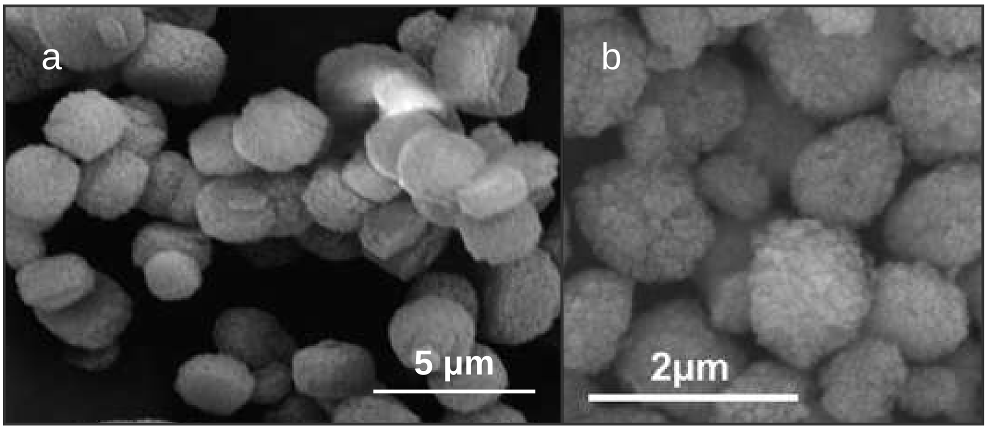

Figure 1.23: SEM images of mesoporous ZSM-5 produced by a) carbon-templating[66] and b) desilication[113]

In general mesoporous zeolites have a sponge-like appearance. It is possible with the carbon-templating method to retain the coffin-shape characteristic of MFI-structured zeolites as shown in Figure 1.23a. Since mesopores generation by desilication is a post-synthesis treatment, the morphology is often retained of the parent sample only with a more sponge-like appearance, Figure 1.23b.

It is possible to obtain a compositional image by detecting back-scattered electrons by which the heavier elements will appear as brighter spots on the images since they are more efficiently scattered. One should be aware that a certain weight difference in the elements should be present. It is thus not possible to distinguish between silicon and aluminum but it is possible to distinguish between silicon and gold. The most widely used signal is however that from secondary electrons since they penetrate deeper into the sample resulting in a more detailed image of the topology.[114]

Often scanning electron microscopes are equipped with Energy-Dispersive Analysis (EDS) which can estimate the chemical composition of a selected area by detection of X-rays emitted from the area. One must be aware that the selected area will provide information about the composition primarily of the surface of the selected area since the volume which the electrons penetrate has a limited depth and size. It is not possible to detect all types of elements by EDS. Rather light elements like carbon have low energy/long wavelength X-rays and are therefore readily adsorbed by the solid. Both the volume which is being analysed and the fraction of the X-rays which are emitted from the sample depend critically on the i) energy of the electron beam, ii) the wavelength of the emitted X-ray and iii) the local atomic weight of the sample. [114] This complexity makes accurate analysis extremely difficult and is in this work EDS is only used qualitative instead of quantitative.

SEM/EDS is used here to investigate the size and shape of the synthesised materials and estimate the chemical composition. Additionally the backscatter detector is used to get an idea whether gold is present on the surface of zeolite crystals. All materials are investigated at Haldor Topsøe A/S on a Philips XL-30 FEG. The samples were placed on a carbon film and Ag or Pt/Pd was evaporated onto the sample for approximately 20 minutes to achieve sufficient conductivity.

Another frequently used electron microscopy technique is Transmission Electron Microscopy (TEM). The main difference between SEM and TEM is that SEM images contrast due to topology of the surface, whereas the electron beam in TEM projects all information on the mass it encounters in a two-dimensional image and thereby provides information about the internal structure.[115] TEM is the most frequently used electron microscopy technique in the study of mesopore formation.[7] Figure 1.24 shows representative images of conventional and mesoporous ZSM-5 crystals from carbon templating and desilication. The conventional zeolite crystals appear to be dense and no distinct contrast difference throughout the crystals whereas mesoporous zeolites have a pronounced contrast difference. The mesopores appear as bright areas in the TEM images for the mesoporous ZSM-5 crystals since they have a reduced mass-density.

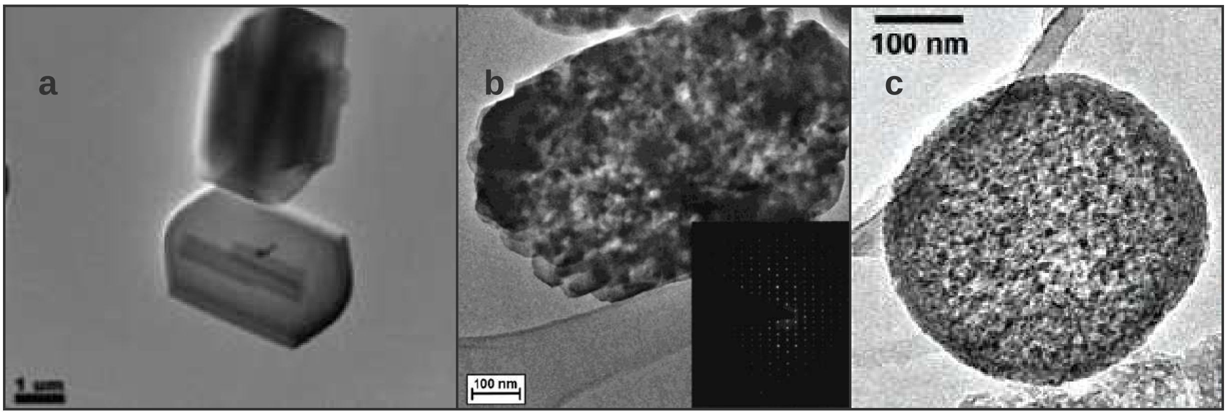

Figure 1.24: TEM images of a) conventional ZSM-5 and mesoporous ZSM-5 from b) carbon templating and c) desilication. Adapted from [35, 66, 116]

To investigate whether crystals are single crystals or polycrystalline agglomerates TEM can be coupled with Selected Area Diffraction (SAD) technique. Applied on the selected area it is possible to obtain an electron diffraction pattern which for a single crystal should be an array of reflections rather than concentric circles which would result from a polycrystalline agglomerate.[114] An example of a SAD pattern is in the inset of Figure 1.24b where the mesoporous ZSM-5 crystal appears to be a single crystal. According to Imai *et al.*[117] care should be taken as SAD patterns can falsely show that a polycrystalline agglomerate appears to be a single crystal, Figure 1.25, which questions whether the mesoporous ZSM-5 resulting from carbon templating is actual a single crystal or a mesocrystal in an ordered environment.

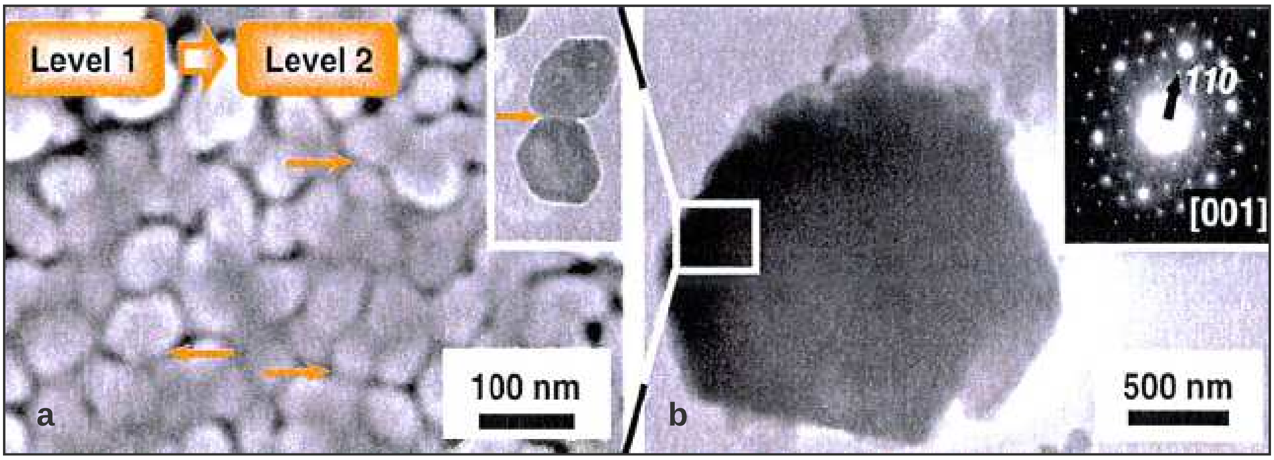

Figure 1.25: Field-emission SEM images of a) magnification of b) aragonite plate consisting of the nanocrystals. In the inset of b) is the spot selected-area electron diffraction pattern of the aragonite plate consisting of the nanocrystals. Adapted from [117]

Almost all electron microscopy techniques share one fundamental limitation; they generate two-dimensional information by projection of a three-dimensional structure. During this work one goal was to encapsulate metal nanoparticles in zeolites crystals. To determine whether the metal nanoparticles are located on the external surface or as intended encapsulated within the zeolite crystal is almost impossible. However TEM can be extended from a two-dimensional to a three-dimensional analysis tool by electron tomography.[118] In electron tomography a serie of images is recorded as a function of the tilt angle. Combining these images makes it possible to create a three-dimensional reconstruction of the sample. In addition tomography also gives a possibility to obtain imaginative slices though the sample and thereby investigate internal details of the specimen. [119] One complication is that the framework of zeolites degenerates rather rapidly under TEM illumination which can result in severe beam damage in the prolonged acquisition times required for a tilt series.

Generally, one should be aware that in TEM and SEM only a small amount of the sample is used and only a small area of the sample is investigated.

In this work TEM is used to investigate the porosity of the synthesised materials and thermal stability of encapsulated Au. Bright field TEM tomography[120, 121] was used to determine whether the metal nanoparticles are present on the external surface of the zeolite crystals or encapsulated. All TEM investigations are performed at Haldor Topsøe A/S at either a CM200-FEG UltraTwin electron microscope (Philips/FEI), a Titan 80-300 SuperTwin electron microscope or a CM300 FEG SuperTwin environmental transmission electron microscope (Philips/FEI).

1.2.5. Miscellaneous

To obtain an accurate elemental analysis Inductively Coupled Plasma Optical Emissions Spectroscopy (ICP-OES) is used. The samples are dissolved in hydrofluoric acid or aqua regia and then analysed for the photon emission specific to each element. The analysis is highly accurate and detects even a few ppm of the element. The limitation of this technique is approximately 0.05 ppm. All ICP-OES measurements are performed at Haldor Topsøe A/S on a PerkinElmer OES Optima 7300 DV.

Thermogravimetric Analysis (TGA) records the mass of the sample as a function of temperature resulting in information on the thermal stability of the sample *i.e.* decomposition temperature. A drop in the obtained curve will reveal a loss of mass at a certain temperature *i.e.* evaporation of a solvent while a plateau corresponds to stability of the material in that temperature range.
TGA can be combined with Differential Scanning Calorimetri (DSC) which records the changes in heat flow as a function of temperature. The complementary information obtained allows differentiation between endothermic and exothermic events with no associated weight loss *i.e.* melting and crystallization and those that involve a weight loss *i.e.* degradation.
TGA/DSC measurements are performed at Haldor Topsøe A/S on a Mettler TGA/DSC-1 apparatus in the temperature range 30 °C to 600 °C, ramping 5 °C/min in air.

1.2.6. Summary

In this thesis several characterization techniques have been applied to reveal information about the synthesised zeolite materials. The framework structure type as well as the phase-purity of zeolite crystals is determined by X-ray powder diffraction (XRPD) which also reveals information of the size of the crystal. Furthermore, XRPD is also used to evaluate whether or not a post-synthesis treatment has induced structural changes. However, care must be taken in determining the crystal size of mesoporous zeolite crystals using XRPD alone since mesoporous crystals may exhibit similar broadened lines as nano-sized crystals. N_2 physisorption measurements are used to investigate the textural properties of the mesoporous zeolite crystals concerning surface area, type and volume of porosity and pore size distribution. One must be aware of the appearance of artefacts in the pore size distribution, especially using the desorption branch and it is recommend to compare the pore size distribution from both the adsorption and desorption branch. The acidic properties of the prepared zeolite materials have been investigated using Temperature-Programmed Desorption of ammonia (NH_3-TPD), Infrared Spectroscopy and ^{27}Aluminum Magic-Angle Spinning Nuclear Magnetic Resonance spectroscopy (^{27}Al MAS NMR). NH_3-TPD is used as a relatively fast technique to estimate the concentration (mmol/g) and the corresponding Si/Al ratio. Infrared Spectroscopy and ^{27}Al MAS NMR is primarily used to investigate the type of acid sites including the presence of extra-framework aluminum. Scanning Electron Microscopy (SEM) and Transmission Electron Microscopy (TEM) techniques are used to investigate the morphology of the crystals as well as obtaining direct visual images of the porosity of the materials. SEM is used to determine the size and morphology of the individual zeolite crystals and to see whether the sample consists of agglomerates of nanosized crystals or contains larger crystals. TEM is used to investigate the porosity of the synthesised materials, thermal stability of encapsulated gold nanoparticles and determine whether the Au metal nanoparticles are located on the external surface or in fact encapsulated in the zeolite crystal. To obtain an accurate elemental analysis of a macroscopic amount of sample Inductively Coupled Plasma Optical Emissions Spectroscopy (ICP-OES) has been used. TGA/DSC is used to investigate the thermal stability of the prepared samples and identification of endothermic and exothermic events.

Chapter 2

Nanosized versus mesoporous zeolites in the MTH reaction

This chapter contains synthesis, characterization and catalytic test of nanosized and mesoporous ZSM-5 zeolites. Their catalytic lifetime was tested in the methanol to hydrocarbon (MTH) reaction and compared to a conventional ZSM-5 zeolite. PhD student Peter N.R. Vennestrøm and PhD Uffe V. Mentzel have conducted the catalytic tests.

2.1. Introduction

The search for future energy sources as alternatives to crude oil is one of the most important issues among scientific topics. Among several alternatives, the conversion of methanol to hydrocarbons (the MTH reaction) has received significant attention since in this process it is possible to produce gasoline from methanol which is virtually identical to normal petrochemical gasoline. Methanol can be prepared from synthesis gas (a mixture of CO_2 and H_2) which can be produced via a reforming or gasification process of coal, natural gas and biomass which are all much more abundant than crude oil or less likely to run out.[122, 123] Even though the MTH reaction was discovered in the 1970s by Mobil[124] using zeolite catalysts the detailed reaction mechanism is still not fully understood. A simplified pathway is shown in Figure 2.1.

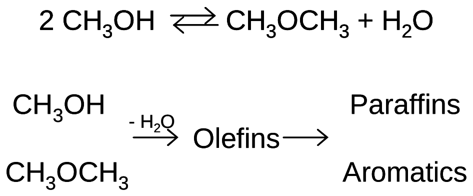

Figure 2.1: Simplified MTH reaction pathway

Initially methanol is partly dehydrated to an equilibrium mixture of methanol, dimethylether (DME) and water. Methanol and DME are then completely dehydrated and catalytically converted to olefins under the formation of carbon-carbon bonds. The formed olefins react further to form paraffins and aromatics. The overall product composition can be expressed as $(CH_2)_n$ corresponding to complete dehydration of methanol. The more detailed reaction mechanism is highly complex and has been debated since the discovery of the reaction.[125-128] One of the most accepted mechanisms is the “hydrocarbon pool mechanism” suggested by Dahl and Kolboe in 1993.[129, 130] The hydrocarbon pool mechanism is described as a catalytic scaffold constituted by large organic species adsorbed inside the zeolite to which methanol is added and in turn split off hydrocarbon products. Produced alkenes are able to be reinserted into the hydrocarbon pool, while alkanes are end products. Even though the hydrocarbon pool mechanism has gained general acceptance, the mechanism is still far from being understood. The complexity of the reaction increases since the zeolite-catalysed MTH reaction does not only depend on the reactor design

and reactor conditions, but also on the type of zeolite catalyst concerning pore architecture and acid site strength/density.[19, 131] By varying these factors the selectivity of the MTH reaction can be shifted towards gasoline products (MTG) or towards production of olefins (MTO).
ZSM-5 zeolite is often chosen as a MTH catalyst owing to its high product selectivity in the gasoline range, high catalytic activity and for zeolites long catalytic lifetime. A high Si/Al ratio is preferred because zeolites with a low concentration of acid sites deactivate more slowly.[132-134] An essential aspect in MTH catalysis is catalyst deactivation. When ZSM-5 is employed as a MTH catalyst the size of the micropores prevents the formation of large polyaromatic compounds (coke) inside the channels of the zeolite, and coking of the ZSM-5 is often described as an external surface phenomenon, eventually leading to blockage of the pore entrances. Especially Svelle *et al.*[18, 19] have ruled out any correlation between the concentration of organics in the pores and the zeolite deactivation. Instead they found that deactivation must result from the formation of large graphitic species on the external surface of the zeolite crystals. The cause of ZSM-5 zeolite catalyst deactivation in the MTH reaction is a ongoing discussion. Recently, Barbera *et al.*[135] found that deactivation is due to coking at internal defects, *i.e.* silanol groups, independent of porosity, preparation method, crystal size and Si/Al ratios, see Figure 2.2. They concluded that activity and deactivation depend on different physical or chemical properties of the catalyst which can be varied independently of each other. The activity correlates with the number of strong acid sites and thereby the catalyst acidity whereas their study clearly indicated that the presence of silanol groups inside the zeolite affects the deactivation rate.

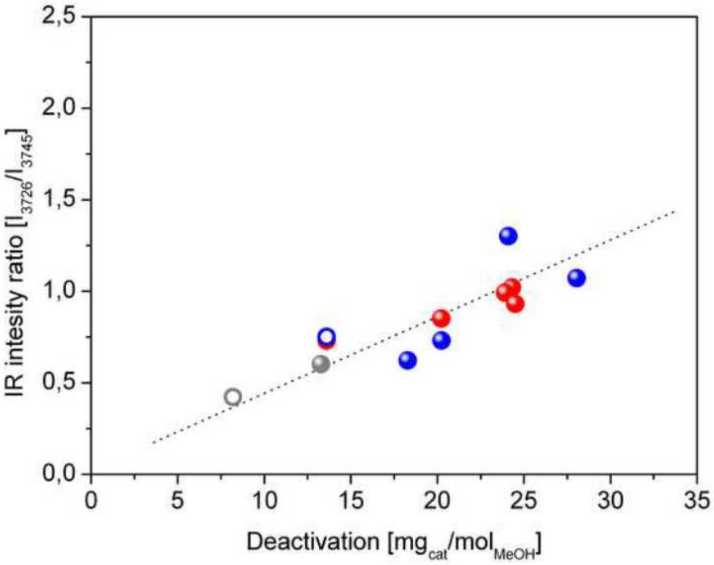

Figure 2.2: Correlation between the deactivation rate and the IR intensity ratio (I_{3726}/I_{3745}) as an estimate for internal defects. The red, blue and grey dots represent conventional ZSM-5 zeolite crystals which vary in crystal size and Si/Al ratios. Open symbols correspond to desilicated materials and thereby mesoporous samples. Adapted from [135]

Regardless where the coking takes place, the formation of coke on the catalyst is an important cost-bearing factor for the industry since frequent catalyst regeneration by burning deposited coke with diluted oxygen is necessary. This is not only valid for the MTH process but also in many other petrochemical processes using zeolite catalysts including hydrocarbon refining and fine-chemical syntheses.[136, 137]

Recently, it was shown[8-10] that mesoporous zeolites have enhanced catalytic lifetimes in the MTH reaction and that hierarchical zeolites displayed lifetimes that were up to 3.5 times the normal lifetime compared with solely microporous zeolites. Kim *et al.*[10] have investigated the catalytic lifetime in the MTH reaction within a series of ZSM-5 samples with a wide variation of mesoporosity while the Si/Al ratio was maintained in a narrow range. According to Kim *et al.* there exists a quantitative correlation between mesoporosity and catalytic lifetime independent of the preparation method. The resulting correlation shows that the catalytic lifetime increased in an approximately linear manner when plotted with respect to the external surface area, see Figure 2.3.

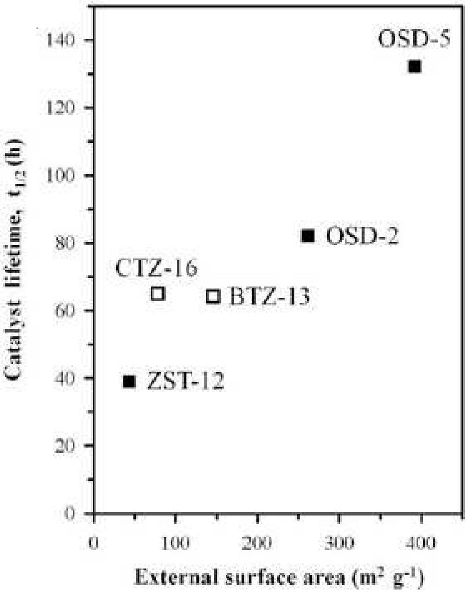

Figure 2.3: Correlation between catalyst lifetime ($t_{½}$) and external surface area. $t_{½}$ is the time at which the catalytic conversion of methanol decreased by 50%. BTZ represents base-treated zeolite, CTZ is carbon-templated zeolite, OSD denotes organosilane-directed zeolite, ZST is assigned to conventional zeolite and the numbers are the Si/Al ratios. Adapted from [10]

It is feasible that the generation of mesopores in ZSM-5 zeolite can lead to significant improvement in the MTH catalytic lifetime due to improved mass transport, when the catalytic lifetime is compared at the same Si/Al ratios. In the work of Kim *et al.* high aluminum contents were introduced in the zeolite samples which often entail extra-framework aluminum. Even though the Si/Al ratios are in the same range the presence of extra-framework aluminum can also affect the catalytic lifetime, which is investigated and discussed in Chapter 3.

Hitherto, no study has been performed on the effect of intercrystalline versus intracrystalline mesopores in ZSM-5 zeolite crystals in the MTH reaction. In the present chapter, the effect of inter- or intracrystalline mesopores in ZSM-5 zeolite crystals is investigated for the catalytic lifetime in the MTH process keeping the Si/Al ratios in the same range and at the same time keeping the presence of extra-framework aluminum to a minimum. Both types of mesoporous zeolite materials are expected to improve the catalytic lifetime compared to a conventional microporous zeolite due to enhanced mass transport. Since intercrystalline mesoporous zeolite materials contain mesopores between nanosized zeolite crystals these are not truly mesoporous. In this work the samples are instead referred to as nanosized zeolites.

2.2. Synthesis strategy

Nanosized and mesoporous zeolites can both be synthesised using carbon as inert template. The nanosized zeolite crystals can be prepared using the confined-space synthesis strategy[34] which involves crystallisation of the zeolites within the mesopores system of an inert carbon material, see Figure 2.4a. The carbon material typically controls the final crystal size by hindering zeolite growth within the pores. A complete calcination of the carbon matrix will lead to isolation of the nanocrystals with intercrystalline mesopores.

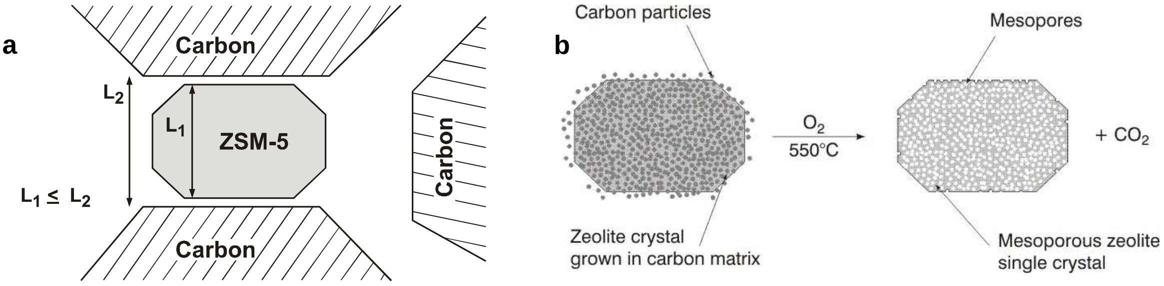

Figure 2.4: Schematic illustration of a) the confined space synthesis and b) encapsulation of carbon. Adapted from [35, 138]

Zeolites prepared by the confined synthesis route have lager external surface areas and posses the same number of acid sites as the corresponding large zeolite crystals.[112] In the confined synthesis method the zeolite components have to be introduced in a soluble form and in an amount exactly equal to (or lower than) that necessary to fill the pore volume of the carbon. By using excess of a zeolite gel it is possible to generate intracrystalline mesopores. Under these synthesis conditions the zeolite will grow around the carbon particles of the inert carbon matrix producing single mesoporous zeolite crystals with intracrystalline mesopores after combustion of the carbon matrix, [35] see Figure 2.4b. It is important that the zeolite nucleation takes places exclusively between the carbon particles for the encapsulation to take place. Consequently, by controlling the amount of zeolite gel it is possible to control whether nanosized or intracrystalline mesoporous zeolites should be generated. By both methods it is possible to produce mesoporous zeolites with various Si/Al ratios and also with different zeolite structures.[67, 138, 139]

In this work nanosized and intracrystalline mesoporous ZSM-5 type zeolites are synthesised, characterised and compared with a prepared conventional ZSM-5 type zeolite in the MTH reaction concerning the catalytic lifetime. All zeolite materials are produce with a Si/Al = 50 in the synthesis gel and the aluminum source is kept the same in all synthesis. Aluminum isopropoxide is chosen as aluminum source. Previous studies show[139] that when aluminum isopropoxide is used much more aluminum is incorporated into the framework than when using for instance sodium aluminate. Even though the Si/Al ratio is kept constant for all zeolite synthesis gels it is not guaranteed that the Si/Al in the final product is the same since zeolites have a very complex crystallisation mechanism. The intracrystalline mesoporous ZSM-5 was synthesised according to the procedure by Jacobsen *et al.*[35] using Carbon Black Pearls (BP-2000) as mesopore template and by stepwise impregnation. The nanosized ZSM-5 was prepared in three different ways all by the use of Pluronic 123 (P123) as mesopore template and carbonised polyfurfuryl alcohol as the carbon source. The idea originates from Huang *et al.*[140] who synthesised Zeolite A nanocrystals using a refinement of the confined space synthesis method. In principle, silica nanoparticles are firstly embedded in a mesoporous carbon matrix and are directly converted into aluminosilicate zeolite nanocrystals by diffusing an aqueous solution though the mesoporous carbon channels. The synthesis procedure is schematically illustrated in Figure 2.5.

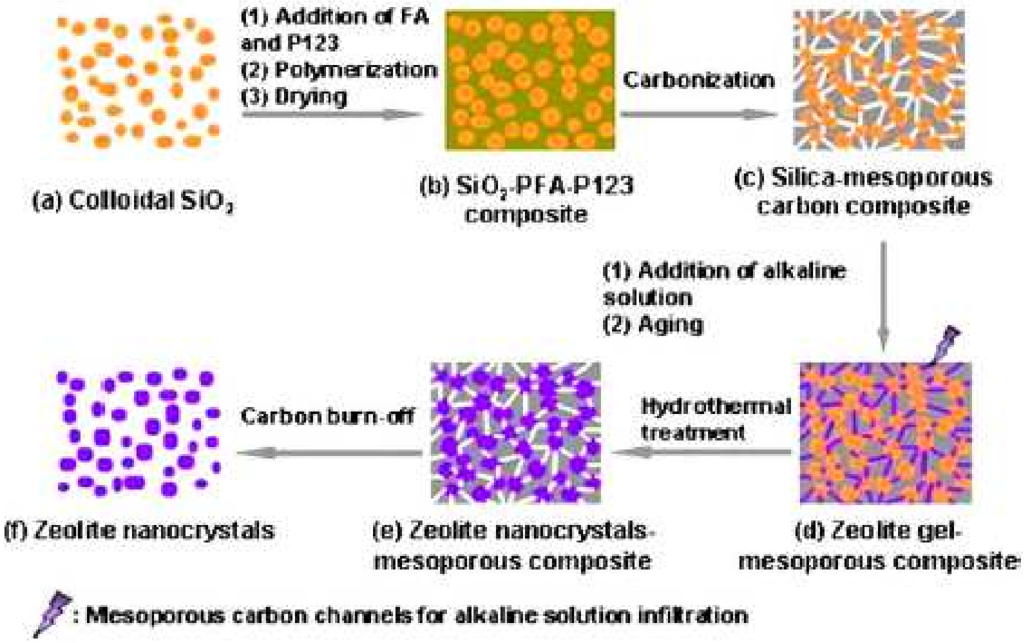

Figure 2.5: Schematic illustration of mesoporous carbon confined conversion of colloidal silica nanoparticles into zeolite nanocrystals. Adapted from [140]

Colloidal silica nanoparticles are employed as the silica source as well as template, since the size and shape of the colloidal silica controls the nanocrystal size distribution, Figure 2.5a. After addition of P123 and furfuryl alcohol (FA), the FA is polymerised to polyfurfuryl alcohol (PFA) and the SiO_2-P123-PFA composite, Figure 2.5b is heated under N_2 yielding a silica-mesoporous carbon composite, Figure 2.5c. At this point PFA is carbonised while P123 is decomposed, creating a mesoporous carbon structure with encapsulated silica nanoparticles. To convert the silica nanoparticles into zeolite crystals, Figure 2.5d, the silica-mesoporous carbon composite is mixed with an aqueous synthesis gel followed by aging and hydrothermal treatment, Figure 2.5e. Finally the zeolite nanocrystals are retrieved by carbon combustion.

The mesoporous carbon composite arises from P123 and FA. P123 is a non-ionic amphiphilic triblock copolymer composed of a hydrophobic poly(propylene oxide) group terminated with two hydrophilic poly(ethylene oxide) groups; $(PEO)_{20}(PPO)_{70}(PEO)_{20}$. In aqueous solution P123 will self-assemble in micelles with a hydrophobic core and a hydrophilic surface, Figure 2.6.

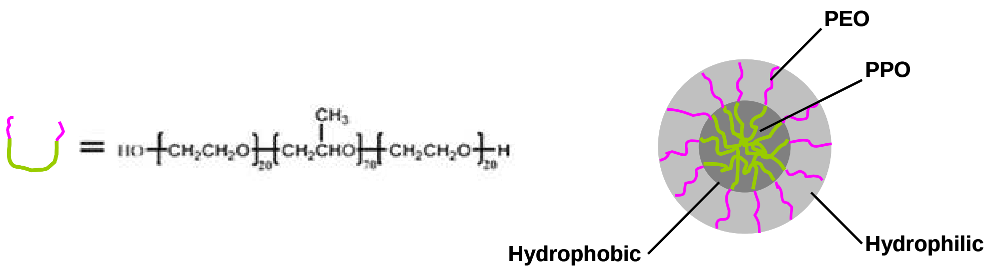

Figure 2.6: The pluronic structure and its micelle

The hydroxyl group on FA can interact with the surface of the micelle thorough formation of hydrogen bonds and FA can subsequently through a polymerisation transform into PFA around the triblock copolymer, Figure 2.7, which stabilises the micelles.[141] The polymerisation of FA is carried out with a strong Brønsted or Lewis acid and due to exothermicity the polymerisation should be carried out with caution.[142] The resulting PFA is a black, highly crosslinked polymer.

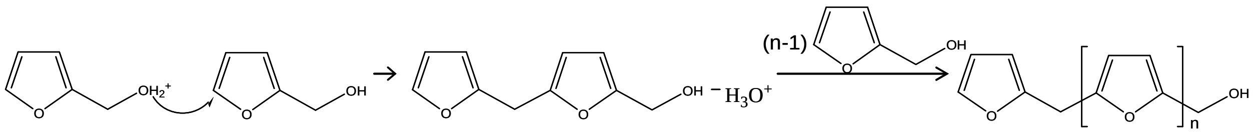

Figure 2.7: Polycondensation of furfuryl alcohol (ideal structure formation). Adapted from [142]

During polymerisation of the FA, formation of Si-O-C bonds takes place with the SiO_2 particles present. The cationic polymerisation of FA is significantly accelerated when it occurs on the surface of silica particles and the result of cationic surface polymerisation on silica with FA is an organically functionalized silica surface, [143] Figure 2.8. So during the polymerisation the SiO_2 nanoparticles will be encapsulated in the P123-PFA assembly.

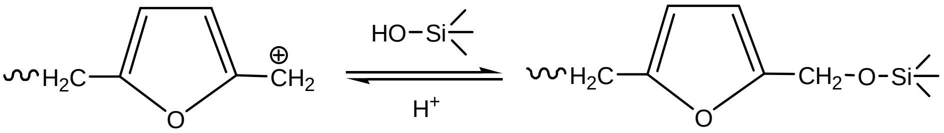

Figure 2.8: Possible reaction of the cationically active polyfurfurylium chain and the silanol groups. Adapted from [143]

Even though Huang *et al.*'s refined confined space synthesis consists of quite a few synthesis steps, it has the advantage that the zeolite crystallisation outside the silica-mesoporous carbon composite is completely eliminated. Zeolite crystallisation in the mesopores in unfavourable due to small mesopores sizes and this makes nanocrystals intergrowth less likely.[140] Another advantage over the original confined space synthesis is the use of carbonised PFA and P123 which is a cheaper alternative to the quite expensive BP-2000 carbon particles.[61]

In this work Huang *et al.*'s refined confined space synthesis has been varied in two different ways which is illustrated in Figure 2.9.

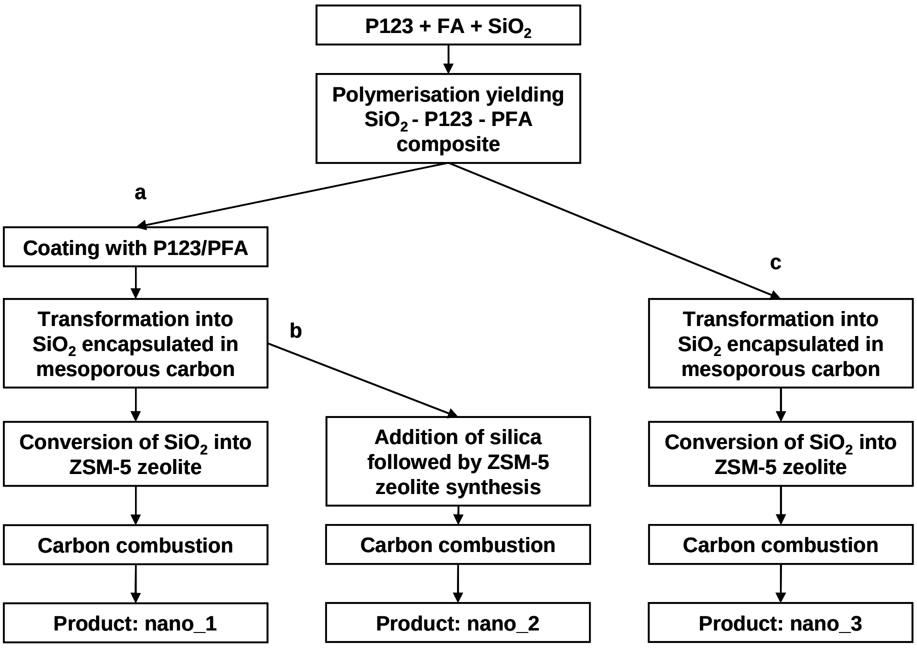

Figure 2.9: The three synthesis strategies for producing nanosized ZSM-5 zeolite crystals. Route a is that of Huang *et al.*[28], while route b and c are variations thereof

By all three synthesis strategies, P123, FA and SiO_2 nanoparticles are mixed followed by polymerisation to the SiO_2-P123-PFA composite. In the original synthesis procedure (route a, Figure 2.9) the SiO_2-P123-PFA composite is coated with a mixture of P123 and PFA to prevent silica from dissolving out of the mesoporous silica-carbon composite particles during the penetration of the zeolite synthesis gel. Hereafter, the SiO_2 nanoparticles are converted into aluminosilicate ZSM-5 zeolite and the zeolite crystals are retrieved by burning off the mesoporous carbon. In the first variation (route b, Figure2.9) half of the used silica is added in the beginning and present as SiO_2 nanoparticles in the mesoporous carbon matrix and the other half is impregnated to the SiO_2-mesoporous carbon composite before conversion to zeolite. The impregnation of silica might induce intracrystalline mesopores if it is possible for the silica to encapsulate the carbon template during zeolite crystallisation. In the second variation (route c, Figure 2.9) the SiO_2-P123-PFA composite is not coated with P123/PFA. Otherwise the original route a) and c) are identical. The idea is to see whether intercrystalline mesoporous zeolites can be obtained without the extra synthesis step, or if it is possible for the zeolite crystals to encapsulate the mesoporous carbon creating intracrystalline mesopores after carbon combustion.

In summary, one mesoporous ZSM-5 with intracrystalline mesopores and three nanosized ZSM-5 zeolites have been synthesised using carbon as mesopores template. The aim is to investigate their catalytic lifetime in the MTH reaction and compare with a conventional ZSM-5. All zeolites are synthesised with Si/Al = 50.

2.3. Experimental

All the reagent were of reagent grade and used without any further purification: Sodium hydroxide (NaOH, 99 wt%, Riedel-de Häen), tetrapropylammonium hydroxide (TPAOH, 40 wt%, AppliChem), aluminum isopropoxide ($C_9H_{21}O_3Al$, 98 wt%, Aldrich), tetraethylorthosilicate (TEOS, 98 wt%, Aldrich), Snow-tex O-40 (colloidal silica, SiO_2, 40 wt% SiO_2, Nissan Chemical industries Ltd), tetrahydrofuran (THF, 99 wt%, Aldrich), Carbon Black Pearls (BP-2000, average diameter of 12 nm, Carbot Corporation), ethanol (C_2H_5OH, EtOH, 99.9 wt%, Kemethyl A/S), ammonium nitrate (NH_4NO_3, 99.5 wt%, Merck), furfuryl alcohol ($C_5H_6O_2$, 98 wt%, Sigma-Aldrich), hydrochloric acid (HCl, 37 wt%, Sigma-Aldrich), Pluronic123: Poly(ethylene glycol)-block-poly(propylene glycol)-block-poly(ethylene glycol) (P123, Aldrich), Methanol (CH_3OH, > 99.9 wt% Aldrich Chromasolv®).

2.3.1. Synthesis of conventional ZSM-5

The conventional ZSM-5 zeolite was synthesised using the following procedure:

> *Firstly, 0.5 g of NaOH was dissolved in 3.6 g H_2O after which 28 g of 40 wt% TPAOH was added and the solution was stirred until a homogeneous solution was obtained. In another beaker 0.53 g aluminum isopropoxide was mixed with 45 ml THF and quickly added to the NaOH/TPAOH mixture simultaneously with 27.09 g TEOS. This white mixture was stirred for 2 h and transferred to a Teflon lined autoclave which was heated to 180 °C for 5 days. After cooling the white suspension was filtered and washed with water until pH was neutral. The white product was left to dry overnight at room temperature. Finally the organic template was removed by combustion in air in a muffle furnace at 550 °C for 5 h. The obtained material was named conv ZSM-5.*

2.3.2. Synthesis of mesoporous ZSM-5 with intracrystalline mesopores

The mesoporous ZSM-5 with intracrystalline mesopores was synthesised using the following procedure:

BP-2000 was dried in an oven (min. 110°C) overnight and 14 g was taken from the batch. Firstly, 0.53 g aluminium isopropoxide was quickly dissolved with 45 ml THF in a beaker and impregnated on the carbon. This mixture was left overnight at room temperature to evaporate THF. In a beaker, 28 g of 40 wt% TPAOH, 3.6 g H_2O and 0.5 g of NaOH was added and stirred until a clear solution was obtained, after which 21 g EtOH was added during stirring. The carbon was impregnated with all the obtained solution resulting in precisely incipient wetness. After evaporation of the EtOH at room temperature overnight, the carbon particles were impregnated with 27.09 g TEOS and then left to hydrolyse overnight. After hydrolysis, the impregnated carbon was transferred to a Teflon beaker which was placed in a stainless steel autoclave with 1 cm water to produce saturated steam. The autoclave was heated slowly to 180 °C and kept there for 72 hours. After crystallisation the autoclave was cooled to room temperature, the black product was suspended in water, filtered by suction and washed repeatedly with water until pH was neutral. Then the product was dried at 110 °C for 10 h and the carbon black was removed by controlled combustion in air in a muffle furnace at 550 °C for 20 h. In this way a white material was obtained and named intra meso ZSM-5.

2.3.3. Synthesis of nanosized ZSM-5

The nanosized ZSM-5 zeolite was synthesised according to Huang *et al.* using the following procedure:

Preparation of SiO_2-P123-PFA composite

Firstly, 16 g of P123 and 40 g FA were mixed in a capped polypropylene bottle under stirring until a homogeneous solution was obtained. To this solution 20 g of Snow-tex O-40 was added and left for stirring overnight at room temperature. To initiate the polymerisation 8 g 2 M HCl was added and left for stirring for 2 days after which the solution turned black and very viscous. The polymerisation was finalised by heating to 70 °C for 2 days.

Surface coating and preparation of mesoporous silica-carbon composite

Prior to coating the SiO_2-P123-PFA composite was crushed into particles with a size ~2 mm. A P123-PFA solution was prepared by thoroughly mixing 16 g P123 and 40 g FA at 50 °C . When the solution was homogeneous 8 g 2 M HCl was added during stirring. The solution was heated to initiate polymerisation of FA. When the solution became viscous, it was removed from the heating, stirred at room temperature and the SiO_2-P123-PFA composite particles were added. The coated SiO_2-P123-PFA composite particles were transferred into a crucible and heated to 70 °C for 5 hours to complete polymerisation.

The surface-coated silica-mesoporous carbon composite was obtained by heating the coated SiO_2-P123-PFA under N_2 flow at a heating ramp of 2 °C/min up to 500 °C and holding this temperature for 5 h.

Confined-space synthesis of ZSM-5 zeolite

The confined-space synthesis of ZSM-5 zeolite was similar to the procedure described for impregnation on BP-2000 particles, using the same crystallisation conditions and ratios between the reactants in the zeolite synthesis gel.

Firstly, 0.53 g aluminium isopropoxide was quickly mixed with 45 ml THF in a beaker and impregnated on the mesoporous silica-carbon composite. This mixture was left overnight at room temperature. In a beaker, 28 g of 40 wt% TPAOH, 3.6 g H_2O and 0.5 g of NaOH was added and stirred until a clear solution was obtained, after which 21 g EtOH was added during stirring. The mesoporous silica-carbon composite was impregnated with the obtained solution to incipient wetness. After evaporation of the EtOH at room temperature overnight, the impregnated material was transferred to a Teflon beaker *which was placed in a stainless steel autoclave with 1 cm water to produce saturated steam. The autoclave was heated slowly to 180 °C and kept there for 72 hours. After crystallisation the autoclave was cooled to room temperature, the black product was suspended in water, filtered by suction and washed repeatedly with water until pH was neutral. Then the product was dried at 110 °C for 10 h and the carbon was removed by controlled combustion in air in a muffle furnace at 550 °C for 20 h. In this way a white material was obtained and named nano_1 ZSM-5.*

In the first variation of the confined space synthesis by Huang *et al.* (Figure 2.9b) the only deviation is the amount of added Snow-tex O-40 to the SiO_2-P123-PFA composite.

Only 10 g Snow-tex O-40 is used instead of 20 g. Instead 13.9 g TEOS was impregnated after the evaporation of EtOH at room temperature overnight. After impregnation of TEOS the material was left to hydrolyse overnight and after hydrolysis, the impregnated carbon was transferred to a Teflon beaker and the crystallisation and isolation of zeolite crystals was identical to the reported confined space synthesis of ZSM-5 zeolite materials. The obtained white material was named nano_2 ZSM-5.

In the second variation (Figure 2.9c) of the confined space synthesis by Huang *et al.* the surface coating with mesoporous carbon (P123-PFA) is omitted. Otherwise, the synthesis route was completely identical. The obtained white product was named nano_3 ZSM-5.

2.3.4. Ion exchange

All the synthesised zeolite materials contain sodium as the charge-compensating cation after the synthesis. The acidic form of each zeolite was prepared by using the following procedure:

Two consecutive ion exchange steps were performed using 1M NH_4NO_3 at 80 °C in ratio 1:30 between mass of Na-zeolite (g) and volume of NH_4NO_3 (ml). After each ion exchange, the NH_4-form of the zeolite was filtered off, washed with water, and dried in air. Finally, the H-form was obtained by heating the NH_4-ZSM-5 in air to 450 °C for 4 h, whereby the NH_3 were evaporated leaving protons as charge-compensating cations.

2.3.5. Conversion of methanol to hydrocarbons

The catalytic tests were conducted using the following procedure:

The conversion of methanol into hydrocarbons was performed in a 10-channel parallel steel reactor setup (i.d. 3.0 mm). Each reactor was loaded with 150 mg zeolite catalyst (150-300 µm sieve fraction) and one channel was left empty for feed analysis. Methanol was fed to the reactor using a syringe pump (ISCO 500D, dual pump system) and evaporated in an argon stream. The methanol conversion was measured under the conditions: 350 °C, 15 bar (14.2 % MeOH in Ar) using a total flow of 350 Nml[*]/min. The reactor exit gas was monitored with an online GAM200 mass spectrometer connected via a channel selector valve (Valco, 10-position valve SC configuration). The individual reactor flows were measured and accounted for in the data analysis, which has been described in further detail elsewhere[144].

---

[*] Nml = normal ml = volume at 1 bar and 25°C

2.4. Results and discussion

The prepared zeolites were characterized using XRPD, SEM, N_2 physisorption, TEM, NH_3-TPD, elemental analysis as well as FTIR. All characterisations were made after ion exchange and calcinations. The catalytic lifetime of the samples were tested in the MTH reaction.

2.4.1. Characterisations

The XRPD patterns for the five prepared zeolite samples are all shown in Figure 2.10. All samples exclusively contain highly crystalline material with the MFI structure[4].

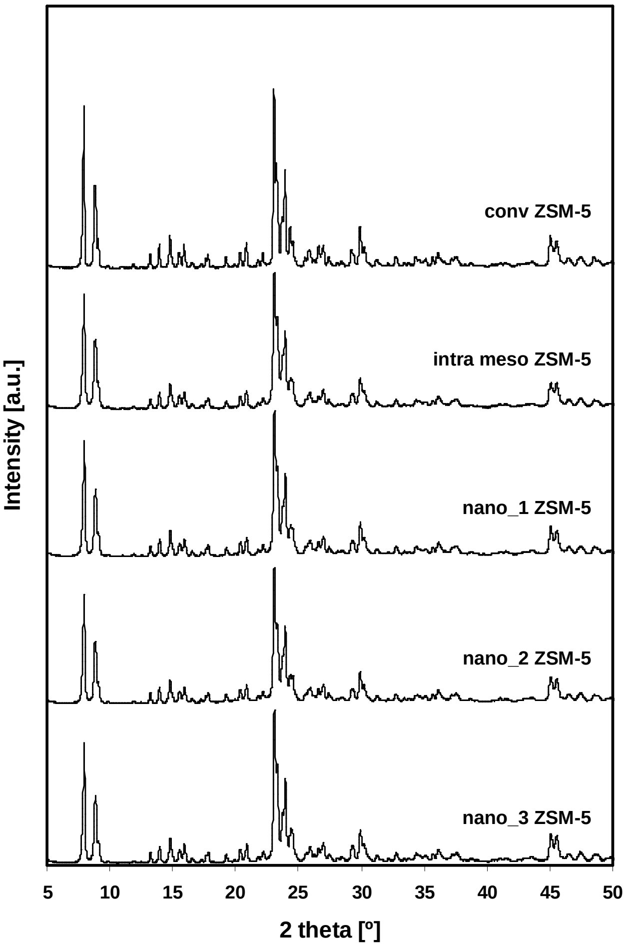

Figure 2.10: XRPD of the five synthesised ZSM-5 zeolites

The XRPD patterns show no background increase in the 2θ region of 15-25°, which is normally indicative of the presence of non-crystalline impurities. The widths of the peaks are rather broad for all five samples indicating that the crystal sizes are quite small. The average crystal sizes determined by the Debye-Scherrer equation are given in Table 2.1.

Table 2.1: Average crystal size of the five synthesised zeolites determined by the Debye-Scherrer equation

	D[101] [Å]	D[200] [Å]	D[103] [Å]	D[113] [Å]	D[303] [Å]	D[313] [Å]
conv ZSM-5	>1000	725	>1000	>1000	>1000	>1000
intra meso ZSM-5	885	445	915	645	>1000	370
nano_1 ZSM-5	900	520	>1000	655	>1000	460
nano_2 ZSM-5	950	520	>1000	720	>1000	575
nano_3 ZSM-5	>1000	555	>1000	730	>1000	425

As it is seen from Table 2.1, the conventional ZSM-5 contains the largest crystals. The size of the zeolite crystals with intracrystalline mesopores lie in the same range as the three nanosized zeolites. This raise the question of whether the mesoporous zeolite is a true single crystal with intracrystalline mesopores or an ordered arrangement of nanosized zeolite crystals. As stated in chapter 1, assuming the mesoporous zeolite is a single crystal Egeblad *et al.*[29] explain that it can be due to the disturbance of the longer-range ordering by the presence of non-crystallographic voids or mesopores and thus, XRPD cannot be applied to determine whether the mesopores in mesoporous zeolite materials are intercrystalline or intracrystalline, *i.e.* whether the individual crystals are nanosized or mesoporous. Furthermore, they suggest the use of more indirect imaging techniques such as electron microscopy when determining the size of individual crystal of mesoporous zeolites. The size of the nanosized zeolite crystals are all in the same range in each direction, so according to XRPD the two synthesis variations of Huang *et al.*'s confined-space synthesis do not affect the crystal size significantly.

All the prepared zeolite samples were studied using SEM and representative images are shown in Figure 2.11.

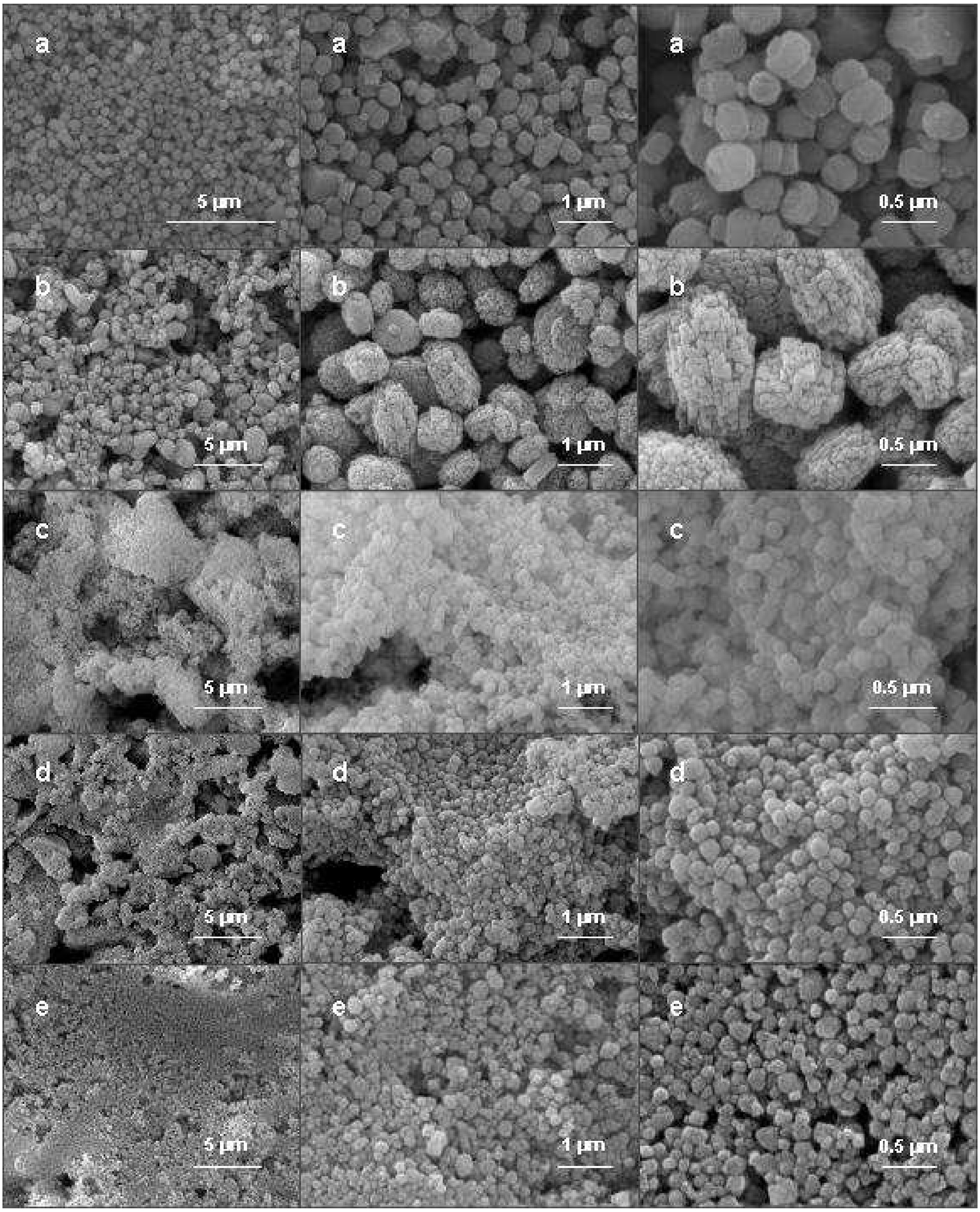

Figure 2.11: Representative SEM images of the five prepared ZSM-5 zeolite; a) conv ZSM-5, b) intra meso ZSM-5, c) nano_1 ZSM-5, d) nano_2 ZSM-5 and e) nano_3 ZSM-5

From the SEM images of the conventional ZSM-5, Figure 2.11a, it can be seen that there exists a rather homogeneous distribution concerning the crystal size of the zeolite particles of around 0.5 µm. Not all the conventional ZSM-5 zeolite crystals have the typical coffin-shape, as some crystals are more rounded. From the SEM images of the intracrystalline mesoporous zeolite, Figure 2.11b, it can be seen that the crystals exist in a size of approximately 0.5-2 µm. The crystals look like very typical mesoporous zeolite crystals since they feature the characteristic sponge-like morphology. Some of the crystals also have the typical coffin-shape. SEM images of the three nanosized zeolites, Figure 2.11 c, d and e, are quite similar concerning size and shape of the crystals. The crystals appear to be round with a rather rough and cracked surface and a crystal size of approximately 0.1-0.2 µm, see the enlarged SEM images in Figure 12. According to SEM the two synthesis variations of Huang *et al.*'s confined-space synthesis do not affect the crystal size and shape significantly.

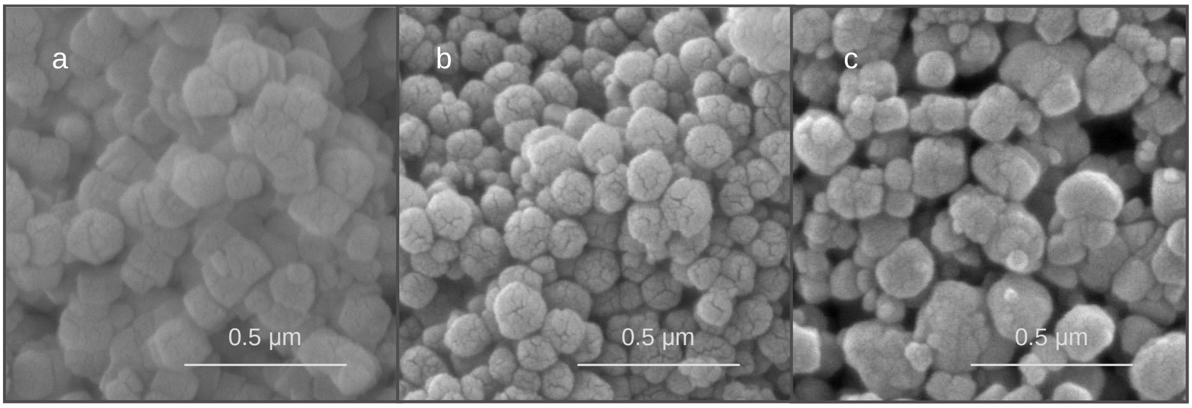

Figure 2.12: Enlarged SEM images of a) nano_1, b) nano_2 and c) nano_3 ZSM-5

Comparing XRPD results with the SEM images the crystal sizes determined by the Debye-Scherrer equation correspond to the particles sizes estimated by SEM except for the intra meso ZSM-5. But it is not possible from the SEM images of the intra meso ZSM-5 to evaluate if the sample is a single crystal or a perfect assembly of nanosized zeolite crystals.

In Table 2.2 is listed the surface areas and pore volumes of the zeolite samples.

Table 2.2: Surface areas and pore volumes of the five prepared zeolite samples

	Surface area[a] [m^2/g]	External surface area[b] [m^2/g]	Micropore volume[b] [cm^3/g]	Mesopore volume[c] [cm^3/g]
conv ZSM-5	384	12	0.17	0.12
intra meso ZSM-5	487	81	0.19	0.55
nano_1 ZSM-5	404	43	0.17	0.33
nano_2 ZSM-5	335	35	0.14	0.44
nano_3 ZSM-5	417	27	0.18	0.27

[a] Calculated using the BET method, [b] determined using the t-plot method and [c] determined using the BJH method (desorption)

Table 2.2 reveals that all zeolite materials are microporous materials with surface areas typical for zeolites, however the surface area for nano_2 ZSM-5 is a little lower than the other two nanosized zeolites. The typical micropore volume for highly crystalline ZSM-5 zeolites[66, 145-147] lies in the range 0.09-0.19 cm^3/g, which means the micropore volumes for all the prepared sample are relatively high compared to the typical value. It is expected that the external surface area is higher for the nanosized zeolites than for the conventional zeolite due to the smaller crystals. This is also observed in Table 2.2 where the external surface areas for the nanosized zeolites are at least twice as high as the external surface area for the conventional zeolite. According to the N_2 physisorption measurements all the prepared zeolite samples contain mesopores. The estimated mesopore volume for the conventional ZSM-5 zeolite is quite low and must be due to interparticle voids. The highest mesopore volume is obtained for the mesoporous zeolite with intracrystalline mesopores. Comparing the mesopores volume for the three nanosized zeolites the highest is obtained for nano_2 ZSM-5. This indicates that introducing silica after the preparation of the silica-carbon composite it is possible to introduce a larger amount of mesopores. On the other hand, if the silica-carbon composite is not coated with P123/PFA it seems to slightly decrease the mesopores volume.

Figure 2.13 shows the physisorption isotherms and pore size distributions for the prepared zeolite samples.

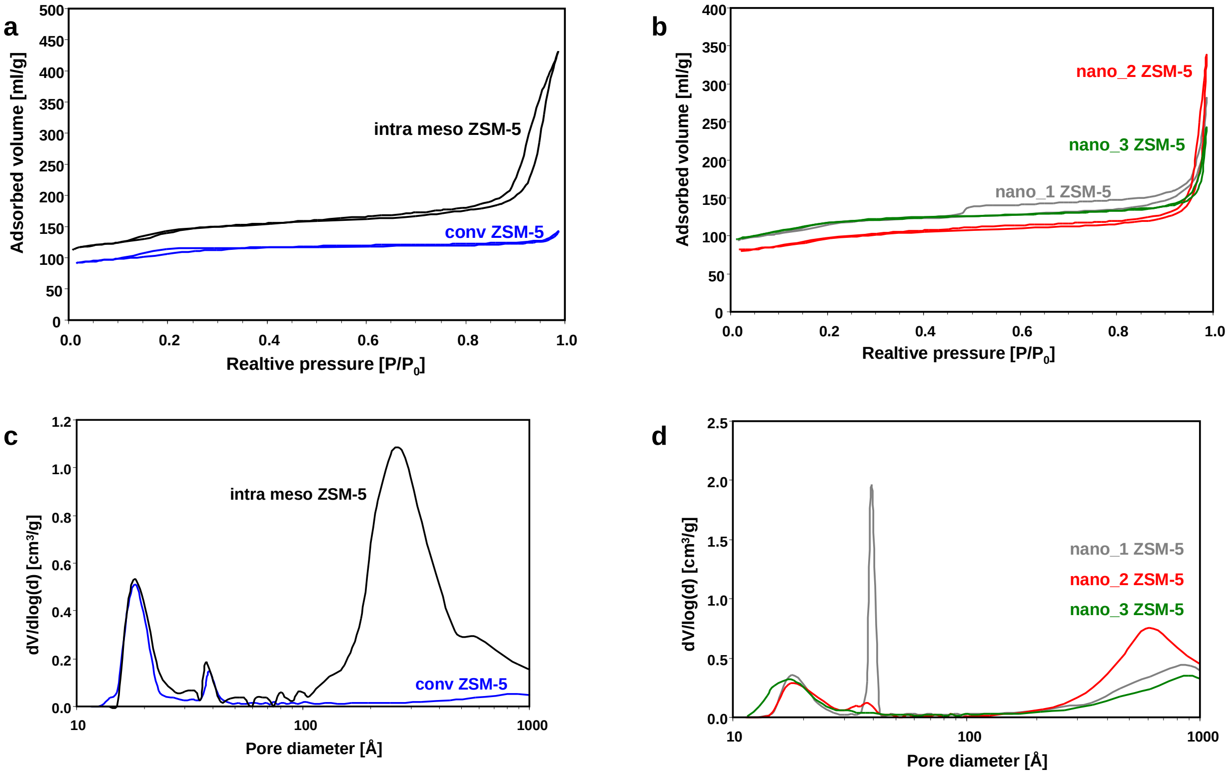

Figure 2.13: N_2 adsorption-desorption isotherms (a and b) and corresponding pore size distribution (c and d) of the five prepared zeolite samples. The pore size distributions are obtained from the desorption branch of the isotherm using the BJH method. In the pore size distributions the peaks at 20 and 40 Å are both artefacts

The physisorption isotherm for the conventional ZSM-5 in Figure 2.13a resembles a Type I isotherm and typical for microporous zeolites. The physisorption isotherm for the mesoporous zeolite samples (Figure 2.13 a and b) all exhibit hysteresis in the region P/P_0 above 0.9 which indicates the presence of mesoporosity. As seen in Figure 2.13c the size distribution of the conventional ZSM-5 zeolite does not contain any significant amount of mesopores contrary to the intra meso ZSM-5 zeolite which contains mesopores centered at 25 nm and also some pores in the macropore region (above 50 nm). The used carbon template, BP-2000, are small carbon particles with an average diameter of 12 nm. The present mesopores in intra meso ZSM-5 are twice the size of the diameter of the used carbon particles suggesting that the encapsulated carbon consists of aggregates of carbon particles that are encapsulated during zeolite. The three nanosized zeolites contain primary pores in the macropore region. In all pore size distributions the artefacts at 2 and 4 nm are present due to the result of phase transition of N_2 and forced closure of the hysteresis loop, respectively.

Figure 2.14 shows representative TEM images of the four mesoporous zeolites. In general it was difficult to obtain the TEM images due to beam damage of the zeolite particles.

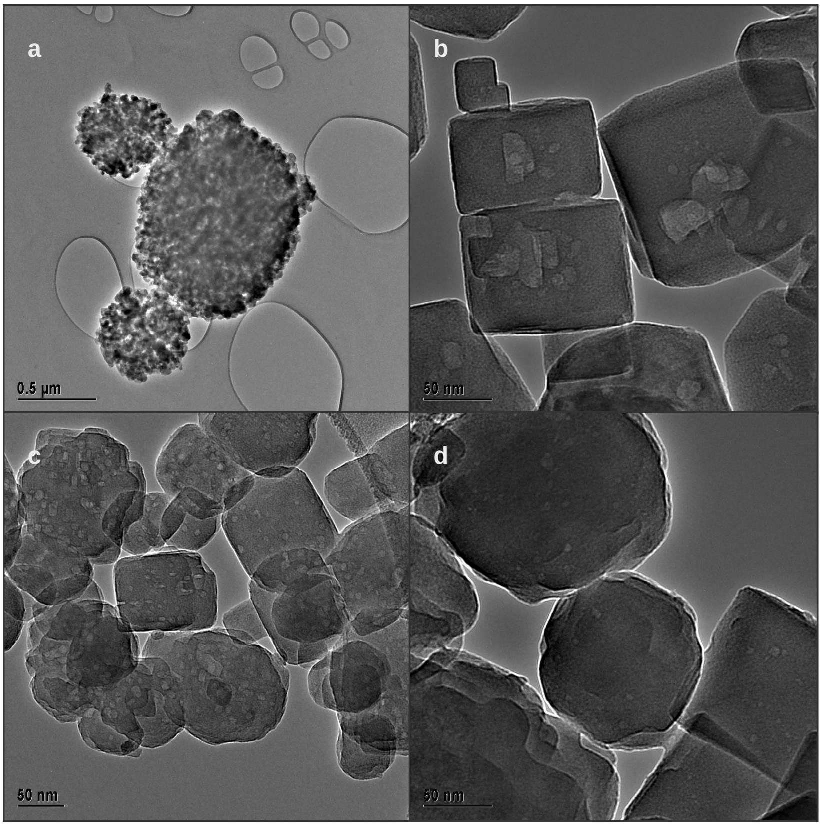

Figure 2.14: Representative TEM images of the four mesoporous zeolites: a) intra meso ZSM-5, b) nano_1 ZSM-5, c) nano_2 ZSM-5 and d) nano_3 ZSM-5

From the TEM images of the mesoporous zeolite with intracrystalline mesopores, Figure 2.14a, it is clearly seen that the crystal is mesoporous. The brighter spots which appear all over the crystal are due to the presence of pores. Conventional and mesoporous zeolites have a very diverse appearance in TEM images. Conventional zeolite crystals have very straight edges and show no change in contrast in TEM whereas mesoporous crystals are very rugged in the edges and show a clear difference in contrast. TEM images of the three nanosized zeolites, Figure 2.14b, c and d, are all quite similar. They all appear denser than the intracrystalline mesoporous zeolite, however all of them contain also bright areas. This indicates that the nanosized zeolites also contain intracrystalline mesopores to a certain extent. Their edges are clearly straighter than the intracrystalline mesoporous zeolite. It seems that nano_2 ZSM-5 contains more bright spots than nano_1 and nano_3 ZSM-5 and therefore it seems to be the most porous one. This is in agreement with the N_2 physisorption measurements where nano_2 ZSM-5 displayed the highest mesopores volume assuming they have the same amount of intercrystalline voids.

From the TEM images of intra meso ZSM-5 it is hard to determine whether the crystal consists of agglomerates or is in fact a single crystal. In the original study by Jacobsen *et al.*[35] SAD patterns were obtained showing that the mesoporous zeolite with intracrystalline mesopores can be produced to what appears to be a single crystal. Still, according to Imai *et al.*[117] care must be taken when using SAD to investigate whether a particle is a single crystal or just a perfectly ordered assembly of nanosized crystals as they can produce the same SAD pattern. It seems therefore almost impossible to determine whether or not the mesoporous zeolite with intracrystalline mesopores is actual a single crystal or a subunit crystals in an ordered environment. SAD was recorded on selected crystals and a representative pattern is given in Figure 2.15 together with the corresponding TEM image.

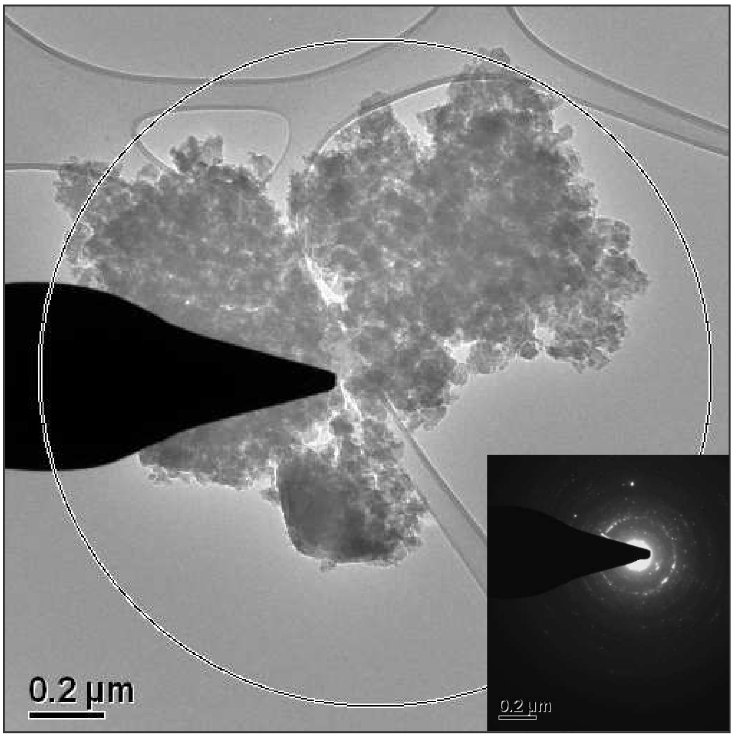

Figure 2.15: TEM image of an isolated single intra meso ZSM-5 crystal and the obtained SAD pattern

As seen in the inset in Figure 2.15 the SAD pattern reveals that the intra meso ZSM-5 is *not* a single crystal. SAD was also performed on other crystals giving the same result. In addition, at larger magnification it could also be observed that the sample consists of nanocrystals with a random orientation (not shown). In conclusion, the prepared mesoporous ZSM-5 with intracrystalline mesopores consists in fact of subunit crystals in a rather ordered environment retaining the coffin-shaped morphology.

In Table 2.3 is given the results from elemental analysis and NH_3-TPD. NH_3-TPD provides information about the part of aluminum, which is responsible for the zeolite acidity while elemental analysis provides information about the total content of aluminum and silicon in the zeolite sample.

Table 2.3: Si/Al ratios estimated by elemental analysis and NH_3 -TPD

	NH_3 -TPD Si/Al	Elemental analysis		
		Si/Al	Si [wt%]	Al [wt%]
conv ZSM-5	43	39	42.9	1.05
intra meso ZSM-5	59	40	42.3	1.02
nano_1 ZSM-5	49	41	41.3	0.96
nano_2 ZSM-5	58	43	43.2	0.96
nano_3 ZSM-5	43	40	42.3	1.03

According to elemental analysis all five samples contain the same amount of aluminum around 1 wt% corresponding to Si/Al ≈ 40. A lower Si/Al corresponds to a higher content of aluminum. In the synthesis gel the Si/Al was 50 meaning a higher amount of aluminum is present in the samples than expected.

Assuming each framework aluminum atom is responsible for the formation of one acid site and that one NH_3 molecule is adsorbed to one acid site, the amount of desorbed NH_3 is proportional to the aluminum content in the framework. For conventional ZSM-5 and nano_3 ZSM-5 the estimated Si/Al ratios from NH_3-TPD and elemental analysis are in good agreement. This means that all aluminum is incorporated into the zeolite framework or at least only a small amount of extra-framework aluminum is present. For the intra meso, nano_1 and nano_2 ZSM-5 a discrepancy is observed between Si/Al ratios determined by NH_3-TPD and elemental analysis, indicating that not all of the aluminum is present in the framework. The presence of extra-framework aluminum in nano_2 ZSM-5 could also explain the lower surface area and micropore volume as the extra-framework aluminum could block the pores. Comparing the three nanosized zeolites the variations of the confined-space synthesis seems to have an effect of the amount of incorporated aluminum in the framework but not on the amount of aluminum present in the sample.

Figure 2.16 shows the FTIR spectra for all five prepared samples. They are recorded to investigate the amount of strong Brønsted acid sites, extra-framework aluminum, terminal silanols and internal defects.

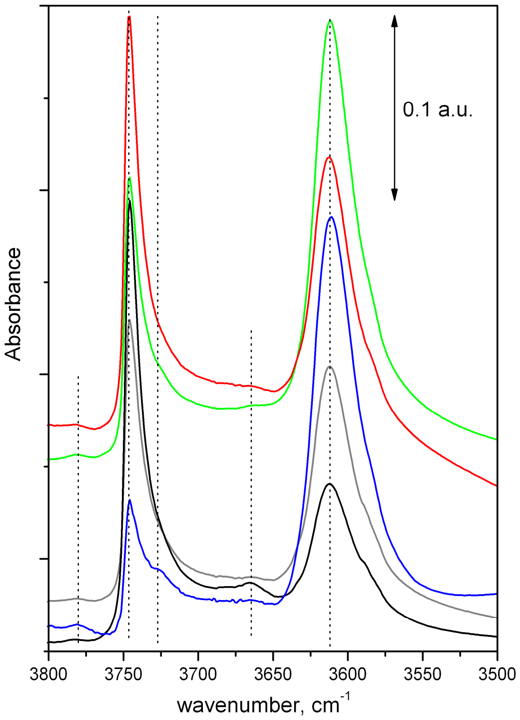

Figure 2.16: FT-IR spectra of the prepared samples. Conv ZSM is blue, intra meso ZSM-5 is black, nano_1 ZSM-5 is grey, nano_2 ZSM-5 is red and nano_3 ZSM-5 is green

The strong Brønsted acid sites appear as a band at 3610 cm^{-1}. According to the FTIR measurements the nano_3 ZSM-5 have the most intense band which is in agreement with NH_3-TPD to be the sample containing the highest amount of acid sites. The three samples intra meso, nano_1 and nano_2 all seem to contain extra-framework aluminum according to NH_3-TPD and elemental analysis. If extra-framework aluminum is present a band should appear in the FTIR spectra at 3660 cm^{-1}. However, this seems to be most pronounced in intra meso ZSM-5. Terminal silanol groups appear primarily on the external surface of the zeolite crystals and should therefore be proportional to the external surface area. The band for terminal silanol groups is located at 3745 cm^{-1} in the FTIR spectra. The external surface area of five samples decreases in the following order: intra meso, nano_1, nano_2, nano_3 and conv ZSM-5 which are almost identical with the order of decreasing intensity of the FTIR band at 3745 cm^{-1}. As an estimate for internal defects the IR intensity ratio between I_{3726} and I_{3745} is used where the band at 3726 cm^{-1} corresponds to perturbed Si-OH sites predominantly located inside the zeolite structure. The calculated ratios are given in Table 2.3.

Table 2.3: IR intensity ratio between I_{3726}/I_{3745} as an estimate for amount of defects

	conv ZSM-5	**intra meso ZSM-5**	**nano_1 ZSM-5**	**nano_2 ZSM-5**	**nano_3 ZSM-5**
IR intensity ratio [I_{3726}/I_{3745}]	0.527	0.275	0.283	0.287	0.345

As seen in Table 2.3 the nanosized and mesoporous zeolites contain approximately the same amount of defect and the conventional zeolite contains the highest amount of defects. In the study of Barbera *et al.*[135] the IR intensity ratio was in the range of 0.5 to 1.5. Therefore, the prepared samples seem to contain a rather low amount of defects compared to other synthesised samples.

2.4.2 Catalytic lifetime in the MTH reaction

To investigate the catalytic lifetime the conversion of methanol is plottet versus amount of methanol passed over the catalyst bed. The catalytic results are shown in Figure 2.17. Due to variations of flow in the different reactor types in the parallel set-up it is chosen to plot the conversion versus amount of methanol passed over the catalyst bed instead of time on stream.

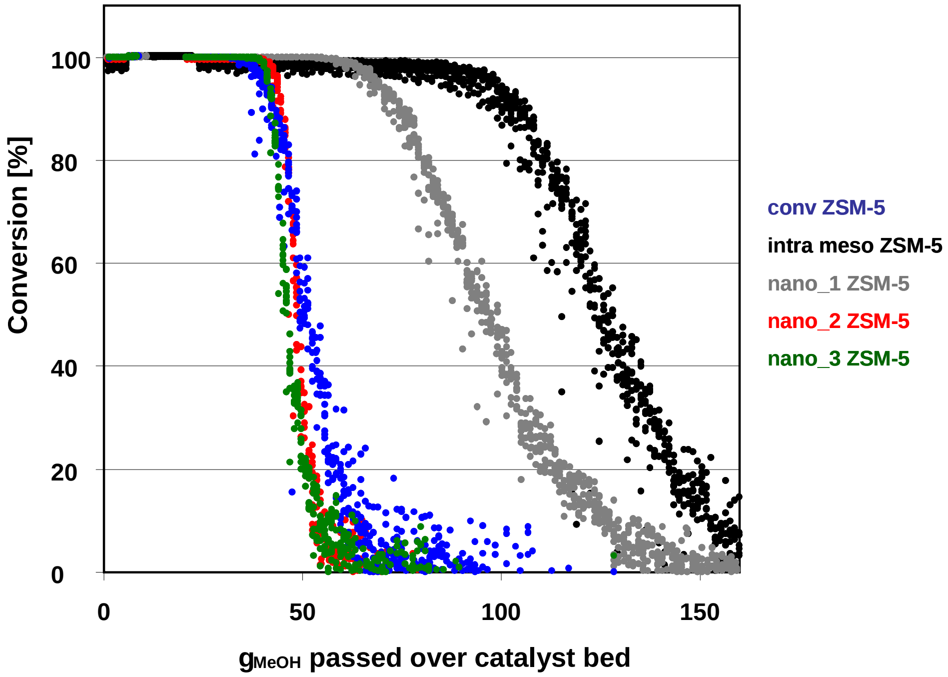

Figure 2.17: Conversion versus mass of methanol passed over the catalyst bed for the five prepared zeolite samples

As seen in Figure 2.17 the mesoporous ZSM-5 with intracrystalline mesopores has the longest lifetime for the conversion of methanol. After this follows: nano_1> conv ≈ nano_2 ≈ nano_3. The catalytic results indicate that nanosized zeolites do not necessarily increase the catalytic lifetime in the MTH reaction as nano_2 and nano_3 ZSM-5 display the same catalytic lifetime as conv ZSM-5. Even though the nano_1 has a significant longer catalytic lifetime than the conventional ZSM-5, the presence of intracrystalline mesopores enhances the catalytic lifetime even further. Nano_1 and intra meso ZSM-5 have comparable amount of mesopores but the intra meso ZSM-5 displays the longest catalytic lifetime. Even though mesopores can in some cases enhance the catalytic lifetime in the MTH reaction, still, other factors must come into play. As stated above a high Si/Al ratio is preferred since previous results show that zeolites with a low concentration of acid sites deactivate more slowly. According to NH_3-TPD intra meso ZSM-5 has the highest Si/Al ratio which is in agreement with previous results as this sample has the longest catalytic lifetime. Nano_2 ZSM-5 has approximately the same Si/Al as intra meso ZSM-5 but a significant lower catalytic lifetime which is identical with that of conv ZSM-5. A high Si/Al ratio will not necessarily result in a long catalytic lifetime despite enhanced porosity.

As stated above, Kim *et al.*[10] has found a correlation between conversion capacity and external surface area. To see if this is the case the conversion capacity determined as the amount of methanol passed over the catalytic bed at 50 % conversion divided by the mass of catalyst is plotted in Figure 2.18 versus the external surface area.

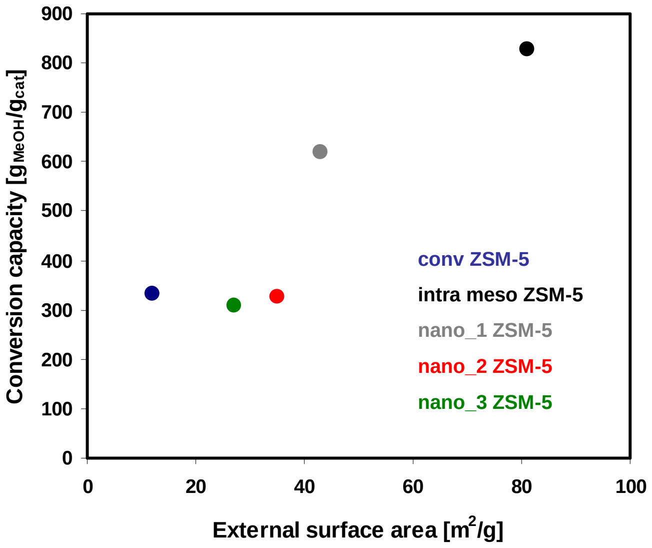

Figure 2.18: Correlation between conversion capacity and external surface area. The conversion capacity is determined as the amount of methanol passed over the catalytic bed at 50 % conversion divided by the mass of catalyst

As seen in Figure 2.18 there is no linear correlation between the conversion capacity and the external area. If this were to be the case nano_2 and nano_3 ZSM-5 should both be considered outliers.

To investigate the correlation between amount of defect and catalytic lifetime, the internal defects are estimated by the IR ratio (I_{3726}/I_{3745})[135] and plotted in Figure 2.19 together with the deactivation rate. The deactivation rate is the rate at which the effective amount of catalyst decreases. For comparison the data are inserted in Figure 2.2.

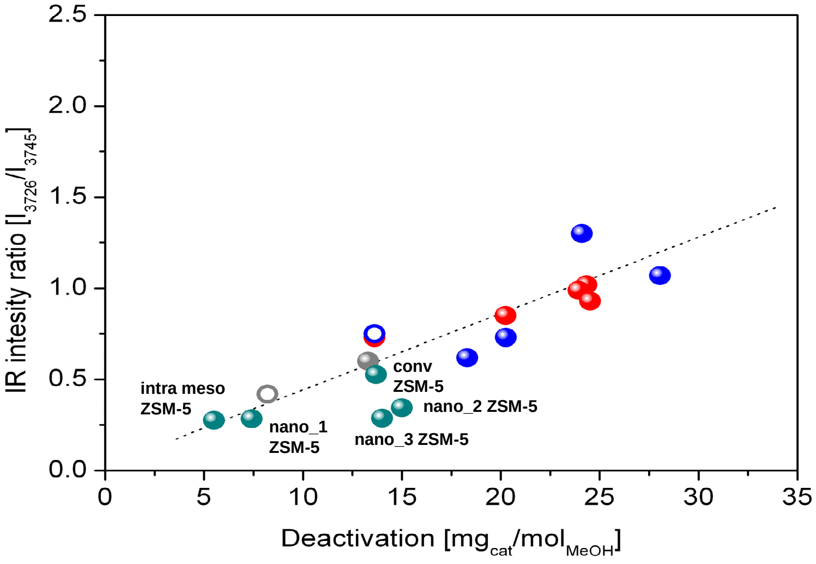

Figure 2.19: Correlation between the deactivation rate and the IR intensity (I_{3726}/I_{3745}) as an estimate for internal defects. The catalytic results are inserted as dark turquoise points in Figure 2.2

It can be observed in Figure 2.19 that conventional, mesoporous and one of the nanosized zeolites correlate well with previous results and verify the correlation between the deactivation rate and internal defects. Two of the nanosized zeolite samples seem though to be slightly of the curve. All the samples contain approximately the same amount of aluminum but according to NH_3-TPD and FT-IR some of the samples contain extra-framework aluminum. Nano_1 and nano_2 ZSM-5 are rather similar materials concerning crystal size, morphology, porosity and aluminum content. Nano_2 ZSM-5 seems to contain a larger amount of extra-framework aluminum than the nano_1 ZSM-5 which could explain the observed difference in the catalytic lifetime. For further investigation conv ZSM-5, nano_1 and nano_2 ZSM-5 were dealuminated by suspension in 1 M oxalic acid at 80 °C for 1 hour to remove potential extra-framework aluminum. After this treatment the three selected samples were again investigated by N_2 physisorption prior to catalytic test and the results are given in Table 2.4.

Table 2.4: Surface areas and pore volumes of three selected samples before and after dealumination

	Surface area[a] [m^2/g]		Micropore volume[b] [cm^3/g]		Mesopore volume[c] [cm^3/g]	
	before	after	before	after	before	after
conv ZSM-5	384	449	0.17	0.20	0.12	0.15
nano_1 ZSM-5	404	453	0.17	0.19	0.33	0.63
nano_2 ZSM-5	335	431	0.14	0.18	0.44	0.54

[a] Calculated using the BET method, [b] determined using the t-plot method and [c] determined using the BJH method (desorption)

Table 2.4 reveals that the surface area, micropore and mesopore volumes are all increased after oxalic acid treatment. The acid treatment has the most pronounced effect concerning surface area and micropore volume for nano_2 ZSM-5 indicating that extra-framework aluminum could have blocked the micropores. The mesopore volume for nano_1 ZSM-5 is almost doubled and is hereby the sample containing the highest degree of mesoporosity.

The three samples, how oxalic acid treated, were tested for their catalytic lifetime in the MTH reaction. For various practical reasons they were tested in a different set-up and under different conditions. The conversion of methanol is shown in Figure 2.20 as function of time on stream.

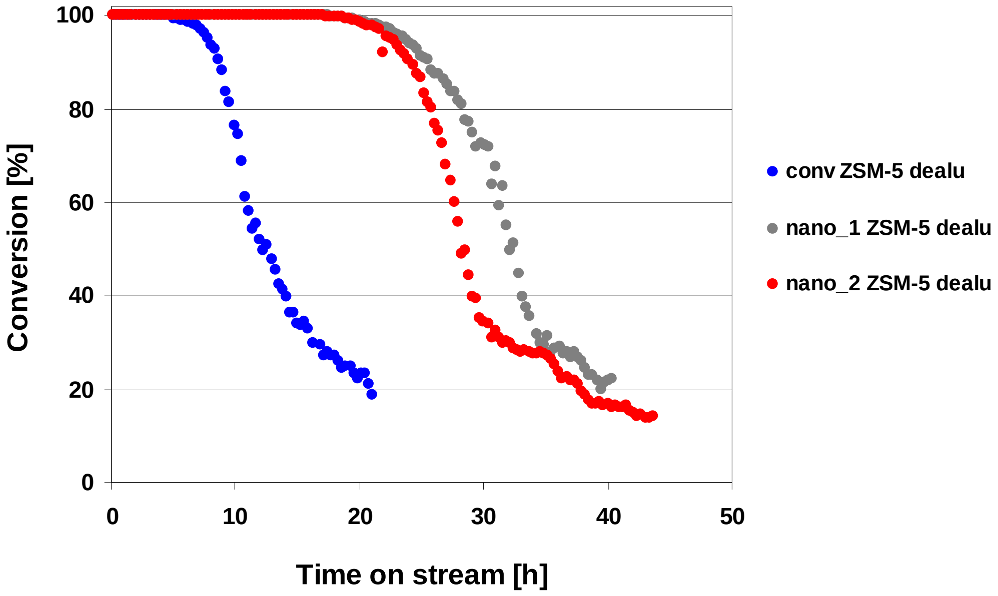

Figure 2.20: Conversion of methanol versus time on stream for the dealuminated versions of conv ZSM-5, nano_1 and nano_2 ZSM-5. The samples are tested in a fixed-bed plug-flow reactor at 350 °C and WHSV = 10.5 h^{-1}

As seen in Figure 2.20 nano_1 and nano_2 ZSM-5 have approximately the same catalytic lifetime in the MTH reaction after acid treatment which are significantly higher than the one for the conventional ZSM-5. The nano_1 ZSM-5 displays the longest catalytic lifetime and also being the sample containing the highest degree of mesoporosity suggests that the presence of mesopores enhance the catalytic lifetime in the MTH reaction. Prior to dealumination the conv ZSM-5 did not contain any remarkable amount of extra-framework aluminum but was still dealuminated for comparing the samples after identical treatments. The catalytic results strongly indicate that extra-framework aluminum has a severe influence on the catalytic lifetime in the MTH reaction.

2.5. Conclusion

In the present chapter nanosized and mesoporous ZSM-5 zeolites were prepared to investigate the effect of inter- or intracrystalline mesopores on the catalytic lifetime in MTH reaction. One mesoporous zeolite with intracrystalline mesopores was synthesised together with three types of nanosized zeolites. They were characterised together with a conventional ZSM-5 zeolite using XRPD, SEM, TEM, N_2 physisorption, NH_3-TPD, elemental analysis as well as FTIR. The characterisations revealed that all synthesised materials are highly crystalline and contain approximately the same amount of aluminum. Even though the three nanosized zeolites differed in synthesis procedures the obtained materials were rather similar regarding crystal size and morphology. They differed though slightly in the porosity and amount of extra-framework aluminum.

In the catalytic test the mesoporous zeolite with the intracrystalline mesopores displayed the significantly longest catalytic lifetime in the MTH reaction. This could to be due to a combination of the presence of mesopores and the effect of a higher Si/Al ratio. The mesoporous zeolite with intracrystalline mesopores has the highest Si/Al ratio which leads to the expectation of slow deactivation as also observed. The presence of mesopores was not the only factor that effects the catalytic lifetime as two of the nanosized zeolites displayed the same catalytic lifetime as the conventional zeolite sample. It seemed to be a correlation between the amount of defects and catalytic lifetime all though two of the nanosized samples were slightly outliers.
It was observed that dealuminating selected samples with oxalic acid enhanced the catalytic lifetime significantly. This must be due to the removal of extra-framework aluminum. However, it is noteworthy that the mesoporous zeolite with intracrystalline mesopores displayed the longest catalytic lifetime even though it seemed to contain the highest amount of extra-framework aluminum.

It is difficult to compare the catalytic lifetime of zeolite catalysts in the MTH reactions since several factors affect the catalytic lifetime *i.e.* Si/Al ratio, porosity and amount of defects. Since the zeolite crystallisation mechanism is quite complex, it is difficult to prepare comparable materials *i.e.* without the presence of extra-framework aluminum and where only one factor is varied. Even though it was attempted to prepare five zeolites where only the porosity differs, the amount of extra-framework aluminum seems to affect the catalytic lifetime severely. A more thoroughly investigation on the effect of extra-framework aluminum in the MTH reaction will be given in the next chapter.

Chapter 3

Effect of extra-framework aluminum in the MTH reaction

This chapter contains investigation of the effect of extra-framework aluminum on the catalytic lifetime in the MTH reaction. This is accomplished though synthesis, characterization and catalytic test of different ZSM-5 zeolite catalysts which have been desilicated, dealuminated or both. This work was done in close collaboration with other students and scientists. PhD student Søren Sørensen has conducted the MAS NMR, PhD Katia Barbera has conducted the IR investigations and PhD student Peter N.R. Vennestrøm has conducted the catalytic tests.

3.1. Introduction

As discussed in Chapter 2 several factors affect the activity and the catalytic lifetime in the MTH reaction. This makes comparison of catalyst performance between (mesoporous) samples not straightforward as the Si/Al ratio, distribution of defects, mesoporosity, particle size and other characteristics will influence the catalytic lifetime in an interdependent manner.[113] Still, in this work the effect of extra-framework aluminum on the catalytic lifetime in MTH is investigated. Extra-framework aluminum can not only emerge during crystallisation but also from post treatment procedures as desilication. Desilication is normally used as an efficient and straightforward method to introduce intracrystalline mesopores. Mesopores are formed by dilute alkali leaching and the extent of mesopore formation depends on several factors, *i.e.* topology of the zeolite[148-151], type of alkali agent[152-154] and treatment parameters like concentration of the alkaline solution, temperature and exposure time[62, 64, 65]. As stated in Chapter 1, especially, the zeolite framework Si/Al ratio influences the degree of mesoporosity. Mesopores are generated as a consequence of hydrolysis of Si-O-Si and Si-O-Al bonds in alkaline medium. Aluminum in framework positions can suppress the extraction of neighbouring silicon [$SiO_{4/2}$] due to repulsion between the negatively charged [$AlO_{4/2}$]$^-$ tetrahedron and OH^-. In comparison, the Si-O-Si bond cleaves easily in the absence of neighbouring aluminum. Groen *et al.*[62] have found that intermediate framework aluminum contents of Si/Al 25-50 appropriately regulate the extent of silicon extraction leading to controlled porosity development in ZSM-5 zeolite crystals. Mesopores are generated due to attack of hydroxide ions on silanol groups in the zeolite framework, as illustrated in Figure 3.1. The eliminated silicate anion is subsequently stabilised by the accompanying alkali cation, leaving a vacancy in the framework.[65]

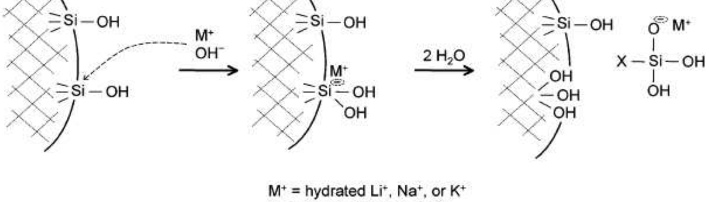

Figure 3.1: Illustration of desilication. Adapted from [65]

Using different accompanying alkali cations Groen *et al.*[65] reported that the best effect was found for NaOH due to the superior capability of sodium ions to stabilise the generated silicate anions compared to *e.g.* potassium ions.

Two modes of mesopores formation upon desilication have been proposed. First, Perez-Ramirez *et al.*[30] have demonstrated that siliceous areas of the zeolite particles may be selectively dissolved. This is apparently controlled by the distribution of trivalent framework atoms, in effect the Si/Al ratio. Second, Ogura *et al.*[155] have emphasised the potential importance of dissolution along boundaries or defects within each particle. These two suggestions were very recently verified by Svelle *et al.*[113] and both types of modes are illustrated in Figure 3.2.

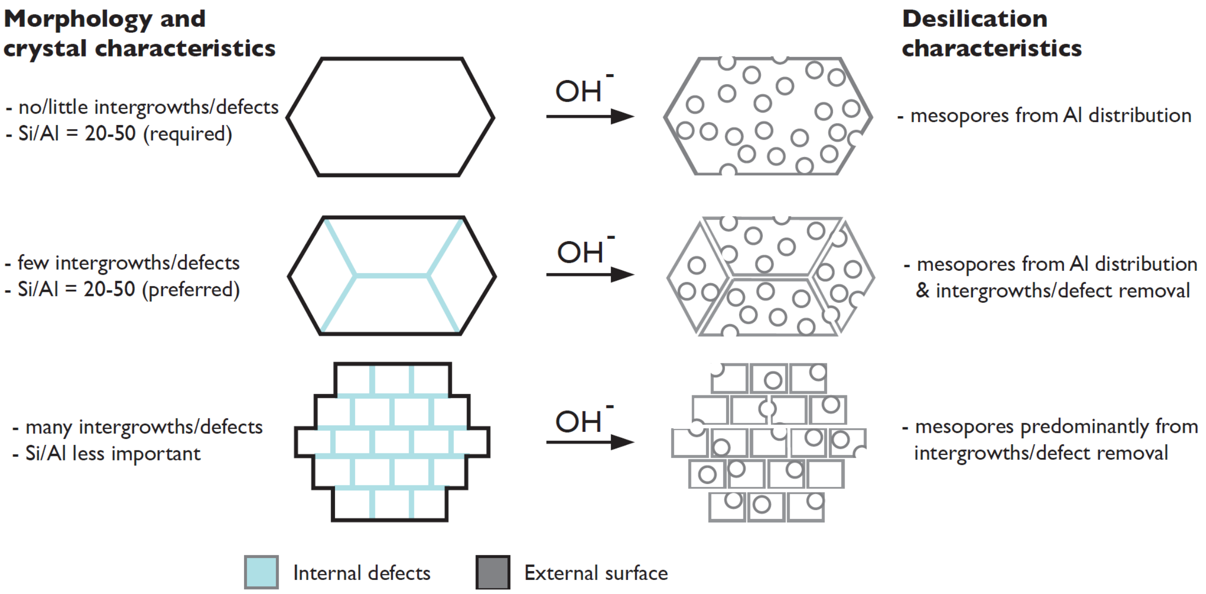

Figure 3.2: Schematic representation of different mesopores formation mechanism. Adapted from [113]

In Figure 3.4 mesopore formation by dissolution of siliceous area leads to holes whereas mesopore "super highways" are formed along crystallite intergrowth boundaries. The intergrowth boundaries can be caused by *e.g.* twinning and defects within each particle. The extent of each mode depends on the Si/Al ratio and the morphology of the zeolite crystal. Particles constructed of fused subunits appear to be very susceptible towards directed mesopore formation by desilication.[113]

The generation of mesopores by desilication does not only affect the porosity but also leads to alterations of the concentration and distribution of surface hydroxyls. These hydroxyls are part of various silanols arrangements, partially extra-framework aluminum and strong Brønsted acid sites. In general there is observed[90] a reduction in the concentration of strong Brønsted acid sites and the appearance of a second family of weaker sites ascribed to extra-framework aluminum located on the external surface or in the newly generated mesopores. The exact structure of the extra-framework species is, however, unknown but the neutral species AlOOH and $Al(OH)_3$, $(Al(OH)_3)_2$

and oxoaluminum cations such as AlO^+, $Al(OH)_2^+$ and $Al(OH)^{2+}$ have been proposed.[90] In addition, defects represented by internal Si-OH sites are removed and free Si-OH sites increase in concentration and point to a selective mechanism for formation of mesopores. The strength of the Brønsted acid sites is though not altered significantly, but only the concentration.

Desilication is an efficient and relative straightforward method to introduce mesoporosity. From a practical point of view the desilication procedure is faster compared to the carbon templating route since the latter of the two requires more preparative steps to achieve the desired hierarchical material. On the other hand, carbon templating can be applied to a wide range of zeolite materials independent on composition and morphology. The size and shape of the mesopores channels can also easier be controlled using carbon templating. Furthermore, during desilication an extensive loss of material and alteration of Si/Al ratios will inevitable occur. The rather harsh alkaline conditions can also have potential side effects *i.e.* crystal collapse. The choice of whether using the carbon templating or the desilication route to introduce mesoporosity also affects the amount of internal silanols/defects. During desilication internal defects are more or less repaired whereas carbon templating leads to a material with a high concentration and wide distribution of surface hydroxyls/defects.[113] An explanation for this high amount of internal silanols by the use of carbon templating could be given by considering the relative high local temperature reached during the combustion of the carbon template via calcination. As stated in Chapter 2, the amount of internal defects affects the catalytic lifetime in the MTH reaction.

Previously, a reduction in deactivation was found for desilicated samples in the MTH reaction.[9, 90, 113] The cause of this could possibly be a combination of an enhanced mass transfer of coke due to introduced mesoporosity[10] or an increased tolerance for coke deposition, *i.e.* that a higher coke loading is required to deactivate the catalyst[156]. Alternatively, the repair of internal defects might improve the catalytic lifetime as proposed by Barbera *et al.*[135]. In the present chapter desilicated ZSM-5 zeolites are used to investigate the effect of generated extra-framework aluminum on the catalytic lifetime in the MTH reaction.

3.2. Synthesis strategy

In this work the effect of extra-framework aluminum is investigated by desilicating a conventional ZSM-5 zeolite to generate extra-framework aluminum. The obtained material is subsequently dealuminated to observe the effect of removing the extra-framework aluminum on the catalytic lifetime in the MTH reaction. Depending on the conditions during dealumination, aluminum can be removed from both framework and extra-framework positions.[7] Framework aluminum can be extracted by either hydrothermal treatment in the presence of steam[157-159] or treatment with strong acids[160-162].The steaming is usually performed at temperatures above 500 °C whit the original zeolite is in its ammonium or hydrogen form. During the contact with steam hydrolysis of

Al-O-Si bonds takes place and aluminum is expelled from the framework causing a vacancy leading to mesopore formation or partial amorphisation of the framework. The effectiveness of strong inorganic acids to extract aluminum from framework positions depends on the zeolite and the nature of the acid.[163] It is also reported that the use of $SiCl_4$[164], EDTA[165] and $(NH_4)_2SiF_6$[166] can remove aluminium from framework positions. The removal of aluminum from the framework will as desilication cause changes in the number and nature of the acid sites and potential creation of amorphous extra-framework material. To remove aluminum only from extra-framework positions it is sufficient to perform a mild aqueous acid-leaching step with either inorganic acids such as dilute nitric acid or organic acids such as oxalic acid.[167-169] In this case mesopores are not actually formed. Instead the pores are emptied, resulting in a higher mesopore volume compared to untreated samples.

In this work four zeolite samples are prepared and the synthesis strategy is schematically illustrated in Figure 3.3.

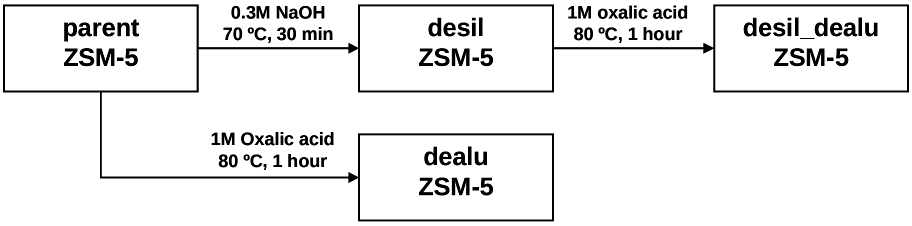

Figure 3.3: Schematic illustration of the four prepared zeolite samples

First a parent conventional ZSM-5 zeolite is prepared which is subsequently desilicated using an aqueous solution of NaOH to generate mesopores and extra-framework aluminum. After desilication the sample, desil ZSM-5, is dealuminated using a dilute solution of oxalic acid to investigate the effect of removing the extra-framework aluminum on the catalytic lifetime in the MTH reaction. To demonstrate that it is not possible to extract aluminum from the framework using the chosen dealumination conditions, a reference material (dealu ZSM-5) is produced by treating the parent ZSM-5 zeolite with the oxalic acid solution.

3.3. Experimental

All the reagent were of reagent grade and used without any further purification: Sodium hydroxide (NaOH, 99 wt%, Riedel-de Häen), tetrapropylammonium hydroxide (TPAOH, 40 wt%, AppliChem), Sodium aluminate ($NaAlO_2$, Al: 29.3 wt%, Riedel-de Häen), Ludox® TMA (SiO_2 34 wt%, Grace GmbH & Co KG), Sodium silicate ($Na_2O(SiO_2)_x{\cdot}xH_2O$, 10.6 wt% Na_2O and 26.5 wt% SiO_2, Sigma-Aldrich), ammonium nitrate (NH_4NO_3, 99.5 wt%, Merck), oxalic acid dihydrate ($C_2H_2O_4{\cdot}2H_2O$, 99.5 wt%, Riedel-de Häen), Methanol (> 99.9 %, Aldrich Chromasolv®).

3.3.1. Synthesis of conventional ZSM-5

Conventional ZSM-5 was synthesised using the following procedure:

> *In a beaker 54.5 g TPAOH (40 wt%) was diluted with 55.31 g H_2O and cooled to 0 °C on a ice bath after which 0.652 g $NaAlO_2$ was added. When a clear solution was obtained 54.29 g Ludox® TMA was slowly added followed by addition of 10.34 g sodium silicate. The homogeneous gel was kept stirring overnight, by which the ice was melted, and the next day the gel was transferred to a Teflon lined stainless steel autoclave and heated to 150 °C for 48 hours under static conditions. After cooling the autoclave to room temperature the white product was isolated by suction filtration and washed several times with water until neutral pH. The product was dried overnight at room temperature and finally the organic template was removed by calcinations in a muffle furnace at 550 °C for 3 hours. The obtained white product was named parent ZSM-5.*

3.3.2. Preparation of desilicated ZSM-5

The parent ZSM-5 sample was desilicated using the following procedure:

> *The calcined parent ZSM-5 was treated with a 0.3 M NaOH solution for 30 minutes at 70 °C, followed by cooling on ice to stop the desilication and then washed three times with water using centrifugation. The ratio between mass of sample (g) and volume of NaOH (mL) was 3:100. The desilicated ZSM-5 was dried overnight at room temperature before further treatment. The obtained product is referred to as desil ZSM-5.*

3.3.3. Ion exchange of parent and desilicated ZSM-5

The acidic form of the parent and the desilicated ZSM-5 samples were prepared using the following procedure:

> *The acidic form of the two samples were produced by two consecutive ion exchanges with a buffer solution of 1.7 M NH_4NO_3/0.94 M NH_3 in the ratio 1:10 between mass of sample (g) and volume of NH_4NO_3/NH_3 (mL). The ion exchanges were performed at 80 °C with stirring for two hours. After each exchange, the NH_4-form of the zeolites was filtered, washed with water, and dried in air at 110 °C. Finally, the H-form of the parent zeolite and desilicated zeolite were obtained by heating the NH_4-form in air to 550 °C for 3 hours.*

3.3.4. Dealumination of parent ZSM-5 and of desilicated ZSM-5

After ion exchange the parent and the desilicated ZSM-5 samples were both dealuminated using the following procedure:

> *The parent and the desilicated H-ZSM-5 were further treated after ion exchange with a 1 M oxalic acid solution for 1 hour at 80 °C to remove potential extra-framework aluminum. After the dealumination the samples were washed with water until neutral pH, then dried overnight at room temperature and finally calcined at 550 °C for 3 hours. The obtained products are named: dealu ZSM-5 and desil-dealu ZSM-5*

3.3.5. Conversion of methanol to hydrocarbons

The parent, desil and desil-dealu ZSM-5 samples were tested for their catalytic lifetime in the MTH reaction using the following conditions:

The catalyst testing was performed in a fixed-bed quartz microreactor (3 mm i.d.) at atmospheric pressure. A feed of 10.5 vol% methanol in nitrogen was created by bubbling an adjustable flow of nitrogen through a liquid solution of methanol kept at a certain temperature. All experiments were performed using 50 mg calcined and fractionised (0.3-0.6 mm) catalyst, a reaction temperature of 370 °C and a total gas flow of 25 ml/min through the reactor; the last resulting in a WHSV of 4.5 $g_{MeOH} \cdot g^{-1}_{cat} \cdot h^{-1}$*. Before each experiment the catalyst was heated from 110 °C to reaction temperature and kept there for 0.5 h under nitrogen flow. Products were analyzed by online gas chromatography using a HP 5890 series II instrument equipped with a PLOT fused silica column and a FID detector. Response factors for methanol (0.776) and dimethyl ether (0.667) were taken into account. For all other hydrocarbons the response factor was treated as being 1.000.*

3.4. Results and discussion

The prepared materials were characterised using XRPD, SEM, N_2 physisorption, NH_3-TPD, elemental analysis, ^{27}Al and ^{29}Si MAS NMR and FTIR with and without probing with CO. The reference material, dealu ZSM-5, is only characterised using XRPD and NH_3-TPD to demonstrate that the crystal structure and the distribution of the acid sites is not significantly altered after attempted dealuminating of the parent sample. All characterisations were performed after ion exchange and calcinations. Selected materials were furthermore tested for the catalytic lifetime in the MTH reaction.

3.4.1. Characterisations

The XRPD patterns for the four prepared samples are all shown in Figure 3.4.

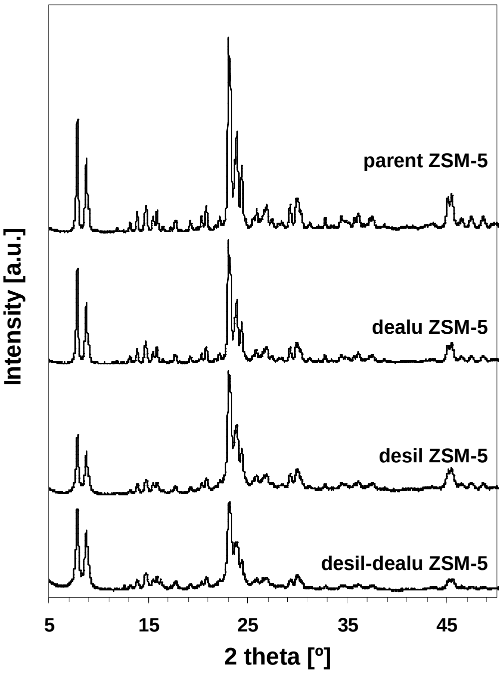

Figure 3.4: XRPD patterns of parent ZSM-5, dealu ZSM-5, desil ZSM-5 and desil-dealu ZSM-5. All patterns are recorded after ion exchange and calcinations

It is seen from Figure 3.4 that all samples exclusively contain highly crystalline material with the MFI structure[4] and it can be concluded that the MFI structure is preserved irrespective to any chemical treatment. The XRPD patterns show no background increase in the 2θ region of 15-25°, which can be attributed to the presence of non-crystalline impurities. The line widths of the XRPD peaks are rather broad for all samples indicating that the crystal sizes are quite small. Table 3.1 shows the crystal size estimated by the Debye-Scherrer equation for all samples.

Table 3.1: Average crystal sizes for parent ZSM-5, desil ZSM-5 and desil-dealu ZSM-5

	D[101] [nm]	D[200] [nm]	D[103] [nm]	D[113] [nm]	D[303] [nm]	D[313] [nm]
parent ZSM-5	68	52	94	74	85	65
dealu ZSM-5	63	49	84	64	80	62
desil ZSM-5	49	39	42	44	60	35
desil-dealu ZSM-5	38	33	38	37	33	32

It is seen from Table 3.1 that the dealumination of the parent sample slightly decreases the average crystal size. A noticeable reduction of the average crystal size is seen after the desilication in all directions and it is further reduced after the subsequently dealumination.

Figure 3.5 shows representative SEM images of the parent, desil and desil-dealu ZSM-5 samples.

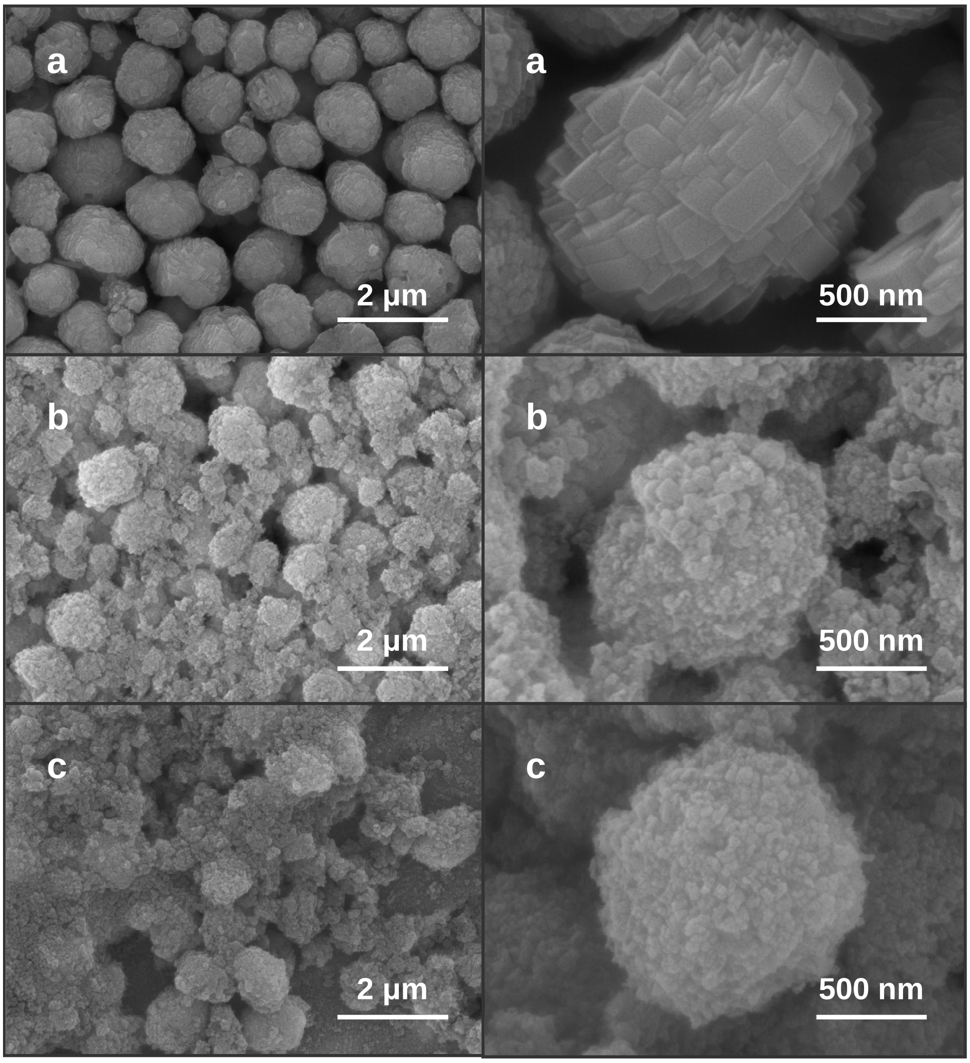

Figure 3.5: Representative SEM images of a) parent ZSM-5, b) desil ZSM-5 and c) desil-dealu ZSM-5

As seen in Figure 3.5a the parent ZSM-5 sample consists of particles around 1 µm and with a rather narrow size distribution. The particles appear to have surface roughness and seem to be formed of smaller subunits. The desilicated ZSM-5 sample, Figure 3.5b, has a sponge-like morphology but the particle size is more or less retained. However, some of the parent particles are fragmented by the post-synthesis treatment and appear as dispersed agglomerates. The subsequent dealumination does not seem to affect the morphology or the particle size, Figure 3.5c. However, as shown in the evaluation of the XRPD analyses, the average crystal size is indeed 10-40 % smaller depending on the crystallographic direction.

The data from the N_2 physisorption measurements are given in Table 3.2.

Table 3.2: N_2 physisorption data of the parent, desil and desil-dealu samples

	Surface area[a] [m^2/g]	External surface area[b] [m^2/g]	Micropore volume[b] [cm^3/g]	Total pore volume[c] [cm^3/g]
parent ZSM-5	439	43	0.17	0.26
desil ZSM-5	537	285	0.09	0.99
desil-dealu ZSM-5	552	287	0.10	0.94

[a] Calculated using the BET method, [b] determined using the t-plot method and [c] volume adsorbed at P/P_0=0.99

The BET surface area increased significantly from 439 m^2/g to 537 m^2/g due to the NaOH treatment which is a characteristic feature of desilication.[9] The increase in BET surface area is mainly caused by the higher external surface area, which can be attributed to dissolution of the zeolite framework and formation of mesopores.[62, 170] The external surface area for the parent ZSM-5 sample is a little high for a conventional ZSM-5 zeolite. A high external surface area can indicate small particles which is in agreement with the observed particle size in the SEM images and the broad peaks observed in the XRPD pattern for the parent ZSM-5.

The total pore volume increases considerably after the desilication treatment from 0.26 to 0.99 cm^3/g and since the micropore volume is decreased by the desilication, the increase must particular be due to the creation of mesopores. The dealumination treatment does not have a pronounced effect on the surface areas or pore volumes. The slight increases can be due to the removal of extra-framework aluminum from the pores.

The nitrogen adsorption/desorption isotherms for the three zeolite samples are all given in Figure 3.6 together with the pore size distributions.

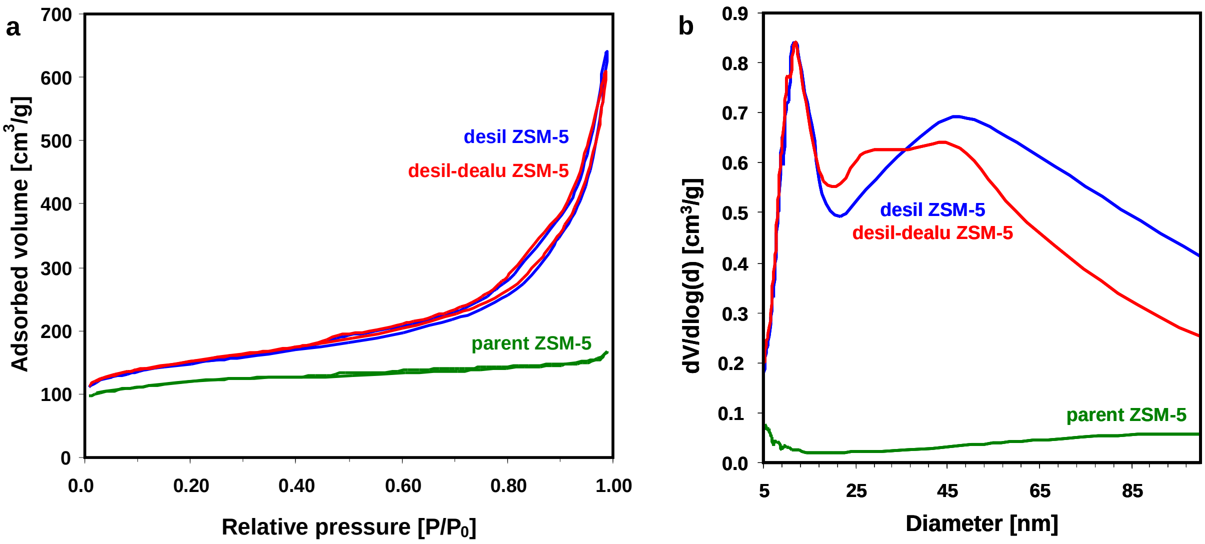

Figure 3.6: a) N_2 adsorption-desorption isotherms and b) corresponding pore size distribution of the parent ZSM-5, desil ZSM-5 and desil-dealu ZSM-5. The pore size distributions are obtained from the desorption branch of the isotherm using the BJH method

The isotherm for the parent ZSM-5 zeolite is the typical isotherm for microporous materials. The isotherms for the desil ZSM-5 and desil-dealu samples are quite similar and contain a hysteresis loop at a relative pressure higher than $P/P_0 = 0.4$ which is a characteristic feature for mesoporous materials. Figure 3.6b shows the pore size distributions for the parent ZSM-5, the desil and the desil-dealu ZSM-5 samples. It is observed that during the desilication both meso- and macropores are formed which are inevitably still present after the dealumination. The mesopore diameter for the desilicated sample is rather narrow and centred at 12 nm. The presence of macropores could be due to interparticle voids caused by the rather harsh desilication method. It is noteworthy that the pore size distribution for the desil ZSM-5 sample contains pores that are larger than the desil-dealu ZSM-5 sample. It was expected to be the other way around since the dealumination should remove extra-framework aluminum leaving larger pores.

In Figure 3.7 is displayed the NH_3-TPD profiles for the parent ZSM-5, desil and desil-dealu samples.

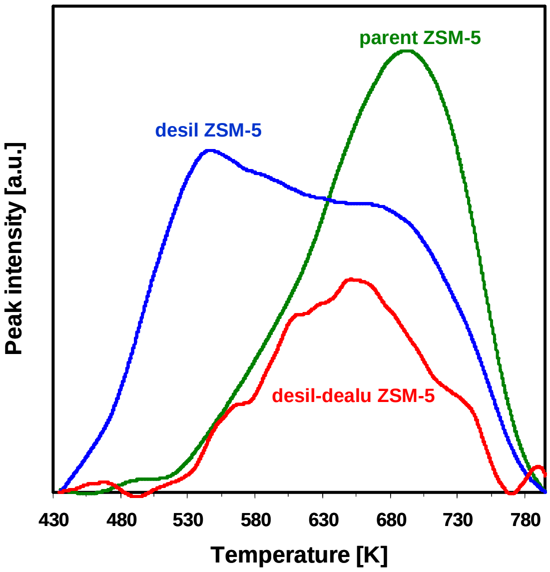

Figure 3.7: NH_3-TPD profiles of the parent ZSM-5, desil ZSM-5 and desil-dealu ZSM-5 samples

From Figure 3.7 it is seen that the NH_3-TPD profile for the parent ZSM-5 sample contains primarily a single peak around 700 K while the NH_3-TPD peak for the desilicated sample contains two peaks centered at 550 K and 675 K respectively. The low-temperature desorption peak (400-600 K) indicates weak adsorption sites which can be caused by extra-framework aluminum while the high-temperature peak (600-800 K) is due to desorption from strong Brønsted acid sites.[14] According to the NH_3-TPD profiles the parent ZSM-5 sample contains therefore primarily strong Brønsted acid sites corresponding to all aluminum being incorporated in the zeolite framework while the desilicated ZSM-5 sample contains both strong Brønsted acid sites and weaker Lewis acid sites potentially caused by extra-framework aluminum emerged during desilication. When the desilicated sample is dealuminated the NH_3-TPD profile contains only a single peak centered at 650 K and with a significant lower intensity than the one observed for the parent sample. It therefore seems that the dealumination treatment does not only remove extra-framework aluminum associated with Lewis acidity but also removes tetrahedrally coordinated aluminum from the framework and thereby decreases the Brønsted acidity.

To investigate whether or not the chosen dealumination conditions are able to remove aluminum from framework positions, the parent sample was dealuminated. According to NH_3-TPD the desorption profiles for the parent and dealu ZSM-5 samples are identical (not shown). Therefore it can be concluded that by using the chosen dealumination conditions the distribution of the strength of the acid sites is not altered. This result indicates that it is not possible to remove aluminum from the framework. One possibility is that the dealumination could remove aluminum which is partly in framework positions. It is possible that after the desilication aluminum can be present at lattice defects where the framework is disrupted, but yet not in extra-framework positions, *e.g.* as trigonal coordinated unsaturated aluminium species with strong Lewis acid character.

The shifts in peak position between the parent sample and the desil-dealu ZSM-5 can possibly reflect the different Si/Al ratios of the samples. Even though NH_3-TPD is a fast technique to investigate the distribution of the strength of the acid sites, it should only be used as a fingerprint since it is almost impossible to distinguish between the different sites. However, the NH_3-TPD shows that the distribution of the acid sites changes upon desilication leading to a considerable formation of weaker acid sites, which are subsequently removed by further dealumination.

The estimated Si/Al ratios from NH_3-TPD, elemental analysis and ^{29}Si MAS NMR are all given in Table 3.3.

Table 3.3: Si/Al ratios for the parent, desil and desil-dealu sample estimated by elemental analysis, NH_3-TPD and ^{29}Si MAS NMR

	NH_3-TPD Si/Al	**Elemental analysis**			**^{29}Si MAS NMR Si/Al**
		Si [wt%]	Al [wt%]	Si/Al	
parent ZSM-5	33	37.6	1.29	28	37
desil ZSM-5	24	35	2.64	13	29
desil-dealu ZSM-5	55	40.7	0.89	44	56

Table 3.3 reveals that the Si/Al ratio decreases after desilication as expected since silicon is removed from the framework. Comparison of the elemental analysis values to those determined using NH_3-TPD reveals three features. First, the values are quite similar for the parent sample, implying that virtually all aluminum atoms are incorporated in the zeolite framework contributing to strong Brønsted acid sites for the untreated sample. Second, for the desilicated sample the two

values do not agree. The Si/Al ratio estimated by NH_3-TPD is higher compared to elemental analysis. This indicates that a fraction of the aluminum does not contribute to any TDP measurable acidity and suggests that extra-framework is formed upon desilication. Third, after dealumination some difference still exists between the value from elemental analysis and NH_3-TPD.

To estimate the Si/Al ratios using ^{29}Si MAS NMR it is necessary to investigate the ^{29}Si MAS NMR spectra of the parent, desil and desil-dealu ZSM-5 samples which are given in Figure 3.8.

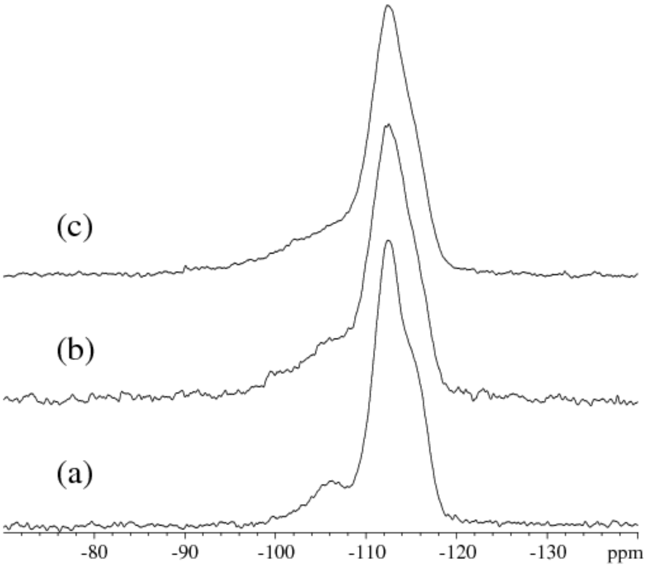

Figure 3.8: ^{29}Si MAS NMR spectra (9.4 T) of a) parent ZSM-5, b) desil ZSM-5 and c) desil-dealu ZSM-5. The spectra are obtained at a spinning speed of ν_R = 10.0 kHz and a recycle delay of 30 s. The spectra b) and c) are vertically expanded by a factor of 2 relative to the spectrum of a) the parent ZSM-5 sample

As seen in Figure 3.8 the ^{29}Si MAS NMR spectra for the three samples are quite similar and include the same type of resonances as observed earlier for ZSM-5 samples.[97, 112, 158, 171, 172] The resonance in the range -95 ppm to -108 ppm originates principally from either Q^4 ($AlOSi(OSi)_3$) or Q^3 ($HOSi(OSi)_3$) sites while the dominating peaks (-110 ppm to – 118 ppm) purely reflect silicious Q^4 ($Si(OSi)_4$) sites. However, if it is assumed that the high-frequency region (-95 ppm to -108 ppm is dominated by resonances from Brønsted $(SiO)_3$-Si-O(H)-Al sites, corresponding to a small number of defect Q^3 ($HOSi(OSi)_3$) sites, the framework Si/Al ratio can be estimated from devolutions of the ^{29}Si MAS NMR spectra using the intensities (I) for the two regions, *i.e.* Si/Al = 4 / [Q^4 ($Si(OSi)_4$)] / [Q^4 ($AlOSi(OSi)_3$)]. These ratios are listed in Table 3.3 for the three selected samples and should be considered as lower values since the Q^4 ($AlOSi(OSi)_3$) intensity may be overestimated due to the presence of Q^3 ($HOSi(OSi)_3$) sites. The estimated Si/Al ratios of the samples by ^{29}Si MAS NMR agree very well with the corresponding ratios from the NH_3-TPD measurements.

To investigate the coordination of aluminum atoms in the zeolite samples ^{27}Al MAS NMR has been conducted and the obtained spectra are shown in Figure 3.9.

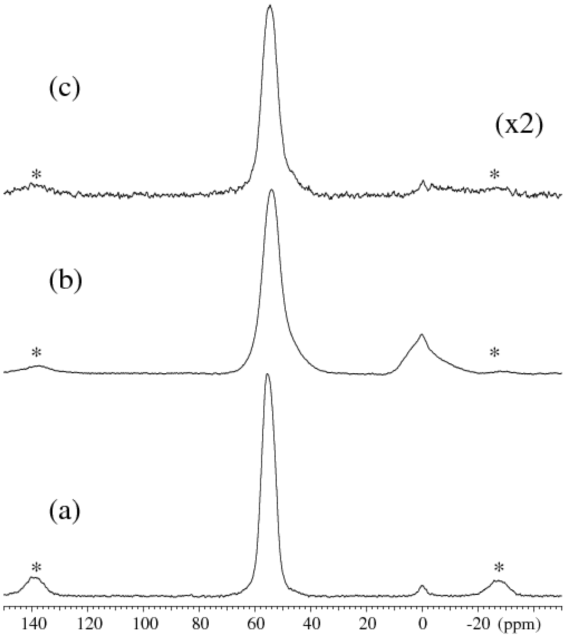

Figure 3.9: ^{27}Al MAS NMR spectra (14.1 T) of a) parent ZSM-5, b) desil ZSM-5 and c) desil-dealu ZSM-5. The spectra are obtained at a spinning speed of ν_R = 13.0 kHz, ^{1}H decoupling and a recycle delay of 2 s. The spectra are shown on a normalised intensity scale, employing a vertical expansion of 2 for the spectrum in c). The asterisks indicate spinning sidebands from the Al^{tetra} signal. Normalised intensities for Al^{tetra} and Al^{octa} are listed in Table 3.4

The ^{27}Al MAS NMR spectra given in Figure 3.9 exhibit resonances from the tetrahedral framework aluminum (δ(Al^{tetra}) ~ 55 ppm) and aluminum in octahedral environments (δ(Al^{octa}) ~ 10 ppm to –10 ppm) assigned to non-framework aluminum. The minor Al^{octa} peak observed at 0 ppm for the parent ZSM-5 sample most likely reflects a small amount of *e.g.* aluminium hydroxide from the synthesis, which is not incorporated in the zeolite framework. The absolute ^{27}Al MAS NMR intensities for Al^{tetra} and Al^{octa} normalised to the total intensity for the parent ZSM-5 sample are summarised in Table 3.4.

Table 3.4: Aluminum distribution in the parent, desil and desil-dealu zeolite determined from ^{27}Al MAS NMR

	Al total	Al^{tetra}	Al^{octa}	Al^{octa}/Al^{tetra}
parent ZSM-5	1	0.977	0.023	0.024
desil ZSM-5	1.582	1.263	0.320	0.253
desil-dealu ZSM-5	0.647	0.552	0.095	0.172

The increase in total intensity for the desil ZSM-5 reflects, as expected, that a substantial amount of silicon is removed by the desilication treatment. Moreover, the increase in Al^{tetra} intensity for the desil ZSM-5 is in accordance with lowering of the Si/Al ratio. The desilication treatment also affects aluminum since a significant part of aluminum is expelled from the framework forming aluminum in octahedral environments. The subsequent dealumination result in an overall decrease in ^{27}Al intensity as a result of a reduction in framework aluminum sites as well as non-framework Al^{tetra} species. Omegna *et al.*[173] have reported similar findings on dealuminated ZSM-5 zeolite and suggest the presence of tetrahedrally coordinated extra-framework aluminum possibly associated with an amorphous silica phase. The reduction in Al^{tetra} intensity should be associated with an increase in Si/Al ratio in agreement with the higher Si/Al ratio observed for the desil-dealu sample by NH_3-TPD.
Combining the ^{27}Al MAS NMR and ^{29}Si MAS NMR data the sequential desilication and dealumination treatment leads to formation of larger fraction of Q^3 ($HOSi(OSi)_3$) defect sites most likely associated with the formation of mesopores in the framework.

The presence of distinct Al^{tetra} sites for ZSM-5 zeolite has been reported earlier by ^{27}Al MAS NMR[108, 174-176] and to detect such possible sites, the selected samples are investigated by ^{27}Al Multi-Quantum MAS NMR. A more detailed description of the measurements and discussion of the results are given in the first appendix. From the ^{27}Al MQMAS NMR it is can be concluded that two different Al^{tetra} sites are present in the samples. The desilication treatment affects the distribution between the different Al^{tetra} environments as the distribution is quite alike for the parent and desil-dealu ZSM-5 samples which differ from the desil ZSM-5 sample. This means that the desilication produces extra-framework aluminum as Al^{octa} and disturbs the distribution between the different Al^{tetra} sites. The subsequent dealumination removes extra-framework aluminum species by dissolution of all Al^{octa} and a significant amount of Al^{tetra} restoring the distribution between the different Al^{tetra} sites. The removal of Al^{tetra} by oxalic acid treatment suggests that different Al^{tetra} species are present and that only some can be removed by dealumination.

Complementary information to that obtained from NH_3-TPD and MAS NMR investigations is available by comparing the IR spectra of the activated samples in the hydroxyls stretching region (3800-3500 cm^{-1}) as displayed in Figure 3.10. For sake of completeness, two activation temperatures were considered (350 and 500 °C). In this case it has been possible to consider changes occurring at different levels of dehydration. All spectra have been normalised with respect to the pellet thickness and the band intensities are therefore within reasonable accuracy representative of the amount of the respective species.

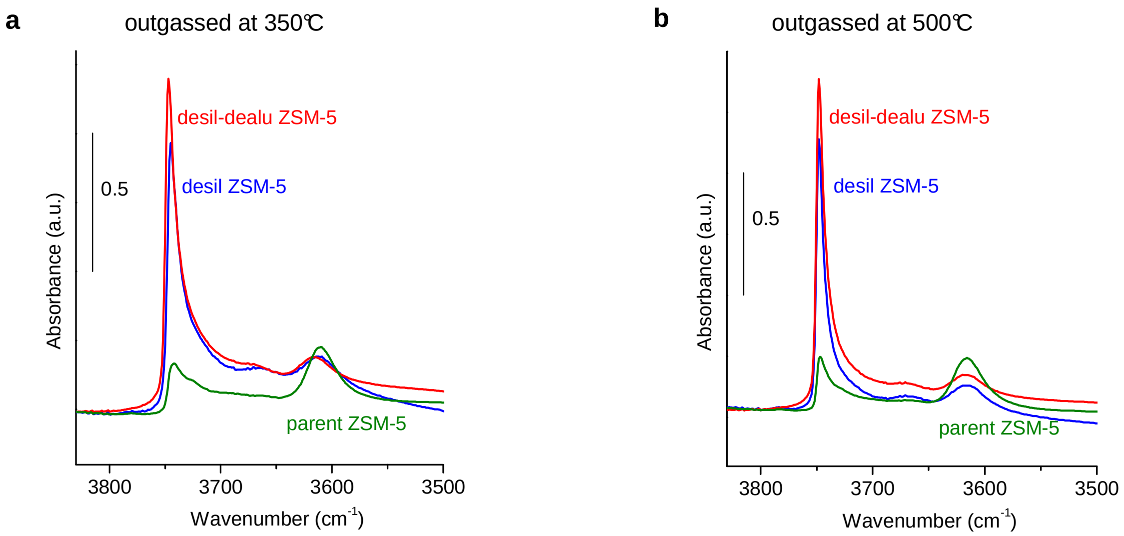

Figure 3.10: FT-IR spectra of the parent (green), desil (blue) and desil-dealu (red) ZSM-5 samples outgassed at 350 and 500 °C

The parent ZSM-5 sample (green line) shows at both temperatures the presence of two main bands at 3742 cm^{-1} and 3610 cm^{-1}, respectively. The band at 3742 cm^{-1} is associated with isolated silanols and the band at 3610 cm^{-1} corresponds to strong Brønsted acid sites, Si(OH)Al.[100, 102] The component at higher frequency is broader in the sample activated at 350 °C than that activated at 500 °C. After desilication (blue line), some relevant changes occur: i) the increase of the very sharp and intense band centered at 3745 cm^{-1}, ii) the significant decrease of the band associated with Brønsted acid sites and iii) the presence of a small broader component at 3664 cm^{-1}. The increase in the concentration of isolated silanols can occur due to the formation of mesopores. The decrease associated with the Brønsted acid sites is attributed to the expelling of aluminum from the framework during desilication forming weak acid sites present as extra-framework as the band at 3664 cm^{-1} is reported[105] for desilicated ZSM-5 zeolites to be associated with extra-framework aluminum. Upon dealumination, no dramatic changes are visible in the OH stretching region, however, a small decrease in the component at 3610 cm^{-1} and a further increase in the band at 3745 cm^{-1} are observed. These observations agree very well with the information gained from NH_3-TPD and MAS NMR showing a tendency for a reduction in the concentration of strong Brønsted acid sites and concurrent formation of weaker acid sites.

For further investigation of the formed extra-framework aluminum CO is used as probe molecule to identify specific features peculiar for each sample. The samples are activated at 350 °C and the obtained CO desorption profiles at 77 K are presented in Figure 3.11. The spectra have conveniently been divided into two intervals, namely C-O (2000-2300 cm^{-1}) and O-H (3000-3800 cm^{-1}) stretching regions. Red lines correspond to the spectra obtained from the activated samples, while the green lines show the effect of the highest CO coverage. Black lines correspond to intermediate CO adsorption pressures.

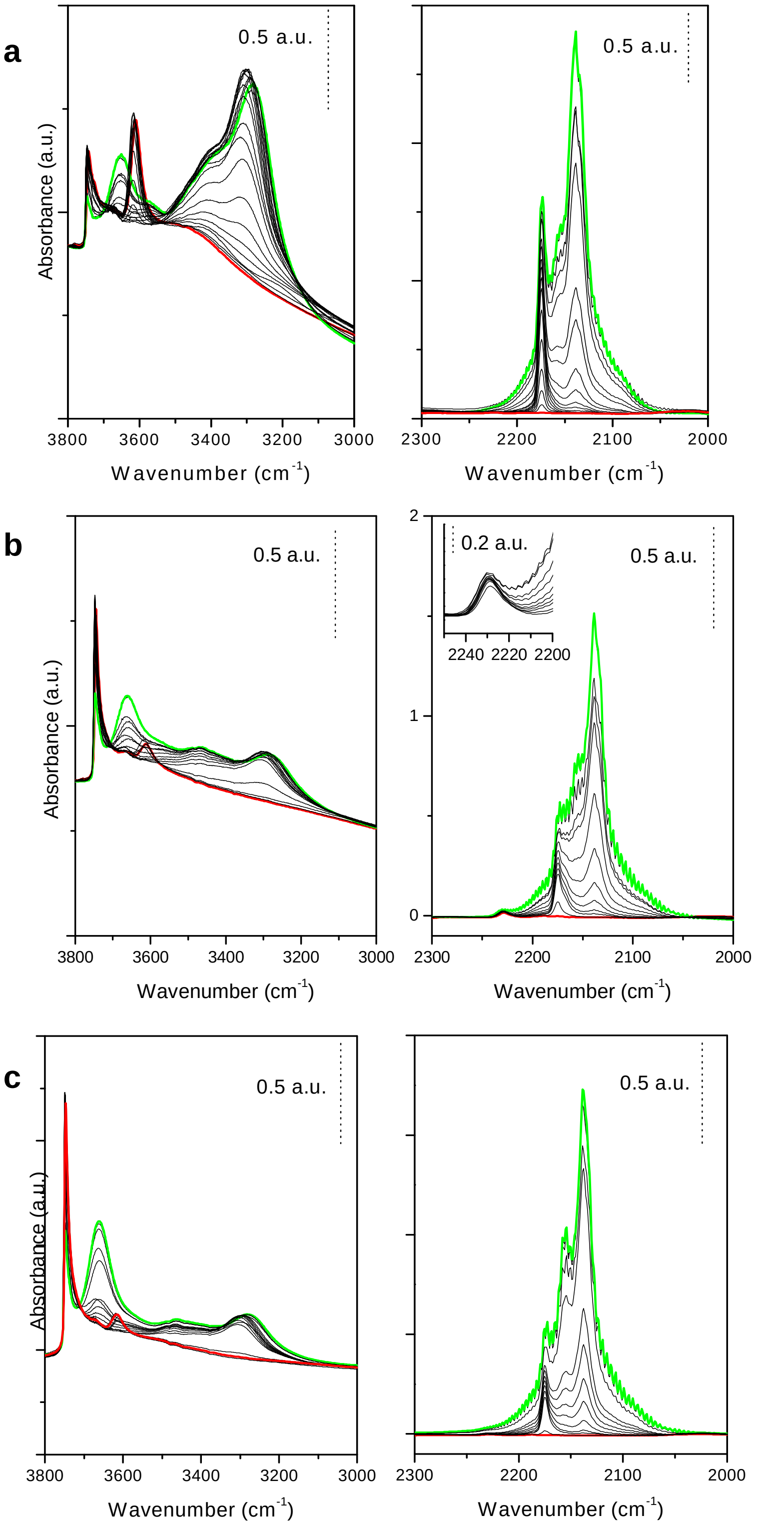

Figure 3.11: CO FT-IR spectra of a) parent, b) desil and c) desil-dealu ZSM-5 samples. The spectra are recorded after activation at 350 °C and measured at 77 K

Concerning the parent ZSM-5 sample, Figure 3.11a, upon CO interaction the band at 3745 cm^{-1} is eroded giving rise to a band at 3652 cm^{-1}. The small band at 3690 cm^{-1} which is partially hydrolysed aluminium undergoes a shift to 3573 cm^{-1} while the band at 3610 cm^{-1} is shifted to 3285 cm^{-1}. In the CO stretching frequency region (2300-2000 cm^{-1}) three components are visible at 2137, 2155 and 2175 cm^{-1}. They are assigned to physisorped CO, CO interacting with silanols and CO interacting with strong Brønsted acid sites, respectively.[19] Note that the component due to silanols is not very well defined, while the band associated to CO interacting with the strong Brønsted acid sites is quite sharp and symmetric. In the desil ZSM-5 sample, Figure 3.11b, the most evident change is the appearance of a small band at 2230 cm^{-1}, due to CO interacting with extra-framework aluminum. An expanded view is given in the inset. Furthermore is observed a decrease in intensity of the band at 2175 cm^{-1} and its broadening with the formation of a visible tail on the low frequency side. Also is the presence of a broad contribution of silanols that is hardly distinguishable as distinct bands only at very high CO coverage appear. After dealumination, Figure 3.11c the main changes are: i) disappearance of CO coordinated to extra-framework aluminum sites (band centered at 2230 cm^{-1}); ii) better definition of the band at 2175 cm^{-1}, iii) the intensities of the band due to the acidic Brønsted sites is further decreased and it becomes more defined and sharp.

The IR investigations support the NH_3-TPD and MAS NMR results as the desilication generates large amount of silanols that behave mainly as isolated species, which can be due to mesopores formation. After desilication Lewis acid sites appear associated with extra-framework aluminum. The dealumination removes the extra-framework aluminum and slightly decreases the amount of framework aluminum. The structure seems more regular than after desilication but with a lower content of aluminum in the framework.

3.4.2. Catalytic lifetime in the MTH reaction

The profound changes in both acidic properties and porosity will inevitably affect the catalytic lifetime in the MTH reaction. Even though the zeolite samples are quite different in Si/Al ratios, the porosity and morphology of the desil and desil-dealu sample are rather similar. The major difference is the amount of extra-framework aluminum. The conversion of methanol into hydrocarbons at 370 °C, atmospheric pressure and WHSV equal to 4.5 h^{-1} for the parent, desil and desil-dealu samples are given in Figure 3.12.

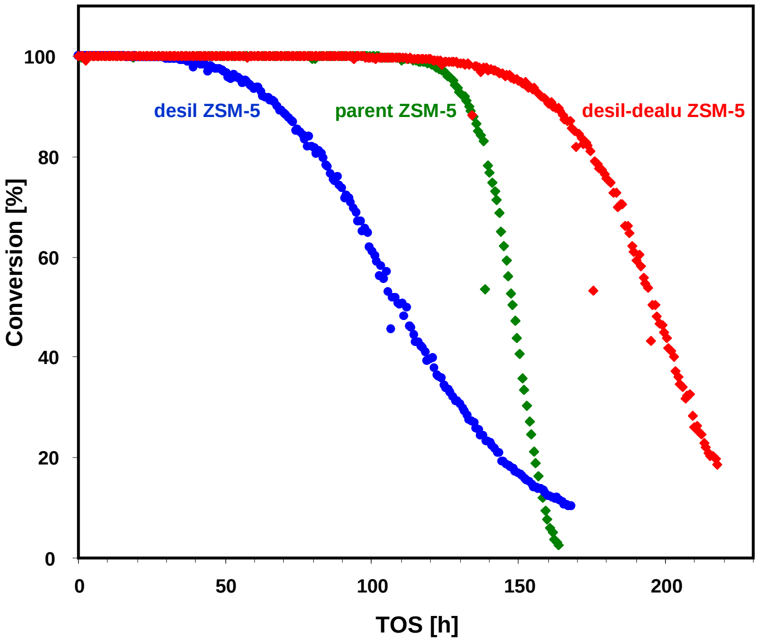

Figure 3.12: Conversion of methanol into hydrocarbons as a function of time on stream at 370 °C, atmospheric pressure and WHSV = 4.5 h^{-1} for the parent (green), desil (blue) and desil-dealu (red) ZSM-5 samples

As seen in Figure 3.12 all three samples initially display 100 % conversion. The parent sample (green line) displays a remarkably high activity seen by the 117 h until methanol breakthrough. After desilication (blue line) the time to methanol breakthrough is surprisingly not increased but rather shortened and appears after 37 h. For this particular sample the desilication procedure does thus not improve the catalytic properties. This behaviour is in contradiction to earlier obtained results, in which the activity and lifetime was improved by desilication caused by the introduction of mesopores and removal of internal structural defects.[9, 90, 113] Upon the consecutive dealumination procedure (red line) the lifetime of the sample was slightly improved with respect to both the desilicated and the parent sample seen by the 123 h to methanol breakthrough.
The deactivation can be modelled using the conversion data and the approach reported by Janssens[144] which is described as a reduction of the effective amount of catalyst, applying the assumptions that the conversion of methanol is first order and the loss of active catalyst is proportional to conversion. From this model the catalyst activity expressed by the rate constant (k), the deactivation rate (a) and the conversion capacity (R_0) can be obtained. The deactivation rate is the rate at which the effective amount of catalyst decreases while the conversion capacity is the maximum amount of methanol that can be converted per gram of catalyst in its lifetime. The results are given in Table 3.5.

Table 3.5: Kinetic model values and time to methanol breakthrough ($t_{MeOH\ break}$) for the parent, desil and desil-dealu ZSM-5 samples in the MTH reaction. *a* is the deactivation rate, *k* is the rate constant and R_0 is the total conversion capacity

	a [m_{cat}/mol]	k [$mol_{MeOH}/g_{cat}/h$]	R_o [g_{MeOH}/g_{cat}]	$t_{MeOH,\ break}$ [h]
parent ZSM-5	5.1	29	657	115
desil ZSM-5	6.8	7.6	495	37
desil-dealu ZSM-5	3.8	17	884	123

Upon desilication the deactivation rate is seen to increase from 5.1 mg_{cat}/mol to 6.8 mg_{cat}/mol, which results in lower conversion capacity as opposite to what is usually seen for desilicated ZSM-5 zeolites. Typical for desilication is also a decrease in activity which here is observed by the change from 29 $mol_{MeOH}/g_{cat}/h$ to 7.6 $mol_{MeOH}/g_{cat}/h$. The normal benefits of desilication like improved diffusion and removal of internal structural defects thus become masked by the generation of extra-framework aluminum. The generation of extra-framework aluminum during desilication has earlier been addressed, where it was found to primarily rest on the external surface including the surface of mesopores.[90] It can therefore, when formed in large amounts, aid the deactivation, but also block the entrance to the zeolite microporous system. Therefore, the presence of extra-framework aluminum may have pronounced effect on the catalytic lifetime of the catalyst. Upon dealumination, where the extra-framework is removed, the activity appears to be partially recovered, but also the typical improvements to the deactivation rate, which are not seen after desilication, become unveiled after the dealumination. It is therefore hypothesised that the improvements to deactivation rates, typically seen upon desilication, can be masked by the extra-framework aluminum, but may be recovered by consecutive dealumination treatment.

In the case investigated here, the Si/Al ratios changes upon the different treatments and comparison may become cumbersome. Generally an increase in the amount of aluminum will increase coking.[134] Oppositely the generation of mesopores will increase the lifetime by increasing the diffusion of the aromatics and thereby shift the preferential location for coke formation to the external surface.[10] More information on the catalyst system is therefore needed and may be extracted by considering the composition of the reactor effluent. Of interest is typically the C_{5+} selectivity which is a rough estimate of the gasoline fraction and the C_4 hydrogen transfer index (HTI) which is defined by the C_4 yields: (*iso*-butane + *n*-butane)/ΣC_4. In the upper part of Figure 3.13 is given the C_4-HTI and in the lower part is given the C_{5+} fraction both shown as a function of time on stream.

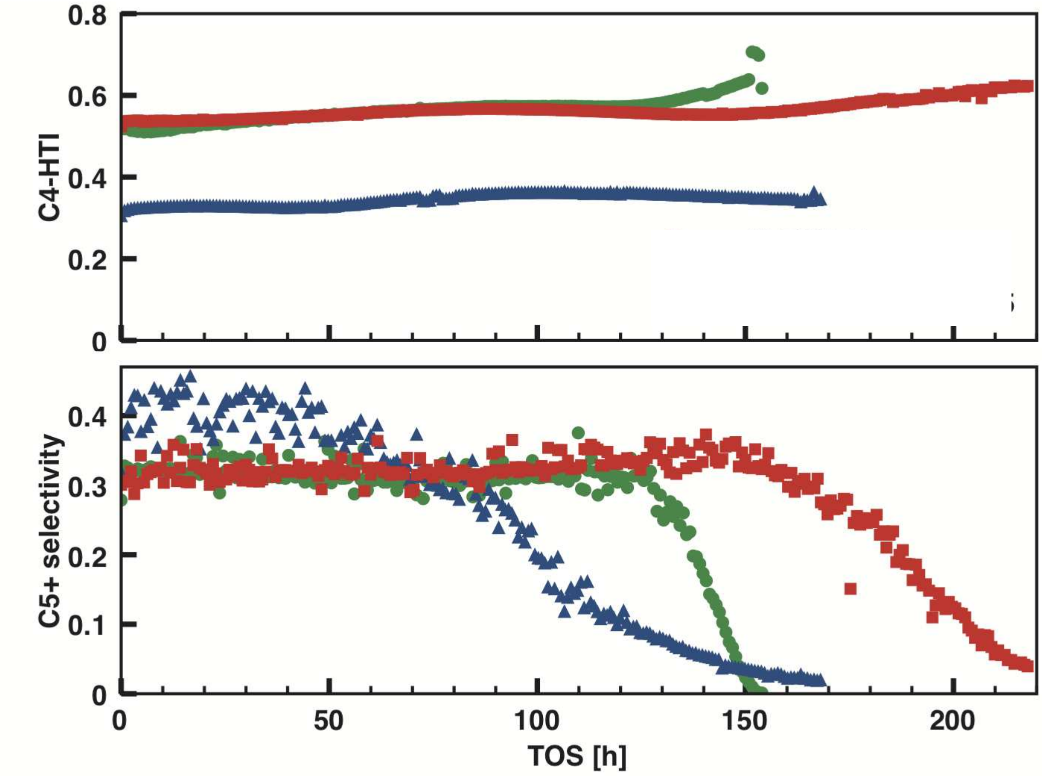

Figure 3.12: On the top, the C_4 hydrogen transfer index (HTI) as function of time on stream. The C_4-HTI is defined according to the C_4 yields as (*iso*-butane+*n*-butane)/ΣC_4. The lower figure shows the C_{5+} selectivity as function of time on stream for the parent (green), desil (blue) and desil-dealu (red) ZSM-5 samples in the MTH reaction

As seen in the lower part of Figure 3.12 when the conversion drops below 100 %, the C_5 selectivity drops in all cases. At full conversion the C_5 selectivity is however different for the desil ZSM-5 compared to the parent and the desil-dealu ZSM-5 samples. Typically the increase in C_{5+} selectivity is explained by the generation of mesoporosity. As the textural properties of the parent and desil-dealu ZSM-5 samples are rather similar this cannot explain the regeneration of the selectivity upon dealumination, but may rather be explained by the presence of extra-framework aluminum. A similar trend is also seen for the C_4-HTI. Upon desilication the HTI decreases and again restored to the original value upon the consecutive dealumination. The restoration of the different selectivity suggests, despite the changes in the Si/Al ratios, that the catalyst systems may be compared. It is therefore interesting to notice that although the mesoporosity is increased it does not necessarily increase the catalytic lifetime, but that the presence of especially extra-framework aluminum has a pronounced effect on the catalyst performance.

3.5. Conclusion

Different ZSM-5 zeolites have been prepared though desilication and/or dealumination treatments of a parent zeolite sample to investigate the effect of extra-framework aluminum on the catalytic lifetime in the MTH reaction. Characterisations showed that the crystal structure was preserved and that the particle sizes were approximately 1 µm independent of any post-synthesis treatment. The morphology of the parent zeolite particles changed upon desilication from particles consisting of densely packed small subunits to a more sponge-like morphology typical for mesoporous zeolites which was not further altered after subsequent dealumination. According to N_2 physisorption measurements all the samples contained micropores and after desilication mesoporosity was introduced.

NH_3-TPD, MAS NMR and FTIR investigations all supported that during desilication mesopores were formed and primarily silicon was removed from the framework resulting in extra-framework aluminum. It was observed that the desilication reduced the amount of strong Brønsted acid sites and instead weaker acid sites were formed. After dealumination the FTIR band corresponding to Brønsted acid sites was slightly reduced whereas the band for tetrahedral bonding in the ^{27}Al MAS NMR was reduced to less than half. This means that not all Al^{tetra} is Brønsted acid sites as the decrease in tetrahedral bonds in the ^{27}Al MAS NMR is not identical with the decrease in the band for Brønsted acid sites in the IR spectrum.
It was found that extra-framework aluminum was removed by dealumination where all aluminum in octahedral positions and a significant amount of aluminum in tetrahedral positions was extracted. The extraction of tetrahedral aluminum during dealumination suggested that different tetrahedral aluminum species were present and that only some can be withdrawn by dealumination. The subsequently dealumination did not seem to alter the textural properties, only the amount of aluminum in the samples was affected.

The prepared materials were tested for their catalytic lifetime in the MTH reaction. The catalytic tests showed that despite the formation of mesopores and repairing of internal defects the desilicated sample displayed a reduced catalytic lifetime compared to the parent ZSM-5 catalyst. It seemed that the normal benefits from desilication thus became masked by the generation of extra-framework aluminum. It is concluded that the extra-framework aluminum has a pronounced effect on the catalytic lifetime in the MTH reaction as the catalytic lifetime was recovered and improved by the subsequent dealumination whereby extra-framework was removed. The presence of extra-framework or partially extra-framework aluminum might lead to faster deactivation due coke formation. From the results obtained in this chapter it can thus be concluded that the introduction of mesoporosity does not in itself necessarily improve the catalytic lifetime but that the catalytic lifetime is highly dependant on the amount of extra-framework aluminum.

Chapter 4

Modified zeolites and gallium containing zeotypes for the MTH reaction

This chapter contains synthesis, characterisation and catalytic testing of modified zeolites and gallium containing zeotypes. The synthesised gallium zeotypes were tested in the MTH reaction and compared to ZSM-5 zeolites regarding their catalytic lifetime, selectivity and deactivation. PhD Uffe V. Mentzel has conducted the catalytic test.

4.1. Introduction

Many different elements can be introduced in zeolite or zeolite-like materials without altering the zeolite structure significantly. The only requirements are that the element must adopt a tetrahedral configuration and have an appropriate size.[12] When gallium is incorporated into the framework minor distortions take place compared to a silicalite-1 analogue.[177] The difference of incorporating gallium instead of aluminium in the framework entails a decrease in the intrinsic acidity of the individual active sites in the gallium zeotype compared to the zeolite analogue.[23, 178] It should be stated that a true zeolite is a pure aluminosilicate. When gallium or other elements are incorporated into the zeolite framework the material is referred to as a zeotype. Gallium can be introduced into zeolites or zeotypes in other ways besides isomorphous substitution of silica in the framework, *i.e.* impregnation, ion-exchange or by physical mixing of zeolite or zeotype crystals and Ga_2O_3. When gallium is incorporated into the crystal framework the general perception is that the catalyst is more stable than in the cases where gallium is impregnated or ion-exchanged.[179] Another advantage of incorporating gallium is that the gallium species may be uniformly distributed all over the tetrahedral silicon framework sites in the structure and thereby not only onto the surfaces of the zeolite or in the outer part of the channels.[180] In this work conventional and mesoporous ZSM-5 zeolites are prepared together with the analogous Ga-MFI zeotypes. In the Ga-MFI zeotypes gallium atoms have replaced all the aluminum atoms in the framework and therefore no aluminum atoms are present in these samples.

The catalytic properties of Ga-MFI have been the subject of many studies. These zeotypes act as catalysts for several reactions such as alkylation[181], isomerisation[182], aromatisation of light alkenes (Cyclar process)[183], NOx reduction[184] and methanol conversion[185-187]. In the conversion of methanol the Si/Ga ratio has a pronounced effect on the catalytic activity.[186] Increasing the amount of gallium induces the presence of a higher amount of Brønsted acid sites leading to a higher activity as for the ZSM-5 analogue. It should be noted that, as for ZSM-5 zeolites (Al-MFI), the strength of each single acid site in Ga-MFI is dependent on the Si/Ga ratio. When the distance between two gallium atoms increases, the strength of each acid site increases meaning, the higher Si/Ga the stronger is the individual acid site. The selectivity is dependent on the concentration and strength of the acid sites. Ga-MFI zeotypes with low gallium contents and thereby strong individual acid sites have a high selectivity towards C_2-C_4 olefins.[187] On the other hand, Ga-MFI zeotypes with high gallium contents seem to favour the production of aromatics produced from olefins.[185, 186] However, it is plausible, that Ga-MFI zeotypes with high gallium contents contain extra-framework gallium which affects the selectivity by acting as weak Lewis acid sites. The Ga-MFI zeotypes have in general a significant higher aromatisation activity than ZSM-5.[186, 188] The distribution of the aromatics is more or less similar, yet Ga-MFI produces a negligible amount of C_{9+} aromatics compared to ZSM-5 zeolites. It should be noted that it is very difficult to compare ZSM-5 and Ga-MFI catalysts since the Si/X (X=Al or Ga) should be approximately the same and at the same time without or with similar amounts of extra-framework aluminum or gallium. The rate of coke formation during the methanol conversion is reported to be somewhat slower for Ga-MFI than for ZSM-5 which could be ascribed to the lower acidity of the individual Brønsted sites.[189] It is important to keep in mind that a slower deactivation might simply reflect differences in activity. Consequently, high activity of the parent ZSM-5 leads to a more rapid coking and to an earlier point of deactivation because active sites which catalyse further conversion of intermediates to hydrocarbons are blocked first.

Even though it has been attempted to apply gallium-based zeotypes in methanol to hydrocarbon processes for commercial purposes, their performance could not compete with the ZSM-5 or SAPO-34 catalysts.[178]

As presented in Chapter 2 and 3 mesoporous ZSM-5 zeolites can be used to catalyse the MTH reaction and the main effect of the mesoporosity, if extra-framework aluminum is removed, is to prolong the catalyst lifetime compared to their conventional counterparts. In this chapter mesoporous Ga-MFI is prepared and tested in the MTH reaction. The catalytic lifetime, selectivity and deactivation is compared to a conventional Ga-MFI and the ZSM-5 zeolite analogues. Especially the difference in deactivation is investigated. It is possible that other factors besides the differences in acid strength could affect the deactivation, *i.e.* the susceptibility of steam which is generated during methanol conversion could have a potential effect on the active sites.

4.2. Synthesis strategy

Conventional and mesoporous Ga-MFI zeotypes are prepared and compared to a conventional and a mesoporous ZSM-5 zeolite. The conventional zeolite is a commercial one obtained from Zeolyst International with Si/Al equal to 40. The mesoporous ZSM-5 is prepared using Carbon Black pearls as template following the synthesis procedure from Jacobsen *et al.*[35] using a Si/Al ratio equal to 50. Previous experience has taught that mesoporous ZSM-5 with a lower Si/Al ratio than 50 is difficult to prepare using carbon as template without creating too much extra-framework aluminum. The conventional and the mesoporous Ga-MFI zeotypes are synthesised using the same silica and gallium sources and both with a Si/Ga ratio equal to 50. The mesoporous Ga-MFI zeotype is prepared using a modified version of the synthesis procedure of mesoporous ZSM-5. The necessary components are still impregnated by incipient wetness but where the procedure for mesoporous ZSM-5 zeolite contains three impregnations, the procedure for mesoporous Ga-MFI contains only two. The two synthesis procedures for the mesoporous materials are shown in Figure 4.1.

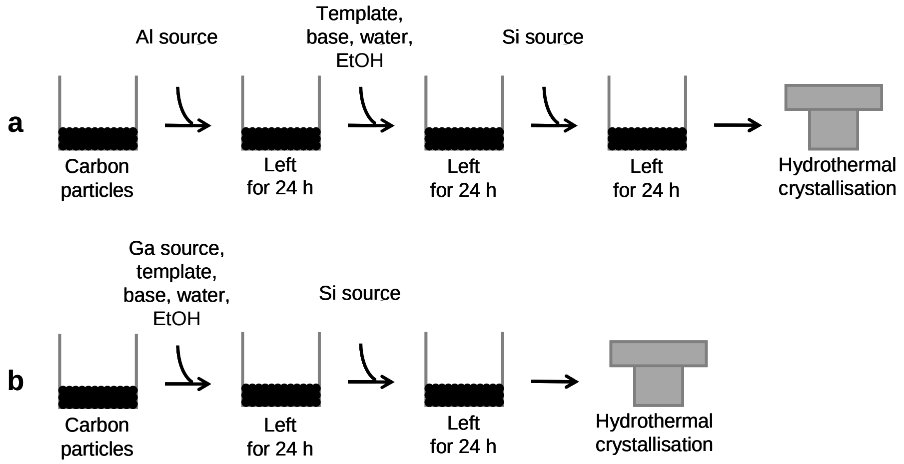

Figure 4.1: Schematic illustration of the preparation of a) mesoporous ZSM-5 and b) mesoporous Ga-MFI

A previous study shows[139] that when aluminum isopropoxide is used much more aluminum is incorporated into the framework than using for instance sodium aluminate. Aluminum isopropoxide is dissolved in tetrahydrofuran and it is therefore necessary to add it in an individual step. In the preparation of mesoporous Ga-MFI the gallium source is gallium nitrate which can without any problem be dissolved in water together with template, base and solvents which thereby avoids an extra synthesis step.

In our first study[190] on preparing mesosporous Ga-MFI zeotype the gallium was introduced in the impregnation solution as gallium oxide and/or hydroxide. The gallium compound was prepared by precipitation from an aqueous solution of gallium nitrate by means of ammonia in excess. The precipitate was further washed twice with water, dried and afterwards added to the zeotype synthesis gel. FTIR and ^{71}Ga MAS NMR investigations showed that all gallium was incorporated in the zeotype framework. Even though we succeeded in preparing a mesoporous Ga-MFI zeotype without any extra-framework gallium only one third of the used gallium ended up in the final product. To optimise the preparation of mesoporous Ga-MFI zeotype gallium nitrate is still used as a gallium source but is added directly to the impregnation solutions to avoid unnecessary loss of gallium.

4.3. Experimental

All the reagent were of reagent grade and used without any further purification: Sodium hydroxide (NaOH, 99 wt%, Riedel-de Häen), tetrapropylammonium hydroxide (TPAOH, 40 wt%, AppliChem), aluminum isopropoxide ($C_9H_{21}O_3Al$, 98 wt%, Aldrich), tetraethylorthosilicate (TEOS, 98 wt%, Aldrich), tetrahydrofuran (THF, 99 wt%, Aldrich), Carbon Black Pearls (BP-2000, average diameter of 12 nm, Carbot Corporation), ethanol (EtOH, 99.9 wt%, Kemethyl A/S), ammonium nitrate (NH_4NO_3, 99.5 wt%, Merck), gallium nitrate hydrate ($Ga(NO_3)_3 \cdot xH_2O$, 99.9 wt%, Aldrich), methanol (> 99.9 % Aldrich Chromasolv®).

4.3.1. Conventional ZSM-5

The conventional ZSM-5 was a commercial one obtained from Zeolyst International in its ammonium form. Prior to use, the zeolite was calcined at 550°C for 4 hours to obtain the acidic form. The obtained product was named conv ZSM-5.

4.3.2. Synthesis of mesoporous ZSM-5

The mesoporous ZSM-5 was synthesised in the following procedure:

> *BP-2000 was dried in an oven (min. 110°) overnight from which 14 g was taken. Firstly, 0.53 g aluminium isopropoxide was dissolved mixed with 45 ml THF in a beaker and impregnated onto the carbon. This mixture was left overnight at room temperature. In a beaker, 28 g of 40 wt% TPAOH, 3.6 g of H_2O and 0.5 g of NaOH was added and stirred until a clear solution was obtained, after which 21 g EtOH was added during stirring. The carbon was impregnated with the obtained solution to incipient wetness. After evaporation of the EtOH at room temperature overnight, the carbon particles were impregnated with 27.09 g TEOS and then left to hydrolyse overnight. After hydrolysis, the impregnated carbon was transferred to a Teflon beaker which was placed in a stainless steel autoclave with 1 cm water to produce saturated steam. The autoclave was heated slowly to 180 °C and kept there for 72 hours. After the autoclave was cooled to room temperature, the black product was suspended in water, isolated by suction filtration and washed repeatedly with water until pH was neutral. Then the product was dried at 110 °C for 10 h and the carbon black was removed by controlled combustion in air in a muffle furnace at 550 °C for 20 h. In this way a white material was obtained and named meso ZSM-5.*

4.3.3. Synthesis of conventional Ga-MFI

The conventional Ga-MFI was synthesised in the following procedure:

> *Firstly, 2.108 g NaOH was dissolved in 68 g H_2O and after complete dissolution 26.52 g TPAOH (40 wt%) was added. In another beaker1.674 g $Ga(NO_3)_3 \cdot xH_2O$ was dissolved in 17g H_2O. The two obtained homogeneous solutions were simultaneously added dropwise to 68 g TEOS with stirring and left for 2 hours with stirring. After approximately 30 min the mixture turned into a white thin gel. The gel was transferred to a Teflon lined autoclave, placed in an oven and heated to 180 °C for 72 h. The greyish product was filtered off after cooling, washed with water and dried overnight at room temperature. At last the product was calcined at 550 °C for 10 h by which a white product was obtained. The obtained product was named conv Ga-MFI.*

4.3.4. Synthesis of mesoporous Ga-MFI

The mesoporous Ga-MFI was synthesised in the following procedure:

> *BP-2000 was dried in an oven (min. 110°) overnight from which 15.6 g was taken. In 4.03 g H_2O 0.667 g $Ga(NO_3)_3 \cdot xH_2O$ and 0.56 g NaOH were dissolved. When a homogeneously solution was obtained 31.08 g TPAOH (40 wt%) and 23.3 g EtOH was added. The carbon was impregnated with the obtained solution to incipient wetness. After evaporation of the EtOH at room temperature overnight, the carbon particles*

were impregnated with 30.2 g TEOS and then left for hydrolysis overnight. After hydrolysis, the impregnated carbon was transferred to a Teflon beaker which was placed in a stainless steel autoclave with 1 cm water to produce saturated steam. The autoclave was heated slowly to 180 °C and kept there for 72 hours. After cooling the autoclave to room temperature, the black product was suspended in water, filtered by suction and washed repeatedly with water until pH was neutral. Then the product was dried at 110 °C for 10 h and the carbon black was removed by controlled combustion in air in a muffle furnace at 550 °C for 20 h. In this way a white material was obtained and named meso Ga-MFI.

4.3.5. Ion exchange

The three synthesised zeolite/zeotype materials contain sodium as the charge-compensating cation after synthesis. The acidic form of each zeolite/zeotype was prepared using the following procedure:

> *Two consecutive ion exchanges were performed using 1M NH_4NO_3 at 80 °C in ratio 1:30 between mass of Na-zeolite or Na-zeotype (g) and volume of NH_4NO_3 (ml). After each ion exchange, the NH_4-form of the zeolite/zeotype was filtered off, washed with water, and dried in air. Finally, the H-form was obtained by heating the NH_4-ZSM-5 or NH_4-Ga-MFI in air to 450 °C for 4 h, whereby the NH_3 evaporated leaving protons as charge-compensating cations.*

4.3.6. Conversion of methanol to hydrocarbons

The conversion of methanol was performed using the following procedure:

> *The catalytic reactions were performed in a fixed bed reactor charged with 300 mg catalyst (355-500 µm), which was pretreated in a flow of helium at the reaction temperature for 30 min prior to the reaction. The reaction was performed at 370 °C and 1 bar, and the liquid reactant was pumped with a HPLC pump and evaporated before reaching the reactor. Helium was used as a carrier gas, with a flow of 40 ml/min, and the products from the reaction were analysed by on-line GC (HP6890) equipped with a Varian CP-PoraPLOT Q-HT capillary column and a FID. The employed feed rate of methanol was 0.25 mol/(g_{cat}·h) corresponding to a WHSV of 7.9 h^{-1}. When calculating the conversion, methanol and DME are considered reactants and response factors of 0.81 (methanol) and 0.63 (DME) are used, while a response factor of 1 is used for all hydrocarbon compounds.*
>
> *The TPO analyses were typically performed with 100 mg of spent cat which was heated in a flow of 5 % O_2 in helium (20 ml/min) with a heating ramp of 2.75 °C/min to an oven temperature of 700 °C. The final temperature was maintained for 2 h to ensure complete combustion of the carbonaceous species. The concentrations of CO and CO_2 in the outlet were monitored continuously by a BINOS detector.*
>
> *Regeneration experiments were conducted by heating the completely deactivated sample in a flow of 5 % O_2 in helium (20 ml/min) with a heating ramp of 2.75 °C/min to an oven temperature of 550 °C. The final temperature was maintained for 4 h to ensure complete combustion of the carbonaceous species.*

4.4. Results and discussion

The materials were characterised by XRPD, NH_3-TPD, elemental analysis, N_2 physisorption and SEM. The mesoporous Ga-MFI was also characterised by FTIR before and after catalytic test to investigate the structural changes during test. All characterisations are recorded after ion exchange and calcinations. The catalytic properties of the samples were tested in conversion of methanol at 370 °C and at atmospheric pressure regarding catalytic lifetime, selectivity and deactivation.

4.4.1. Characterisation

The XRPD patterns for the conventional and mesoporous ZSM-5 and Ga-MFI materials are all shown in Figure 4.2.

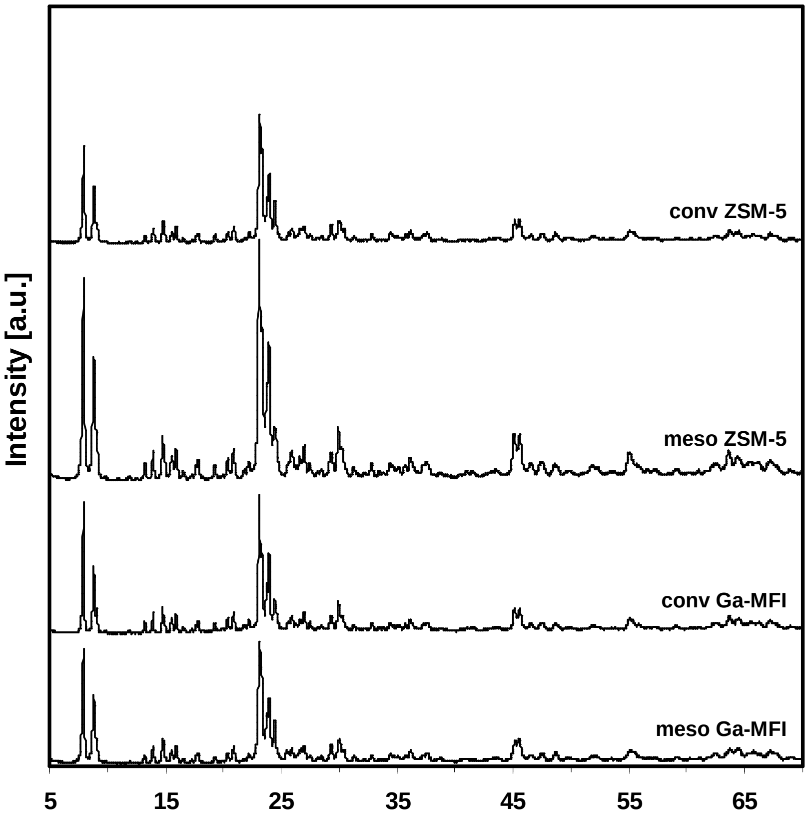

Figure 4.2: XRPD patterns of the conventional and mesoporous ZSM-5 and Ga-MFI materials

From Figure 4.2 it is seen that all four samples exclusively contain highly crystalline material with the MFI structure[4] and no traces of amorphous material are present.

The gallium and aluminium contents from elemental analysis are listed in Table 4.1 together with the estimated Si/X (X=Al or Ga) from NH_3-TPD.

Table 4.1: Aluminum and gallium contents determined by elemental analysis together with estimated Si/X ratios from NH_3-TPD with X=Al or Ga

	Elemental analysis		NH_3-TPD
	Al or Ga content [wt%]	Si/X (X=Al or Ga)	Si/X (X=Al or Ga)
conv ZSM-5	0.97	36	38
meso ZSM-5	1.02	40	59
conv Ga-MFI	1.35	77	93
meso Ga-MFI	1.45	71	74

According to elemental analysis the two types of ZSM-5 include rather similar amount of aluminium, *i.e.* 0.97 and 1.02 wt% for the conventional and mesoporous ZSM-5, respectively. This corresponds to a Si/Al for the conventional ZSM-5 to 36 and 40 for the mesoporous ZSM-5. A high Si/Al ratio corresponds to a low amount of aluminum and vice versa. According to NH_3-TPD the Si/Al ratios are 38 for the conventional and 59 for the mesoporous ZSM-5. Comparing the Si/Al from elemental analysis and NH_3-TPD reveals that they are in agreement for the conventional ZSM-5 meaning that all the aluminum is expected to be incorporated in the zeolite framework creating one acid site per aluminum atom. Contrary, the Si/Al ratio for the mesoporous ZSM-5 is higher by NH_3-TPD than by elemental analysis indicating that not all aluminum atoms create an acidic site, but may instead be present as extra-framework aluminum. This is verified by FTIR (not shown) where a band at 3666 cm^{-1} appears indicating the presence of extra-framework aluminum. The conventional and the mesoporous Ga-MFI contain approximately the same amount of gallium determined by elemental analysis, *i.e.* 1.35 and 1.45 wt%, which correspond to Si/Ga equal to 71 and 77, respectively. The attempt was to synthesise Ga-MFI and ZSM-5 with a Si/X equal to 50. Since the Si/Ga is higher than the intended value and also higher than the Si/Al for the mesoporous ZSM-5 it seems that gallium is not as easy introduced to the zeolite-like structure as aluminum. This could be due to the larger difference in size between silicon and gallium versus silicon and aluminum.

A discrepancy is observed for the Si/Ga ratio determined by elemental analysis and NH_3-TPD for the conventional Ga-MFI. The higher Si/Ga ratio estimated by NH_3-TPD indicates the presence of extra-framework gallium. On the other hand, the mesoporous Ga-MFI seems only to contain gallium in the framework.

In our previous study[190] on the preparation of mesoporous Ga-MFI one third of the used gallium nitrate was incorporated in the zeotype framework. By adding gallium nitrate directly to the impregnation solution approximately two thirds of the gallium are successfully introduced to the final product and it is therefore not necessary to prepare gallium oxide prior to synthesis.

To investigate the distribution of the strength of the acidic sites NH_3-TPD curves for all four samples are shown in Figure 4.3. It should be noted that NH_3-TPD curves should only be used as a fingerprint to investigate the distribution of the strength of the acid sites since it is almost impossible to distinguish between the different sites. A more reliable technique would be FTIR. NH_3-TPD curves are in this work primarily used to investigate the effect of the incorporation of gallium.

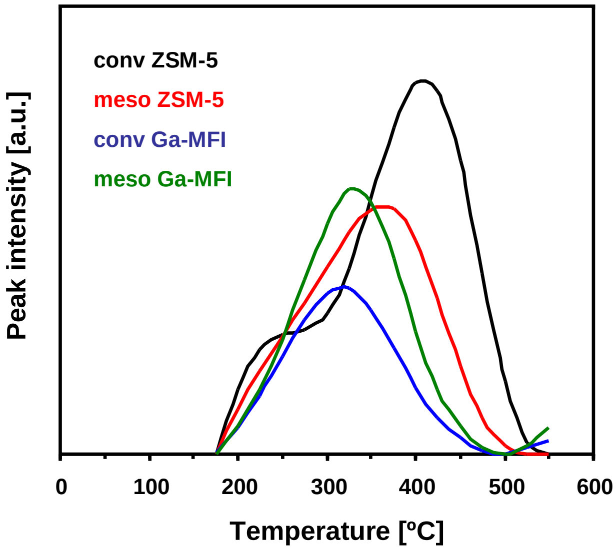

Figure 4.3: NH_3-TPD curves of conventional and mesoporous ZSM-5 and Ga-MFI

As seen in Figure 4.3 desorption curves for NH_3 for the conventional and the mesoporous ZSM-5 do not have exactly same shape. The conventional ZSM-5 displays two peaks located at 250 and 425 °C, respectively whereas the curve of the mesoporous ZSM-5 consists primarily of one peak centred at 375 °C. This means that the two samples have a different distribution of the strength of the acidic sites. Since the conventional ZSM-5 has peaks in both the low- and high-temperature region the material entails both weakly acidic sites and stronger acidic sites. The mesoporous ZSM-5 has a more smooth desorption curve of NH_3 primarily centred in the high-temperature region and seems therefore to primarily contain strong acidic sites. Still, the peak for the mesoporous ZSM-5 is shifted to lower temperatures compared to the highest peak for the conventional ZSM-5 due to contribution of lower acid sites. It should be noted that the conventional ZSM-5 is a purchased, commercial material with an unknown synthesis and history. The shape of the desorption curves for the conventional and mesoporous Ga-MFI are quite similar. They both contain one peak centred at 325 °C. The peaks are shifted to a lower temperature compared to the highest peaks for the conventional and mesoporous ZSM-5 zeolites. This is expected since incorporation of gallium in the framework decreases the intrinsic acidity of the individual active sites compared to the incorporation of aluminum.

To investigate the morphology of the prepared zeolite and zeotype samples representative SEM images are shown in Figure 4.4.

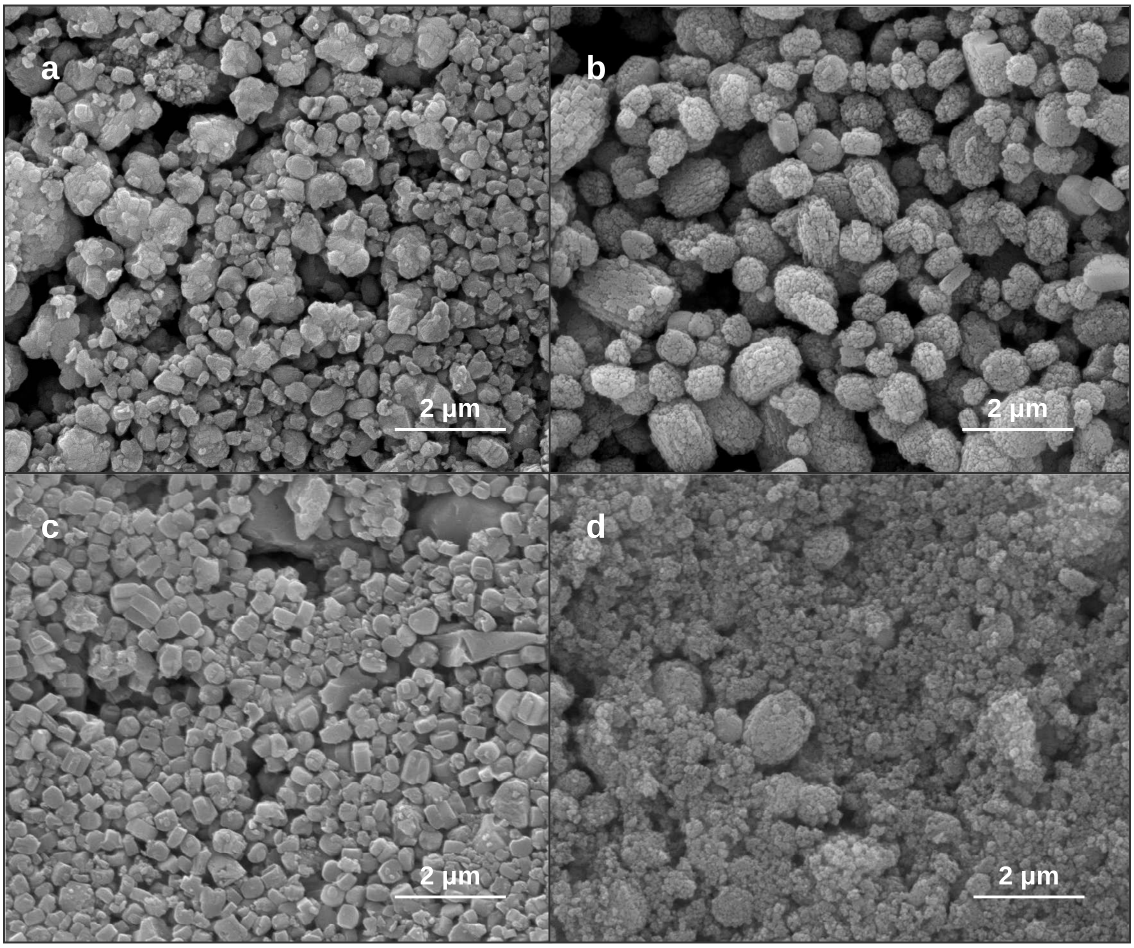

Figure 4.4: Representative SEM images of a) conv ZSM-5, b) meso ZSM-5, c) conv Ga-MFI and d) meso Ga-MFI

From the SEM image of the conventional ZSM-5, Figure 4.4a, it can be seen that the particle sizes of the conventional H-ZSM-5 are in the range of 0.5-2 µm, showing no preferential shape. The mesoporous H-ZSM-5 zeolite (Figure 4.4b) also consists of particles of approximately 0.5-2 µm in size, but they have a sponge like appearance which is characteristic for mesoporous zeolites. The conventional Ga-MFI material, Figure 4.4c, consists primarily of smaller particles around 0.5-1 µm but in between is also larger particles. Most of the particles have the coffin-shape morphology but also inter-grown particles and particles with undefined shapes are present. The mesoporous Ga-MFI sample (Figure 4.4d) consists mainly of very small particles around 1-2 µm, with some agglomerates also present.

In Table 4.2 is given the surface areas and pore volumes of the zeolite and zeotype samples determined by N_2 physisoption.

Table 4.2: Surface areas and pore volumes of the prepared zeolite and zeotype samples

	Surface area[a] [m^2/g]	Micropore volume[b] [cm^3/g]	Mesopore volume[c] [cm^3/g]
conv ZSM-5	428	0.17	0.19
meso ZSM-5	487	0.19	0.55
conv Ga-MFI	285	0.13	0.11
meso Ga-MFI	415	0.18	0.45

[a] Calculated using the BET method, [b] determined using the t-plot method and [c] determined using the BJH method

Table 4.2 reveals that all zeolite and zeotype materials are microporous materials with surface areas typical for zeolites, however the surface area and micropore volume for the conventional Ga-MFI are lower than the other samples. According to elemental analysis and NH_3-TPD the conventional Ga-MFI seems to contain extra-framework gallium. This could possible block the micropores whereby the surface area and micropore volume would decrease. It can also be observed from Table 4.2 that all samples contain mesopores. The formation of mesopores are commonly observed in conventional zeolites and zeotypes but rarely reported. The mesopores are highly probable due to interparticle voids and the volume is dependent on the size, shape and packing of the crystals which can obviously be packed more or less loosely. The mesopores volume for conventional ZSM-5 and Ga-MFI are rather low and are ascribed to interparticle voids. The mesoporous ZSM-5 and Ga-MFI have comparable mesopore volumes around 0.5 cm^3/g which are in the range of previous results using BP-2000[139, 190] as carbon template.

Figure 4.5 shows the obtained isotherms and corresponding pore size distributions. The pore size distributions are determined from the desorption branch of the isotherms using the BJH method. Using the desorption branch care should be taken since artefacts at 2 and 4 nm are present due to the result of phase transition of N_2 and forced closure of the hysteresis loop, respectively.

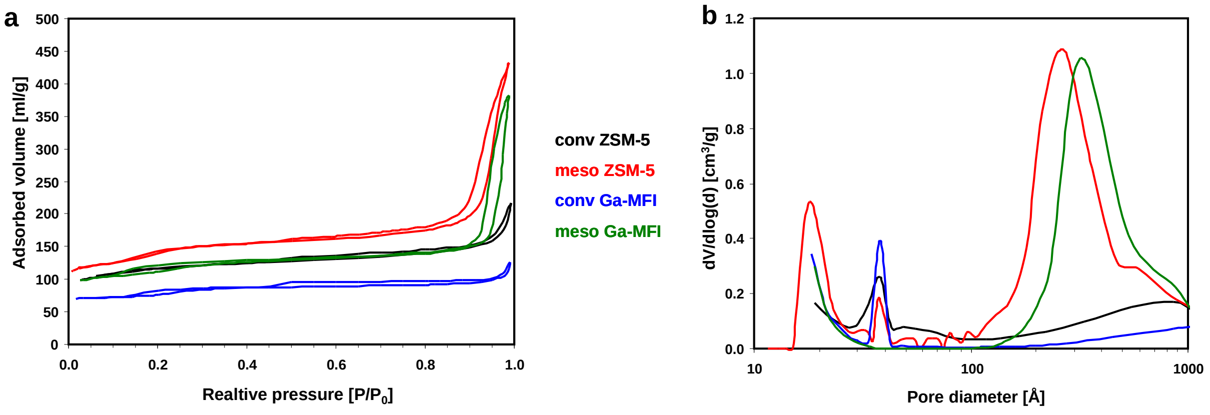

Figure 4.5: a) N_2 adsorption-desorption isotherms and b) corresponding pore size distribution of the prepared zeolite and zeotype samples. The pore size distributions are obtained from the desorption branch of the isotherms using the BJH method. In the pore size distribution artefacts at 20 and 40 Å are present for all four materials

As seen in Figure 4.5a the isotherms for the meso ZSM-5 and meso Ga-MFI materials both exhibit hysteresis in the region P/P_0 above 0.9 which indicates the presence of mesoporosity. The isotherm for the conventional ZSM-5 and Ga-MFI resemble both a Type I isotherm and typical for microporous zeolites. The conventional materials also exhibit hysteresis which is ascribed to intercrystalline voids as stated above. The pore size distributions in Figure 4.5b show that the conventional materials have only little porosity in the mesopore region due to interparticle voids, whereas the mesoporous ZSM-5 and Ga-MFI clearly contain mesopores and macropores (<50 nm). Even though the same carbon template is used to prepare the two mesoporous sample the pore size distributions are not completely identical. The pore size distribution for the mesoporous ZSM-5 is centred at 27 nm whereas the mesoporous Ga-MFI is centred at 32 nm. This is interesting since the used carbon template, BP-2000, are small carbon particles with an average diameter of 12 nm. The observed mesopores in both materials are at least twice the size of the diameter of the used carbon particles suggesting that the encapsulated carbon consists of aggregates of carbon particles that are encapsulated during crystallisation as opposed to individual carbon particles.

4.4.2. Conversion of methanol to hydrocarbons

The four prepared materials are tested in the conversion of methanol to hydrocarbons (MTH) to investigate differences in catalytic lifetime, selectivities and deactivation. It is difficult to compare the four materials directly since the Si/Al and Si/Ga ratios differ for each type of material. However, the Si/Al and Si/Ga ratios are rather similar for the conventional and mesoporous counterparts. The conversion of methanol at 370 °C and 1 bar for the four prepared materials are shown in Figure 4.6 together with the yield of aromatics. Both are plotted versus time on stream.

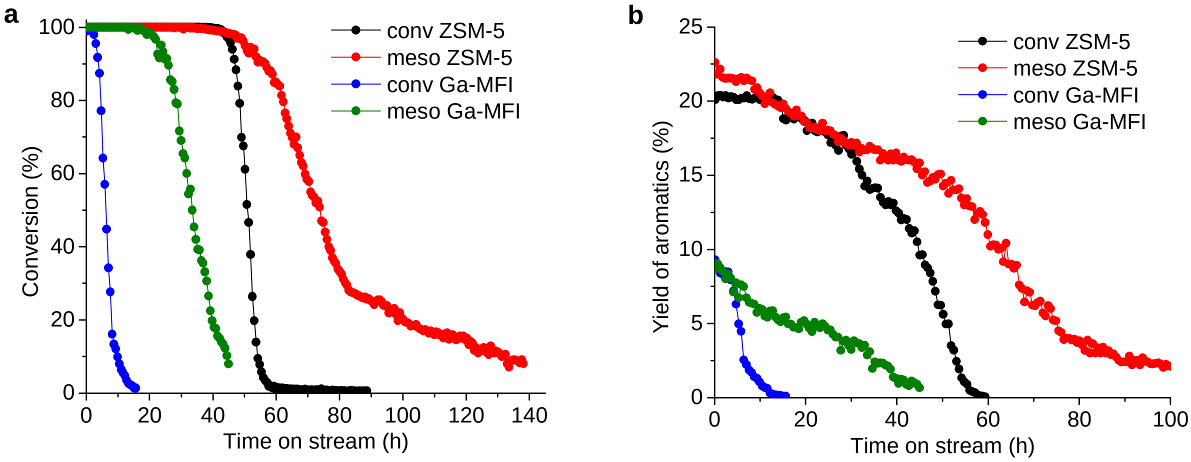

Figure 4.6: a) Conversion of methanol versus time on stream and b) corresponding yield of aromatics versus time on stream. The catalytic experiments are conducted at 370 °C and 1 bar

As seen in Figure 4.6 all four materials have the traditional S form curve observed in conversion versus time on stream curves for the MTH reaction in fixed bed reactors.[126,144,191] First is a period with full conversion followed by a rather rapid declining due to deactivation. According to Janssens[144] active catalysts show a more sudden decrease in conversion with time on stream.The curves for both microporous materials have a more sudden drop in conversion compared to the mesoporous counterparts. This indicates that the conventional ZSM-5 and Ga-MFI have a higher activity than mesoporous ZSM-5 and Ga-MFI. Since the zeolites have a higher acid strength for each individual acid sites and a higher acid density (lower Si/Al ratios than Si/Ga ratios) it was expected that the Ga-MFI zeotypes would deactivate slower than the ZSM-5 zeolites. As seen in Figure 4.6a the Ga-MFI zeotypes exhibit a shorter catalytic lifetime than the corresponding ZSM-5 zeolites, *i.e.* opposite to previous results[189]. In particular the conventional Ga-MFI deactivates very fast which could be affected by the presence of extra-framework gallium. As expected the mesopores for both types of materials improve the catalytic lifetime due to enhanced mass transport. The mesoporous Ga-MFI deactivated much slower than the conventional one, and has a lifetime which is close to the conventional ZSM-5. Even though the breakthrough of methanol is observed slightly earlier for the mesoporous ZSM-5 than for the conventional ZSM-5 the decline in conversion is slower resulting in a somewhat longer catalytic lifetime for the mesoporous ZSM-5. The yield of aromatics versus time on stream is shown in Figure 4.6b. It is clear by comparing the conventional and the mesoporous counterparts that a higher amount of aromatics is produced for the mesoporous samples due to less steric hindrance. As expected the gallium based zeotypes have a distinct lower selectivity towards aromatics compared to ZSM-5. Although the gallium based zeotypes have a lower acid density than the corresponding ZSM-5 zeolites, which make direct comparison difficult, the lower selectivity towards aromatics is most likely a consequence of the intrinsic lower acidity of the individual active sites. For all catalysts the production of aromatics declines with time on stream due to loss of catalyst activity.

For more detailed information on the selectivity, the initial product yields of aliphatics and aromatics are given in Figure 4.7a and b.

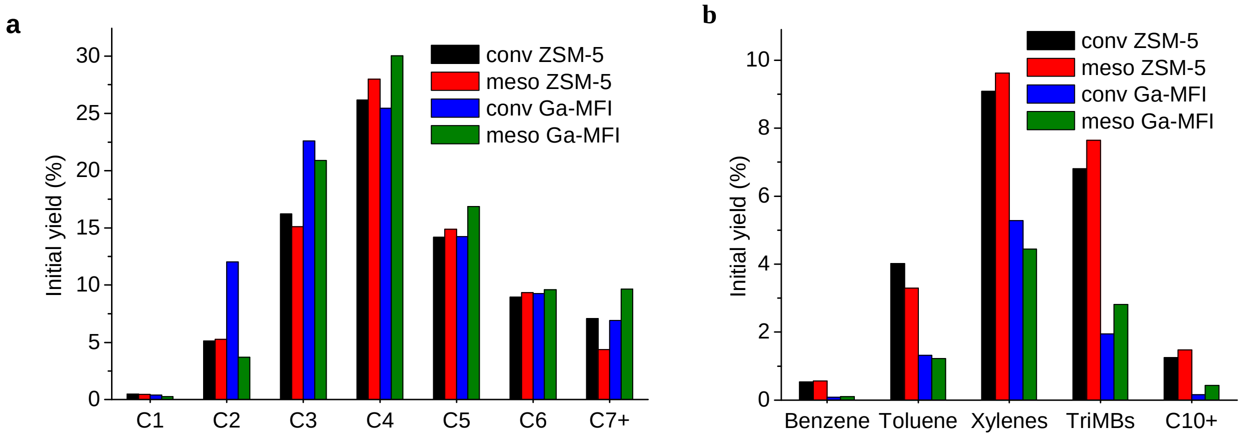

Figure 4.7: Initial product yields of a) aliphatics and b) aromatics for conversion of methanol over the prepared materials. The catalytic experiments are conducted at 370 °C and 1 bar

Comparing Figure 4.7a and b the selectivities for the four different catalysts are quite similar apart from the higher amount of aromatics produced from the two ZSM-5 zeolite based catalysts. The mesoporous zeolites produce slightly larger amounts of large aromatic compounds than their conventional counterparts, which has been observed in other studies[9,90] as well and can be explained as a direct effect of the mesoporosity leading to a shorter diffusion path for the larger compounds. The conventional Ga-MFI produces large amounts of ethene and propene while the mesoporous Ga-MFI produces larger amounts of long chain aliphatics, indicating a lower cracking activity of this catalyst. This is in all in agreement with previous results[187] that state that gallium containing zeotypes with low gallium contents have a higher selectivity towards small alkenes.

To investigate the deactivation the coke deposition on the various materials has been investigated though TPO analyses of the spent catalyst. The resulting carbon content on completly deactivated catalysts is shown in Figure 4.8a. Another way to compare the deposition of coke is by the ratio between the amount of carbon atoms converted and the amount of carbon deposited on the catalyst during the entire catalyst lifetime which is shown in Figure 4.8b.

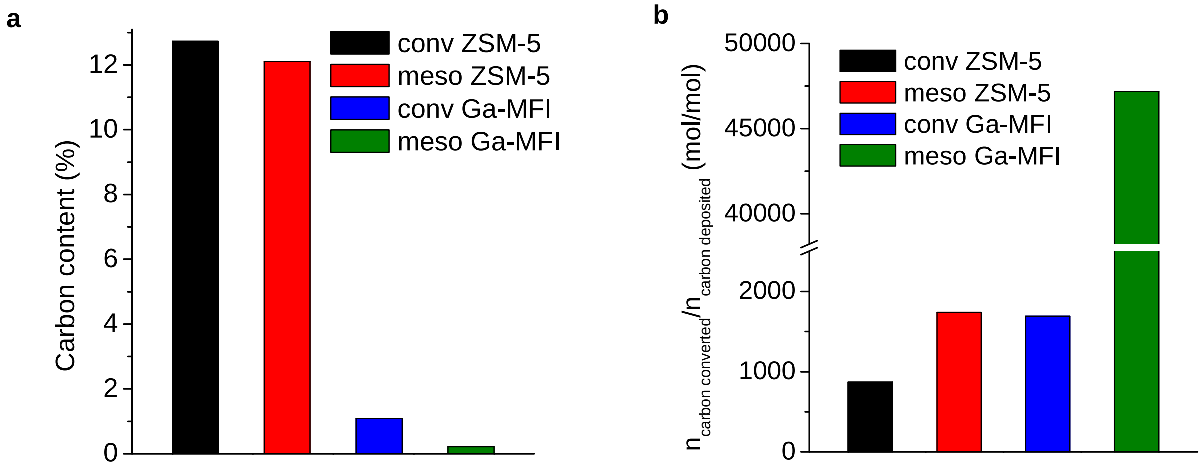

Figure 4.8: a) Carbon content in completely deactivated catalysts and b) the molar ratios between the amount of carbon converted and the amount of carbon deposited as coke on the catalyst during the entire lifetime of the catalyst for conversion of methanol at 370 °C and 1 bar

In general the zeolites contain much more coke than the gallium based zeotypes as observed in Figure 4.8a. Even though the catalysts are completely deactivated the conventional Ga-MFI contains only 1 % carbon, while the mesoporous Ga-MFI contains as little as 0.2 %. It does not seem to be any correlation between the coke content and the catalytic lifetime. The conventional Ga-MFI has a shorter catalytic lifetime than the mesoporous counterpart but contains a higher amount of coke. The mesoporous Ga-MFI have a comparable catalytic lifetime with conventional ZSM-5 but contains significant lower amount of coke. The conventional and mesoporous ZSM-5 have approximately the same amount of coke and the mesoporous ZSM-5 displays the longest catalytic lifetime.

Looking at the amount of converted carbon atoms per carbon deposited in Figure 4.8b the combination of reasonable conversion capacity and a very small amount of deposited coke leads to a remarkable high value for the mesoporous Ga-MFI. This catalyst is able to convert over 20 times as much carbon (in the form of methanol) per carbon atom deposited than any of the other catalysts even though it has a shorter lifetime than any of the zeolites.

From visual inspection of the spent and completely deactivated catalysts it is apparent that the mesoporous Ga-MFI has a low coke content compared to the zeolite samples. As seen in Figure 4.9 the mesoporous Ga-MFI is light grey, while both the conventional and mesoporous ZSM-5 are completely black. The conventional Ga-MFI (not shown) was also light grey.

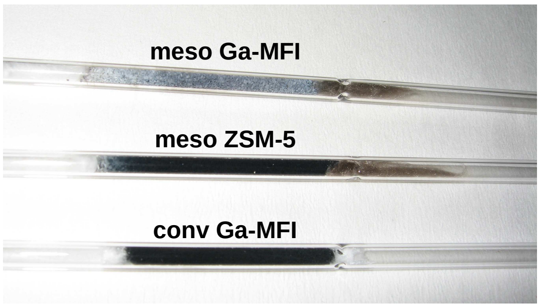

Figure 4.9: Picture of selected deactivated catalysts upon conversion of methanol at 370 °C and 1 bar

From Figure 4.9 another interesting detail can be observed. The quartz wool holding the catalyst in place is dark at the end of the catalyst bed for both mesoporous materials. This indicates that large hydrocarbon compounds *i.e.* presumably heavy aromatics, are able to leave the catalyst instead of forming coke. This might be part of the explanation of their superior lifetime compared to their conventional counterparts.

For conversion of methanol coke is deposited on the ZSM-5 catalyst at a constant rate throughout the entire experiments until the catalyst is completely deactivated.[16] For the gallium-based zeotypes methanol does not form significant amounts of coke but the catalysts are still completely deactivated. It is clear that the usually assumed deactivation mechanism of MFI, which is explained by the formation of external coke can not be the reason for the observed activity loss, since large amounts of external coke would be necessary to impede the diffusion of reactants into the pores of the catalyst. This means, that the catalyst is either very sensitive towards the presence of coke, *i.e.* very small amount of coke is enough to deactivate it or it is deactivated in another way than coke deposition or a combination of both. In order to investigate if the gallium based zeotypes deactivate due to high sensitivity towards the presence of coke the mesoporous Ga-MFI was regenerated by combustion of the deposited coke and subjected to methanol again in order to investigate the catalytic activity. Figure 4.10 shows the conversion of methanol versus time on stream before and after coke combustion. For comparison conventional ZSM-5 is also tested before and after coke combustion.

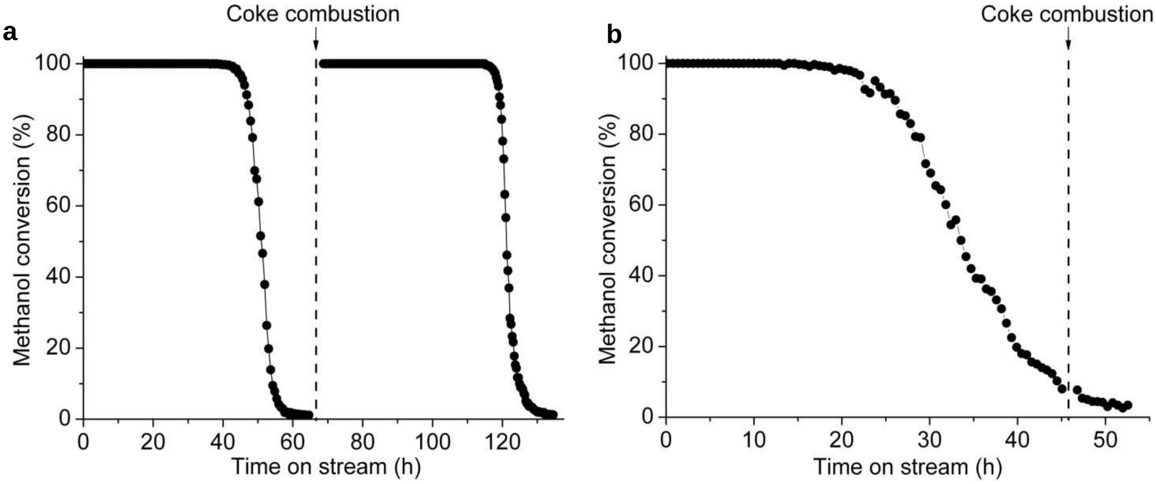

Figure 4.10: Conversion of methanol versus time on stream before and after regeneration for a) conv ZSM-5 and b) meso Ga-MFI. The catalytic tests are conducted at 370 °C and 1 bar

As seen in Figure 4.10a it is possible to regenerate the conventional ZSM-5 and obtain approximately the same catalytic lifetime. Contrary, the mesoporous Ga-MFI does not regain any activity for the conversion of methanol upon combustion of coke. Since it is not possible to regenerate the mesoporous Ga-MFI deposited coke can not be responsible for the deactivation. During conversion of methanol steam is generated and one possible explanation is that the presence of steam could hydrolyse the gallium-oxygen bond leading to a degree of gallium elimination from the framework and thereby loss of catalytic active Brønsted acid sites, as illustrated in Figure 4.11.

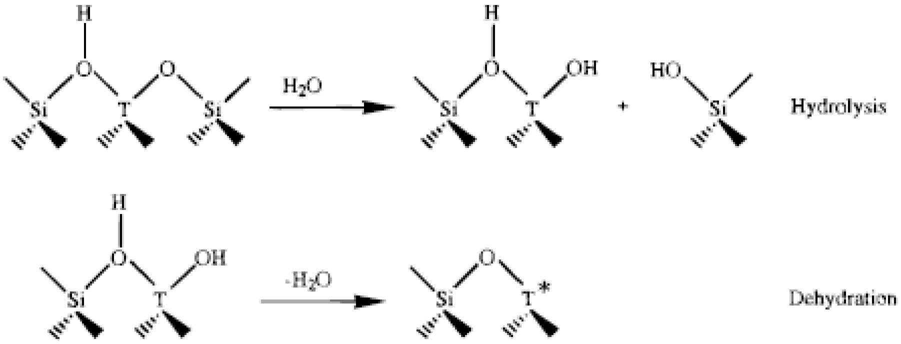

Figure 4.11: Partial elimination of gallium from the zeotype framework by either hydrolysis or dehydration. T represents a gallium atom. Adapted from [192]

Gallium in partial extra-framework positions is still linked to the framework in the form of low coordinated and isolated species as illustrated in Figure 4.11. After hydrolysis of Si-O-Ga bonds dehydration can take place leading to formation of new non-bridged Brønsted Ga-OH sites and finally to trigonal coordinated unsaturated Ga* species with strong Lewis acid character. The Ga* atom is now at a lattice defect where the framework is disrupted, but not yet in extra-framework position. However, hydrolysis does not necessarily stop at this stage but can continue up to the point where all bonds linking the gallium atom to the framework are broken with attendant formation of a silanol nest. The $Ga(OH)_3$ or GaOOH species thus produced can freely migrate and ultimately form after aggregation and dehydration small clusters of a Ga_2O_3 phase entrapped into the zeotype channels.

Areán *et al.*[192] have investigated the stability of the Si-O-Ga bonds. They found that on high-temperature treated samples, the gallium atoms show a tendency to go into partial or fully extra-framework positions and this phenomenon is particular relevant for temperatures above 900 K and low Si/Ga ratios. On the other hand, it appears that thermal degalliation of samples with high Si/Ga is negligible. This implies that a relatively high gallium concentration is needed to render the zeotype framework unstable towards thermal treatment in the 800-900 K range. Areán *et al.* stated that the presence of a small amount of steam can strongly favour the elimination process.

A control experiment where the mesoporous Ga-MFI was subjected to water vapour in a concentration corresponding to what would be expected from methanol dehydration for 48 h at the reaction temperature and subsequently tested in methanol conversion has been performed. The catalyst was not active for methanol conversion upon this treatment which indicates that steaming is a plausible explanation for the loss of activity.

To investigate the possible changes of the active sites of the mesoporous Ga-MFI during the catalytic test, FTIR has been conducted. As a reference the mesoporous Ga-MFI was steamed at 370 °C for 48 h – the same time as the catalytic reaction lasted. The spectra for a fresh, a regenerated and a steamed fresh sample of mesoporous Ga-MFI are given in Figure 4.12. To compare the OH groups the obtained spectra are normalised to the overtones of the framework vibrations in the 2200-1600 cm^{-1} (not shown) and same amount of sample is used.

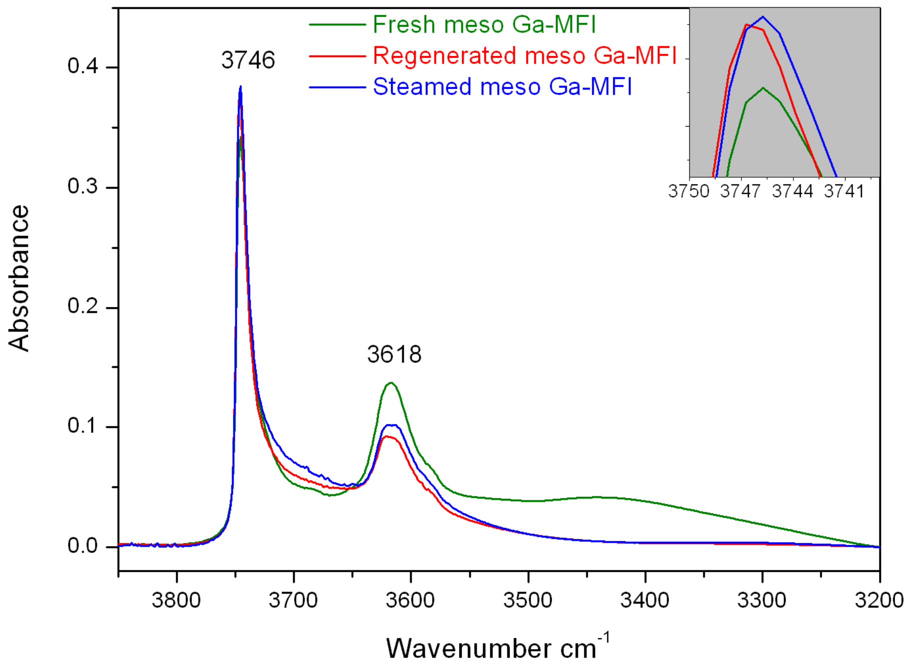

Figure 4.12: FT-IR spectra of fresh, regenerated and steamed mesoporous Ga-MFI

As seen in Figure 4.12 the spectra of the three samples are similar to those reported in the literature[192-194] as they all show the characteristic O-H band of the Si(OH)Ga-bridged Brønsted groups at 3618 cm^{-1} and external silanol groups at 3746 cm^{-1}. In addition the fresh sample shows a band at 3400 cm^{-1} which is ascribed to silanol nests or defects primarily located at the surface. The spectra for the regenerated and steamed samples are quite identical. One could argue that possible structural changes could occur during the thermal regeneration instead of during the reaction. Since the spectra for the regenerated and the steamed samples are practically identical the differences in OH-bands from the fresh sample must occur during steaming since the steaming affects the structure in the same extent as the regeneration. In addition, Areán *et al.* states that gallium zeotypes with high Si/Ga ratios are not significantly affected by high temperature treatment alone.

Upon methanol conversion, the intensity of the Brønsted acid band at 3618 cm^{-1} is decreased significantly. The decrease in the density of Brønsted acid sites must be due to hydrolysis and possible dehydration during the reaction which will lead to migration of the gallium atoms into extra-framework or partially extra-framework positions by formation of GaOOH species and ultimately Ga_2O_3 clusters. In the inset in Figure 4.11 the intensity of the bands at 3746 cm^{-1} is enlarged. It appears that the regenerated and steamed samples contain a higher amount of terminal silanols than the fresh sample. This might be explained by the disintegration of the

agglomerates into small primary particles which where initially connected via hydrogen bridges as apparent from the broad band at 3400 cm^{-1}, resulting in non-interacting terminal silanol groups. According to Areán *et al.* it is difficult to probe all the extra-framework gallium with either CO or N_2 and to verify the presence of extra-framework gallium one possibility would be to conduct ^{71}Ga MAS NMR. This is though beyond the scope of this work.
In summary, the deactivation of the mesoporous Ga-MFI zeotype appears to be due to loss of active Brønsted acid sites which happens due to hydrolysis and dehydration of Si-OH-Ga bonds. As a result of hydrolysis extra-framework gallium seems to be produced which is catalytically inactive in the conversion of methanol. This is in contrast to the deactivation of ZSM-5 zeolites which deactivate due to coke formation. The difference in mode of deactivation could also explain the unexpected longer catalytic lifetime observed for conventional and mesoporous ZSM-5.

4.5. Conclusion

In the present chapter an improved synthesis strategy for mesoporous Ga-MFI was reported. The obtained material was compared to conventional Ga-MFI plus conventional and mesoporus ZSM-5. The materials were characterised using XRPD, NH_3-TPD, elemental analysis, N_2 physisorption and SEM. The characterisations showed that all materials were crystalline with the MFI structure but vary concerning crystal size, shape and morphology. According to elemental analysis and NH_3-TPD the mesoporous ZSM-5 and conventional Ga-MFI seemed to contain extra-framework aluminum or gallium. It was also observed that aluminum was easier introduced into in the zeolite framework than gallium was introduced into the framework of zeotypes. This could be explained by the difference in size. Using NH_3-TPD it was verified that the incorporation of gallium in the framework decreased the intrinsic acidity of the individual acid sites. N_2 physisorption measurements revealed that mesoporous ZSM-5 and Ga-MFI were both mesoporous materials with comparable mesopores volume around 0.5 cm^3/g and pore size distributions centred at 27 and 32 nm, respectively.

All synthesised materials were tested for catalytic conversion of methanol at 370 °C and 1 bar. The catalytic lifetime of the gallium based zeotypes was in general shorter than the corresponding zeolites. However, the mesoporous Ga-MFI had catalytic lifetime almost comparable to that of conventional ZSM-5. As expected the presence of mesopores improved the catalytic lifetime for both the zeolites and the gallium based zeotypes. The Ga-MFI zeotypes showed a higher selectivity towards small alkenes which was ascribed to the lower acidity of the individual active sites compared to zeolites. Comparing the conventional and the mesoporous counterparts a higher amount of aromatics was produced for the mesoporous materials due to less steric hindrance. The gallium base zeotypes contained only very small amounts of coke when completely deactivated. In fact, for conversion of methanol mesoporous Ga-MFI was able to convert more than 20 times the amount of carbon per carbon atom deposited as coke than any of the ZSM-5 zeolites. This was quite remarkable, but despite the very low content of coke the catalyst was still completely deactivated. It was found that the ZSM-5 zeolites deactivated due to coke formation as it was possible to regenerate the catalytic activity and obtain approximately the same catalytic lifetime after coke combustion. In contrast, the catalytic activity of the mesoporous Ga-MFI could not be restored after coke combustion. FTIR was performed to investigate the structural changes of the active sites before and after regeneration. It was found that during methanol conversion the mesoporous Ga-MFI deactivates due to loss of the catalytically active Brønsted acid sites leading to formation of inactive extra-framework gallium species.

Chapter 5

Encapsulation of gold nanoparticles in MFI type crystals

This chapter describes synthesis, characterisation and catalytic test of encapsulated gold nanoparticles in MFI type zeolites. The obtained hybrid materials are shown to be substrate-size selective oxidation catalysts. The synthesis work was carried out in collaboration with then master student Anders B. Laursen, TEM investigations were performed by PhD Søren B. Simonsen and PhD Lars F. Lundegaard and the catalytic tests were conducted by PhD Søren Kegnæs.

5.1. Introduction

In heterogeneous catalysis, metal nanoparticles supported on high surface area carriers play a crucial role as active and selective catalysts for numerous chemical reactions.[11] Inevitably, and this is particular true for high temperature applications, nanoparticle sintering occurs during operation. Regarding gold, it was for many years considered to be chemically inert and hence not regarded as a potential catalyst.[195] Over the past decade, the investigation of gold catalysis has increased rapidly.[196-199] It has been established that when gold is highly dispersed as small nanoparticles with a diameter less than 10 nm it becomes a highly active oxidation catalyst for many reactions.[200-202] The gold catalysts deactivate as the average size of the gold particles increases via sintering and it is necessary to find a way to produce stable gold catalysts. Over the years many strategies have been developed to produce sintering stable gold nanoparticles including encaging the metal nanoparticles by protective shells[203], depositing in mesoporous silica such as MCM-41[204-206] or entrapping in the cavities of certain zeolites[207]. Materials containing metal nanoparticles that are only accessible via zeolite micropores are intriguing for catalytic applications, since the micropore system of molecular dimensions allows for shape-selective catalysis. Furthermore zeolites are often more thermally stable materials than mesoporous silica and it is possible to tune the acidic and/or redox properties of the zeolite material.[208] Depositing gold nanoparticles in zeolites has been pursued in several ways, but in general it is done in post-synthesis steps after zeolite crystallisation by either impregnation[209], ion-exchange[210-212] sublimation[213-215], or the so-called ship-in-a-bottle method[207] all followed by reduction of the introduced Au^+/Au^{3+} component.

The most commonly practiced techniques for preparing supported catalysts are incipient wetness impregnation and ion exchange. In the latter, the interaction between the deposited salt and the support is stronger than in the former. Consequently, the exchanged sample can achieve much higher metal dispersion and more homogeneous metal distribution than the impregnated sample. The amount of metal that can be introduced into the zeolite by ion exchange is limited by the Si/Al ratio, which places demands on the zeolite material. The sublimation method seems to be a feasible way to introduce gold into zeolite crystals, but the preparation is on the other hand quite complex requiring working under inert atmosphere. At the same time it is difficult to control the size of the gold nanoparticles. By using the so-called ship-in-a-bottle method it is possible to synthesise gold nanoparticles in the cages of certain zeolites by taking advantage of the uniform cage size to constrain the cluster size. Even though it was possible for Fierro-Gonzalez *et al.*[207] to synthesise gold nanoparticles trapped inside the α-cages of zeolite Y in the range 0.3-1 nm, this type of synthesis is restricted to certain types of zeolites with cages or cavities. Not surprising, most work concerning the introduction of gold nanoparticles into zeolites is done using zeolites containing cages and cavities like zeolite A and Y, except a few investigations performed on MFI type zeolites.[213,216] Even though it is possible by post-synthesis treatments to introduce gold nanoparticles into zeolite crystals, a more sintering-stable catalyst would be obtained if the gold nanoparticles were encapsulated by the zeolite framework. By post-synthesis treatments the gold nanoparticles are in the cages and/or in the pores of the zeolite and it can be difficult to control the size and location of the gold nanoparticles. By encapsulation the gold nanoparticles are immobilised and sustained in the entire zeolite crystals and are therefore not able to sinter. In this way it becomes possible to produce a stable size-selective catalyst, since the stable gold nanoparticles are accessible only though zeolite micropores. Yang *et al.*[217] have presented a procedure that entails crystallisation of the zeolite from a gel containing platinum metal ions which should be immobilised in the zeolite during crystallisation. Using this approach it is very difficult to control the particle size of the metal particles and their location in the structure. Concerning encapsulation of gold nanoparticles in zeolite crystals Hashimoto *et al.*[218] reported an approach featuring downsizing Au flakes to ca. 40 nm particles by laser ablation and subsequently embedding these particles during crystallisation. A reduction of the particle sizes by an order of magnitude is needed for an efficient use of gold in catalytic applications. For both procedures reported by Yang *et al.* and Hashimoto *et al.* no clear evidence is presented to prove whether the metal nanoparticles are in fact encapsulated or just present at the external surface of the zeolite crystals.

In this chapter a synthetic procedure for producing hybrid materials comprising sintering-stable gold nanoparticles accessible only through zeolite micropores is presented. The gold nanoparticles are embedded during zeolite synthesis and by using electron tomography it is proved that the gold nanoparticles are in fact embedded in the zeolite crystal framework. Moreover, it is shown that the encapsulated gold is only accessible though the micropores, making this hybrid material a substrate-size selective oxidation catalyst. As structure type the MFI type is chosen and both silicalite-1 and ZSM-5 are used as models.

5.2. Synthesis strategy

The synthetic approach for encapsulating gold nanoparticles in silicate-1 crystals comprises three steps, which is schematically illustrated in Figure 5.1.

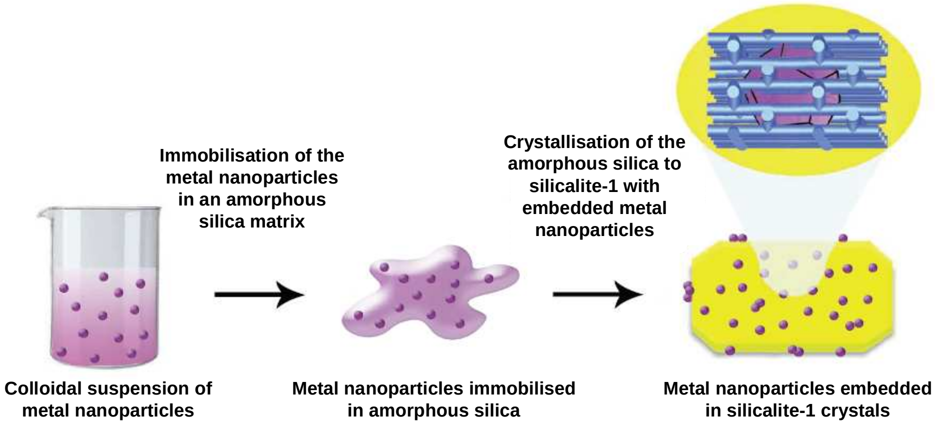

Figure 5.1: Schematic illustration of the encapsulation of gold nanoparticles in pure silicalite zeolite crystals

First a gold nanoparticles colloid with suitable anchoring point for generation of a silica shell is prepared. The second step entails encapsulation of the particles by an amorphous silica matrix creating core/shell motif. Finally, the silica-nanoparticle precursor is subjected to hydrothermal treatment to crystallise the amorphous silica into silicalite-1 type crystals.
The gold colloidal suspension is synthesised following a procedure from Haider *et al.*[202] using $HAuCl_4{\cdot}3H_2O$ as gold precursor and tetrakis(hydroxymethyl)phosphonium chloride (THPC) as reducing agent. Unreacted THPC will act to stabilise the colloid resulting in a colloidal suspension with a mean diameter of 1.3 nm. The following coating of the gold nanoparticles with amorphous silica was performed using a slightly revised procedure from Liz-Marzán *et al.*[219], *i.e.* by using another linker molecule. It is necessary to add a linker molecule prior to coating with silica. Gold metal has very little affinity for silica since the surface charge (zeta potential) is negative thus repelling silicate anions.[220] Unlike most other metals, gold does not form an oxide film in solutions and it is necessary to add stabilising molecules to prevent the particles from coagulating. These stabilisers also render the gold surface vitreophobic[*]. To modify the gold surface and make it vitreophilic one way is to use a silane coupling agent or a linker molecule. The effect of the linker molecule arises from the interaction between the gold and the linker molecule and it has to be rather strong in order to minimise the dissociation of the linker at the elevated temperature necessary for zeolite crystallisation to avoid sintering. At the same time the competitive adsorption of THPC onto the gold surface should be diminished. The used linker molecule was 3-mercaptopropyltrimethoxy-silane ($HS(CH_2)_3Si(OCH_3)_3$, MPTMS), which was chosen due to the rather strong bond between the gold surface and the thiol group on the linker. The amount of linker was found by trial and error as the addition of excess amounts resulted in a visible dark precipitate. It is important that a fresh solution of MPTMS is used since MTPMS can self-polymerise in water. A schematic illustration of the core/shell motif is illustrated in Figure 5.2a.

---

[*] Repelling silica

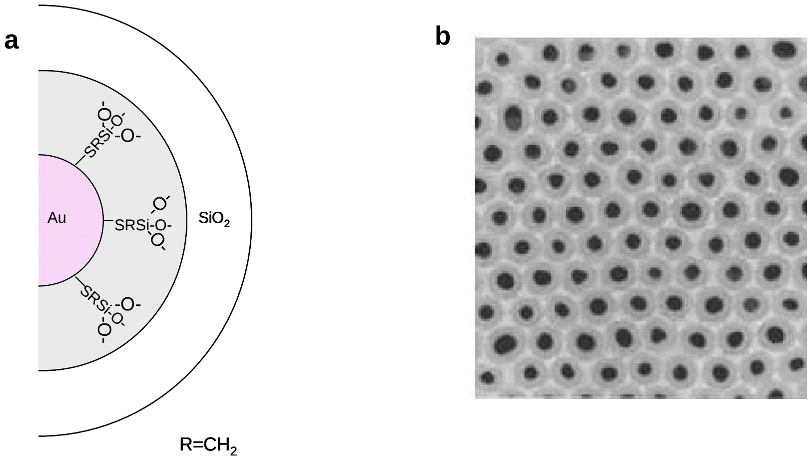

Figure 5.2: a) Schematic illustration of silica coating of gold nanoparticles and b) TEM image of 15 nm Au particles covered by 10 nm silica. Adapted from [219]

After addition of the linker molecule a slow condensation of silica is followed to achieve the core/shell motif. The need for a slow condensation arises from the need that the solute silica species should coat rather than nucleate on their own. Figure 5.2b shows a TEM image of gold nanoparticles covered in silica.

The silica coating must be carried out at pH values around 9 because at that point a favourable equilibrium exists between dissolved and solid silica. To obtain a smooth coating, the first layer is applied by adding a diluted water-glass solution, which is left for 24 h. To further thicken the silica shell the particles are suspended in a water/ethanol mixture and the shell is grown via the Stöber method[221] for synthesising silica colloids. The silica is added in the form of tetraethylorthosilicate (TEOS) and to catalyse the condensation hydroxide ions must be added which is done in the form of aqueous ammonia. TEOS may be added at 24 h intervals to obtain coats of varied thickness. The aim is to synthesise gold nanoparticles with a mean diameter of 1.3 nm coated silica shell to obtain a precursor material containing 2 wt% gold.

It is important that the crystallisation of amorphous silica into silicalite-1 crystals happens under rather restricted conditions. Usually the zeolite synthesis gel is quite alkaline which inadvertently could dissolve all the coated silica. Ethanol is added to the synthesis mixture of the silicalite-1, since the presence of ethanol reduces the crystallisation rate by lowering the solubility of the silicate ions.[222] The reduction in solubility should decrease the chance of removing all the silica shell at once. The crystallisation of amorphous silica into silicalite-1 crystals is based on a synthesis by Botella *et al.*[223]. They introduce cetyltrimethylammonium bromide (CTAB) into a core/shell structure of gold embedded in amorphous silica in order to synthesise the mesoporous silica MCM-41 around the gold cores. In this work, the original synthesis is modified so that three times the molar amount of template is used in place of CTAB. This is done to mimic other zeolite syntheses procedures[224] since in general zeolite syntheses have a higher ratio between silica and template than the syntheses of mesoporous silicas like MCM-41. Furthermore, a longer reaction time is employed to counter the effect of ethanol on the crystallisation rate and also the crystallisation temperature is rather low compared to other typical syntheses.

Even though nothing seems to limit the choice of structure type that could encapsulate the gold nanoparticles the MFI structure is chosen and using the above described synthesis gold nanoparticles are encapsulate in silicalite-1 crystals. By introducing an extra synthesis step it is possible to encapsulate gold nanoparticles in true zeolite crystals containing both silicon and aluminum. Introducing aluminum in the zeolite structure allows for tuning the properties of the zeolite matrix regarding the acidity and hydrophilicity. The ZSM-5 type zeolite is chosen as a model and the two synthesis strategies are for comparison schematically shown in Figure 5.3.

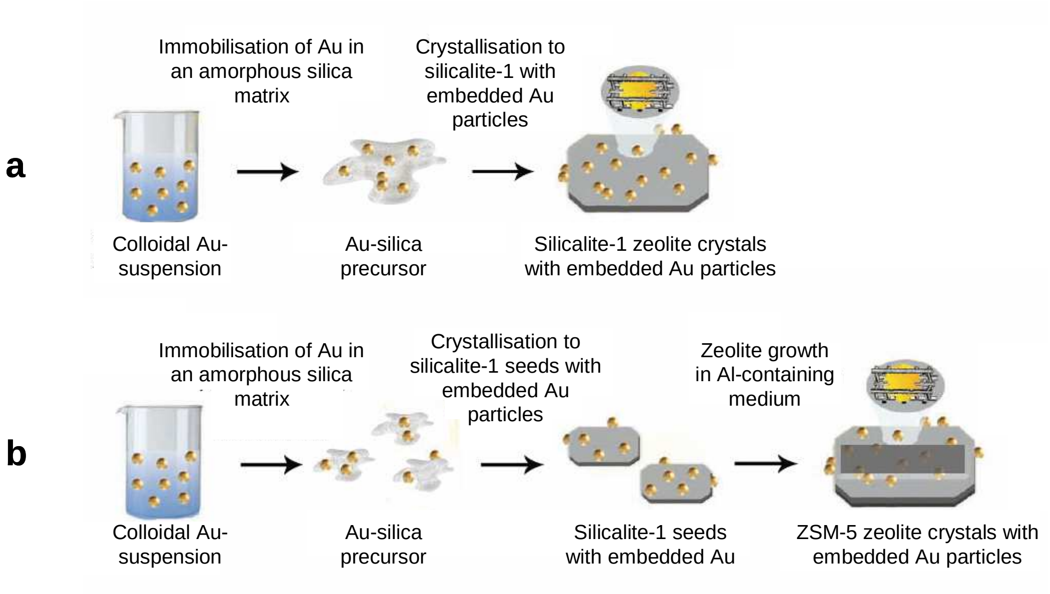

Figure 5.3: Synthesis scheme for encapsulating gold nanoparticles in a) silicalite-1 crystals and b) ZSM-5 zeolite crystals

In both synthesis strategies gold nanoparticles are first immobilised in amorphous silica followed by crystallisation into silicalite-1 crystals or silicalite-1 seeds. In the synthesis strategy producing gold nanoparticles in ZSM-5 zeolite, Figure 5.3b, the gold-silica precursor contains a higher amount of gold resulting in silicalite-1 seeds with a higher gold content than the silicalite-1 product in Figure 5.3a. The silicalite-1 seeds are subsequently suspended in a ZSM-5 growth medium containing aluminum and synthesised into embedded gold nanoparticles in ZSM-5 zeolite crystals. The immobilised gold nanoparticles for encapsulation in ZSM-5 crystals were synthesised using Wu *et al.*[225] using MPTMS as stabiliser instead of phenylethylthiol. The reason for using a different approach for preparing immobilised gold nanoparticles in amorphous silica was primarily to prepare smaller gold nanoparticles in order to obtain smaller encapsulated gold nanoparticles in zeolite crystals. Using the second described synthesis strategy it should be possible to expand the synthesis to other structure types of zeolites and zeotypes by varying the zeolite template and type of added elements. This is beyond the scope of this work.

In order to verify that the encapsulated gold nanoparticles are accessible only though the micropores, catalytic experiments are performed with aerobic oxidation of a mixture of benzaldehyde and 3,5-dimethylbenzaldehyde in methanol solution to the corresponding methyl esters. The presence of embedded gold nanoparticles in the zeolite crystals should enhance the selectivity towards the stericly less hindered methyl benzoate for both hybrid materials, as illustrated in Figure 5.4 making the hybrid materials substrate-selective oxidation catalysts.

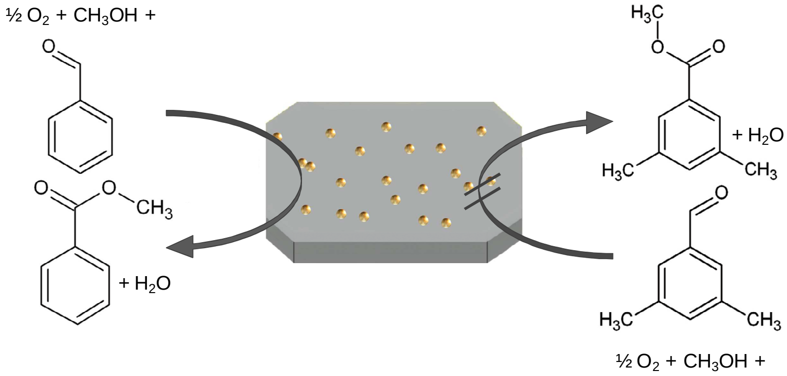

Figure 5.4: Schematic drawing of the size-selectivity in the benzaldehyde and 3,5-dimethylbenzaldehyde oxidation reaction

5.3. Experimental

All the chemicals were of reagent grade and used without any further purification: Gold(III) chloride trihydrate ($HAuCl_4 \cdot 3H_2O$, 99+ wt% Sigma-Aldrich), tetrakis(hydroxymethyl)phosphonium chloride (THPC, 80 wt%, Sigma-Aldrich), 3-mercaptopropyltrimethoxysilane (MPTMS, 95 wt%, Sigma-Aldrich), ammonia (NH_3, 25 wt%, Fluka), tetraethylorthosilicate (TEOS, 98 wt%, Sigma-Aldrich), sodium hydroxide (NaOH, 99 wt%, Riedel-de Häen), tetrapropylammonium hydroxide (TPAOH, 40 wt%, AppliChem), Ethanol (C_2H_5OH, 99 wt%, Kemetyl A/S), water glass (“$Na_2Si_3O_7$”, 27 wt% SiO_2, Riedel-de Häen), tetrahydrofuran (C_4H_8O, THF, 99.9 wt%, Sigma-Aldrich), sodium borohydride ($NaBH_4$, 99 wt%, Sigma-Aldrich), sodium aluminate (“$NaAlO_2$”, 29.3 wt% Al, Riedel-de Häen), silica gel 100 (SiO_2, Merck), benzaldehyde (C_7H_6O, 99 wt%, Sigma-Aldrich), 3,5-dimethylbenzaldehyde ($C_9H_{10}O$, 97 wt%, Sigma-Aldrich), methanol (CH_3OH, 99 wt%, Sigma-Aldrich), sodium methoxide (CH_3ONa, 25 wt% in methanol, Sigma-Aldrich), anisol (C_7H_8O, 99 wt%, Sigma-Aldrich).

5.3.1. Synthesis of Au@silicalite-1

The precursor consisting of immobilised gold nanoparticles in silica was synthesised using the following procedure:

To prepare 1 l of Au colloid, 900 ml of deionised water, 60 ml 0.2 M NaOH and 20 ml 0.25 M THPC was mixed. Furthermore, 0.404 g $HAuCl_4 \cdot 3H_2O$ was dissolved in 20 ml water and added to the vigorously stirred alkaline solution of THPC by which it turned dark brown/orange.

To immobilise the Au nanoparticles in amorphous silica, first, 70 ml 1 mM MPTMS (the maximum amount of MPTMS is 0.0684 mol pr mol Au) was added to the 1 l of the Au colloid and the resulting mixture was stirred for 30 min to ensure complete complexation of the sulfur group with the gold surface. Then, 500 ml of water glass (diluted with water to 0.16 wt% SiO_2) was added and the mixture was stirred for 24 h, so that the dissolved silica polymerises onto the gold particle surface. The aqueous reaction mixture was then diluted with a 4-fold volume excess of ethanol (absolute) and 6 ml ammonia was added. Then, 33.87 ml TEOS was added under stirring in portions of 1.62 ml 3 times a day. After addition of the TEOS the reaction mixture was stirred for another 8 hours before the mixture was allowed to settle overnight after addition of a NaCl solution. The solid product was separated from the mother liquor by decantation, washed 8 times by centrifugation (15 min at 9000 rpm) and dried at 100 °C for 16 h. The obtained purple material was named Au@silica.

The hybrid gold silicalite-1 material was synthesised from the precursor material using the following procedure:

To a mixture of 2.91 g of TPAOH (40 wt%), 0.11 g NaOH, 23 g ethanol and 90 g deionised water was added 0.76 g of the precursor Au@silica and the resulting mixture was stirred for 15 min. Then the mixture was transferred to a Teflon-lined autoclave which was kept at 100 °C for 72 hours. After quenching to room temperature, the solid product was recovered by filtration, washed with deionised water and dried at 100 °C for 16 h before it was calcined in air under static conditions for 3 h. The obtained purple material was named Au@silicalite-1

5.3.2. Synthesis of Au@ZSM-5

The precursor with the immobilised gold nanoparticles in silica was synthesised using the following procedure:

Firstly, 0.62 g $HAuCl_4 \cdot 3\,H_2O$ was dissolved in 44 ml THF in a tri-necked round-bottomed flask, and the resulting yellow solution was cooled to 0 °C in an ice bath over a period of 30 min. Then 1.6 ml MPTMS was slowly added and the speed was reduced to approximately 60 rpm and left for stirring for 16 h. As the yellow solution had not turned completely colourless overnight, 0.8 ml MPTMS was further added. After 2 h the solution turned colourless and the speed was changed to fast stirring (~1200 rpm). Quickly, an ice-cold solution of 0.6 g $NaBH_4$ dissolved in 15 ml water was added all at once by which the solution turned brown. The was left for stirring for 3 hours and after that, the ice bath was removed and the solution was warmed to room temperature. The reaction was allowed to further proceed over 60 h. The final solution was a brownish yellow liquid with a black precipitate, which was removed by filtration under suction.

To coat the gold clusters in silica 25 ml of the obtained colloid (0.36 wt% Au) was diluted with 500 ml THF under stirring followed by addition of 5.25 ml aqueous ammonia. After 15 min of stirring 0.39 ml TEOS was added and left for 8 h. Four more of such additions were made at approximately 8 hours interval. The obtained purple solid precursor product was recovered by evaporation of the solvents at 100 °C overnight.

The hybrid gold ZSM-5 material was synthesised from the precursor material using the following procedure:

> *The zeolite seeds were prepared by dissolving 0.16 g NaOH in 119 ml deionised water and added 19 g EtOH and 2.79 g TPAOH. After obtaining a homogeneous solution 1.23 g precursor material was suspended and stirred for 15 min. The suspension was transferred to a Teflon-lined autoclave and heated to 100 °C and left for 5 days. After quenching the autoclave to room temperature the zeolite seeds were recovered by centrifugation at 9000 rpm for 30 min. The brownish solid was washed by re-suspending the solid in deionised water followed by centrifugation. This cycle was repeated 5 times. Finally, the zeolite seeds were dried at 100 °C overnight.*
>
> *A ZSM-5 growth medium was prepared by dissolving 0.079 g NaOH and 0.098 g $NaAlO_2$ in 7.9 ml deionised water. Silica was added in small portions until 0.876 g SiO_2 gel 100 was added. The resulting suspension was mixed by shaking for 1 h. Finally, 0.126 g seeds were added and shaken for another hour. The obtained mixture was transferred to a Teflon lined autoclave and heated to 180 °C for 40 h. After quenching the autoclave the zeolite crystals were recovered by filtration and washed with deionised water until pH reached 7. After drying the purple zeolite product at 100 °C for 16 h it was calcined in air under static conditions for 3 h. The obtained product was named Au@ZSM-5.*

5.3.3. Catalytic oxidation of aldehydes

The catalytic oxidation of benzaldehyde and 3,5-dimethylbenzaldehyde using Au@silicalite-1 and Au@ZSM-5 as catalysts were performed as follows:

> *In a typical experiment, a mixture of 0.5 mmol aldehyde (benzaldehyde or 3,5-dimethylbenzaldehyde), 60 mmol methanol and 0.1 mmol sodium methoxide were charged into a 10 ml two-neck round-bottom flask equipped with a condenser and a septum together with the gold catalyst (0.1 mol% Au). The reactor system was connected to an O_2 cylinder and it was flushed with O_2. The reaction mixture was magnetically stirred and small samples were taken at selected times, filtered directly through a syringe filter and analysed by GC and GC-MS. The GC column Agilent Technologies Inc. HP-5 was used. The amounts of substrates and products were quantified using anisol as internal standard. For the oxidation reactions a commercial reference catalyst was used. The used reference catalyst was gold supported on titanium dioxide, 1% Au/TiO_2 supplied by Mintek.*

5.4. Results and discussion

The precursor material Au@silica is characterised by using XRPD, elemental analysis and TEM to investigate the amount of gold and the size of the immobilised gold particles in amorphous silica. The Au@silicalite-1 and Au@ZSM-5 are characterised by using XRPD, elemental analysis, N_2 physisorption and SEM. Furthermore, the Au@silicalite-1 is investigated using TEM. Bright field TEM tomography is used to uniquely determine the relative positions of the gold nanoparticles with respect to the matrix material. To address if the embedment stabilises the gold nanocrystals, TEM images are recorded before, during and after calcinations in air at 550 °C for 3 h. Furthermore, Au@silicalite-1 and Au@ZSM-5 are both tested in the aerobic oxidation of a mixture of benzaldehyde and 3,5-dimethylbenzaldehyde in methanol to the corresponding methyl esters.

5.4.1. Characterisation of the precursor material Au@silica

The preparation of the precursor material Au@silica is as a starting point very time consuming, since TEOS has to be added in small portions every 24th hour to ensure the generation of a homogeneous silica shell. As a consequence the synthesis would take up to three weeks which is not a viable solution. To reduce the preparation time TEOS is instead added approximately every 8th hour.

The XRPD patterns for the precursor material Au@silica and bulk gold are given in Figure 5.5. The XRPD pattern shows the presence of amorphous silica and according to the Debye-Scherrer equation ~ 4 nm sized gold nanoparticles measured in the D[200] direction.

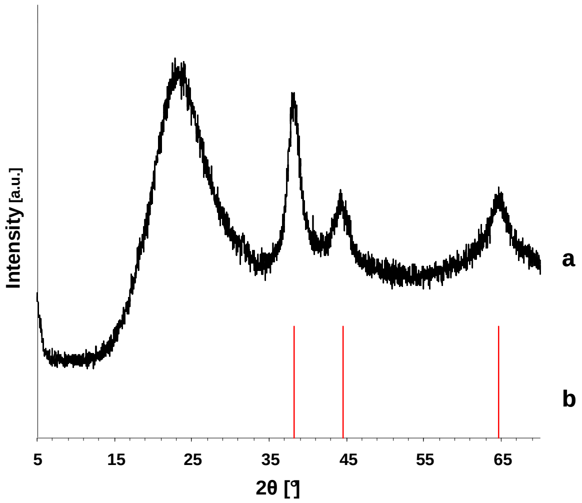

Figure 5.5: XRPD pattern for a) precursor Au@silica and b) bulk Au

The aim for the precursor material was 2 wt% gold. According to elemental analysis the precursor material contains only 0.32 wt% gold which is significantly lower than expected. One explanation could be that not all of the gold colloid is settled using a solution of sodium chloride as precipitation agent.

The precursor material was also studied using TEM and representative images are shown in Figure 5.6.

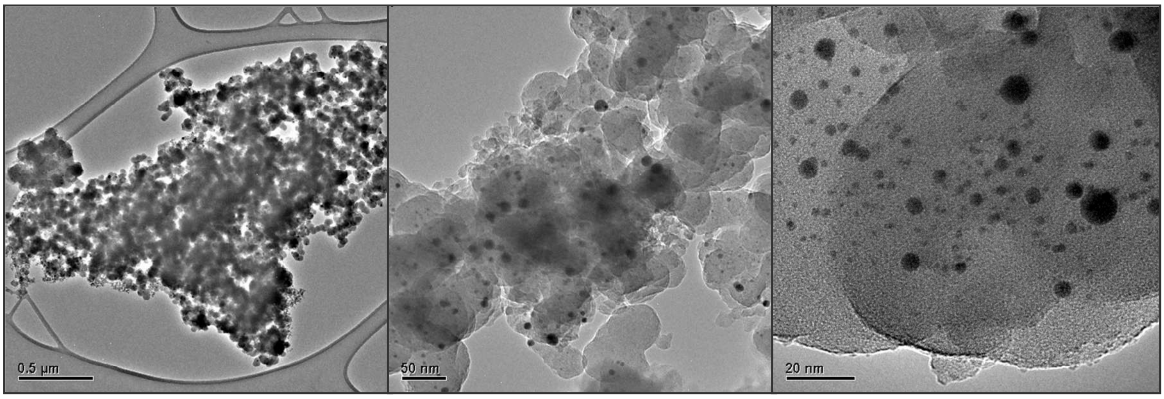

Figure 5.6: TEM images of the prepared precursor material Au@silica

The images given in Figure 5.6 show that the gold nanoparticles are homogeneously distributed in a silica matrix rather than creating homogeneously covered core/shell materials or perfect spheres. The gold nanoparticles are around 1-20 nm and quite uniform in shape. According to Haider *et al.*[202] the prepared gold nanoparticles should have a mean diameter around 1.3 nm so during the coating with silica some of the gold nanoparticles seem to sinter. One explanation could be that the stabilising THPC ligands repel the MTPMS ligands by which it is not possible for the gold nanoparticles to be coated with silica due to gold's vitreophobic character.
According to Liz-Marzán *et al.*[219] the key to obtain homogeneously coated particles is the control of solubility of silica at defined times. This means that silica must be added sparingly at first to avoid coagulation and at the same time the coating should be fast enough to avoid aggregation of the spheres. Liz-Marzán *et al.* use a low concentration of water glass to make the first thin coat and ethanol is added to condense any dissolved silica slowly onto the shells. Even though this is attempted the faster addition of silica quantities in the form of TEOS every 8th hour instead of every 24th hour could affect the coating and thereby the sintering of the gold. It is obvious that more investigations have to be made to create homogeneous coated gold nanoparticles.

5.4.2. Characterisation of Au@silicalite-1

The XRPD patterns for the hybrid material Au@silicalite-1 and bulk Au is shown in Figure 5.7. The pattern is recorded after the zeolite synthesis and prior to calcination.

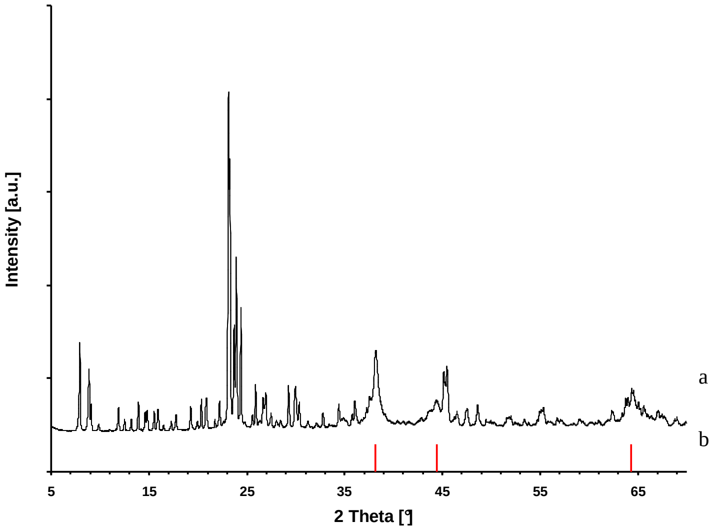

Figure 5.7: XRPD pattern for a) Au@silicalite-1 prior to calcinations and b) bulk Au

From Figure 5.7 it is seen that the sample contains highly crystalline material with the MFI structure along with gold particles. According to the Debye-Scherrer equation the gold particles in Au@silicalite-1 are approximately 16 nm in the D[200] direction, so during the zeolite synthesis the gold particles sinter from 4 to 16 nm. After calcination the gold particles are estimated to 48 nm in the [200] direction. The significant increase in the average gold particle size could be due to sintering of gold particles on the external surface of the zeolite crystals, where they are able to sinter freely.

According to elemental analysis the hybrid Au@silicalite-1 material contain 1.37 wt% gold. Compared with the precursor material (0.32 wt%), the gold content is significantly higher in the hybrid material. The more than 4 times higher amount of gold in the hybrid material could be due to dissolution of the coating of silica during crystallisation of silicalite-1. Instead of crystallisation into silicalite-1 crystals the silica could be dissolved and washed out during filtration. This is supported by the rather low yield. Only 0.25 g of hybrid material was obtained prior to calcination corresponding to a yield of 32.9 %.

In Figure 5.8 the N_2 adsorption/desorption isotherm is shown which is obtained after calcination. The isotherm clearly demonstrates that the Au@silicalite-1 material is primarily a microporous material with no significant amount of mesoporosity. The observed hysteresis loop between P/P_0 0.5 and 0.95 could be due to interparticle voids.

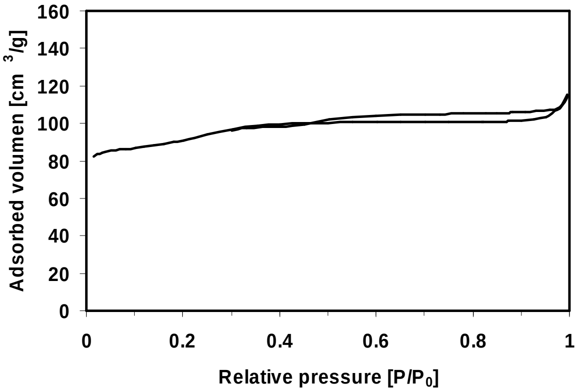

Figure 5.8: Nitrogen adsorption/desorption isotherms for the Au@silicalite-1

In Table 5.1 the BET surface area, micro-and mesopore volume of the hybrid Au@silicalite-1 are given.

Table 5.1: Surface area, micro- and mesopore volumen for the hybrid Au@silicalite-1 material according to [a] the BET method, [b] the t-plot method and [c] the BJH-method (adsorption)

	Surface area [m^2/g]^a	Micropore volume [cm^3/g]^b	Mesopore volume [cm^3/g]^c
Au@silicalite-1	341	0.15	0.07

The surface area and micropore volume lie in the same range as previous results for ZSM-5 zeolite[66, 145]. The mesopore volume is low compared to mesoporous zeolites[66, 145] and the observed mesoporosity could be due to interparticle voids or intercrystalline mesopores rised from decomposition of the used linkers.

Figure 5.9 shows representative SEM images of the Au@silicalite-1. The SEM images are recorded using both the secondary and backscatter detector to investigate the morphology of the crystals and to get an indication if gold is present on the external surface of the crystals.

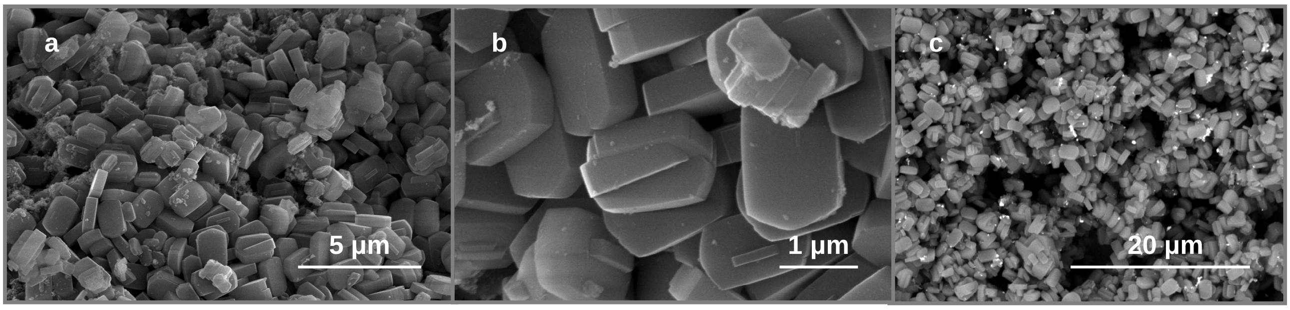

Figure 5.9: Representative SEM images of the Au@silicalite-1. a) and b) are recorded using secondary detector before calcination while c) is recorded using backscatter detector and after calcination

The images (Figure 5.9.a and 5.9.b) reveal that the material is primarily composed of ca. 1-2 µm long coffin-shaped crystals with a minor fraction of intergrown coffin-shaped crystals and irregularly shaped crystals. The coffin-shaped morphology is commonly observed for MFI-structured zeolite materials. Using the backscatter detector (Figure 5.9c) the gold particles appear as bright spots on the crystallite surfaces and show that not all gold is encapsulated in the silicalite-1 crystals.

To investigate the location and stability of the gold particles in the silicalite-1 crystals TEM is used. A mosaic TEM image is shown in Figure 5.10 composed of 10 TEM images. This reveals an overall uniform contrast extending over the entire crystal superimposed by areas of darker and brighter contrast. The varying contrast is attributed to varying mass-thickness contrast and so that the darker areas correspond to gold particles and the brighter areas correspond to voids in the crystal.

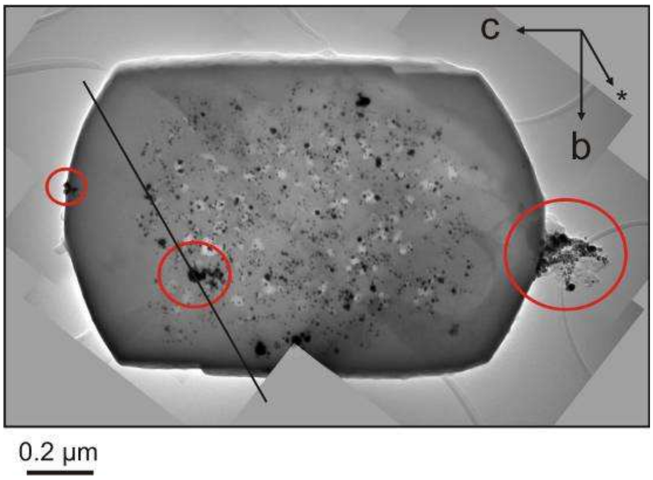

Figure 5.10: Mosaic composed of 10 TEM bright-field images showing a representative crystal as seen along the [100] zone axis. The crystal lattice is indexed based on the standard Pnma space group setting. Black represents high density regions and therefore corresponds to gold particles. Voids are observed as light regions within the silicalite-1 crystal. Red circles mark gold particles which are obviously on the surface or later shown to be on the surface of the crystals (Figure 5.11)

The very small voids in the crystal shown in Figure 5.10 are consistent with small mesoporosity measured by N_2 physisorption. The mesoporosity could result from decomposition of the linker molecules since the voids appear to be concentrated in the centre of the crystal, around the gold particles. Similar observations, that formation of metal nanoparticles induces secondary pore formation in zeolites, were reported years back, for instance for platinum nanoparticles in NaX zeolite.[226] Gold particles are seen as dark particles both in the profile view, *i.e.* on the edge of the silicalite-1 crystal perimeter and in the plane view *i.e.* in the centre of the silicalite-1 crystals. Gold particles imaged in plane view in the crystal are ca. 1-2 nm whereas those imaged in profile view at the crystal edges are significantly larger and more agglomerated.

Since a TEM image is a two-dimensional projection of the specimen, it is not possible to determine whether the small particles are located on the crystal surfaces or inside the silicalite-1 crystal. To uniquely determine the relative positions of the gold nanoparticles with respect to the silicalite-1 crystal, 3-dimensional imaging was pursued by means of bright field TEM tomography and reconstructed tomograms are shown in Figure 5.11.

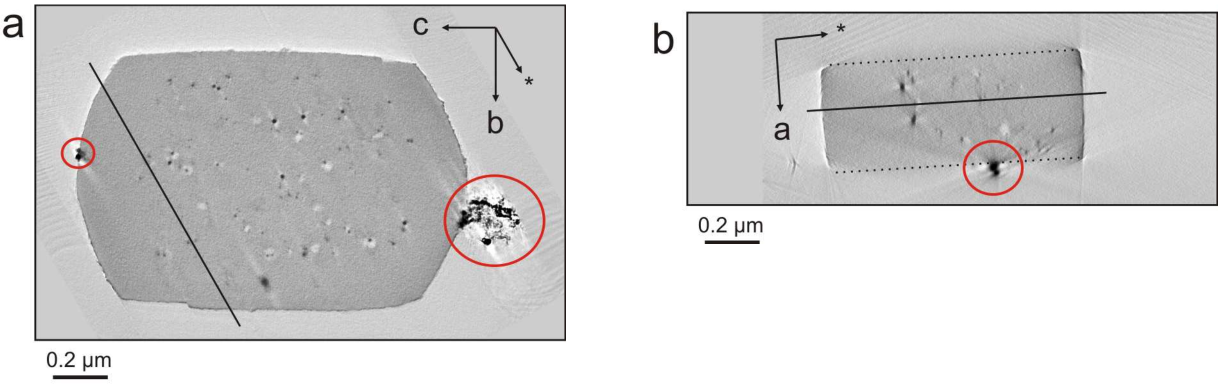

Figure 5.11 Sections through tomogram reconstruction. Images in a) and b) are tomogram sections approximately perpendicular to and parallel to the [1 0 0] zone axis, respectively. The full lines in each section correspond to the intersection of the other tomogram section. The missing wedge of the tilt series parallel to the [1 0 0] zone axis results in low contrast on crystal surfaces normal to this direction. Dotted lines have therefore been added to clearly show the position of the {1 0 0 } surfaces b). Red circles mark gold particles on the surface of the crystals (compare to Figure 5.10)

The reconstructed tomograms in Figure 5.11 show all the characteristic features observed in the TEM images in Figure 5.10. From the tomogram sections shown in Figure 5.11 it is clear that significant amounts of gold are observed inside the silicalite-1 crystal. Investigation of all tomogram sections shows that all of the gold particles shown in Figure 5.10 (except those marked by red circles) are encaged in the silicalite-1 crystal.

To investigate if the embedment stabilises the gold nanoparticles, TEM images were recorded before and after calcination in air at 550 °C for 3 h (Figure 5.12a and b). Before calcination, the majority of the gold particles are generally ca. 1 nm (Figure 5.12a). After calcination, however, the particles imaged in profile view at the edges are larger and more rounded in shape (Figure 5.12b), whereas the majority of the particles imaged in plane view in the crystal remain unaltered in size, indicating that the gold particles embedded within the silicalite-1 crystals have an enhanced stability towards sintering despite the smaller gold particles size. The sintering of the large gold crystals in the profile view could also the explained the observed increase in the gold particle size before and after calcination investigated by XRPD. Thus, the present synthesis approach yields a hybrid Au@silicalite-1 material with an enhanced sintering stability of the metal nanoparticles.

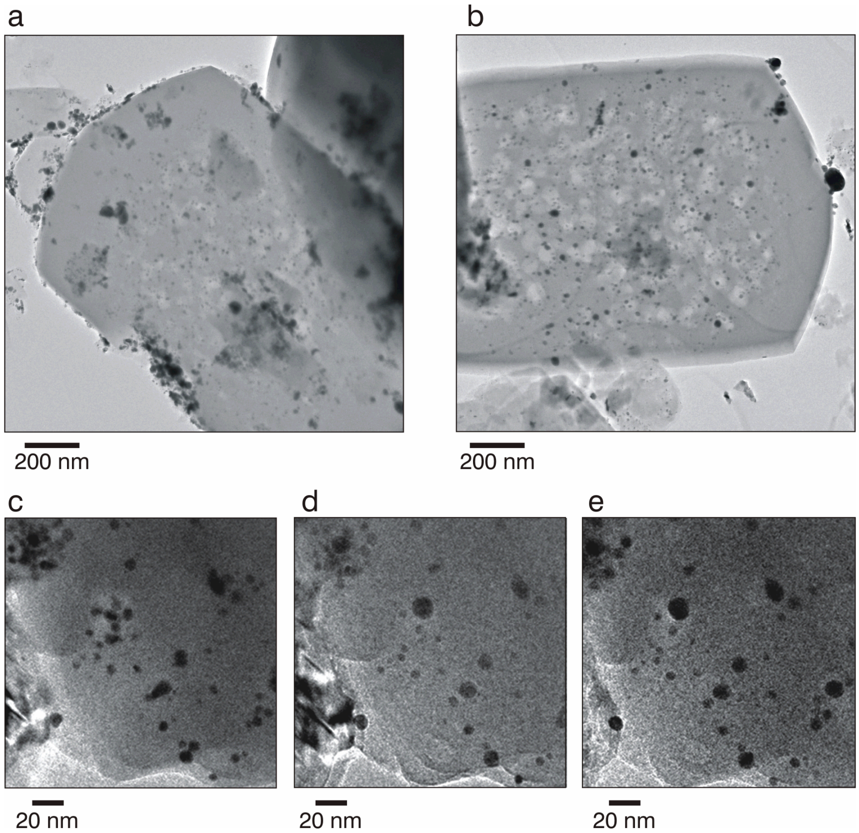

Figure 5.12: TEM images a) before and b) after calcination (550 °C, 3 h). *in situ* TEM images obtained in O_2 atmosphere at c) 25 °C, d) 300 °C and e) 500 °C

The enhanced stabilisation of the gold nanoparticles is further corroborated by a series of *in situ* TEM images (Figure 5.12 c, d and e) obtained during exposure of the material to an O_2 atmosphere at temperatures from 25 °C to 500 °C. At 25 °C, the sample area contains gold particles of different sizes (Figure 5.12c). By heating to 300 °C and further up to 500 °C, it is preferentially the larger gold particles that sinter, while the smallest particles are stable. This could be regarded as unexpected since the sintering rate of nanoparticles usually scales inversely with their size. However, in this material, the small nanoparticles are less prone to sintering because they are fixed in the zeolite crystal. On the basis of the information in Figure 5.12a and b, the *in situ* observation is fully consistent with the finding that particle embedment improves the stability towards sintering.

In summary, a hybrid material comprising 1-2 nm sized gold nanoparticles embedded in silicalite-1 zeolite crystals is prepared. During the rather time consuming preparation of the precursor material the gold nanoparticles sinter primarily due to imperfect silica coating. This results in further sintering of the gold particles during the silicalite-1 synthesis. It is shown by 3-dimensional TEM tomography that some gold particles are embedded within and some are on the external surface of the silicalite-1 crystals in the final hybrid material. Moreover, calcination experiments by both *ex situ* and *in situ* TEM indicate that the nanoparticles embedded in the silicalite-1 crystals are highly stable towards sintering, whereas the particles located at the outer surface of the zeolite tend to sinter.

5.4.3. Characterisation of Au@ZSM-5

By introducing an extra synthesis step aluminum can be incorporated in the matrix material yielding a true zeolite as matrix material. As recapitulation, the gold nanoparticles are first immobilised in amorphous silica followed by crystallisation into silicalite-1 seeds. The seeds are subsequently suspended in a ZSM-5 growth medium containing aluminum and synthesised into embedded gold nanoparticles in ZSM-5 zeolite crystals.

The XRPD analysis of the zeolite seeds containing gold yields an amorphous phase of silica and another unidentified amorphous phase. There is no evidence of gold nanoparticles which could be due to very small crystal size of the gold particles. An amorphous phase of silica is not entirely unexpected as the thin coat of silica might not crystallise into zeolite crystals. Alternatively the zeolite crystals could be so small that they resemble an amorphous phase. The XRPD pattern for the hybrid product Au@ZSM-5 together with the reference for bulk gold is shown in Figure 5.13 and is recorded prior to calcination.

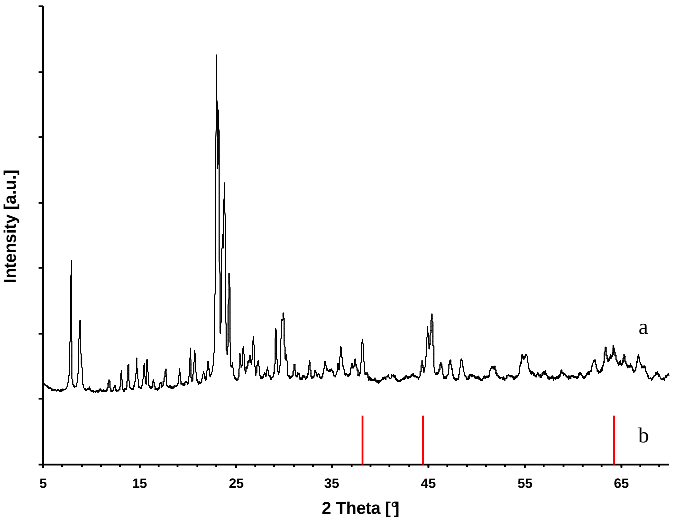

Figure 5.13: XRPD pattern for a) Au@ZSM-5 prior to calcinations and b) bulk Au

It is seen from Figure 5.13 that the Au@ZSM-5 material contains highly crystalline material with the MFI structure as well as gold particles. This indicates that by introducing the seeds into a zeolite growth medium it is possible to obtain crystalline ZSM-5 zeolites. According to the Debye-Scherrer equation the gold particles have an average particle diameter in the D[200] direction of 48 nm prior to calcination and after calcination an average particle diameter of 63 nm. The large particle diameter indicates that a large amount of the gold must have sintered during the ZSM-5 synthesis and calcination. One explanation could be that the preparation of homogeneous silica shells on the gold particles was not successful and therefore the gold could sinter during the ZSM-5 synthesis and even more during calcination. Another explanation could be that the ZSM-5 growth medium is too alkaline and could dissolve the seeds prior to ZSM-5 growth. Future studies on the homogeneous shells using longer reaction times for the preparation of seeds or other conditions for the ZSM-5 zeolite growth might prove prudent at reducing the average particle size of gold. The significant increase of the average particle size of gold also indicates that not all gold is encapsulated in the zeolite crystals but is instead present on the external surface.

In Table 5.2 is given the gold content from elemental analysis together with the results from N_2 physisorption measurements.

Table 5.2: Au content determined from elemental analysis together with the surface area and micropore and mesopore volumen for the hybrid Au@ZSM-5 material. Au content and N_2 physisorption measurements are recorded after calcination

	Au content [wt%]	Surface area [m^2/g]^a	Micropore volume [cm^3/g]^b	Mesopore volume [cm^3/g]^c
Au@ZSM-5	3.34	285	0.11	0.02

determined by ^{a} the BET method, ^{b} the t-plot method and ^{c} the BJH method (adsorption)

The gold content in Au@ZSM-5 is significantly higher than that of Au@silicalite-1 material (3.34 wt% versus 1.37 wt%) demonstrating that it is possible to introduce a higher amount of gold by the second synthesis route. The higher amount of gold is believed to be due to a loss of either gold during Au@silicalite-1 synthesis or loss of zeolite precursor during Au@ZSM-5 synthesis. The surface area of the Au@ZSM-5 is rather low compared to Au@silicalite-1 which might be due to blockage of the micropores of the gold nanoparticles or the presence of a small amount of amorphous material. The latter, however, seems contradicted as the XRPD pattern shows only crystalline zeolite and gold. The micropore volume lies in the range of previous result for conventional zeolites, though in the lower end of the interval. The mesopore volume is very low which illustrates that the hybrid material is purely microporous. The surface area and micropore volume for the Au@ZSM-5 show that the embedment of the gold particles in the material is not expected to influence its performance as a conventional zeolite in respect to size selectivity.

Representative SEM images of the Au@ZSM-5 zeolite are shown in Figure 5.14 and the images are recorded using both the secondary and backscatter detector. By using the backscatter detector the gold particles will appear as bright spots. SEM is recorded after calcination.

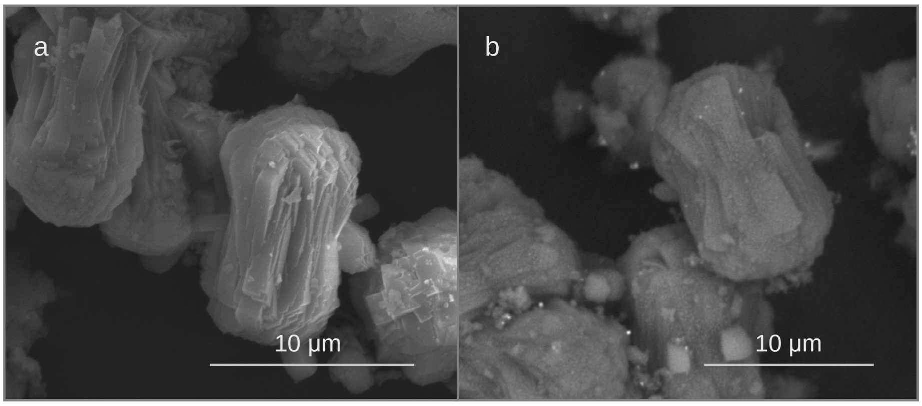

Figure 5.14: Representative SEM images of the Au@ZSM-5 using a) the secondary and b) the backscatter detector. The images are recorded after calcination

From the SEM images in Figure 5.14 it can be seen that the size of the ZSM-5 zeolite crystals is significantly larger than the silicalite-1 crystals. The ZSM-5 crystals are around 10 µm and have a less distinct smooth morphology than the previous Au@silicalite-1 material although the overall morphology is still coffin shape-like. The differences in size and morphology are ascribed to the differences in the synthesis procedures. From the SEM image obtained using the backscatter detector (Figure 5.14 b) it can be seen that high reflecting gold is present on the zeolite surface. It should be emphasized that the resolution of the SEM images does not allow for detection of the small gold particles and the conclusions are only based on the larger particle agglomerates. The ratio of silica to aluminum in the zeolite is estimated by EDS measurement to be 14. This shows that the expanded synthesis results in a zeolite which may be made acidic by ion exchange making a bi-functional catalyst. However, in the present study the catalytic reaction is primarily used to prove the active gold nanoparticles are embedded in the zeolite crystals and therefore the potential bi-functionality is not utilised. This is left for future work.

To investigate the size of the gold particles and whether the gold particles are only on the external surface of the ZSM-5 zeolite crystals or also embedded in the zeolite crystals TEM tomography should be used. However, it is not possible to conduct a TEM investigation due to the large ZSM-5 crystals. One attempt was pursued to cut the product into a lamella thin enough for TEM investigation. This technique uses a focused beam FIB that cuts through the crystal with great accuracy and the produced lamella has to be lifted out using an electrostatic charged glass rod and place it on a copper grid for further TEM characterisation. This was done by hand as an *in situ* lift-out instrument was not available. Unfortunately the lamella was lost either during handling or the actual lift out.

In summary, it is possible to prepare a hybrid material comprising gold particles dispersed in ZSM-5 zeolite crystals. This synthesis entails an extra synthesis step compared to the preparation of the hybrid Au@silicalite-1 material and consists of three steps. Firstly, the gold particles are coated with amorphous silica followed by crystallisation of the silica into zeolite seeds and subsequently zeolite growth in a zeolite synthesis gel containing aluminum. During the zeolite growth the gold particles severely sinter which could be due to inadequate coating of the gold particles with amorphous silica or too harsh zeolite growth conditions which might dissolve the silica. The obtained zeolite crystals are significantly larger than the silicalite-1 crystals and have at the same time a less smooth morphology. Due to the large zeolite crystals it is not possible to conduct TEM investigations to indisputable prove if the gold nanoparticles are embedded in the ZSM-5 zeolite crystals rather than just present on the external surface of the zeolite crystals. By introducing the extra synthesis step it is though possible to introduce aluminum into the MFI structure producing a potential bi-functional catalyst. This synthesis may be expanded to introduce other types of elements than aluminum in the zeolite structure and could further be expanded to other zeolite structures than MFI.

5.4.4. Catalytic oxidation of aldehydes

Catalytic experiments are performed in order to verify that the encapsulated gold nanoparticles are in fact embedded in the zeolite matrices and accessible only though the micropores of the zeolites. It is well-known that gold nanoparticles can oxidise aldehydes to esters.[227, 228] The prepared materials Au@silicalite-1 and Au@ZSM-5 are both tested in the size-selective oxidation of benzaldehyde and 3,5-dimethylbenzaldehyde and the reaction schemes are given in scheme 5.1.

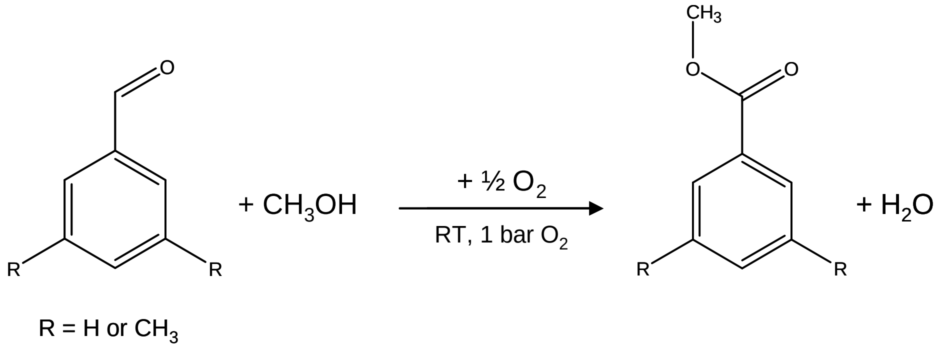

Scheme 5.1: Reaction scheme for the catalytic test reaction using two different reagent: R = H the istericly unhindered benzaldehyde and R = CH_3 the stericly hindered 3,5-dimethylbenzaldehyde

The chemical behaviour of benzaldehyde corresponds largely to that of aliphatic aldehydes[229] which make the oxidation of benzaldehyde a suitable model reaction of organic aldehydes in general. At the same time the oxidising agent is air, a cheap and abundant resource, which makes it a “green” oxidation method.[227, 230] The benzaldehyde should be able to diffuse into the zeolite crystals via the ~0.55 nm large micropores and be oxidised at the surface of the embedded gold particles. However, the more bulky 3,5-dimethylbenzaldehyde molecules can only be oxidised on gold nanoparticles located on the external surface of the zeolite crystals. If the two hybrid materials can oxidise benzaldehyde and not 3,5-dimethylbenzaldehyde catalytic active gold nanoparticles below 10 nm must be embedded in the zeolite crystals yielding a size-selective oxidation catalyst. The activity measurements are illustrated in Figure 5.15.

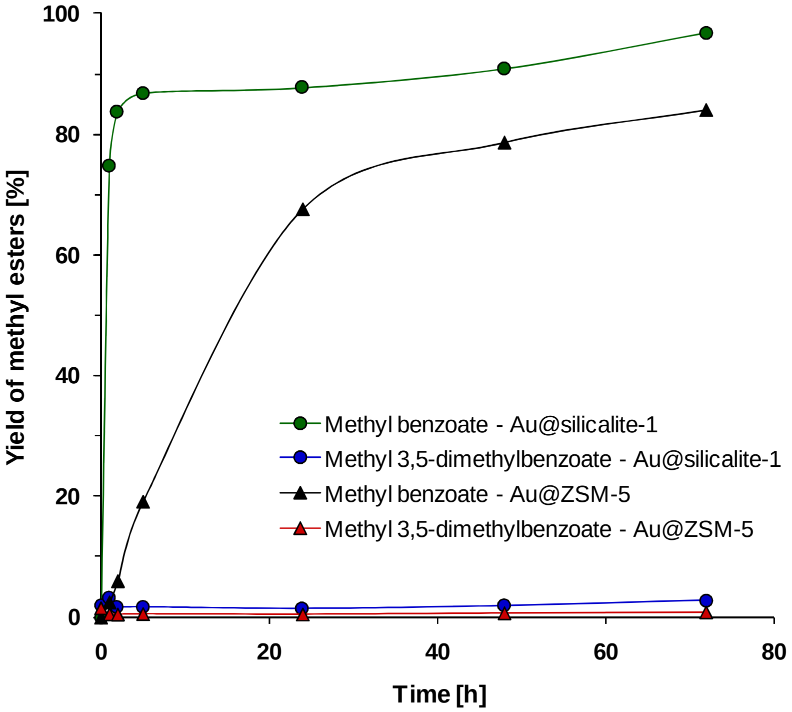

Figure 5.15: Gold catalysed oxidation of benzaldehyde and 3,5-dimethylbenzaldehyde in methanol to form the methyl esters. The yield is plottet as a function of time and the catalytic tests were carried out in an open flask at room temperature, atmospheric pressure and with the following ratios: 5 Aldehyde ; 600 CH_3OH ; 1 $NaOCH_3$ and with 0.1 mol% Au@MFI

Figure 5.15 reveals that both Au@silicalite-1 and Au@ZSM-5 are able to catalyse the oxidation of benzaldehyde giving yields of 97% and 84%, respectively. Au@silicalite-1 reaches full conversion (>99%) after 5 hours whereas Au@ZSM-5 reaches full conversion after 72 hours. For both hybrid materials the major by-product is benzoic acid. In the case of 3,5-dimethylbenzaldehyde the activities of the two catalysts are orders of magnitude lower resulting in yields of <3 %. A reference experiment was carried out using a commercial Au on TiO_2 (Mintek, 1 wt%) as catalyst. These experiments showed no size-selectivity and was highly cable of oxidising both benzaldehyde and 3,5-dimethylbenzaldehyde and full conversion was reached after 1-2 hours. Bearing in mind that conversion depends on the amount of aldehyde disappearing from the reaction mixture the difference in conversion and selectivity can be due to mass-transfer limitations. Using the commercial Au/TiO_2 no diffusion limitation is present and the reaction is expected to proceed rather fast. Using the Au@silicatlite-1 or Au@ZSM-5 it is plausible that longer reaction time is needed to reach full conversion due to diffusion limitations in the micropore system. Some of the aldehyde or ester could also be trapped inside the micropore system of the zeolite. If this is the case the trapped aldehydes would be taken into account in the conversion since they are not present in the reaction mixture. On other hand the trapped esters would not be encountered in the selectivity as they are not measurable. It is also reasonable that the two hybrid materials have different mass-transfer limitations since a significant difference regarding the crystal size exists. Another explanation for the difference in selectivity is the difference in the presence of water. The major bi-product for both reactions is benzoic acid. Benzoic acid can be formed from oxidation of benzaldehyde or substitution of the methyl benzoate, both requiring water. It is reasonable that the Au@ZSM-5 contain more water in the micropore system comparing to Au@silicalite-1 since the presence of aluminum in the zeolite framework makes it more hydrophilic. Since none of the hybrid materials are dried prior to catalytic tests it is expected that the materials inherently contain water.

The catalytic results prove that the embedded gold nanoparticles are accessible and catalytic active through the zeolite micropores since it is possible to oxidise benzaldehyde. Furthermore, since it is almost impossible to oxidise the more bulky 3,5-dimethylbenzaldehyde it is the embedded gold particles which are catalytically active and that surface gold plays a very minor role if any. The catalytic results also show that the gold nanoparticles are active even after calcinations at 550 °C. Hereby, it is verified that the gold nanoparticles are sinter-stable in both hybrid materials when encapsulated.

5.5. Conclusion

In the present chapter it was shown that a hybrid material comprising 1-2 nm sized gold nanoparticles embedded in silicalite-1 crystals can be prepared. The synthesis involved firstly coating gold nanoparticles by amorphous silica followed by crystallisation of the amorphous silica into silicalite-1 crystals. The rather time consuming coating with amorphous silica did not work as intended creating gold nanoparticles dispersed in a silica matrix rather than creating perfect spheres. As a consequence sintering could not be avoided during the silicalite-1 synthesis. Future work should therefore involve optimisation of the coating procedure to yield a more homogeneous coating which might minimise the amount of sintering during the silicalite-1 synthesis. TEM tomography was used to indisputably prove that some gold nanoparticles were embedded within and some were on the external surface of the silicalite-1 crystals in the final hybrid material. By the use of calcination experiments obtained both *in situ* and *ex situ* TEM indicated that the gold nanoparticles embedded in the silicalite-1 crystals are highly stable towards sintering, whereas the particles located at the outer surface tend to sinter.

It is also shown that the implementation of an additional synthesis step allows for introduction of aluminum in the matrix yielding a hybrid material comprising gold nanoparticles distributed in ZSM-5 zeolite crystals. The two hybrid materials obtained differed though in size and morphology which is ascribed the difference in synthesis procedures. The incorporation of aluminum in the zeolite structure allows for tuning the zeolite matrix producing a potential bi-functional catalyst. The synthesis could therefore be further expanded to introduce other types of elements in the zeolite matrix and by the use of other templates in the crystallisation of zeolite crystals or seeds the amount of zeolite or zeotypes hybrid material seems almost to be infinite. This is an obvious choice to pursue in future work.

Furthermore, both hybrid materials were tested in the aerobic oxidation of benzaldehyde and 3,5-dimethylbenzaldehyde in methanol. It was shown that the gold nanoparticles were encapsulated in both hybrid materials and were only accessible through the micropores, since it was not possible to oxidise 3,5-dimethylbenzaldehyde whereas benzaldehyde was readily oxidised. The catalytic experiments also demonstrate that both hybrid materials were sintering-stable materials since they were catalytic active after calcinations at 550 °C. Hybrid materials such as these might find application as sinter-stable and size-selective nanoparticle catalysts or in other areas of material science.

Chapter 6

New HDS catalyst by anchoring molecular $CoMo_6$ species on mesoporous ZSM-5

This chapter contains synthesis, characterisation and catalytic test of anchored molecular $CoMo_6$ species on mesoporous ZSM-5. The $CoMo_6$ species were also just impregnated on mesoporous ZSM-5 to investigate if the anchoring improves the catalytic activity for HDS catalysis due to an improved dispersion of the catalytic active species.

As preparation of relevant reference materials for comparison is not straightforward this chapter is primarily a presentation of the theory and experiment of anchoring species on zeolites. Some activity and characterisation data will be presented and the results look promising, but a full understanding of the potential of the method will require further work.

6.1. Introduction

With the growing awareness that crude oil is a finite resource, it is a very important task to try to utilise it as effectively as possible whilst limiting its environmental impact. Catalytic hydrotreating is an important process in petroleum refining used to remove typically > 99 % of natural contaminants such as sulfur, nitrogen, oxygen and metals from the hydrocarbon matrix by the use of hydrogenation.[231] If the contaminants are not removed environmental issues, such as acid rain and smog can arise.[232] Hydrotreating is done prior to processes such as catalytic reforming and catalytic cracking, as the contaminants can severely affect the catalysts, the equipment, and the quality of the final products as they travel though the refinery processing units.

The role of the hydrotreating catalyst is primarily to remove sulfur, nitrogen and aromatics present in the refinery streams by promoting hydrodesulfurisation (HDS), hydrodenitrogenation (HDN) and hydrogenation (HYD) reactions, and examples hereof are shown in Figure 6.1.

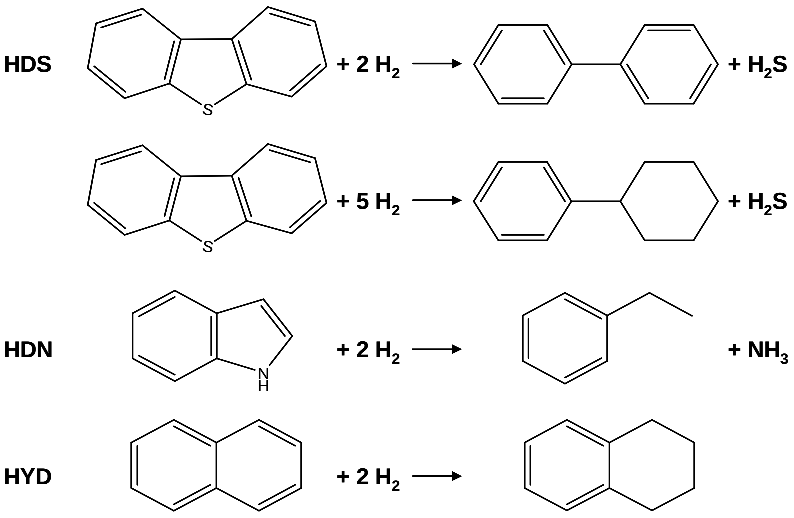

Figure 6.1: Examples of hydrotreating processes

In particular HDS of petroleum feedstocks has become more and more important to protect the environments by producing sulfur-free fuels. Environmental regulations have been introduced in many countries around the world to reduce the sulfur content of *e.g.* diesel fuel to ultra low levels (10 ppm) with the aim of lowering the diesel engine's harmful exhaust emission and improving air quality.[233] Sulfur can be present in crude oil in many forms *e.g.* thiols (mercaptans), sulfides, disulfides, thiophenes and thiophenic compounds containing both benzo- and dibenzothiophene structures. The sulfur content of crude oil varies significant with their origin and may be as low as 0.1 wt% but may increase up to 2-5 wt%.[231]

Catalysts consisting of molybdenum supported on high surface area support and promoted with cobalt or nickel are traditionally used in hydrotreating processes. Typical support materials in industry are alumina and silica-alumina, while silica, zeolites, kieselguhr and magnesia have been and is explored in research. Usually the surface areas are in the range of 100 to 300 m^2/g. The metals are added to the support by impregnation yielding a final composition of metals with 8-16 wt% molybdenum and 1-4 wt% cobalt or nickel.[231] The choice of catalyst type and the type of feed varies according to the application, desired activity and the process conditions for a given reaction. Often CoMo catalysts are chosen as HDS catalysts rather than the NiMo counterpart. Dibenzothiophene is an important structure in HDS of diesel fuel and Figure 6.1 shows that there exist two different products depending on whether the sulfur atom is directly abstracted from dibenzothiophene or takes place due to prehydrogenation of the polyaromatic compound. CoMo catalysts are better than NiMo catalysts, to directly remove sulfur from dibenzothiophene. The use of CoMo catalysts therefore entails lower direct hydrogen consumption and is often the preferred choice as industrial catalyst.[231]

The active sites and the mechanism for the HDS have been characterised through various studies.[234-237] The catalytic active species is Co-Mo-S nanoparticles whose structure is based on MoS_2. This means the catalyst has to be sulfided before achieving the active state. The molybdenum disulfide is present as single or multi-layer S-Mo-S slabs with an average size of 2-3 nm under operating conditions[231, 238, 239], see Figure 6.2.

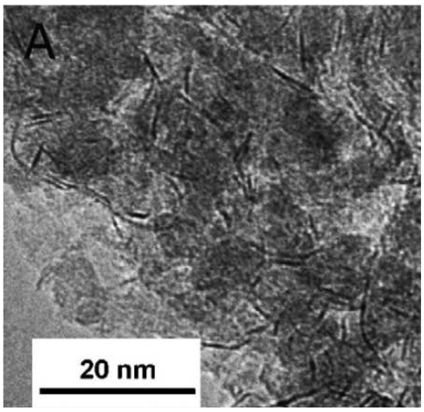

Figure 6.2: HRTEM of supported Co-Mo-S catalysts. Adapted from [239]

Only a small amount of cobalt or nickel relative to the amount of molybdenum is needed to increases the activity by more than an order of magnitude. Cobalt can be present in three different phases in the catalyst (Figure 6.3a); cobalt sulfide, incorporated in the support or the catalytically active Co-Mo-S nanoparticles. The active Co-Mo-S nanoparticles have a MoS_2-like structure into which cobalt atoms are incorporated. More precisely the MoS_2 nanoclusters are found to adopt an almost hexagonal shape with cobalt atoms preferentially located at the edges of the MoS_2 single layers[235], as illustrated in Figure 6.3b.

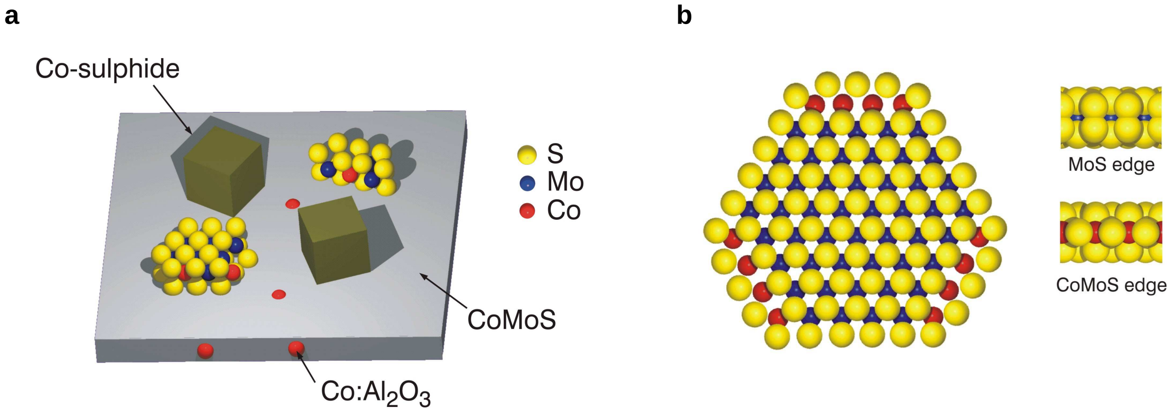

Figure 6.3: a) Illustration of the nanoparticles in a sulfided Co-Mo catalyst and b) ball model of the Co-Mo-S active specie. Adapted from [235]

It is only the edges that are catalytically active. The basal plane sites have no activity and it has been proposed that the cobalt atoms located at the edge positions create new and more active sites such as vacancies compared to unpromoted MoS_2.[235, 238, 239]

As sulfur specifications in transport fuels keeps going down it is a constant challenge for the industry to have sufficient activity to desulfurise diesel feed streams to even lower sulfur levels.[240] With traditional catalyst types this requires severe operating conditions, such as high temperature, low space velocity and high hydrogen partial pressure. Such severe processing conditions generally lead to rapid catalyst deactivation, shorter cycle times and reduced throughput. The development and application of more active and stable catalysts is therefore desirable. One possibility is to investigate other support materials. The support has to provide a high surface area to maximise the active nanoparticle dispersion and should at the same time give the catalyst mechanical strength. Alumina is the most widely used support material in hydrotreating catalysis because it combines the high surface area and high mechanical strength. Additionally, the porosity can easily be tuned and it is relative inexpensive. Despite these advantages great interest has still been shown in new supports for HDS catalysts.[241, 242] Among others, both conventional and mesoporous zeolites have been tested as supports.[243, 244] and showed promising results.

Usually the precursor to catalytically active species is impregnated onto the support. In this work the aim is to anchor molecular $CoMo_6$ species on mesoporous ZSM-5 zeolites to obtain a better dispersion of the catalytically active specie. As a reference, the molecular $CoMo_6$ species are also introduced to mesoporous ZSM-5 by simple impregnation to investigate if the anchoring improves the catalytic activity in HDS due to an improved dispersion.

6.2. Synthesis strategy

Typically, HDS catalysts are prepared by pore volume impregnation of dissolved metal salts onto a porous alumina support and during calcination surface metal oxides are formed. During the preparation critical factors influence the catalytic activity, *i.e.* size of the formed metal oxides, dispersion of the metal oxides, and stoichiometry of the metals. One way to control the metal oxides is to use small metal oxides with well-defined stoichiometry such as polyoxometalates (POMs). POMs are polyatomic ions, usually anions that consist of three or more transition metal oxyanions linked together by shared oxygen atoms to form a large, closed 3-dimensional framework[245]. The framework of transition metal oxyanions may enclose one or more hetero atoms sharing neighbouring oxygen atoms with the framework, see Figure 6.4.

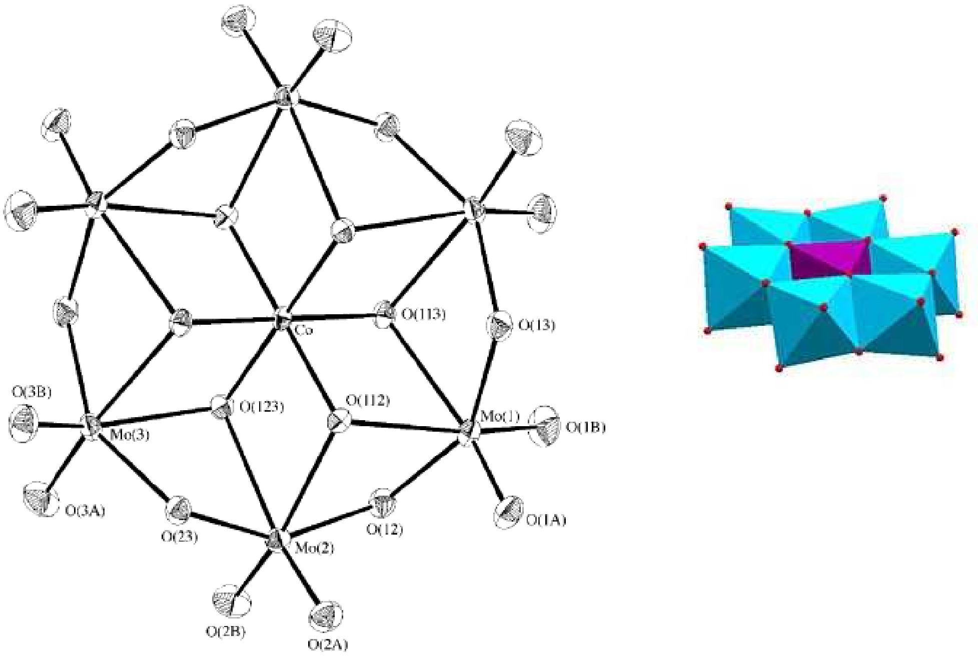

Figure 6.4: View of a polyoxometalate, $[H_6CoMo_6O_{24}]^{3-}$. Adapted from [246]

Using POMs as metal sources for HDS catalysts could enhance the probability to form the active Co-Mo-S nanoparticle after sulfidation as the promoter metal is introduced directly with the catalytically active metal. The chosen POM is $[H_6CoMo_6O_{24}]^{3-}$ which is a hexanuclear metal oxide, referred to as an Anderson ion[247]. The Anderson ion exhibit a characteristic planar configuration and consists of a central CoO_6 octahedron edge-shared by surrounding six MoO_6 octahedra in a hexagonal arrangement, see Figure 6.4. The six central oxygen atoms surrounding the cobalt(III) are bound to six non-acidic hydrogen atoms (not shown in Figure 6.4). Besides containing crystal water the chosen compound also contains a number of cations to achieve charge neutrality. The total formula is thus $Na_3[Co(OH)_6Mo_6O_{18}]\cdot 8H_2O$. The use of this Anderson ion entails a quite desirable ratio between cobalt and molybdenum, creating the possibility to produce a catalyst with 1 wt% cobalt and ~10 wt% molybdenum.

To improve the dispersion of the final active Co-Mo-S nanoparticle the idea is to anchor the molecular $CoMo_6$ species onto a mesoporous ZSM-5 zeolite surface. Previous mesoporous amorphous materials such as MCM-41 and SBA-15 have been used as supports for immobilisation of several catalysts.[248-253] Here, zeolites are chosen as a support as they in general have higher thermal and chemical stability than the mesoporous silicas[208] and still feature large surface areas. The mesopore walls in hierarchical zeolites are composed of microporous crystalline zeolite frameworks which are terminated with silanol groups at the wall surface. These silanol groups make it possible to functionalise the surface with various alkoxysilanes which can be used as a linkers to anchor different types of molecules[254] *i.e.* POMs. Due to the large mesopore surface area the amount of silanol groups is very high compared with that on the external surface of conventional zeolite crystals. In addition, in conventional zeolites the solely microporous structure makes the incorporation of bulky moieties difficult also micropores are too small for reactant and product diffusion. Therefore, mesoporous zeolites are chosen as support rather than conventional zeolites. In addition, if the prepared functionalised ZSM-5 material is active as a HDS catalyst it might be possible to use the same catalyst is two different reactions, first, as a HDS catalyst and afterwards or simultaneously as *e.g.* a hydrocracking catalyst due to the zeolites acidity.

The chosen linker molecule is (3-aminopropyl)trimethoxysilane (APTMS) and the organic functionalisation of the mesoporous zeolite is illustrated in Figure 6.5.

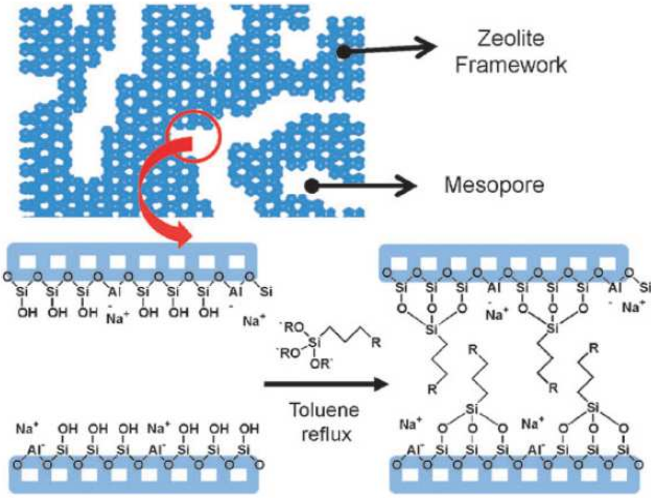

Figure 6.5: Organic functionalisation of mesoporous zeolites. Using APTMS as linker R corresponds to NH_2 and ´R corresponds to CH_3. Adapted from [254]

The reaction between mesoporous zeolite silanol groups and alkoxysilanes is carried out by refluxing in toluene solution containing APTMS, as previous reported by Lee *et al.*[254]. Even though Lee *et al.* found that the reactions were completed after 3 hours the solution was left overnight to ensure complete functionalisation.

The grafting mechanism of APTMS is reported[255] to proceed through the flip mechanism shown in Figure 6.6.

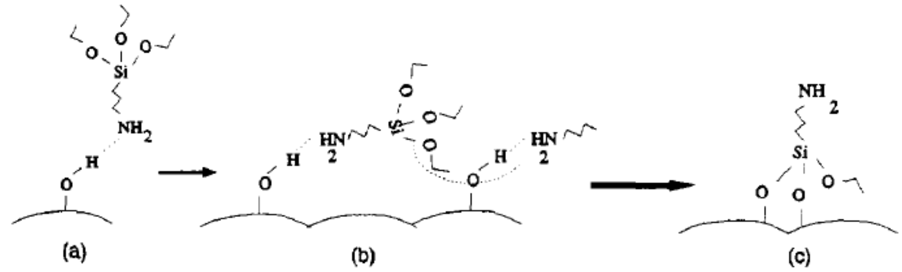

Figure 6.6: Grafting of APTMS by the flip mechanism through a) physisorption, b) condensation and c) curing. Adapted from [255]

In the first step, Figure 6.6a the APTMS is adsorbed by hydrogen bonding of the amine to the surface hydroxyl group. After adsorption the amine group can catalyse the condensation of the silicon side of the silane molecule with a surface silanol and form a covalent siloxane bond. In this step three methanol groups are formed and subsequently removed. The aminosilane molecule turns from the original amine-down position in the reaction phase, Figure 6.6a, towards an amine-up position after condensation, Figure 6.6b and c and is thus called the flip mechanism.

After modifying the surface with APTMS the material is treated with hydrochloric acid to convert the amine group into the corresponding hydrochloric salt. Hereafter, it is possible to attach the Anderson ion to the surface by ion exchange as illustrated in Figure 6.7.

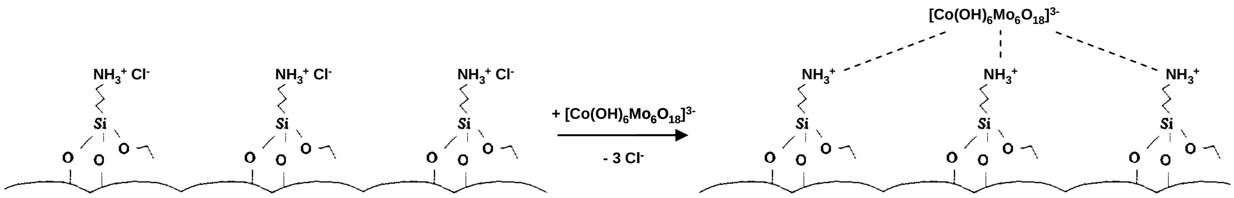

Figure 6.7: Anchoring of molecular $CoMo_6$ specie to the mesoporous zeolite by ion exchange

Reference sample was obtained by simple dissolving $Na_3[H_6CoMo_6O_{24}]$ in water and impregnated on mesoporous ZSM-5. The aim is to prepare both types of catalysts (anchored and impregnated) with 1 wt% Co and ~10 wt% Mo.

The prepared catalysts were tested for HDS activity. Due to the complexity of natural oil in terms of hydrocarbon matrix and the various sulfur compounds present, the use of real oil in these screening experiments has been avoided. As a model activity test reaction the conversion of dibenzothiophene (DBT) is chosen, as it is a representative sulfur compound in real oil and is here used in its pure form dissolved in a matrix of a pure hydrocarbon, *in casu n*-heptane. Besides containing 3 % DBT, the model oil also contains 0.5 % indole, 1 % naphthalene and 2.5 % dimethyldisulfide in n-heptan to mimic real oil. Using this feed it is also possible to investigate HDN and HYD but in this work the focus is on the performance of the catalysts in HDS. Dimethyldisulfide is present in the model feed to keep the catalyst in a fully sulfided state. Thus DMDS decomposes in the presence of H_2 much below reaction temperature to create a partial pressure of H_2S inside the reactor.

Prior to catalytic test the materials need to be activated to the sulfided form by exposure to a stream of dimethylsulfide dissolved in n-heptane to sulfide the precursor catalysts. This activation is conveniently performed *in situ* in the test reactor before the actual activity test.

6.3. Experimental

All reagents were of reagent grade and used without any further purification: Sodium molybdate dihydrate ($Na_2MoO_4{\cdot}2H_2O$, ≥99.5 wt%, Sigma-Aldrich), nitric acid (HNO_3, 65 wt%, Sigma-Aldrich), cobalt(II) sulfate heptahydrate ($CoSO_4{\cdot}7H_2O$, 99 wt%, Sigma-Aldrich), sodium peroxodisulfate ($Na_2S_2O_8$, ≥99 wt%, Aldrich), sodium hydroxide (NaOH, 99 wt%, Riedel-de Häen), ammonium nitrate (NH_4NO_3, 99.5 wt%, Merck), ammonia (NH_3, 25 wt%, Fluka), toluene (C_7H_8, 99.7 wt%, Fluka), (3-aminopropyl)trimethoxysilane (APTMS, 97 wt%, Aldrich), hydrochloric acid (HCl, 37 wt%, Sigma-Aldrich).

6.3.1. Synthesis of $Na_3[Co(OH)_6Mo_6O_{18}]\cdot 8H_2O$

$Na_3[Co(OH)_6Mo_6O_{18}]$ was synthesised according to Nolan *et al.*[246] using the following procedure:

> *First, 30.26 g $Na_2MoO_4{\cdot}2H_2O$ was dissolved in 50 ml H_2O and acidified to pH 4.51 with HNO_3 (65 wt%). In another beaker 5.75 g $CoSO_4{\cdot}7\ H_2O$ was dissolved in 10 ml H_2O and then added to the molybdate solution under stirring. A solution of 7.53 g $Na_2S_2O_8$ dissolved in 8.8 ml H_2O was then added to the Co/Mo mixture as an oxidising agent. The obtained solution was heated to reflux until a dark turquoise solid precipitated. Upon further refluxing, the precipitate was redissolved and the original red colour of the solution returned. Following this, the solution gradually turned dark green, a color change indicating oxidation of the cobalt (II) to cobalt (III). Boiling was continued until evolution of oxygen ceased, by which time the solution was permanently dark turquoise. Finally the hot solution was filtered and the filtrate was left to precipitate dark green crystals upon cooling and consecutive evaporation of the solvent. The product is referred to as $CoMo_6$.*

6.3.2. Synthesis of mesoporous ZSM-5

The mesoporous ZSM-5 was prepared by desilication of a commercially available zeolite using the following procedure:

> *A 0.3 M NaOH solution was used to desilicate the PZ-2/100 ZSM-5 zeolite in the ratio 33 ml per gram zeolite materal for 30 min at 70 °C. The selective silicon leaching was stopped by quenching the solution on, and then washed three times with water by centrifugation. The desilicated ZSM-5 was dried*

overnight at room temperature before further treatment. To obtain the ammonium form of the desilicated sample two consecutive ion exchange steps were carried out using a 1.7 M NH_4NO_3/0.94 M NH_3 buffer solution with 10 ml solution per gram zeolite, at 80 °C under stirring for 2 hours. After each exchange, the NH_4-form of the zeolite was isolated by filtration, washed with water and dried in air at 110 °C. After the last ion exchange, the H-form of the desilicated zeolite was finally obtained by calcining the NH_4-form in air to 550°C for 3 h.

6.3.3. Anchoring $CoMo_6$ on mesoporous ZSM-5

The molecular $CoMo_6$ species were anchored on the mesopores surface of mesoporous ZSM-5 using following procedure:

Mesoporous ZSM-5 was functionalised with (3-aminopropyl)trimethoxysilane (APTMS) by suspending 4 g of mesoporous ZSM-5 in 160 ml toluene, heating to 65°C and adding 11 g APTMS. The suspension was stirred overnight, filtered and the obtained product washed with toluene and dried at room temperature.

Before anchoring of the molecular $CoMo_6$ species 2 g of functionalised mesoporous ZSM-5 were stirred overnight in 150 ml 3 M HCl, filtered and left for drying at room temperature.

Finally the $CoMo_6$ was attached to the mesoporous ZSM-5 by ion exchange. The mesoporous ZSM-5 was added to a solution of 0.323 g $Na_3[Co(OH)_6Mo_6O_{18}]$ in 60 ml H_2O and pH was adjusted to 4.18 with HNO_3 (65 wt%). Then, 1.5 g functionalised and acidified mesoporous ZSM-5 was added and the mixture was stirred overnight. After stirring for 12 h, the solid was filtered off, washed with water and dried at room temperature. The product was named $CoMo_6$-ZSM-5_anc.

6.3.4. Impregnation of $CoMo_6$ on mesoporous ZSM-5

The impregnated reference material was prepared in the following way:

A solution of 0.095 g $Na_3[Co(OH)_6Mo_6O_{18}]\cdot 8H_2O$ dissolved in 0.7 g H_2O was firstly prepared. After drying 0.36 g mesoporous ZSM-5 powder was impregnated with the obtained solution and left for drying at 110 °C overnight. The obtained product was named $CoMo_6$-ZSM-5_imp

6.3.5. Catalytic HDS test

The HDS test reaction was conducted using the following conditions:

Catalytic testing was performed in a fixed bed reactor charged with 300 mg catalyst in the fraction 600-850 µm. To achieve a steady flow the catalyst was mixed with Ballotini glass balls (150-250 µm) until a final volume of 1 ml was obtained. Prior to catalytic test the catalyst was sulfidised in a flow of 2.5 % DMDS dissolved in n-heptane at 350 °C and 50 bar for 4 hours. Helium was used as a carrier gas with a flow of 250 Nml/min[*] and the sulfidation gas flow was 0.3 ml/min.

After 4 hours of sulfidation the feed was changed to the model oil feed. The catalytic reaction was also performed at 350 °C, 50 bar and using helium as a carrier gas with a flow of 250 Nml/min. The employed feed rate of oil was 0.3 ml/min and the total WHSV was 68 h^{-1}. The products from the reaction were analysed by an on-line GC equipped with a FID and using n-nonane as an internal standard. The reaction was allowed to stabilise over 4 hours to obtain steady state conditions after changing to the oil feed prior to catalytic measurements. Afterwards eight GC analyses of the product stream were made with 1 hour intervals.

---

[*] Nml = normal ml = volume at 1 bar and 25°C

The activity was determined as a pseudo first order rate constant, k which is calculated on the basis of the 8 measured conversions of DBT. The rate constant k was calculated using the equation for the first order rate law (Eq. 6.1) and the correlation between residence time t and WHSV:

$$ln\left(\frac{[DBT]}{[DBT]_0}\right) = -kt \Leftrightarrow ln\left(\frac{[DBT]_0 - conv.\cdot[DBT]_0}{[DBT]_0}\right) = -kt \Leftrightarrow ln(1-conv.) = -kt \qquad \text{(Eq. 6.1)}$$

where [DBT] is the concentration of DBT at the time t, $[DBT]_0$ is the concentration of DBT at the time t=0 and conv. is the fractional conversion of DBT.
At steady state conditions the catalyst produces a product stream of steady composition. The time t in the first order kinetic equation is therefore the residence time of the feed in the reactor. This residence time is equal to the reciprocal Weight Hourly Space Velocity (WHSV) defined as:

$$WHSV = \frac{flow \times feed\ density}{catalyst\ mass} \qquad \text{(Eq. 6.2)}$$

and thus get:

$$k = -WHSV \cdot ln(1-conv.) \qquad \text{(Eq. 6.3)}$$

6.4. Results and discussion

XRPD was used to verify the crystal structure of the $CoMo_6$ precursor compound and of ZSM-5 before and after desilication. Furthermore, ZSM-5 before and after desilication were characterised using SEM and N_2 physisorption. The cobalt and molybdenum contents of the prepared catalysts were determined using elemental analysis after calcination at 500 °C for 3 hour with a heating ramp of 2 °C/min. To investigate whether or not APTMS was grafted to the surface of mesoporous ZSM-5 TGA combined with DSC was performed. In addition, the spent catalyst of the anchored version was investigated by TEM and XRPD. Both prepared catalyst materials were tested in HDS at 350 °C and 50 bars.

The obtained XRPD pattern for the $CoMo_6$ precursor compound is shown in Figure 6.8 together with the XRPD patterns for ZSM-5 before and after desilication.

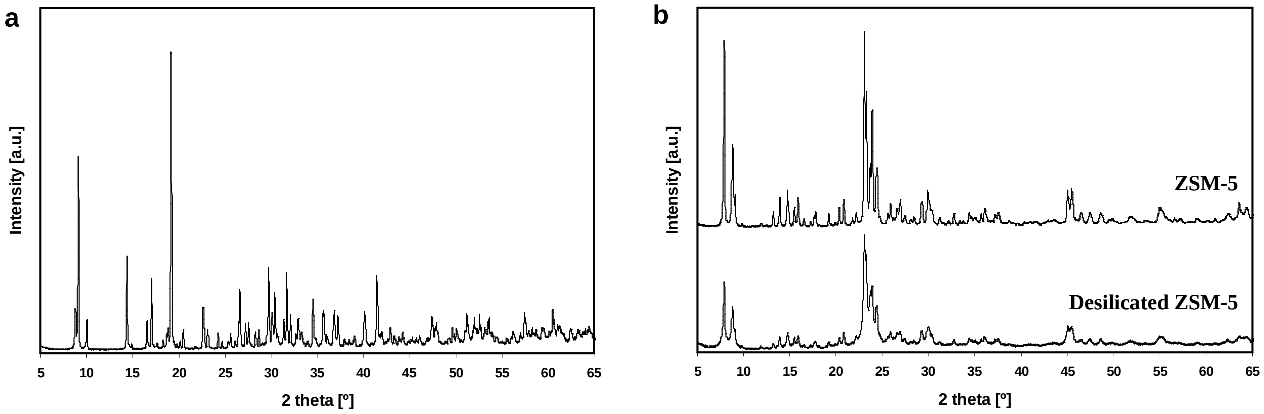

Figure 6.8: XRPD patterns of a) $Na_3[Co(OH)_6Mo_6O_{18}]\cdot 8H_2O$ and b) ZSM-5 before and after desilication

As seen in Figure 6.8a the prepared $Na_3[Co(OH)_6Mo_6O_{18}]\cdot 8H_2O$ is a crystalline material with the desired phase[246]. The XRPD patterns for ZSM-5 before and after desilicated (Figure 6.8b) show that the MFI structure[4] is preserved after the formation of mesopores. The peaks for the desilicated ZSM-5 are slightly broader than the ZSM prior to desilication indicating smaller crystals. This is though not surprising since desilication removes silicon from the framework and hence the crystals will inevitable become smaller. Alternatively, the presence of intracrystalline mesopores could disturb the longer-range ordering.

Figure 6.9 gives representative SEM images of the parent and desilicated ZSM-5 samples.

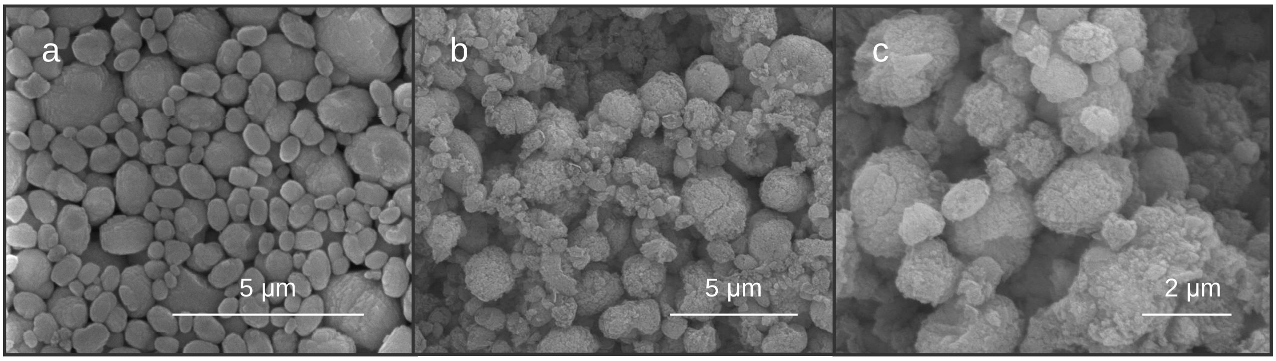

Figure 6.9: Representative SEM images of ZSM-5 before (a) and after desilication (b, c)

The parent ZSM-5 sample consists of particles in the range of ~0.5-3 µm, Figure 6.7a, and the shape is more oval-like than the typical coffin-shaped zeolites. From the SEM images of the desilicated sample the particles appear sponge-like, typically for mesoporous zeolites, but retain more or less their original size. Additionally, some particles are fragmented, probably as a result of the desilication and could also explain the broader peaks in the XRPD pattern for the desilicated sample.

The pore volumes and surface areas calculated from the N_2 physisorption measurements are listed in Table 6.1. Figure 6.10 shows the physisorption isotherms given by the parent and desilicated ZSM-5 samples and the pore size distributions derived from the desorption isotherm.

Table 6.1: Surface areas and pore volumes of the parent and desilicated zeolite samples

	Surface area[a] [m^2/g]	External surface area[b] [m^2/g]	Micropore surface area[b] [m^2/g]	Micropore volume[b] [cm^3/g]	Total pore volume[c] [cm^3/g]
Parent ZSM-5	430	48	382	0.17	0.26
Desilicated ZSM-5	521	221	300	0.13	1.07

[a] Calculated using the BET method, [b] determined using the t-plot method and [c] volume adsorbed at P/P$_0$=0.99

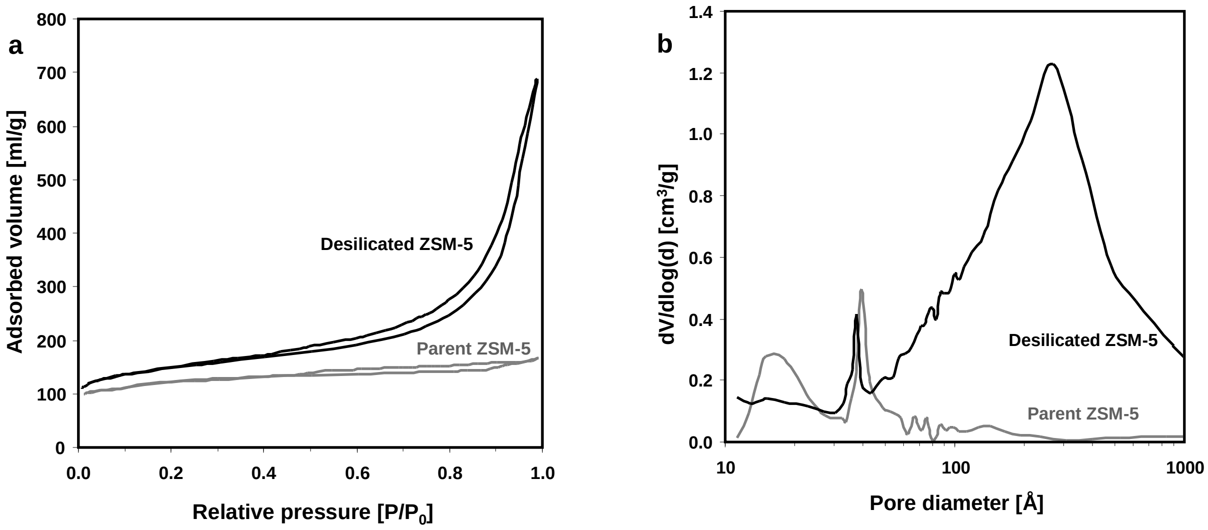

Figure 6.10: N_2 adsorption-desorption isotherms (a) and corresponding pore size distribution (b) of the parent and desilicated ZSM-5 zeolites. The pore size distributions are obtained from the desorption branch of the isotherm using the BJH method

The isotherm from the desilicated sample in Figure 6.10s exhibits a hysteresis typical for mesoporous materials. The sample can therefore be classified as a hierarchical zeolite. Contrary, the isotherm of the parent sample does not contain any significant amount of hysteresis and displays an isotherm typical for solely microporous materials.

Figure 6.10b shows the pore isze distributions, including the artefacts at 2 and 4 nm due to the well-known phase transition of N_2 and forced closure of the hysteresis loop, respectively. For the desilicated sample pore size distribution is spread over the mesopores and macropore region centred at 27 nm.

Table 6.1 quantitatively reveals the large increase in total pore volume and external surface area upon the desilication treatment calculated from the isotherms. It is noteworthy to mention that the large increase in pore volume and external surface area only occurs at a small expense of the micropore volume and surface area. This indicates that most of the intrinsic properties of the ZSM-5 zeolite are preserved after the treatment.

To verify the grafting of APTMS on the surface of the mesoporous zeolite surface the carbon content has been determined. According to Lee *et al.* it is possible to graft APTMS corresponding to an organic content of 1.13 mmol/g zeolite after 3 hours. According to elemental analysis the prepared functionalised mesoporous zeolite contain 9.82 wt% carbon corresponding to 2.7 mmol APTMS/g zeolite. This is rather high compared to previous results[254] which is most likely due to larger mesopores and higher external surface area.

To investigate the grafting of APTMS in further detail TGA combined with DSC is performed and the profiles are shown in Figure 6.11.

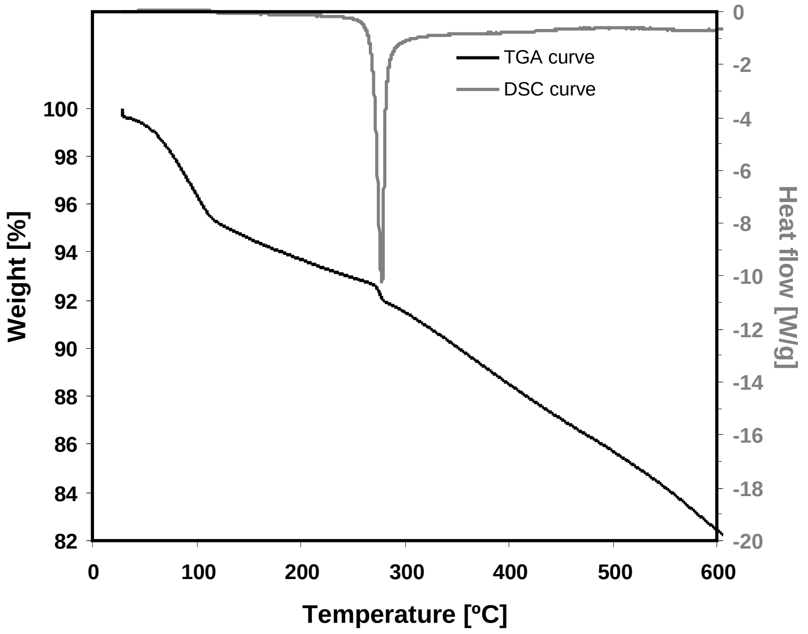

Figure 6.11: TGA/DSC profiles of functionalised mesoporous ZSM-5 with APTMS

The TGA measurement (black line in Figure 6.11) shows a 5 % weight loss until 120 °C attributed to water evaporating from the zeolite. Around 280 °C a small weight loss of ~1.5 % is observed and from the DSC profile (grey line in Figure 6.11) an exothermic peak is seen at this temperature which could correspond to decomposition of part of the APTMS. As the elemental analysis revealed that 9.82 wt% of the material is carbon, the weight loss attributed to decomposition of grafted APTMS should be more pronounced; approximately 15 wt% assuming decomposition of $H_2N(CH_2)_3$. A reason for this could be that the decomposition of grafted APTMS is rather complex and might consist of several steps.

Table 6.2 shows the cobalt and molybdenum contents determined by elemental analysis after calcination together with the catalytic test results in HDS for the impregnated and anchored version of the prepared catalysts.

Table 6.2: Cobalt and molybdenum contents [a] and catalytic test results

	Co [wt%]	Mo [wt%]	k(HDS) [h^{-1}]	k(HDN) [h^{-1}]	k(HYD) [h^{-1}]
$CoMo_6$-ZSM-5_anc	0.97	10.1	32.4	18.4	11.8
$CoMo_6$-ZSM-5_imp	0.89	8.72	8.6	3.1	2.9

[a] determined by elemental analysis after calcination at 500 °C for 3 hours

The aim was to prepare mesoporous ZSM-5 with 1 wt% Co and ~10 wt% Mo. Table 6.2 reveals that the anchored version contains the desired ratios while the impregnated version contains slightly lower amounts of metals. From Table 6.2 it can be observed that the anchored version has a significantly higher catalytic activity for HDS, HDN and HYD than the corresponding impregnated version. The difference in catalytic activity can not only be attributed to the differences in metal loading but must also be ascribed to an improved distribution of the metals throughout the zeolite support. It can also be concluded that the chosen Anderson ion is active in HDS.
Even though the two materials are similar concerning type of support and metal loads other factors than distribution of the active sites can affect the catalytic activity. Previous, it was found[256] that the sodium content affects the HDS activity in a negative manner. As the Anderson ion compound contains sodium ions the impregnated version contain inevitable sodium. The anchored version is expected to contain a lower amount of sodium as the residual sodium arose during ion exchange is at least to some extent removed during washing. This means that the presence of a higher amount of sodium in the impregnated version can potential decrease the catalytic activity in HDS, making comparison more difficult. However, Venezia *et al.* has reported[257] that the effect of sodium on the HDS activity of Co-Mo catalysts depends on the type of support. In the case of amorphous aluminosilicate, the presences of sodium ions promoted the HDS activity up to a sodium load of 4 wt%, exhibiting a maximum at around 3 wt% sodium. In contrast, the addition of sodium to amorphous silica resulted in a severe decrease in the HDS activity of the supported Co-Mo catalyst.

To investigate the effect of sodium using mesoporous ZSM-5 zeolite as support for HDS catalysts one way is to impregnate *e.g.* sodium nitrate in different amounts on one of the prepared materials. This is though left for future work. Instead, an aqueous solutions containing dissolved $(NH_4)_6Mo_7O_{24}\cdot 4H_2O$ and $Co(H_2O)_6(NO_3)_2$ was impregnated on mesoporous ZSM-5 followed by calcination to remove ammonium and nitrate. The obtained reference material contained 0.88 wt% Co and 9.4 wt% Mo and showed a HDS activity of 19.3 h^{-1}. Hereby, it was shown that even though the anchored version might contain sodium, the anchoring improves the HDS activity due to improved dispersion.

Another way to cast light on the sodium issue is by the preparation of two reference materials using commercial high surface area alumina as support with a surface area above 200 m^2/g. First, a solution containing cobalt and molybdenum was prepared and impregnated onto the support, resulting in a catalyst with 1 wt% Co and 10.3 wt% Mo (Co-Mo/Al_2O_3). Second, a solution containing the $CoMo_6$ Anderson ion was impregnated onto the support, resulting in a catalyst with 0.96 wt% Co and 9.63 wt% Mo ($CoMo_6/Al_2O_3$). Alumina is generally believed to exert stronger interaction with the active nanoparticles compared to *e.g.* silica, carbon or titania.[231] The strong support interactions are in many regards advantageous since they are responsible for the fact that highly dispersed molybdenum sulfide structures can easily be prepared and remain stable during operation. Also a strong support interaction can facilitate redispersion during regeneration. However, the strong support interactions in alumina-supported catalysts also have negative aspects, since these interactions are probably responsible for the formation of a less active Co-Mo-S nanoparticles. In the case of silica, the molybdenum-support interaction is weaker than the Co-Mo interaction. Upon sulfiding of silica-supported catalysts significant amounts of Co_9S_8 are formed together with large MoS crystals resulting in a less active HDS catalyst.

Sodium has a severe negative effect on the HDS activity using alumina as support. As the Anderson ion compound contains sodium opposite to the Co-Mo impregnation solution the difference in activity of the two reference catalyst may primarily be due to the effect of sodium. If the difference in activity is smaller between the two reference catalysts than the two prepared zeolite support materials, the sodium effect must be smaller using mesoporous ZSM-5 as support material. The Co-Mo/Al_2O_3 was prepared to represent a commercial HDS catalyst whereas the $CoMo_6/Al_2O_3$ was prepared to also investigate the effect of the support besides the effect of sodium.

The HDS activities for the Co-Mo/Al_2O_3 and the $CoMo_6/Al_2O_3$ were 60.1 h^{-1} and 48.1 h^{-1} respectively. In general, the alumina supported catalysts displayed a higher activity for HDS than the mesoporous zeolite supported catalysts, the commercial look-alike (Co-Mo/Al_2O_3) being the most active. The catalyst using the Anderson ion as precursor was 8 times as active using alumina as support material than using mesoporous zeolite as support material. The difference in activity is 12 h^{-1} for the alumina supported materials and is 23.8 h^{-1} for the zeolite supported materials. This means that sodium must not have as pronounced effect on the HDS activity using mesoporous zeolite as support material than using alumina as support material. Still, further work should be performed to investigate sodium's effect using mesoporous zeolite as support material.

After sulfidation and catalytic testing the anchored version was characterised using TEM. In general it was difficult to conduct TEM especially at high magnifications due to the electron beam sensitivity of the zeolite framework. Representative TEM images are given in Figure 6.12.

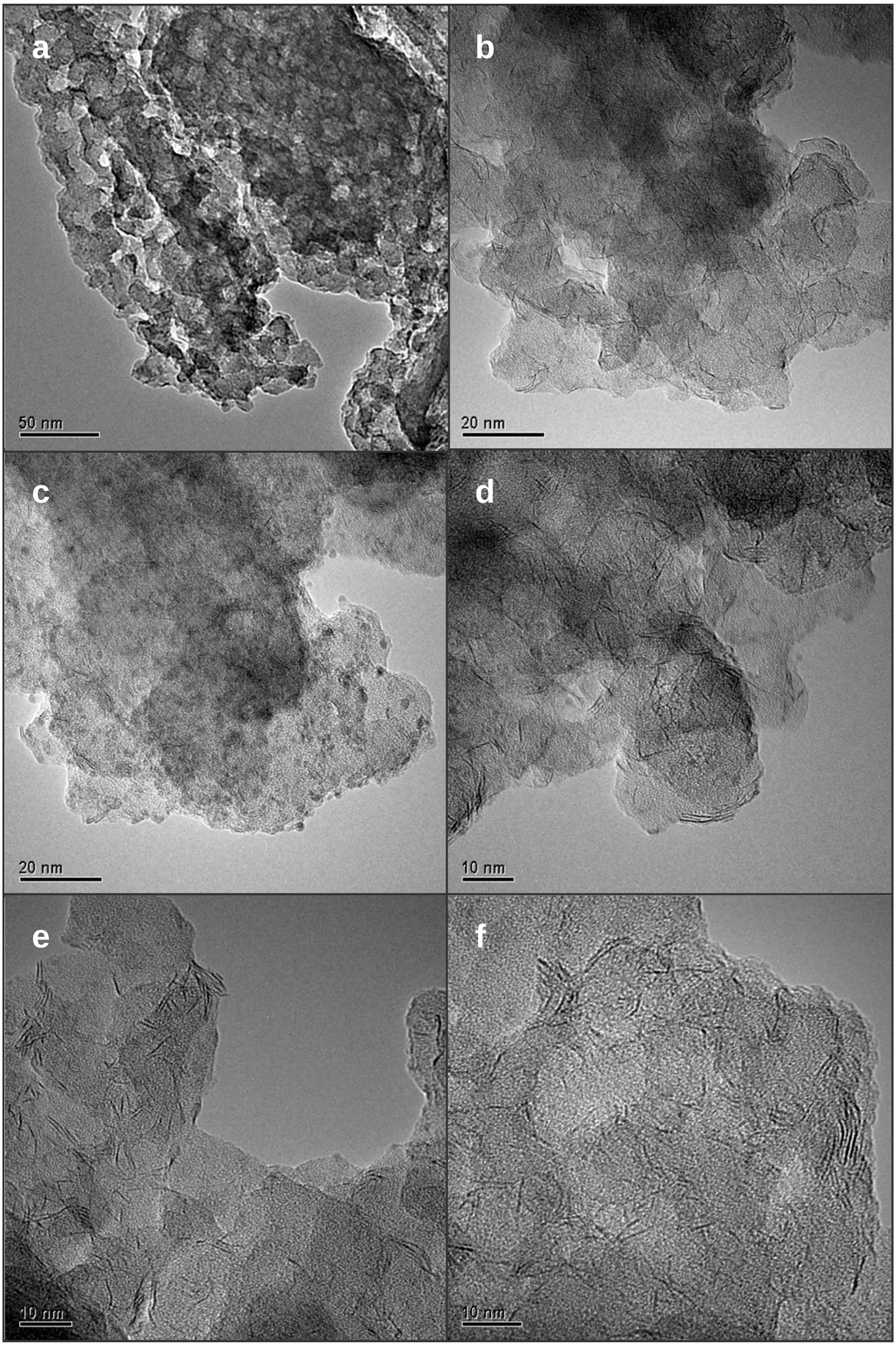

Figure 6.12: Representative TEM images of the spent catalyst whose precursor contained anchored molecular $CoMo_6$ species

The mesoporous nature of the zeolite can clearly be recognised by the pronounced contrast differences shown in Figure 6.12. Throughout the sample MoS_2 slabs are present both as single and double sheets. The MoS_2 slabs are primarily located in the mesopores since they are too large to fit into the micropore system of the zeolite. The MoS_2 slabs are estimated to 2-3 nm. To further explore the location of the MoS_2 inside the zeolite particles one possibility is to conduct TEM tomography, which is left for future work.

In selected areas small round particles of homogeneous size distribution at around 1 nm can be observed, especially apparent in Figure 6.12c and d. XRPD of the spent catalyst did only detect crystalline ZSM-5 together with an undefined amorphous phase. This could be due to the very small particles size of both the undefined particles and MoS_2 slabs. Most likely the small particles are due to non or only partially sulfided CoMo nanoparticles. Further evaluation of the undefined particles could be performed by EDS-mapping to estimate the distribution of the elements.

6.5. Conclusion

A new HDS catalyst was successfully prepared by anchoring Anderson ions to functionalised mesoporous ZSM-5 zeolite. The Anderson ion was $[Co(OH)_6Mo_6O_{18}]^{3-}$. The advantage of using this Anderson ion as metal sources for HDS catalysis was that the active metal and the promoter metal were introduced together in the same chemical species which would be expected to enhance the possibility of forming the active Co-Mo-S nanoparticles. The Anderson ions were anchored to the surface of mesoporous ZSM-5 by using APTMS as linker molecule. As a reference material the molecular $CoMo_6$ species were impregnated on mesoporous ZSM-5 to investigate if the anchored version improved the catalytic activity due to improved dispersion of the active phase. According to catalytic test the anchored version displayed a significant higher activity in HDS catalysis compared to the impregnated version. TEM investigations of the spent catalyst showed the presence of both single and double MoS_2 slabs and undefined round particles of approximately 1 nm.

Based on sodium or non-sodium containing CoMo alumina and non-sodium containing CoMo on mesoporous ZSM-5 catalysts activities, the inhibiting effect of sodium is low and cannot explain dramatic increase in activity when anchoring rather than impregnating on mesoporous ZSM-5. This new type of material provides new opportunities in the design of catalyst materials. It would be interesting to combine the intrinsic properties of the zeolites *i.e.* acidity and size-selectivity with the possibility to anchor active metal species to the surface and utilise the dual functionality.

Conclusion

In the present thesis, focus has been on the development of new modified zeolites for catalytic applications. Zeolites have been modified regarding the porosity and the introduction of different metals and were used as solid acid catalysts, as an inert matrix for stabilising metal nanoparticles and as an anchoring material for active phase precursors in the form of molecular metal oxide species. The modifications are schematically illustrated in Figure 1.

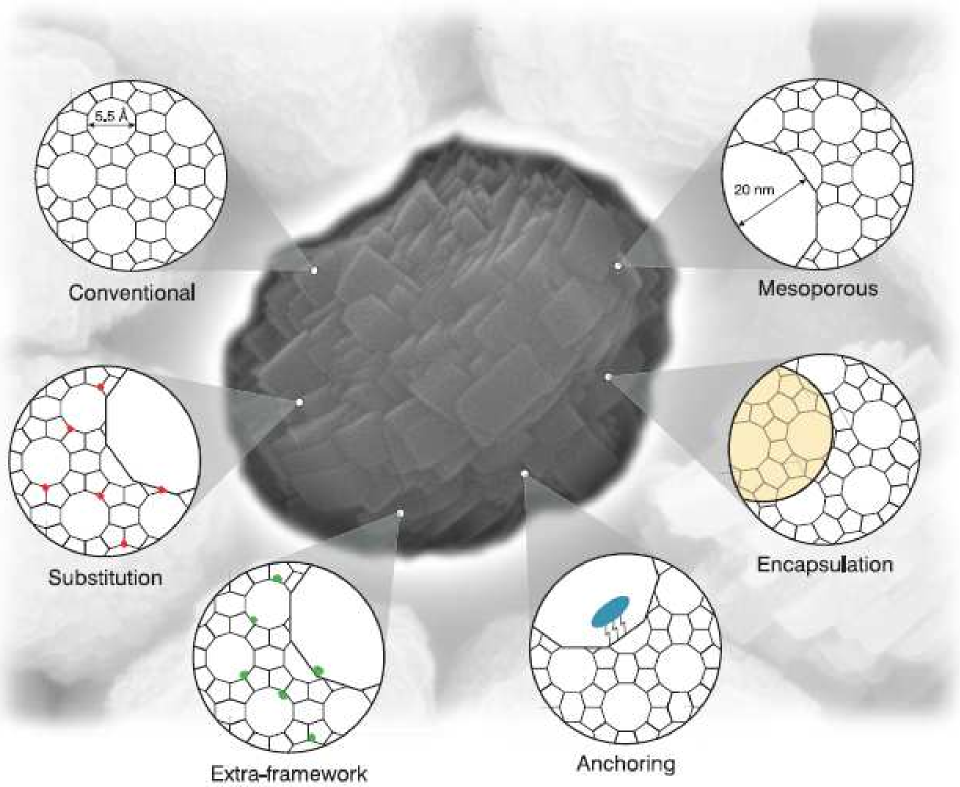

Figure 1: Schematic illustration of the different approaches to modify zeolite crystals

Initially, in Chapter 1 an introduction was given to the field of zeolites with respect to their structure, properties, diffusion effects and implementation of mesoporosity. It was explained that much of the success of conventional zeolites results from their inherent micropore system which make them useful for adsorption, separation and catalysis. However, it was also explained that molecular diffusion is very slow in these micropores and that this hinders the effectiveness of zeolites for catalytic applications. Their effectiveness can be improved by the implementation of either inter- or intracrystalline mesopores. Furthermore, an evaluation of the used characterisation techniques was given concerning advantages and pitfalls.

In Chapter 2, nanosized and mesoporous zeolites were prepared to investigate the effect of inter- or intracrystalline mesopores on the catalytic lifetime in the conversion of methanol to hydrocarbons (MTH). One mesoporous zeolite with intracrystalline mesopores and three types of nanosized ZSM-5 zeolites were synthesised together with a conventional ZSM-5 zeolite. The characterisations revealed that all synthesised zeolites were highly crystalline and contained approximately the same amount of aluminum. Even though the three nanosized zeolites differed slightly in the synthesis procedure, the obtained materials were rather similar regarding crystal size and morphology. However, they differed slightly in the porosity and amount of extra-framework aluminum.

The mesoporous ZSM-5 with intracrystalline mesopores displayed the significantly longest catalytic lifetime in the MTH reaction while one of the nanosized zeolites showed an improved catalytic lifetime compared to the conventional counterpart.

It was found that several factors influence the catalytic lifetime in the MTH reaction *e.g.* Si/Al ratios, porosity and amount of defects which makes comparison difficult. As the zeolite crystallisation mechanism is quite complex, it is difficult to prepare comparable materials where only one factor varies but it was clearly indicated that the presence of extra-framework aluminum had a severe negative effect on the catalytic lifetime in the MTH reaction.

In Chapter 3, a more in-depth discussion of the effect of extra-framework aluminum on the catalytic lifetime in the MTH reaction was given. The extra-framework aluminum was produced by desilicating a conventional ZSM-5 zeolite. The sample was subsequently dealuminated to remove the generated extra-framework aluminum to investigate the effect of this. Characterisations showed that the crystal structure was preserved and the porosity changed primarily upon desilication.

NH_3-TPD, MAS NMR and FTIR investigations all supported that upon desilication mesopores were formed and primarily silicon was removed from the framework resulting in extra-framework aluminum. The desilication reduced the amount of strong Brønsted acid sites and instead weaker acid sites were formed. The subsequent dealumination by oxalic acid removed all aluminum in octahedral positions but also a significant amount of aluminum in tetrahedral positions was extracted. The removal of tetrahedral aluminum during dealumination suggested that different tetrahedral species were present and that only some can be extracted by the dealumination method.

The catalytic test showed that despite the formation of mesopores and repairing of internal defects the desilicated sample displayed a reduced catalytic lifetime compared to the parent ZSM-5 catalyst. After the subsequently dealumination the catalytic lifetime was recovered and improved compared to the parent sample. Therefore, it was concluded that the introduction of mesoporosity does not necessarily improve the catalytic lifetime as the normal benefits from desilication became masked by the generation of extra-framework aluminium. The main conclusion is thus that the catalytic lifetime is severely dependent on the amount of extra-framework aluminum.

Usually ZSM-5 catalysts deactivate in the MTH reaction due to coke formation. In Chapter 4 was presented synthesis and characterisation of conventional and mesoporous ZSM-5 zeolites and the Ga-MFI zeotype analogues to investigate the differences in activity, selectivity and mode of deactivation in the MTH reaction. It was found that it was easier to introduce aluminum than gallium into the crystal structure and it was verified that the incorporation of gallium decreased the intrinsic acidity of the individual acid sites.

The catalytic lifetime of the gallium based zeotypes was in general shorter than the corresponding zeolites and the presence of mesopores improved the catalytic lifetime for both types of materials. The Ga-MFI zeotypes showed a higher selectivity towards small alkenes which was ascribed to the lower acidity of the individual active sites compared to zeolites. Both mesoporous materials produced a higher amount of aromatics than their conventional counterparts due to less steric hindrance.

It was confirmed that the ZSM-5 zeolites deactivated due to coke formation as it was possible to regenerate the catalytic activity and obtain approximately the same catalytic lifetime after coke combustion. In contrast, the catalytic activity of the mesoporous Ga-MFI could not be restored after coke combustion. Instead it was found that during methanol conversion the mesoporous Ga-MFI deactivates due to loss of the catalytically active Brønsted acid sites caused by hydrolysis of Ga-O bonds leading to formation of inactive extra-framework gallium species.

In Chapter 5 it was described that zeolite or zeotype materials can be used as an inert matrix to produce a hybrid material comprising 1-2 nm sized gold nanoparticles embedded in silicalite-1 or ZSM-5 crystals. TEM tomography was used to indisputably prove that some gold nanoparticles were embedded within and some were on the external surface of the crystals in the final hybrid material. By the use of calcination experiments obtained both *in situ* and *ex situ* TEM indicated that the gold nanoparticles embedded in the crystals are highly stable towards sintering, whereas the particles located at the outer surface tend to sinter.

The produced hybrid materials were tested in the aerobic oxidation of benzaldehyde and 3,5-dimethylbenzaldehyde in methanol. The catalytic tests proved that the gold nanoparticles were encapsulated and immobilised yielding a sintering-stable substrate-size selective oxidation catalyst as the active gold nanoparticles were only accessible through the micropores.

Even though further work should involve optimisation of the coating of gold nanoparticles this new synthesis procedure could easily be expanded to other types of incorporated metals and other types of zeolite or zeotype structures by varying the template and type of added elements. Future work should also contain the utilisation of the potential bi-functionality of these hybrid materials as the zeolite might be made acidic by ion exchange.

Chapter 6 presents preliminary work on anchoring the Anderson ion $[Co(OH)_6Mo_6O_{18}]^{3-}$ on functionalised mesoporous ZSM-5 utilising zeolites as a support material. The idea was to produce a bi-functional catalyst featuring both a hydrogenation and a cracking capability in close connections to apply in simultaneous hydrodesulfurisation (HDS) and cracking reactions. The presented work contained synthesis, characterisation and catalytic test using HDS as test reaction leaving the hydrocracking potential for future work.

To investigate whether the anchoring improves the dispersion of the molecular $CoMo_6$ species a reference material was made by simple impregnation of the Anderson ion on mesoporous ZSM-5. According to the catalytic tests the anchored version displayed a significant higher activity in HDS catalysis compared to the impregnated counterpart. Based on sodium or non-sodium containing CoMo alumina and non-sodium containing CoMo on mesoporous ZSM-5 catalyst activities, the inhibiting effect of sodium was found to be low and cannot explain dramatic increase in activity when anchoring rather than impregnating on mesoporous ZSM-5. Still, further work should include a more thoroughly investigation of the effect of sodium and also the hydrocracking ability of the prepared material.

I hope and believe that my thesis will be of use to others. Particularly, I believe my work has contributed significantly to the science of zeolite catalysis for two very important reasons. First of all, I have demonstrated that zeolites can be modified in a wealth of possible ways. This was achieved by introducing an auxiliary system of mesopores in addition to the intrinsic micropore system by different approaches, introduction of different elements into zeolite crystals both in framework positions, by anchoring and as nanoparticles immobilised in zeolite crystals. Secondly, I have thoroughly investigated how extra-framework aluminum and the presence of inter- or intracrystalline mesopores affect the catalytic lifetime in the MTH reaction. Thus, I trust my work clearly demonstrates the diversity and usability of zeolite materials in catalytic applications.

References

[1] R. Szostak, *Molecular Sieves – Principles of Synthesis and Identification*, Blackie Academic & Professional, London, 2nd Edition (**1998**)

[2] K.S.W. Sing, D.H. Everett, R.A. W. Haul, L.Moscou, R.A. Pierotti, J.Rouquerol, T.Siemieniewska, Pure Appl. Chem. 57 (**1985**) 603-619

[3] C.R. Marcilly, Top. Catal. 13 (**2000**) 357-366

[4] Website of the International Zeolite Association: www.iza-structure.org/databases/ (1st of June 2011)

[5] F. Fajula, F. Di Renzo, Stud. Surf. Sci. Catal. 157 (**2005**) 1-12

[6] J.A. Rabo, M.W. Schoonover, Appl. Catal. 222 (**2001**) 261-275

[7] S. van Donk, A.H. Janssen, J.H. Bitter, K.P. de Jong, Catal. Rev. 45 (**2003**) 297-319

[8] T.V.W. Janssens, S. Dahl, C.H. Christensen, US Patent 7078587(**2006**)

[9] M. Bjørgen, F. Joensen, M.S. Holm, U. Olsbye, K.-P. Lillerud, S. Svelle, Appl. Catal. A: General 345 (**2008**) 43-50

[10] J. Kim, M. Choi, R. Ryoo, J. Catal. 269 (**2010**) 219-228

[11] G. Ertl, H. Knözinger, F. Schüth, J. Weitkamp, *Handbook of Heterogeneous Catalysis*, Vol. 1, Wiley-VCH, Weinheim, (**2008**)

[12] A. Corma, J. Catal. 216 (**2003**) 298-312

[13] W. Löwenstein, Am. Mineral. 39 (**1954**) 92-96

[14] A. Corma, Chem. Rev. 95 (**1995**) 559-614

[15] M.E. Davis, R.F. Lobo, Chem. Mater. 4 (**1992**) 756-768

[16] U.V. Mentzel, PhD Thesis, *Towards a methanol economy: Zeolite catalyzed production of synthetic fuels*, (**2010**) Department of Chemistry, Technical University of Denmark

[17] C.D. Chang, A.J. Silvestri, ChemTech. 17 (**1987**) 624-631

[18] S. Svelle, F. Joensen, J. Nerlov, U. Olsbye, K.-P. Lillerud, S. Kolboe, M. Bjørgen, J. Am. Chem. Soc. 128 (**2006**) 14770-14771

[19] M. Bjørgen, S.Svelle, F. Joensen, J. Nerlov, S. Kolboe, F. Bonino, L. Palumbo, S. Bordiga, U. Olsbye, J. Catal. 249 (**2007**) 195-207

[20] D. Barthomeuf, Stud. Surf. Sci. Catal. 5 (**1985**) 55-64

[21] L.A. Pine, P.J. Marcher, W.A. Watcher, J. Catal. 85 (**1984**) 466-476

[22] B. Beagley, J. Dwyer, F.R. Fitch, R. Mann, J. Walters, J. Phys. Chem. 88 (**1984**) 1744-1751

[23] C.T.-W. Chu, C.D. Chang, J. Phys. Chem. 89 (**1985**) 1569-1571

[24] J.C. van der Waal, H. van Bekkum, J. Porous Mater. 5 (**1998**) 289-303

[25] C.S. Cundy, P.A. Cox, Chem. Rev. 103 (**2003**) 663-701

[26] A. Corma, Chem. Rev. 97 (**1997**) 2372-2419

[27] A. Corma, M.E. Davis, ChemPhysChem 5 (**2004**) 304-314

[28] R.J. Francis, D. O´Hara, J. Am. Chem. Soc., Dalton Trans. (**1998**) 3133-3148

[29] K. Egeblad, C.H. Christensen, M. Kustova, C.H. Christensen in *Zeolites: From model materials to industrial catalysts*, J. Cejka, J. Perez-Pariente, W.J. Roth; Eds., Research Signpost (**2008**) 391-422

[30] J. Perez-Ramírez, C.H. Christensen, K. Egeblad, C.H. Christensen, J.C. Groen, Chem. Soc. Rev. 37 (**2008**) 2530-2542

[31] M.S. Holm, E. Taarning, K. Egeblad, C.H. Christensen, Catal. Today 168 (**2011**) 3-16

[32] K. Egeblad, C.H. Christensen, M. Kustova, C.H. Christensen, Chem. Mater. 20 (**2008**) 946-960

[33] R. Ryoo, S.H. Joo, S. Jun, J. Phys. Chem. B 103 (**1999**) 7743-7446

[34] C. Madsen, C.J.H. Jacobsen, Chem. Commun. (**1999**) 673-674

[35] C.J. H. Jacobsen, C. Madsen, J. Houzvicka, I. Schmidt, A. Carlsson, J. Am. Chem. Soc. 122 (**2000**) 7116-7117

[36] S.-S. Kim, J. Shah, T.J. Pinnavaia, Chem. Mater. 15 (**2003**) 1664-1668

[37] Z. Yang, Y. Xia, R. Mokya, Adv. Mater. 16 (**2004**) 727-732

[38] H. Li, Y. Sakamoto, Z. Liu, T. Ohsuna, O. Terasaki, M. Thommes, S. Che, Micropor. Mesopor. Mater. 106 (**2007**) 174-179

[39] L. Tosheva, V. Valtchev, J. Sterte, Micropor. Mesopor. Mater. 35-36 (**2000**) 621-629

[40] Y. Tao, H. Kanoh, K. Kaneko, Langmuir 21 (**2005**) 504-507

[41] W.-C. Li, R. Palkovits, W. Schmidt, B. Spliethoff, F. Schüth, J. Am. Chem. Soc. 127 (**2005**) 12595-12600

[42] F.-S. Xiao, L. Wang, C. Yin, K. Lin, Y. Di, J. Li, R. Xu, D.S. Su, R. Schlögl, T. Yokoi, T. Tatsumi, Angew. Chem. Int. Ed. 45 (**2006**) 3090-3093

[43] H. Wang, T.J. Pinnavaia, Angew. Chem. Int. Ed. 45 (**2006**) 7603-7606

[44] S.A. Davis, S.L. Burkett, N.H. Mendelson, S.Mann, Nature 385 (**1997**) 420-423

[45] A. Dong, Y. Wang, Y. Tang, N. Ren, Y. Zhang, Y. Yue, Z. Gao, Adv. Mater. 14 (**2002**) 1369-1375

[46] V. Valtchev, M. Smaihi, A.-C. Faust, L. Vidal, Angew. Chem. Int. Ed. 42 (**2003**) 1369-1375

[47] B. Zhang, S.A. Davis, S. Mann, Chem. Mater. 14 (**2002**) 1369-1375

[48] C.J.H. Jacobsen, J. Houzvicka, I. Schmidt, C. Madsen, A. Carlsson, US Pat. 6565826 (**2003**)

[49] H. Zhu, Z. Liu, Y. Wang, D. Kong, X. Yuan, Z. Xue, Chem. Mater. 20 (**2008**) 1134-1139

[50] M. Choi, H.S. Cho, R. Srivastava, C. Venkatesan, D.-H. Choi, R.Ryoo. Nat. Mater. 5 (**2006**) 718-723

[51] M. Choi, R. Srivastava, R. Ryoo, Chem. Commun. (**2006**) 4380-4382

[52] V. Meynen, P. Cool, E.F. Vansant, Micropor. Mesopor. Mater. 104 (**2007**) 26-38

[53] J.Cejka, S. Mintova, Catal. Rev. Sci. Eng. 49 (**2007**) 457-509

[54] D. Trong-On, S. Kaliaguine, Angew, Chem. Int. Ed. 40 (**2001**) 3248-3251

[55] D. Trong-On, D. Lutic, S. Kaliaguine, Micropor. Mesopor. Mater. 44-45 (**2001**) 435-444

[56] D. Trong-On, S. Kaliaguine, Angew. Chem. Int. Ed. 41 (**2002**) 1036-1040

[57] D. Trong-On, S. Kaliaguine J. Am. Chem. Soc. 125 (**2003**) 618-619

[58] S.C. Larsen, J. Phys. Chem. C 111 (**2007**) 18464-18474

[59] M.A. Camblor, A. Corma, S. Valencia, Micropor. Mesopor. Mater. 25 (**1998**) 59-74

[60] Y. Tao, H. Kanoh, L. Abrams, K. Kaneko, Chem. Rev. 106 (**2006**) 896-910

[61] R. Chal, C. Gérardin, M. Bulut, S. van Donk, ChemCatChem 3 (**2011**) 67-81

[62] J.C. Groen, J.C. Jansen, J.A. Moulijn, J. Perez-Ramírez, J. Phys. Chem. B 108 (**2004**) 13062-13065

[63] M. Ogura, S.-Y. Shinomiya, J. Tateno, Y. Nara, M. Nomura, E. Kikuchi, M. Matsukata, Appl. Catal. A: General 5 (**2001**) 33-43

[64] J.C. Groen, L.A.A. Peffer, J.A. Moulijn, J. Perez-Ramírez, Colloid Surface A 241 (**2004**) 53-58

[65] J.C. Groen, J.A. Moulijn, J. Perez-Ramírez, Ind. Eng. Chem. Res. 14 (**2007**) 4193-4201

[66] K. Zhu, K. Egeblad, C.H. Christensen, Eur. J. Inorg. Chem. 25 (**2007**) 3955-3960

[67] M.Y. Kustova, P. Hasselriis, C.H. Christensen, Catal. Lett. 96 (**2004**) 205-211

[68] C.H. Christensen, K. Johannsen, I. Schmidt, C.H. Christensen, J. Am. Chem. Soc 125 (**2003**) 13370-13371

[69] I. Schmidt, A. Krogh, K. Wienberg, A. Carlsson, M. Brorson, C.J.H. Jacobsen, Chem. Commun. (**2000**) 2157-2158

[70] I. Melian-Cabrera, S. Espinosa, J.C. Groen, B. Linden, F. Kapteijn, J.A. Moulijn, J. Catal. 238 (**2006**) 250-259

[71] A.R. West, *Basic Solid State Chemistry*, John Wiley & Sons, LTD: Chichester, England, 2nd Ed. (**2004**)

[72] L.B. McCusker, C. Baerlocher, Stud. Surf. Sci. Catal. 157 (**2005**) 41-64

[73] R.E. Morris, P.S. Wheatley, Stud. Surf. Sci. Catal. 168 (**2007**) 375-401

[74] J.C. Groen, J. Perez-Ramírez, Appl. Catal. A: General 268 (**2004**) 121-125

[75] J.C. Groen, L.A.A. Peffer, J. Perez-Ramírez, Micropor. Mesopor. Mater. 60 (**2003**) 1-17

[76] M. Thommes, Stud. Surf. Sci. Catal. 168 (**2007**) 495-523

[77] S. Lowell, J. E. Shields, M. A. Thomas, M. Thommes, *Characterization of Porous Solids and Powders: Surface Area, Pore Size and Density*, B. Scarlett; Kluwer Academic Publishers, Dordrecht, The Netherlands, (**2004**)

[78] S. Brunauer, P.H. Emmett, E.Teller, J. Am. Chem. Soc. 60 (**1938**) 309-319

[79] J. H. Lippens, J. de Boer, J. Catal. 4 (**1965**) 319-323

[80] P.Hudec, A.Smiesková, Z. Zidek, P. Schneider, O.Solcová, Stud. Surf. Sci. Catal. 142 (**2002**) 1587-1594

[81] E.P. Barrett, L.G. Joyner, P.P. Halenda, J. Am. Chem. Soc. 73 (**1951**) 373-380

[82] J. Choma, M. Jaroniec, W. Burakiewicz-Mortka, M. Kloske, Appl. Surf. Sci. 196 (**2002**) 216-223

[83] P.I. Ravikovitch, A.V. Neimark, Colloid Surface A 187-188 (**2001**) 11-21

[84] P. L. Llewellyn, J.P. Coulomb, Y. Grillet, P. Patarin, G. Andre, J. Rouquerol, Langmuir 9 (**1993**) 1852-1856

[85] O. Kadlec, M.M. Dubinin, J. Colloid Interf. Sci. 31 (**1969**) 479-489

[86] C.V.G. Burgess, D.H. Everett, J. Colloid Interf. Sci. 33 (**1970**) 611-614

[87] J.W. Ward, J.Catal. 9 (**1967**) 225-236

[88] D. Barthomeuf, Mater. Chem. Phys. 17 (**1987**) 49-71

[89] R.T. Sanderson, *Chemical Bonds and Bond Energy: Physical Chemistry 21*, Academic Press, New York, (**1976**)

[90] M.S. Holm, S. Svelle, F. Joensen, P. Beato, C.H. Christensen, S. Bordiga, M. Bjørgen, Appl. Catal. A: General 356 (**2009**) 23-30

[91] N.-Y. Topsøe, K. Pedersen, E.G. Derouane, J. Catal. 70 (**1981**) 41-52

[92] B.M. Lok, B.K. Marcus, C.L. Angell, Zeolites 6 (**1986**) 185-194

[93] C.V. Hidalgo, H. Itoh, T. Hattori, M. Niwa, Y. Murakami, J. Catal. 85 (**1984**) 362-369

[94] M. Sawa, M. Niwa, Y. Murakami, Zeolites 10 (**1990**) 532-538

[95] H. Sato, Catal. Rev. Sci. Eng. 39 (**1997**) 395-424

[96] N. R. Meshram, S.G. Hegde, S.B. Kulkarni, Zeolites 6 (**1986**) 434-438

[97] G.L. Woolery, G.H. Kuehl, H.C. Timken, A.W. Chester, J.C. Vartuli, Zeolites (**1997**) 288-296

[98] F. Lónyi, J. Valyon, Micropor. Mesopor. Mater. 47 (**2001**) 239-301

[99] C. Pazé, S. Bordiga, C. Lamberti, M. Salvalaggio, A. Zecchina, J. Phys. Chem. B 101 (**1997**) 4740-4751

[100] J.A. Lercher, A. Jentys, Stud. Surf. Sci. Catal. 168 (**2007**) 435-476

[101] T. Montanari, M. Bevilacqua, G. Busca, Appl. Catal. A: General 307 (**2006**) 21-29

[102] A. Zecchina, S. Bordiga, G. Spoto, L. Marchese, G. Petrini, G. Leofanti, M. Padovan, J. Phys. Chem. 96 (**1992**) 4991-4997

[103] I. Kiricsi, C. Flego, G. Pazzuconi, W.O. Parker, R. Millini, C. Perego, G. Bellussi, J. Phys. Chem 98 (**1994**) 4627-4634

[104] A. Zecchina, S. Bordiga, G. Spoto, D. Scarano, G. Petrini, G. Leofanti, M. Padovan, J. Chem. Soc. Faraday Trans. 88 (**1992**) 2959-2569

[105] B. Gil, L. Mokrzycki, B. Sulikowski, Z. Olejniczak, S. Walas, Catal. Today 152 (**2010**) 24-32

[106] A. Gedeon, C. Fernandez, Stud. Surf. Sci. Catal. 168 (**2007**) 403-434

[107] E. Lippmaa, S. Samoson, M. Magi, J. Am. Chem. Soc. 108 (**1986**) 1730-1735

[108] C.A.Fyfe, G.C. Gobbi, J. Klinowski, J.M. Thomas, S. Ramdas, Nature 296 (**1982**) 530-533

[109] C.A. Fyfe, G.C. Gobbi, J.S. Hartman, J. Klinowski, J.M. Thomas, J. Phys. Chem. 86 (**1982**) 1247-1250

[110] D. Freude, T. Fröhlich, H. Pfeifer, G. Scheler, Zeolites 3 (**1983**) 171-177

[111] J. Klinowski, J.M. Thomas, C.A. Fyfe, G.C. Gobbi, J.S. Hartman, Inorg. Chem. 22 (**1983**) 66-71

[112] C.J.H. Jacobsen, C. Madsen, T.V.W. Janssens, H.J. Jakobsen, J. Skibsted, Micropor. Mesopor. Mater. 39 (**2000**) 393-401

[113] S. Svelle, L. Sommer, K. Barbera, P.N.R. Vennestrøm, U. Olsbye, K.-P. Lillerud, S. Bordiga, Y.-H. Pan, P. Beato, Catal. Today 168 (**2011**) 38-47

[114] P.J. Goodhew, J. Humphreys, R. Beanland, *Electron Microscopy and Analysis*, Taylor & Francis: London, 3rd Ed. (**2001**)

[115] I. Chorkendorff, J. W. Niemantsverdriet, *Concept of Modern Catalysis and Kinetics*, Wiley-VCH Verlag GmbH&Co. KGaA, Weinheim, (**2003**)

[116] J.C. Groen, T. Bach, U. Ziese, A.M. Paulaime-van Donk, K.P de Jong, J.A. Moulijn, J. Perez-Ramirez, J. Am. Chem. Soc. 125 (**2005**) 10792-10793

[117] H. Imai, Y. Oaki, MRS Bull. 35 (**2010**) 138-144

[118] M. Weyland, Top. Catal. 4 (**2002**) 175-183

[119] A.K. Datye, J. Catal 216 (**2003**) 144-154

[120] H. Friedrich, P.E. de Jongh, A.R. Verkleij, K.P. De Jong, Chem. Rev. 109 (**2009**) 1613-1629

[121] P.A. Midgley, R.E. Dunin-Borkowski, Nat. Mater. 8 (**2009**) 217-280

[122] J.H. Lunsford, Catal. Today 63 (**2000**) 165-174

[123] M. Stöcker, Angew. Chem. Int. Ed. 47 (**2008**) 9200-9211

[124] C.D. Chang, A.J. Silvestri, J. Catal. 47 (**1977**) 249-259

[125] M. Stöcker, Micropor. Mesopor. Mater. 29 (**1999**) 3-48

[126] F.J. Keil, Micropor. Mesopor. Mat. 29 (**1999**) 49-66

[127] T. Mokrani, M. Scurell, Catal. Rev. 51 (**2009**) 1-145

[128] J.F. Haw, W. Song, D.M. Marcus, J.B. Nicholas, Acc. Chem. Res. 36 (**2003**) 317-326

[129] I.M. Dahl, S. Kolboe, Catal. Lett. 20 (**1993**) 329-336

[130] I.M. Dahl, S. Kolboe, J. Catal. 149 (**1994**) 458-464

[131] D.M. Bibby R.F. Howe, G.D. McLellan, Appl. Catal. A: General 93 (**1992**) 1-34

[132] K.G. Ione, G.V. Echevskii, G.N. Nosyreca, J. Catal. 85 (**1984**) 287-294

[133] S.M. Campbell, D.M. Bibby, J.M. Coddington, R.F. Howe, J. Catal. 161 (**1996**) 350-358

[134] D.B. Luk'yanov, Zeolites 12 (**1992**) 287-291

[135] K. Barbera, F. Bonino, S. Bordiga, T.V.W. Janssens, P. Beato, J. Catal. 208 (**2011**) 196-205

[136] J.R. Rostrup-Nielsen, Catal. Today 37 (**1997**) 225-232

[137] A.T. Aguayo, A.G. Gayubo, J.M. Ortega, M. Olazar, J. Bilbao, Catal. Today, 37 (**1997**) 239-248

[138] I. Schmidt, C. Madsen, C.J.H. Jacobsen, Inorg. Chem. 39 (**2000**) 2279-2283

[139] M. Kustova, A. Kustov, C.H. Christensen, Stud. Surf. Sci. Catal. 158 (**2005**) 255- 262

[140] Y. Huang, J. Ho, Z. Wang, P. Nakashima, A.J. Hill, H. Wang, Micropor. Mesopor. Mater. 17 (**2009**) 490-496

[141] Y. Meng, D. Gu, F. Zhang, Y. Shi, H. Yang, Z. Li, C. Yu, B. Tu, D. Zhao, Angew. Chem. Int. Ed. 44 (**2005**) 7053-7059

[142] H.E. Hoydonckx, W.M. Van Rhijn, W. Van Rhijn, D.E. De Vos, P.A. Jacobs, *Furfural and Derivatives* in Ullmann's Encyclopedia of Industrial Chemistry, 7th ed., John Wiley & Sons Inc. (**2007**)

[143] H. Müller, P. Rahak, C. Jäger, J. Hartmann, N. Meyer, S. Spange, Adv. Mater. 12 (**2000**) 1671-1675

[144] T.V.W. Janssens, J. Catal. 264 (**2009**) 130-137

[145] M.Y. Kustova, S.B. Rasmussen, A.L. Kustov, C.H. Christensen, Appl. Catal. B 67 (**2006**) 60-67

[146] K. Egeblad, M. Kustova, S.K. Klitgaard, K. Zhu, C.H. Christensen, Micropor. Mesopor. Mater. 101 (**2007**) 214-223

[147] R. Ghezini, M. Sassi, A. Bengueddash, Micropor. Mesopor. Mater. 113 (**2008**) 370-377

[148] A. Bonilla, D. Baudouin, J. Perez-Ramirez, J. Catal. 265 (**2009**) 170-180

[149] X.T. Wei, P.G. Smirniotis, Micropor. Mesopor. Mater. 97 (**2006**) 97-106

[150] J. Perez-Ramirez, S. Abello, L.A. Villaescusa, A. Bonilla, Angew. Chem. Int. Ed. 47 (**2008**) 7913-7917

[151] L. Sommer, D. Mores, S. Svelle, M. Stöcker, B.M. Weckhuysen, U. Olsbye, Micropor. Mesopor. Mater. 132 (**2010**) 384-394

[152] S. Abello, A. Bonilla, J. Perez-Ramirez, Appl. Catal. A 364 (**2009**) 191-198

[153] M.S. Holm, M.K. Hansen, C.H. Christensen, Eur. J. Inorg. Chem. 9 (**2009**) 1194-1198

[154] R. Caicedo-Realpe, J. Perez-Ramirez, Micropor. Mesopor. Mater 128 (**2010**) 91-100

[155] M. Ogura, E. Kikuchi, M. Matsukata, Stud. Surf. Sci. Catal. 135 (**2001**) 216-223

[156] M. Choi, K. Na, J. Kim, Y. Sakamoto, O. Terasaki, R. Ryoo, Nature 461 (**2009**) 246-250

[157] R.A. Beyerlein, C. Choi-Feng, J.B. Hall, B.J Huggins, G.J. Ray, Top. Catal. 4 (**1997**) 27–42

[158] C.S. Triantafillidis, A.G. Vlessidis, L. Nalbandian, N.P. Evmiridis, Micropor Mesopor Mater. 47 (**2001**) 369–388

[159] R.M. Lago, W.O. Haag, R.J. Mikovsky, D.H. Olson, S.D. Hellring, K.D. Schmitt, G.T. Kerr, Stud. Surf. Sci. Catal. 28 (**1986**) 677-684

[160] H. Najar, M. S. Zina, A. Ghorbel, Reac. Kinet. Mech. Catal. 100 (**2010**) 385–398

[161] P. Matias, J.M. Lopes, P. Ayrault, S. Laforge, P. Magnoux, M. Guisnet, F. R. Ribeiro, Appl. Catal. A: General 365 (**2009**) 207–213

[162] M. Tromp, J. A. van Bokhoven, M. T. Garriga Oostenbrink, J. H. Bitter, K. P. de Jong, D. C. Koningsberger, J. Catal. 190 (**2000**) 209–214

[163] R. Giudici, H.W. Kouwenhoven, R. Prins, Appl. Catal A: General 203 (**2000**) 101–110

[164] D. Goyvaerts, J.A. Martens, P.J. Grobet, P.A. Jacobs, Stud. Surf. Sci. Catal. 63 (**1991**) 381-395

[165] G.T. Kerr, J. Phys. Chem. 72 (**1968**) 2594-2596

[166] G. Garralón, V. Fornés, Zeolites, 8 (**1988**) 268-272

[167] S. Morin, P. Ayrault, N.S. Gnep, M. Guisnet, Appl. Catal. A: General 166 (**1998**) 281-292

[168] J. Lynch, F. Raatz, C. Delande, Stud. Surf. Sci. Catal. 39 (**1987**) 547-557

[169] J. Lynch, F. Raatz, P. Dufresne, Zeolites 7 (**1987**) 333-340

[170] J.C. Groen, J.A. Moulijn, J. Perez-Ramirez, Micropor. Mesopor. Mater. 87 (**2005**) 153-161

[171] C.A. Fyfe, G.C. Gobbi, G.J. Kennedy, J. Phys. Chem. 88 (**1984**) 3248-3253

[172] P. Sazama, J. Dedecek, V. Gabova, B. Wichterlova, G. Spoto, S. Bordiga, J. Catal. 254 (**2008**) 180-189

[173] A. Omegna, M. Haouas, A. Kogelbauer, R. Prins, Micropor. Mesopor. Mater. 46 (**2001**) 177-184

[174] O.H. Han, C.S. Kim, S.B. Hong, Angew. Chem. Int. Ed. 41 (**2002**) 469-472

[175] D. Massiot, B. Touzo, D. Trumeau, J.P. Coutures, J. Virlet, P. Florian, P.J. Grandinetti, Solid State Nucl. Magn. Reson. 6 (**1996**) 73-83

[176] S. Sklenak, J. Dedecek, C. Li, B. Wichterlova, V. Gabova, M. Sierka, J. Sauer, Angew. Chem. Int. Ed. 46 (**2007**) 7286-7289

[177] H. Kosslick, V.A. Tuan, B. Parlitz, R. Fricke, C. Peuker, W. Storek, J. Am. Chem. Soc. Faraday Trans 89 (**1993**) 1131-1138

[178] R. Fricke, H. Kosslick, G. Lischke, M. Richter Chem. Rev. 100 (**2000**) 2303-2404

[179] A. Hagen, F. Roessner, Catal. Rev. Sci. Eng. 42 (**2000**) 403-437

[180] C.R. Bayense, J.H.C. van Hooff, Appl. Catal. A 79 (**1991**) 127-140

[181] A. Raj, J.S. Reddy, R. Kumar, J. Catal. 138 (**1992**) 518-524

[182] R. Kumar, K.R. Reddy, Micropor. Mater. 3 (**1994**) 195-200

[183] J.R. Mowry, R.F. Anderson, J.A. Johnson, Oil Gas J. 83 (**1985**) 128-131

[184] K. Yogo, S. Tanaka, M. Ihara, T. Hishiki, E. Kikuchi, Chem. Lett. (**1992**) 1025-1028

[185] E. Lalik, X. Liu, L. Klinowski J. Phys. Chem. 96 (**1992**) 805-809

[186] V.R. Choudhary, A.K. Kinage Zeolites 15 (**1995**) 732- 738

[187] V.N. Romannikov, L.S. Chumachenko, V.M. Mastikhin, K.G. Ione, React. Kinet. Catal. Lett 29 (**1985**) 85-91

[188] V.R. Choudhary, V.S. Nayak, Zeolites 5 (**1985**) 325-328

[189] G.P. Handreck, T.D. Smith J. Catal 123 (**1990**) 513-522

[190] K.T. Leth, A.K. Rovik, M.S. Holm, M. Brorson, H.J. Jakobsen, J. Skibsted, C.H. Christensen, Appl. Catal. A: General 348 (**2008**) 257-265

[191] F. Bleken, M. Bjørgen, L. Palumbo, S. Svelle, K.P. Lillerud, U. Olsbye, Top. Catal. 52 (**2009**) 218

[192] C.O. Areán, G.T. Palomino, F. Geobaldo, A. Zecchina, J. Phys. Chem. 100 (**1996**) 6678-6690

[193] A.Y. Khodakov, L.M. Kustov, T.N. Bondarenko, A.A. Dergachev, V.B. Kazansky, M.K. Minachev, G. Borbely, H.K. Beyer, Zeolites (**1990**) 603-607

[194] I. Mirsojew, S. Ernst, J. Weitkamp, H. Knözinger, Catal. Lett. 24 (**1994**) 235-248

[195] G.C. Bond, P.A. Sermon, G. Webb, D.A. Buchanan, P.B. Wells, J. Chem. Soc., Chem. Commun. 13 (**1973**) 444-445

[196] A. Stephen, K. Hashmi, G.J. Hutchings, Angew. Chem. Int. Ed 45. 45 (**2006**) 7896-7936

[197] E. Taarning, A.T. Madsen, J.M. Marchetti, K. Egeblad, C.H. Christensen, Green Chem. 10 (**2008**) 408-414

[198] C.H. Christensen, B. Jørgensen, J. Rass-Hansen, K. Egeblad, R. Madsen, S.K. Klitgaard, S.M. Hansen, M.R. Hansen, H.C. Andersen, A.A. Riisager, Angew. Chem. Int. Ed. 45 (**2006**) 4648-4651

[199] C.D. Pina, E. Falletta, L. Prati, M. Rossi, Chem. Soc. Rev. 37 (**2008**) 2077-2095

[200] A. Wolf, F. Schüth, Appl. Catal. A 226 (**2002**) 1-13

[201] M. Haruta, Chem. Rec. 3 (**2003**) 75-87

[202] P. Haider, B. Kimmerle, F. Krumeich, W. Kleist, J.-D. Grunwaldt, A. Baiker, Catal. Lett. 125 (**2008**) 169-176

[203] P. M. Arnal, M. Comotti, F. Schüth, Angew. Chem. Int. Ed. 45 (**2006**) 8224-8227

[204] R.I. Nooney, A.E. Ostafin, T. Dhanasekaran, Y. Chen, R. Josephs, Adv. Mater 14 (**2002**) 529-532

[205] A. Chaumonnot, A. Coupe, C. Sanchez, C. Boissiere, D. Grosso, US Patent 7807598 (**2008**)

[206] Q. Wang, D.F. Shantz, J. Solid State Chem. 181 (**2008**) 1659-1669

[207] J. C. Fierro-Gonzalez, Y. Hao, B. C. Gates, J. Phys. Chem. C 111 (**2007**) 6645-6651

[208] W.J. Roth, J.C. Vartuli, Stud. Surf. Sci. Catal. 157 (**2005**) 91-110

[209] T.M. Salama, R. Ohnishi, T. Shido, M. Ichikawa, J. Catal. 156 (**1996**) 169-178

[210] Y.-M. Kang, B.-Z. Wan, Appl. Catal. A: General 128 (**1995**) 53-60

[211] D. Guillemot, M. Polisset-Thfoin, J. Fraissard, Catal. Lett. 41 (**1998**) 143-148

[212] S.M. Kanan, C.P. Tripp, R.N. Austin, H.H. Patterson, J. Phys. Chem. B 105 (**2001**) 9441-9448

[213] Z.X. Gao, Q. Sun, H.-Y. Chen, X. Wang, W.M.H. Sachtler, Catal. Lett. 72 (**2001**) 1-5

[214] K. Kuge, G. Calzaferri, Micropor. Mesopor. Mater. 66 (**2003**) 15-20

[215] I. Mekkawy, M.M. Mohamed, Egypt. J. Sol. 25 (**2002**) 115-123

[216] T.M. Salama, R. Ohnishi, M. Ichikawa, Chem. Commun. (**1997**) 105-106

[217] H. Yang, H. Chen, J. Chen, O. Omotoso, Z. Ring, J. Catal. 243 (**2006**) 36-42

[218] S. Hashimoto, T. Uwada, H. Masuhara, T. Asahi, J. Phys. Chem. C 112 (**2008**) 15089-15093

[219] L.M. Liz-Marzán, M. Giersig, P. Mulvaney, Langmuir, 12 (**1996**) 4329-4335

[220] D.V. Goia, E. Matijevic, Colloid Surface A 146 (**1999**) 139-152

[221] W. Stöber, A. Fink, E. Bohn, J. Colloid Interf. Sci. 26 (**1968**) 62-69

[222] C.S. Cundy, P.A. Cox, Micropor. Mesopor. Mater. 82 (**2005**) 1-78

[223] P. Botella, A. Corma, M.T. Navarro, Chem. Mater. 19 (**2007**) 1979-1983

[224] IZA homepage, High-alumina ZSM-5 zeolite synthesis (www.iza-online.org/synthesis/recipes/high-alumina\%20ZSM-5.html, 10.04.09

[225] Z. Wu, J. Suhan, R. Jin, J. Mater 19 (**2009**) 622-626

[226] J. Rathousky, A. Zukal, N. Jaeger, G. Schulz-Ekloff, Nanostruct. Mater. 1 (**1992**) 355-360

[227] C. Marsden, E. Taarning, D. Hansen, L. Johansen, S.K. Klitgaard, K. Egeblad, C.H. Christensen, Green Chem. 10 (**2008**) 168-170

[228] S.K. Klitgaard, A.T. DeLa Riva, S. Helveg, R.M. Werchmeister, C.H. Christensen, Catal. Lett. 126 (**2008**) 213-217

[229] F. Brühne, E. Wright, *Benzaldehyde* in Ullmann's Encyclopedia of Industrial Chemistry, Wiley-VCH, Weinheim, 6 (**2002**) 1-13

[230] T. Mallat, A. Baiker, Chem. Rev. 104 (**2004**) 3037-3058

[231] H. Topsøe, B.S. Clausen, F.E. Massoth, *Hydrotreating Catalysis - Science and Technology*, Springer-Verlag Berlin Heidelberg, New York, (**1996**)

[232] C. Baird, M. Cann, *Environmental Chemistry*, 3rd Edition, W. H. Freeman, New York, (**2005**)

[233] US EPA, Diesel Fuel Quality: Advance Notice of Proposed Rulemaking, EPA420-F-99-011, Office of Mobile Sources, May (**1999**)

[234] M. Brorson, A. Carlsson, H. Topsøe, Catal. Today 123 (**2007**) 31-36

[235] J.V. Lauritsen, J. Kibsgaard, G.H. Olesen, P.G. Moses, B. Hinnemann, S. Helveg, J.K. Nørskov, B.S. Clausen, H. Topsøe, E. Lægsgaard, F. Besenbacher, J. Catal. 249 (**2007**) 220-233

[236] J.V. Lauritsen, M. Nyberg, J.K. Nørskov, B.S. Clausen, H. Topsøe, E. Lægsgaard, F. Besenbacher J. Catal. 224 (**2004**) 94-106

[237] J. Kibsgaard, J.V. Lauritsen, E. Lægsgaard, B.S. Clausen, H. Topsøe, F. Besenbacher J. Am. Chem. Soc. 128 (**2006**) 13950-13958

[238] K.G. Knudsen, B. Cooper, H. Topsøe, Appl. Catal. A: General (**1999**) 205-215

[239] H. Topsøe, Appl. Catal. A: General 322 (**2007**) 3-8

[240] B. Pawelec, R.M. Navarro, J.M. Campos-Martin, J.L.G. Fierro, Catal. Sci. Tech. 1 (**2011**) 23-42

[241] M. Breysse, P. Afanasiev, C. Geantet and M. Vrinat, Catal. Today, 86 (**2003**) 5–16

[242] G. Muralidhar, B. N. Srinivas, M. S. Rana, M. Kumar and S. K. Maity, Catal. Today, 86 (**2003**) 45–60

[243] R. Tian, B. Shen, F. Wang, C. Lu and C. Xu, Energy Fuels, 23 (**2009**) 55–59

[244] T. D. Tang, C. Yin, L. Wang, Y. Ji and F. S. Xiao, J. Catal., 257 (**2008**) 125–133

[245] M.T. Pope, *Heteropoly and Isopoly Oxometalates*, Springer-Verlag, Berlin, (**1983**)

[246] A.L. Nolan, C.C. Allen, R.C. Burns, D.C. Craig, G.A. Lawrance, Aust. J. Chem. 51 (**1998**) 825-834

[247] J.S. Anderson, Nature 150 (**1937**) 850

[248] L. Chen, K. Zhu, L.-H. Bi, A. Suchopar, M. Reicke, G. Mathys, H. Jaensch U. Kortz, R.M. Richards, Inorg. Chem. 46 (**2007**) 8457-8459

[249] A. Corma, H. Garcia, A. Moussaif, M.J. Sabater, R. Zniber, A. Redouane, Chem. Commun. (**2002**) 1058-1059

[250] S. Xiang, Y. Zhang, Q. Xin, C. Li, Angew. Chem. Int. Ed. 41 (**2002**) 821-824

[251] M.C. Jones, R. Raja, J.M. Thomas, B.F.G. Johnson, D.W. Lewis, J. Rouzaud, K.D.M. Harris, Andew. Chem. Int. Ed. 42 (**2003**) 4326-4331

[252] Y. Cao, J.C. Hu, P. Yang, W.L. Dai, K.N. Fan, Chem. Commun. (**2003**) 908-909

[253] C. Hess, M.H. Looi, S.B.A. Hamid, R. Schlögl, Chem. Commun. (**2006**) 451-453

[254] D.-H. Lee, M. Choi, B.-W- Yoo, R. Ryoo, Chem. Commun. (**2009**) 74-76

[255] K.C. Vrancken, K. Possemiers, P. van Der Voort, E.F. Vasant, Colloid Surface A: Phys. Eng. 98 (**1995**) 235-241

[256] G. Muralidhar, F.E. Massoth, J. Shabtai, J. Catal. 85 (**1984**) 44-52

[257] A.M. Venezia, F. Raimondi, V. La Parola, G. Deganello, J. Catal. 194 (**2000**) 393-400

Appendix

Characterization of mesoporous H-ZSM-5 zeolites after desilication and dealumination by FTIR and solid-state NMR spectroscopy

Søren Sørensen[a], Karen T. Højholt[b,c], Peter N. R. Vennestrøm[b], Katia Barbera[d],
Francesca Bonino[d], Silvia Bordiga[d], Henrik Fordsmand[b],
Pablo Beato[b,*], Jørgen Skibsted[a,*]

[a] Instrument Centre for Solid-State NMR Spectroscopy, Department of Chemistry and Interdisciplinary Nanoscience Center (iNANO), Aarhus University, DK-8000 Aarhus, Denmark

[b] Haldor Topsøe A/S, Nymøllevej 55, 2800 Kgs. Lyngby, Denmark

[c] Center for Catalysis and Sustainable Chemistry, Department of Chemistry, Technical University of Denmark, Building 206, DK-2800 Kgs. Lyngby, Denmark

[d] Department of Inorganic, Physical and Materials Chemistry, NIS Centre of Excellence and Centro di Riferimento INSTM, University of Turin, I-10125 Torina, Italy

[*] Email: pabb@topsoe.dk, fax: +45 4527 2999

---

*Corresponding authors:

[*] E-mail addresses: pabb@topsoe.dk (P. Beato) and jskib@chem.au.dk (J. Skibsted)

1. Introduction

Zeolites are crystalline microporous aluminosilicates composed of AlO_4 and SiO_4 tetrahedra, widely used as catalysts in the petrochemical industry for interconversion of organic molecules in the liquid and gaseous phase [1-3]. The microporous structural character of zeolites with well-defined pores and cavities of molecular dimensions provides high selectivity in catalytic and separation processes for a wide range of molecules of the dimensions of roughly 5 – 12 Å. but the sole microporous network also limits the mass-transfer properties of reactants and products for large zeolite particles. The Zeolite Socony Mobil 5 (ZSM-5) zeolite [4-6] can convert methanol to hydrocarbons (MTH) similar to those in the gasoline fraction of conventional petroleum and thus, it offers a powerful alternative route to the production of gasoline from crude oil. Recent years significant increase in energy prices have made the methanol-to-gasoline (MTG) process very attractive and provided well-established routes for conversion of coal, natural gas and bio-mass feedstocks to methanol [7-9].

The unique properties of ZSM-5 are related to its high internal surface area, channel shapes and sizes (5.3x5.6 Å) that makes it attractive for the MTH process as well as its slow rate of deactivation as compared to other catalysts [10,11,12]. Moreover, the strength and number of strong Brønsted acid sites in the zeolitic framework, mainly obtained by substitution of Al^{3+} into the tetrahedral framework sites, can be tailored by acid treatment for specific applications. However, the microporosity of the samples may result in an inefficient utilization of the internal surfaces as a result of diffusion resistance for large molecules and the fact that only the channels near to the surface of the grains are accessible to catalytic reactions. In recent years there has been an increasing research interest for improving the diffusional properties of zeolites through creation of mesopores in the zeolite particles without altering the molecular scale channels and cavities [11,12-24]. Generally, two approaches are used corresponding to mesopore-templating and post-synthesis chemical treatment. The formation of mesopores not only improves the molecular diffusion in the hierarchical zeolite but also entails slower formation of deactivating coke, thereby improving the catalyst life-time in the MTH/MTG processes.

This work focuses on mesoporous H-ZSM-5 samples used in the MTG process and the structural changes that occur, particularly for the catalytical sites, upon mesopore formation by alkali leaching. This includes a parent, microporous H-ZSM-5 sample and the mesoporous samples prepared from this material by disilication and sequential desilication–dealumination post-treatment. The three samples are initially characterized by powder X-ray diffraction, scanning-electron microscopy, temperature-programmed desorption of ammonia, N_2 adsorption and more thoroughly by FT-infrared spectroscopy and ^{27}Al and ^{29}Si MAS NMR techniques. Finally, activity measurements have been conducted to provide complimentary structural information.

2. Experimental

2.1 Synthesis of ZSM-5 zeolites

The synthesis of conventional, microporous ZSM-5 employed 54.5 g tetrapropylammonium hydroxide (TPAOH, 40wt%), diluted with 55.31g H_2O. This mixture was cooled to 0 °C on an ice bath and 0.652 g $NaAlO_2$ was added and stirred until a clear solution was obtained. 54.29 g Ludox® TMA was then slowly added followed by addition of 10.34 g sodium silicate, resulting in the following composition of the synthesis gel: $SiO_2{\cdot}0.05Na_2O{\cdot}0.15TPA_2O{\cdot}20.5H_2O{\cdot}0.01Al_2O_3$. The homogeneous gel was subjected to stirring over night, by which the ice was melted, and the next day the gel was transferred to a Teflon-lined stainless steel autoclave and heated to 423 K for 48 hours under static conditions. After cooling the autoclave to room temperature the white product was isolated by suction filtration and washed several times with water until neutral pH was obtained. The product was dried overnight at room temperature and finally the organic template was removed by calcination in a muffle furnace at 823 K for 3 hours. The calcined conventional ZSM-5 was treated with a 0.3 M NaOH solution for 30 minutes at 343 K, followed by cooling on ice to stop the desilication and then washed three times with water followed by centrifugation. The ratio between mass of sample (g) and volume of NaOH (mL) was 3:100. The desilicated ZSM-5 was dried over night at room temperature before further treatment.

The acidic form of the parent zeolite and the desilicated zeolite were produced by two consecutive ion exchanges with a buffer solution of 1.7 M NH_4NO_3/0.94 M NH_3 in the ratio 1:10 between mass of sample (g) and volume of NH_4NO_3/NH_3 (mL). The ion exchanges were performed at 353 K with stirring for two hours. After each exchange, the NH_4-form of the zeolites were filtered, washed with water, and dried in air at 383 K. Finally, the H-form of the parent zeolite and desilicated zeolite were obtained by heating the NH_4-form in air to 823 K for 3 hours. The desilicated H-ZSM-5 was further treated with a 1.0 M oxalic acid solution for 1 hour at 353 K to remove extra-framework aluminum possibly formed during the desilication. After dealumination the sample was washed with water until neutral pH was obtained, then dried overnight at room temperature, and finally calcined at 823 K for 3 hours. The three prepared samples will in the following be designated H-ZSM-5 (no treatment), H-ZSM-5-desil (desilicated) and H-ZSM-5-desil/dealu (desilicated and dealuminated).

2.2 Characterization techniques

All characterization was made after ion exchange and calcination of the three samples. Powder X-ray diffraction (XRD) patterns of the zeolite samples were recorded on a Phillips diffractometer using Cu $K_{\alpha 1}$ radiation (λ = 1.541 Å) in the 2θ interval 5 – 70°. Elemental analysis was performed by Inductively Coupled Plasma Optical Emission Spectroscopy (ICP-OES) and used to determine the exact amount of Si and Al in the three ZSM-5 type zeolites. Surface area, pore volume and the adsorption isotherms were determined by nitrogen adsorption and desorption measurements at liquid nitrogen temperature on a Micromeritics ASAP 2020 instrument. The samples were outgassed in vacuum at 573 K for 16 h prior to measurements. The total surface area was calculated according to the BET method, the micropore volumes were determined by the t-plot method and the mesopore volume was determined by the BJH method. The crystal size and morphology of the zeolites were examined by scanning electron microscopy (SEM) on a Philips XL-30 FEG. The calcined zeolite samples were placed on a carbon film and Ag was evaporated onto the sample for approximately 20 minutes to achieve sufficient conductivity.

CO-FTIR measurements at 77 K have been performed on self supporting pellets pre-activated in vacuo and heated up to 150, 350°C and 500°C for 1 h respectively. CO adsorption at low temperature has been performed on sample pre-activated at 350 and 500°C. The spectra have been registered at decreasing pressure of CO in the cell, using a Nicolet 6700 spectrometer operating in transmission mode with a resolution of 2 cm^{-1} and a MCT detector.

^{27}Al MAS NMR spectra were recorded on a Varian Direct Drive VNMRS-600 spectrometer (14.1 T, ^{1}H decoupling) using a home-built CP/MAS probe for 4mm o.d. rotors and a spinning speed of ν_R = 13.0 kHz. The single-pulse spectra employed a 0.5 μs excitation pulse for an rf field strength of $\gamma B_1/2\pi$ = 60 kHz, a 2-s repetition delay, and ^{1}H decoupling ($\gamma B_1/2\pi$ ≈ 60 kHz) during acquisition. The MQMAS spectra were obtained with the three-pulse *z*-filter sequence [25] with ^{1}H decoupling during both the evolution (t_1) and detection (t_2) periods, using rf field strengths of $\gamma B_1/2\pi$ = 60 kHz for the triple-quantum excitation and conversion pulses and $\gamma B_1/2\pi$ ≈ 25 kHz for the soft *z*-pulse, 72 increments in the t_1 dimension, a 144 step phase cycle, a 2-s relaxation delay, and 864 scans. The ^{29}Si MAS NMR spectra were recorded on a Varian INOVA-400 Spectrometer (9.4 T) using a home-built CP/MAS probe for 5 mm o.d. rotors, a spinning speed of ν_R = 10.0 kHz, a 2.5 μs excitation pulse (~ 45° flip angle for $\gamma B_1/2\pi$ ≈ 50 kHz), and a recycle delay of 30 s. The ^{29}Si{^{1}H} CP/MAS NMR spectra (9.4 T, ν_R = 3.0 kHz) employed rf field strengths of $\gamma B_1/2\pi \approx \gamma B_2/2\pi \approx$?? kHz for ^{29}Si and ^{1}H , respectively, during the CP contact period and ($\gamma B_2/2\pi \approx$?? kHz for the initial 90° ^{1}H pulse and the ^{1}H decoupling during acquisition. Chemical shifts are referenced to $AlCl_3{\cdot}6H_2O$ and tetramethyl silane (TMS) for ^{27}Al and ^{29}Si, respectively.

The acidic properties of the zeolites were characterized by temperature programmed desorption of ammonia (NH_3-TPD), using the following procedure: 40 mg of the sample was loaded into a quartz tube reactor and pre-treated by heating the sample to 500°C in a flow of nitrogen (75 ml/min, heating ramp 20 ºC). The temperature was kept for 120 min before cooling to 150 °C. At this temperature the NH_3 gas was adsorbed by switching to 2% NH_3/He (75ml/min) for 30 min. To remove physically adsorbed ammonia the sample was flushed with N_2 (75 ml/min) at 150 ºC for 4 hours prior to desorption measurements. Subsequently, the sample was heated to 600 ºC (heating ramp 10 ºC/min). The rate of NH_3 desorption was monitored by measuring the weight loss of the sample with TGA. The total amount of desorbed NH_3 was calculated from the area under the TPD curve assuming one NH_3 molecule per acid site. The crystal size and morphology of the different zeolite samples was examined by scanning electron microscopy (SEM) on a Phillips XL-30 FEG. The calcined zeolite samples were placed on a carbon film and Ag was evaporated onto the sample for approximately 20 minutes to achieve sufficient conductivity.

2.3 Catalytic experiments

The catalytic tests were performed in a fixed-bed quartz microreactor (3mm i.d.) at atmospheric pressure. A feed of 10.5 % methanol in nitrogen was created by bubbling an adjustable flow of nitrogen through a liquid solution of methanol kept at a fixed temperature. All experiments were performed using 50 mg calcined and fractionized catalyst, a reaction temperature of 370 °C and a total gas flow of 25 mL/min through the reactor, resulting in a WHSV of 4.5 $g_{MeOH}\cdot g^{-1}{}_{cat}\cdot h^{-1}$. Before each experiment the catalyst was heated from 110 °C to the reaction temperature and kept there for 0.5 h under nitrogen flow. Products were analyzed by online gas chromatography using a HP 5890 series II instrument equipped with a PLOT fused silica column and a FID detector. Response factors for methanol (0.776) and dimethyl ether (0.667) were taken into account. For all other hydrocarbons the response factor was treated as being 1.000.

3. Results and Discussion

3.1 Basic structure and texturial properties

XRD patterns for the three ZSM-5 samples are shown in Fig. 1. It is clearly seen that all samples exclusively contain highly crystalline material with the MFI structure [26], demonstrating that the overall framework structure is preserved after desilication and dealumination. The XRD patterns show no increase in background signal in the 2θ region of 15 – 25^{o}, which would indicate the presence of non-crystalline impurities. However, the reflexions are rather broad, in particular for the desilicated and dealauminated samples, indicating that the zeolite crystals are rather small.

The SEM micrographs (Fig. 2) show that the fresh ZSM-5 crystals display a well-defined topology with separated crystals ranging in size from approx. 0.6 to 1.0 μm. Although the crystal sizes are very similar after desilication and dealumination, it is apparent that the treatment with NaOH results in significant changes, including intergrowth between the individual crystals and erosion along the edges, resulting in spongy grains with a less well-defined crystal topology compared to the parent ZSM-5. Following treatment with oxalic acid no additional textural changes appears, however, the individual crystals seem slightly more well-defined after the dealumination treatment.

3.2 Ammonia TPD and Nitrogen absorption/desorption

The NH_3-TPD profiles for the three samples (Fig. 3) allow determination of the acidic strength and the number of acid sites from the peak positions and curve areas, respectively. The NH_3-TPD profile for the parent sample has a single peak around 700 K while the NH_3-TPD profile for the desilicated sample contains two peaks centered at 550 K and 675 K. The low-temperature desorption peak (400 – 600 K) indicates weak adsorption sites which can be caused by extra-framework aluminium with no catalytical importance while the high-temperature peak (600-800 K) reflects ammonia desorption from strong Brønsted acid sites [2]. The slight shifts in peak positions can possibly reflect the difference in Si/Al ratios for the three samples as it is well established that ZSM-5 with different Si/Al-ratios exhibit different acidic properties [ref]. According to the NH_3-TPD profiles, the parent H-ZSM-5 contains primarily strong Brønsted acid sites corresponding to all aluminium being incorporated in the zeolite framework while the desilicated sample contains both framework and extra-framework aluminium sites. The H-ZSM-5-desil/dealu sample contains only a single peak centered at 650 K, with a significantly lower intensity (XX % reduction) as compared to the parent H-ZSM-5. This indicates that the dealumination treatment must not only remove extra-framework aluminium, (Al(6)), associated with Lewis acidity, but also remove tetrahedrally coordinated aluminium from the framework (Al(4)) and thereby decrease the Brønsted acidity. This agrees very well with the ^{27}Al MAS NMR spectra (*vide infra*) where a similar decrease (XX % reduction) in Al(4) is observed.

The nitrogen adsorption/desorption isotherms for the three H-ZSM_5 samples are all given in Figure 4a. The isotherm for the conventional H-ZSM-5 zeolite is the typical type 1 isotherm for microporous materials. The isotherms for the desilicated and desilicated/dealuminated sample contain a hysteresis loop at a relative pressure higher than $p/p_0=0.4$ which is a characteristic feature for mesoporous materials [6,9]. Fig. 4b shows the pore size distributions for the parent H-ZSM-5, the desilicated and the desilicated/dealuminated H-ZSM-5 samples. It is observed that during the desilication both meso- and macropores are formed which are inevitable still present after the dealumination. The mesopore diameter for the desilicated sample is rather narrow and centred around 12 nm. The presence of macropores could be due to interparticle voids caused by the rather harsh desilication method.

Table 1 shows data from the N_2 adsorption/desorption measurements and indicates that desilication/dealumination treatment causes a significant increase of external surface area. This fact is in perfect agreement to what is observed by IR spectroscopy, when we compare the spectra obtained for the three samples. The N_2 adsorption/desorption data shows a significant increast in BET surface area from 378 m^2/g to 482 m^2/g due to the NaOH treatment which is a typical characteristic feature of desilication [27]. The increase in BET surface area is mainly caused by the higher external surface area, which can be attributed to dissolution of the zeolite framework and formation of mesopores. [28,29]. The external surface area for the parent sample H-ZSM-5 is rather high for a conventional ZSM-5 which can indicate small particles in agreement with the broad peaks observed in the XRPD pattern for the H-ZSM-5 and the SEM micrographs. The total pore volume increases considerably after the desilication treatment from 0.26 to 0.99 mL/g and since the micropore volume is almost unaffected by the desilication, the increase must be due to the creation of mesopores. The dealumination treatment does not have a pronounced effect on the surface areas or pore volumes.

3.2 Solid-state NMR spectroscopy

The ^{29}Si MAS NMR spectra of the three H-ZSM-5 samples (Fig. 5) are quite similar and include the same type of resonances as observed earlier for ZSM-5 samples [30-34]. The dominating resonance at –112 ppm and the low-frequency shoulder at –116 ppm reflect purely silicious $Q^4(Si(OSi)_4)$ sites while the peaks in the range –98 ppm to –108 ppm originate from either $Q^4(AlOSi(OSi)_3)$ or $Q^3(HOSi(OSi)_3)$ sites. To obtain an improved assignment of the resonances in the latter spectral region, the H-SZSM-5-desil sample has been investigated by variable-contact time ^{29}Si{^{1}H} CP/MAS NMR (Fig. 6). The build-up of ^{29}Si magnetization in these spectra reflect the cross-polarization time (T_{SiH}) which depends on the ^{1}H – ^{29}Si dipolar couplings and thereby the internuclear ^{1}H – ^{29}Si distances. Thus, a determination of T_{SiH} for the individual peaks may assist the assignment of the resonances. The ^{29}Si{^{1}H} CP/MAS NMR spectra in Fig.4 can be deconvolved using four partly overlapping resonances at –92 , –101, –106, and –112 ppm, resulting in the intensity variations ($M_{\mathrm{x}}(t)$) with CP contact time (t) shown in Fig. 7. These intensity variations can be simulated using the expression [35]

$$M_x(t) = \frac{M^H(0)}{1 - T_{SiH}/T_{1\rho}^H}\exp(-t/T_{1\rho}^H)\left[1 - \exp\left(\left(\frac{1}{T_{1\rho}^H} - \frac{1}{T_{SiH}}\right)t\right)\right] \qquad [1]$$

where $M^{\mathrm{H}}(0)$ is the ^{1}H magnetization after the $90^{\mathrm{o}}{}_{\mathrm{y}}$ pulse and $T_{1\rho}^{\mathrm{H}}$ is the ^{1}H rotating-frame relaxation time. The expression in Eq. (1) is derived using the inverse spin-temperature approach [35] and assumes a much faster rotating-frame relaxation rate for ^{1}H as compared to ^{29}Si ($T_{1\rho}^{\mathrm{Si}} >> T_{1\rho}^{\mathrm{H}}$). The intensity for the –112 ppm resonance increases with increasing contact time for the full period of 8 ms, reflecting that $T_{1\rho}^{\mathrm{H}}$ is much longer than T_{SiH}. Thus, the simulation of the intensity assumes $T_{1\rho}^{\mathrm{Si}}, T_{1\rho}^{\mathrm{H}}$ >> T_{SiH} and thereby that the build-up of magnetization for the –112 ppm resonance (Fig. 7) is only governed by T_{SiH}, reflecting the fact the rotating-frame relaxation cannot be detected within CP contact-time of 8.0 ms which is the maximum safe value for our CP/MAS NMR probe. The ^{29}Si{^{1}H} CP parameters, $T_{1\rho}^{\mathrm{H}}$ and T_{SiH}, resulting from least-squares analysis of the data in Fig. 5 are listed in Table 2 for the 4 resonances. The large T_{SiH} value for the resonance at –112 ppm reflect the long Si–H distances for these species in agreement with the assignment as $Q^4(Si(OSi)_4)$ sites. The smallest value is observed for the –99 ppm resonance and thus, this is assigned to $Q^3(HOSi(OSi)_3)$ sites, while a somewhat larger values is observed for the $Q^4(AlOSi(OSi)_3)$ sites, i.e., Brønsted $(SiO)_3$–Si–O(H)–Al sites.

The single-pulse ^{29}Si MAS NMR spectra (Fig. 5) can all be simulated satisfactory using four overlapping peaks at -102, -106, -112, and -116 ppm, corresponding to $Q^3(HOSi(OSi)_3)$, $Q^4(AlOSi(OSi)_3)$ and two $Q^4(Si(OSi)_4)$ sites, respectively, as illustrated for the parent H-ZSM-5 sample (Fig. 5a). The resulting intensities allow calculation of the Si/Al ratio for the ZSM-5 framework, using the relationship

$$\mathrm{Si/Al} = \frac{4I(Q^4(Si(OSi)_4) + 4I(Q^4(AlOSi(OSi)_3) + 3I(Q^3(HOSi(OSi)_3)}{I(Q^4(AlOSi(OSi)_3)} \qquad [2]$$

which is the well-known formula for zeolites modified to include the non-neglible fraction of $Q^3(HOSi(OSi)_3)$ sites. The framework Si/Al ratios from this ^{29}Si MAS NMR analysis are listed in Table 2 along with the bulk Si/Al ratio from elemental analysis and the Si/Al ratio estimated from the number of acid sites from NH_3 TPD.

Additional information is achieved from the ^{27}Al MAS NMR spectra (Fig. 7), which exhibit resonances from the tetrahedral framework aluminum (δ(Al(4)) ~55 ppm) and aluminum in octahedral environments (δ (Al(6)) ~ 10 ppm to -10 ppm) assigned to non-framework Al. The minor Al(6) peak observed at 0 ppm for the parent H-ZSM-5 sample most likely reflects a small amount of un-reacted aluminum (i.e., $Al(H_2O)_6^{3+}$ species) from the synthesis, which is not incorporated in the zeolite framework. The absolute ^{27}Al NMR intensities for Al(4) and Al(6), normalized to the total intensity for the parent H-ZSM-5 sample, are summarized in Table 3. The increase in total intensity for H-ZSM-5-desilicated reflects, as expected, that a substantial amount of Si is removed by the desilication treatment. Moreover, the increase in Al(4) intensity for H-ZSM-5-desilicated is in accordance with a lowering of the Si/Al ratio (Table 3). The desilication treatment also affects aluminum since a significant part of Al (20%) is dislodged from the framework forming Al in octahedral environments. The subsequent dealumination results in an overall decrease in ^{27}Al intensity as a result of a reduction in framework Al sites as well as non-framework Al(4) species. Omegna et al. have reported similar findings on dealuminated ZSM-5 zeolites [26] and suggests the presence of tetrahedrally coordinated extra-framework Al possibly associated with an amorphous-silica phase. The reduction in Al^{tetra} intensity should be associated with an increase in Si/Al ratio, in agreement with the higher Si/Al ratio observed for H-ZSM-5-desilicated/dealuminated by NH_3-TPD (Table 3). Combining the ^{27}Al and ^{29}Si MAS NMR data the sequential desilication and dealumination treatments leads to formation of a larger fraction of Q^3 [$(SiO)_3$-SiOH] defect sites most likely associated with the formation of mesopores in the zeolite.

The presence of distinct Al(4) sites for ZSM-5 has been reported earlier by ^{27}Al MAS NMR [37-40] and to detect such possible sites for our H-ZSM-5 samples, we have investigated these by ^{27}Al MQMAS NMR (Fig. 8) in order to achieve an improved resolution by the removal of the second-order quadrupolar broadening in the isotropic (F1) dimension. The MQMAS spectra are quite similar, in particular for H-ZSM-5-desilicated and H-ZSM-5-desilicated/dealuminated. At first sight, the summed projections onto the F1 axes indicate the presence of two different Al(4) sites with isotropic triple-quantum (3Q) shifts of $\delta_{3Q} = -30.2$ ppm and $\delta_{3Q} = -29.0$ ppm for the parent H-ZSM-5. These values correspond to isotropic chemical shifts of $\delta_{iso} = 54.9 \pm 0.1$ ppm and $\delta_{iso} = 52.7 \pm 0.1$ ppm, respectively, assuming quadrupolar product parameters in the range $P_{\mathrm{Q}} = C_Q \sqrt{1 + \eta_Q^2} = 0.5 - 2.0$ MHz [29] and using the relationship

$$\delta_{3Q}^{calc} = \frac{17}{31}\delta_{iso} \quad \frac{3}{1550}\frac{\mathrm{C}_Q^2 (1 + \eta_Q^2 / 3)}{v_L^2} \times 10^6 \qquad [3]$$

for the 3Q shift of a spin $I = 5/2$. nucleus [41]. However, the contours in the MQMAS spectra are diagonal without any distinct features parallel to the F2 axis for the apparent two different Al^{tetra} sites. Thus, the F1 summations reflect a distribution in isotropic chemical shifts for correspondingly small variations/distributions in the quadrupole coupling parameters. This is most clearly seem from the plots of summed F2 slices projected onto the F1 axis in Figure 10, covering the full Al^{tetra} resonance in the MQMAS NMR spectrum. The dispersion in isotropic chemical shifts is ascribed to the distribution of Al over the large number of tetrahedral sites in the ZSM-5 structure [31]. The variation in δ_{3Q} shifts for the parent H-ZSM-5 from $\delta_{3Q} = -28.8$ ppm to -32.9 ppm correspond to isotropic chemical shifts in the range 51.2 ppm $< \delta_{iso} \leq$ 58.9 ppm in good agreement with the F2 summations in Figure X(b) and earlier reported chemical shift values for ZSM-5 samples [25,28]. A close examination of the F1 summations in Fig. 11 shows that following desilication treatment the Al^{tetra} resonances is broadened and shifts slightly towards lower δ_{3Q} frequency as compared to the parent H-ZSM-5. The desilicated/dealuminated sample appears similar to the parent H-ZSM-5 in Fig. 11. The peak maxima for the three samples are $\delta_{3Q} = -30.2$ ppm, -30.9 ppm, and -30.9 ppm, respectively, corresponding to isotropic chemical shifts of 54.7 ± 0.2 ppm, 56.0 ± 0.2 ppm, and 56.0 ± 0.2 ppm, and the variation may reflect that the desilication process has an impact on the Al^{tetra} environments in the present ZSM-5 samples.

3.3 Infrared spectroscopy

FTIR spectra of all samples, recorded at 350 and 500 °C, are displayed in figure 12. For sake of completeness, two activation temperatures were considered. In this case it has been possible to consider changes occurring at different levels of dehydration. The differences in band intensity are real and all spectra have been normalized to the pellet thickness. Parent zeolite (blue lines) shows (at both temperatures) the presence of two main features: one at 3742 cm^{-1} and 3610cm^{-1}, associated with isolated silanols and strong acid Brønsted sites, respectively. The component at higher frequency is broader in the sample activated at 350°C than that activated at 500°C. After desilication, some relevant changes occur: i) the increase of a very sharp and intense band now centered at 3745 cm^{-1}, ii) the significant decrease of the band associated with Brønsted sites and the presence of a small broader component at 3664 cm^{-1}, which was recently reported by Gil et al [35] for desilicated ZSM5 zeolites using different concentrations of NaOH as associated with extra-framework Al. Upon dealumination, no dramatic changes are visible in the OH stretching region however, a small decrease in the components at 3610 cm^{-1} and a further increase in the band at 3745 cm^{-1} are observed.

CO desorption profiles at 77K are presented in Figure 13, where it is possible to identify specific features peculiar for each sample. The spectra have been conveniently divided into two intervals namely C-O (2000-2300 cm-1) and O-H (3000-3800 cm-1) stretching regions. Red lines correspond to the spectra obtained of the activated samples, while green lines show the effect of the highest CO coverages. Black lines correspond to intermediate CO adsorption pressures. Concerning the parent sample, upon CO interaction, the band at 3745cm^{-1} is eroded giving rise a band at 3652 cm^{-1}. The small band at 3690 cm^{-1} (Al partially hydrolyzed) undergoes a red shift to 3573 cm^{-1} while the band at 3610 cm^{-1} is red shifted to 3285 cm^{-1}. In the CO stretching frequency region three components are visible at 2137, 2155 and 2175 cm^{-1}. These are assigned to physisorbed CO, CO interacting with silanols and CO interacting with strong acidic Brøndsted sites, respectively [36]. Note that the component due to silanols is not very well defined, while the band associated to CO interacting with the strong Brøndsted sites is quite sharp and symmetric.

In the desilicated sample shown in Figure 13b, the most evident changes are: i) appearance of a small band at 2230 cm^{-1}, due to CO interacting with extra-framework aluminium (an expanded view is reported in the inset); the decrease in intensity of the component centered at 2175 cm^{-1}, from CO interacting with strong Brønsted sites, and its broadening with the formation of a visible tail on the low frequency side. Moreover the presence of a broad contribution in the region of silanols that is hardly distinguishable as a distinct band is observed at very high coverages. After dealumination (Figure 8c) the main changes are: i) disappearance of CO coordinated to extra-framework Al sites (band centered at 2230 cm^{-1});

ii) better definition of the band at 2175 cm^{-1} (Brønsted sites), iii) the intensities of the band due to the acidic Brøndsted sites is further decreased but it becomes more defined and sharp.

Activity data on the three H-ZSM-5 samples are presented in figure 14. The parent sample displays high conversion efficiency up until approx. 150 hours on stream while the sequentially desilicated/dealuminated zeolite maintains high conversion longer and moreover the deactivation rate is slightly slower. The desilicated H-ZSM-5 displays a decreased conversion efficiency already around 50 hours on stream indicating a faster deactivation rate of this sample.

4. Conclusions

Mesoporous ZSM-5 zeolites have been prepared using sequential desilication and dealumination treatment without loss of crystallinity or microporous volume thereby substantially improving diffusion properties and lifetime of the catalyst in the MTG reaction. Analysis show that during desilication primarily Si is removed from the framework and a minor fraction of Al resulting in extra-framework Al species after the treatment. The mesopores formed during desilication does not disrupt the microporous network of the zeolite but a reduction in the acidic strength is seen from NH_3-TPD. Removal of unwanted extra-framework Al species is done by dealumination where all Al(6) and a significant amount of Al(4) (%) are removed. The removal of Al(4) by oxalic acid treatment suggests that different Al(4) species are present and that only some can be removed by dealumination. Further evidence for the presence of different Al(4) species is provided by the ^{27}Al MQMAS NMR spectra displaying a distribution in chemical shift values in the isotropic dimension. The distribution is slightly broader for the desilicated sample. Following dealumination a large reduction in the number of acidic sites is seen with NH_3-TPD but with a strength more similar to that of the parent zeolite. Finally the activity measurements show an increased life-time of the hierarchical zeolite particles which is attractive for many catalytical applications.

Acknowledgements

The authors wish to thank Aino Nielsen (H. Topsøe A/S) for assistance wit the SEM measurements. The use of the facilities at the Instrument Centre for Solid-State NMR Spectroscopy, Aarhus University, sponsored by the Danish Natural Science Research Council, the Danish Technical Science Research Councils, is acknowledged. The Danish Council for Independent Research | Natural Sciences (FNU) is acknowledged for equipment grants.

References:

[1] A. Corma, Chem. Rev. 97 (1997) 2373 – 2419.

[2] Corma A., Chem. Rev. 95 (1995) 559 – 614.

[3] W. Vermeiren, J.P. Gilson, Topics Catal. 52 (2009) 1131 – 1161.

[4] R.J. Argauer, G.R. Landholt, U. S. Patent 3 702 886 (1972).

[5] F.G. Dwyer, E.E. Jenkins, U. S. Patent 3 941871 (1976).

[6] G.T. Kokotailo, S.L. Lawton, D. H. Olson, W. M. Meier, Nature 272 (1978) 437 – 438.

[7] G. W. Huber, S. Iborra, A. Corma, Chem. Rev. 106 (2006) 4044 – 4098.

[8] M. A. Nowak, A. D. Paul, R. D. Srivastava, A. Radziwon, *Encyclopedia of Energy,* Vol 1 (2004) Elsevier Inc.

[9] R. G. Mallinson, Encyclopedia of Energy, Elsevier Inc. 4 (2004) 235 – 247.

[10] P. Dejaifve**,** A. Auroux**,** P.C. Gravelle, C. Jacques, J. C. Védrine**,** Z. Gabelica**,** E. G. Derouane, J. Catal. 70 (1981) 123 – 136.

[11] D.E. Walsh, L. D. Rollmann, J. Catal. 56 (1979) 195 – 197.

[12] H. Schulz, Catalysis Today 154 (2010) 183 – 194.

[13] J.C. Groen, J.A. Moulijn, J.P. Ramirez, J. Mater. Chem. 16 (2006) 2121 – 2131.

[14] J.C. Groen, L.A.A. Peffer, J.A. Moulijn, J.P. Ramirez, Chem. Eur. J. 11 (2005) 4983 – 4994.

[15] J. Fang, C. Yagang, R. Zebao, L. Yongdan, Mater. Res. 25 (2010) 272 – 282.

[16] Y. Tao, H. Kanoh, L. Abrams, K. Kaneko, Chem. Rev. 106 (2006) 896 – 910.

[17] S.S. Kim, J. Shah, T.J. Pinnavaia, Chem. Mater. 15 (2003) 1664 – 1668.

[18] J. Kim, M. Choi, R. Ryoo, J. Catal. 269 (2010) 219 – 228.

[19] T. Wakihara, K. Sato, S. Inagaki, J. Tatami, K. Komeya, T. Meguro, Y. Kubota, Applied Materials & Interfaces 10 (2010) 2715 – 2718.

[20] M. Ogura, S. Shinomiya, J. Tateno, Y. Nara, E. Kikuchi, M. Matsukata, Chem. Lett. 8 (2000) 882 – 883.

[21] M. Ogura, S. Shinomiya, J. Tateno, Y. Nara, M. Nomura, E. Kikuchi, M. Matsukata, Appl. Catal. A 219 (2001) 33 – 43.

[22] J. C. Groen, T. Bach, U. Ziese, A.M.P.V Donk, K. P. de Jong, J.A. Moulijn, J. Perez-Ramirez, *J. Am. Chem. Soc.* 127 (2005) 10792 – 10793.

[23] A. Petushkov, S. Yoon, S. C. Larsen, Microp. Mesopor. Mater. 137 (2011) 92 – 100.

[24] P. Sazama, B. Wichterlova, J. Dedecek, Z. Tvaruzkova, Z. Musilova, L. Palumbo, S. Sklenak, O. Gonsiorova, Microp. Mesopor. Mater. 143 (2011) 87 – 96.

[25] J.P. Amoureux, C. Fernandez, S. Steuernagel, J. Magn. Reson. Ser. A. 123 (1996) 116 – 118.

[26] Database of zeolite structures: http://www.iza-structure.org/databases/.

[27] M. Bjørgen, F. Joensen, M. S. Holm, U. Olsbye, K.-P. Lillerud, S. Svelle, Appl. Catal. A. General 345 (2008) 43-50

[28] J.C. Groen, J.C. Jansen, J.A. Moulijn, J. Perez-Ramires, J. Phys. Chem. B. 108 (2004) 13062-13065,

[29] J.C. Groen, J.A. Moulijn, J. Perez-Ramires, Micropor. Mesopor. Mater. 87 (2005) 153-161

[30] C. A. Fyfe, G. C. Gobbi, G. J. Kennedy, J. Phys. Chem. 88 (1984) 3248.

[32] G. L. Woolery, G. H. Kuehl, H. C. Timken, A. W. Chester, J. C. Vartuli, Zeolites 19 (1997) 288.

[34] C. J. H. Jacobsen, C. Madsen, T. W. Janssens, H.J. Jakobsen, J. Skibsted, Microp. Mesop. Mater. 39 (2000) 393.

[25] C. S. Triantafillidis, A. G. Vlessidis, L. Nalbandian, N. P. Evmiridis, Microp. Mesop. Mater. 47 (2001) 369.

[36] M. Mehring, Principles of high resolution of NMR in solids, 2nd ed, Springer-Verlag Berlin, 1983.

[37] P. Sazama, J. Dedecek, V. Gabova, B. Wichterlova, G. Spoto, S. Bordiga, J. Catal. 254, 180 (2008).

[38] Omegna A., Haouas M., Kogelbauer A., Prins R. *Microporous and Mesoporous Materials* 46 (2001) 177-184.

[39] Fyfe C.A., Gobbi G.C., Klinowski J., Thomas M., Ramdas S., *Nature* 296, 530 (1982).

[40] Han O. H., Kim C.S., Hong S.B., *Angew. Chem. Int. Ed*. 41, 469 (2002).

[41] Massiot, D.; Touzo, B.; Trumeau, D.; Coutures, J.P.; Virlet, J.; Florian, P.; Grandinetti, P.J. *Solid State Nucl. Magn. Reson.* 1996, 6, 73 - 83.

[42] Sklenak S., Dedecek J., Li C., Wichterlova B., Gabova V., Sierka M., Sauer J. *Angew. Chem. Int. Ed.* (2007), 46, p.7286-7289

[43] Gil B., Mokrzycki L., Sulikowski B., Olejniczak Z., Walas S. *Catalysis Today* 152 (2010) 24-32

[44] Bjørgen M., Svelle S., Joensen F., Nerlov J., Kolboe S., Bonino F., Palumbo L., Bordiga S., Olsbye U., *J. Catal.* 249 (2007) 195–207

Figure Captions

Figure 1.

XRPD patterns of the parent, desilicated, and desilicated – dealuminated samples of H-ZSM-5. All patterns are recorded for the calcined samples after ion-exchange to the acidic forms.

Figure 2.

SEM micrographs of (a, b) the parent H-ZSM-5, (c, d) the desilicated H-ZSM-5, and (e, f) the desilicated/dealuminated H- ZSM-5 samples. The left column images (13 x 18 μm) show the overall textures of the grains wheras the expansion in the right column (1.7 x 2.2 μm) display particle intergrowth and erosion for the desilicate and dealuminated samples.

Figure 3.

NH_3-TPD profiles of the parent, desilicated and desilicated/dealuminated samples.

Figure 4.

(a) N_2 adsorption/desorption isotherms of i) H-ZSM-5, ii) desilicated H-ZSM-5 and iii) desilicated/dealuminated H-ZSM-5. b) Pore size distribution determined from the desorption branch using the BJH method. The isotherms for the desilicated and desilicated/dealuminated ZSM-5 were off set by X and X cm^3 g^{-1}, respectively.

Figure 5.

^{29}Si MAS NMR spectra (9.4 T) of (a) the parent, (b) desilicated , and (c) desilicated/-dealuminated H-ZSM-5 samples obtained a spinning speed of ν_R = 10.0 kHz and a recycle delay of 30 s. The spectra in (b) and (c) are vertically expanded by a factor of 2 relative to the spectrum of the parent H-ZSM-5 (a).

Figure 8.

^{27}Al MAS NMR spectra (14.1 T) of the (a) parent, (b) desilicated, and (c) desilicated/-dealuminated H-ZSM-5 samples obtained with a spinning speed of ν_R = 13.0 kHz, ^{1}H decoupling and a recycle delay of 2 s. The spectra are shown on a normalized intensity scale, employing a vertical expansion of 2 for the spectrum in (c). The asterisks indicate spinning sidebands from the Al^{tetra} signal. Normalized intensities for Al^{tetra} and Al^{octa} are listed in Table 4.

Figure 3.

^{27}Al MQMAS NMR spectra (14.1 T, ν_R = 13.0 kHz) of (a) the parent, (b) the desilicated H-ZSM-5 and (c) the desilicated/dealuminated sample obtained with the three-pulse *z*-filter MQMAS sequence.

Figure 4.

Sliced spectra in the F1dimension of the ^{27}Al MQMAS spectrum for the parent, desilicated and desilicated/dealuminated H-ZSM-5 sample. The slices are taken in frequency steps of 0.5 ppm in the F2 dimension from 50.5 ppm to 59.0 ppm. Summations over the isotropic dimension (F1) of the ^{27}Al MQMAS NMR spectra for the different H-ZSM-5 samples are displayed above the sliced spectra.

Figure 11.

Summations over the F1 dimension for the three H-ZSM-5 samples.

Figure12.

FTIR spectra of zeolite samples activated at 350 and 500°C respectively

Figure 13.

CO-FTIR spectra of parent, desilicated and desilicated/dealuminated H-ZSM-5 samples.

Figure 14.

Activity data on MTH reaction for the three samples as a function of Time on Stream (ToS).

Table 1

N_2 physisorption data for the parent, desilicated and desilicated/dealuminated H-ZSM-5 samples

Sample	S_{BET} [m^2/g]	S_{ext}[a] [m^2/g]	S_{micro}[a] [m^2/g]	V_{total}[b] [mL/g]	V_{micro}[b] [mL/g]
H-ZSM-5	378	160	218	0.26	0.11
H-ZSM-5-desil	482	287	195	0.99	0.10
H-ZSM-5-desil/dealu	498	310	188	0.94	0.10

[a] Calculated by *t*-plot method, [b] Volume adsorbed at p/p_0=0.99

Table 3

Si/Al ratios for the parent, desilicated and desilicated/deauluminated H-ZSM-5 samples estimated from elemental analysis, NH_3 TPD and ^{29}Si MAS NMR

Sample	Elemental analysis[a] Si/Al	NH_3 TPD		^{29}Si NMR
		Si/Al	NH_3 capacity [mmol/g]	
H-ZSM-5	28	33	0.5	37
H-ZSM-5-desil	13	24	0.61	29
H-ZSM-5-desil/dealu	-	55	0.3	56

[a] measured by ICP-OES

Table 4

Normalized ^{27}Al NMR intensities[a] for the three H-ZSM-5 zeolites obtained from ^{27}Al MAS NMR at 14.1 T

Sample	Al (total)	Al(4)	Al(6)	Al(6)/Al(4)
H-ZSM-5	1	0.977	0.023	0.172
H-ZSM-5-desil	1.582	1.263	0.320	0.253
H-ZSM-5-desil/dealu	0.647	0.552	0.095	0.024

(a) The intensities have been normalized according to the actual amount of sample in the NMR rotor and relative to the total intensity for the parent H-ZSM-5.

Figures

Figure 1

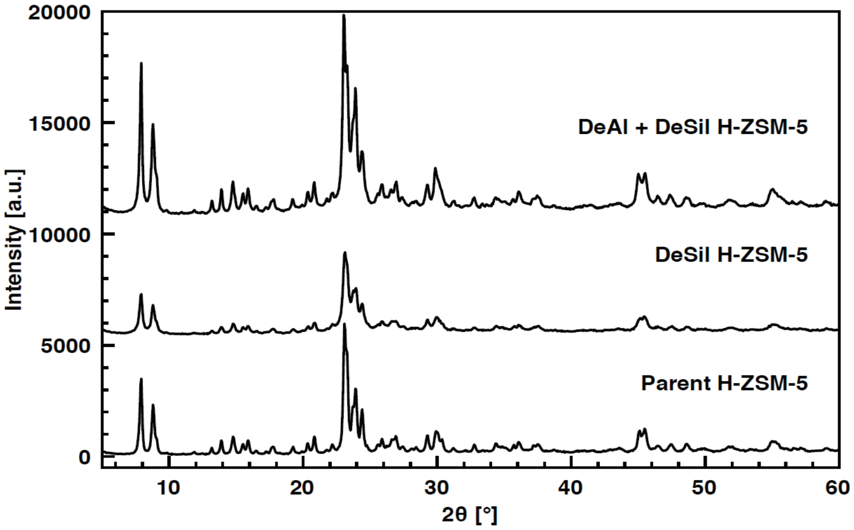

Figure 2

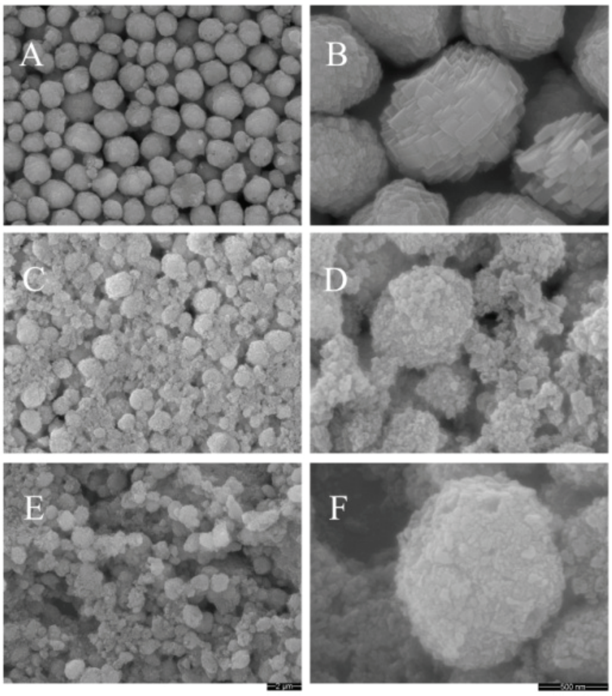

Figure 3

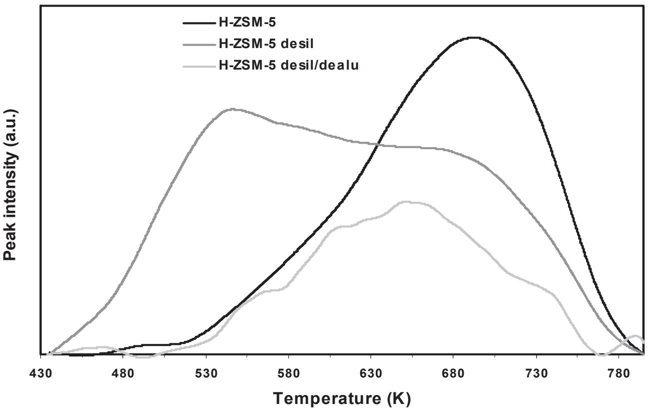

Figure 4

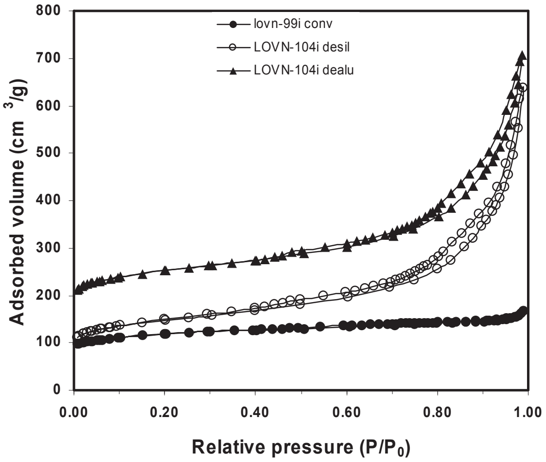

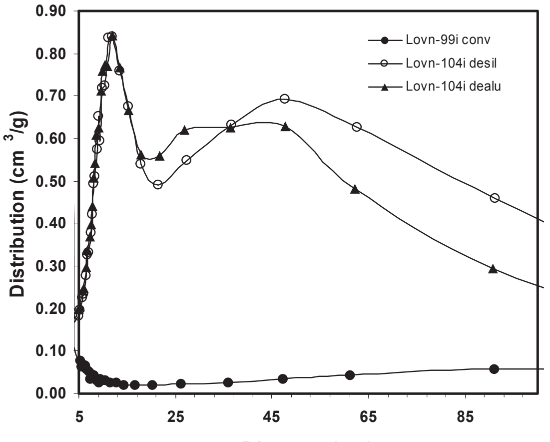

Figure 5

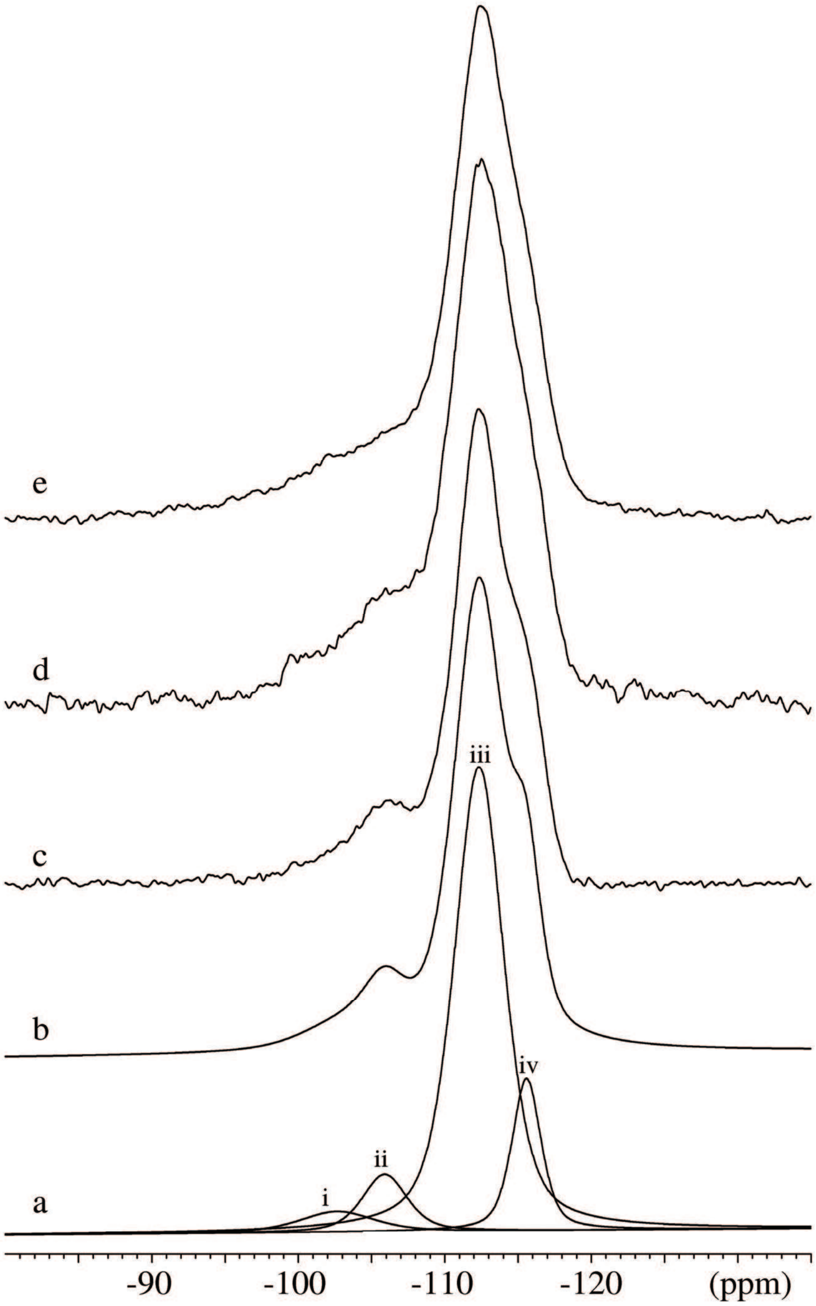

Figure 6

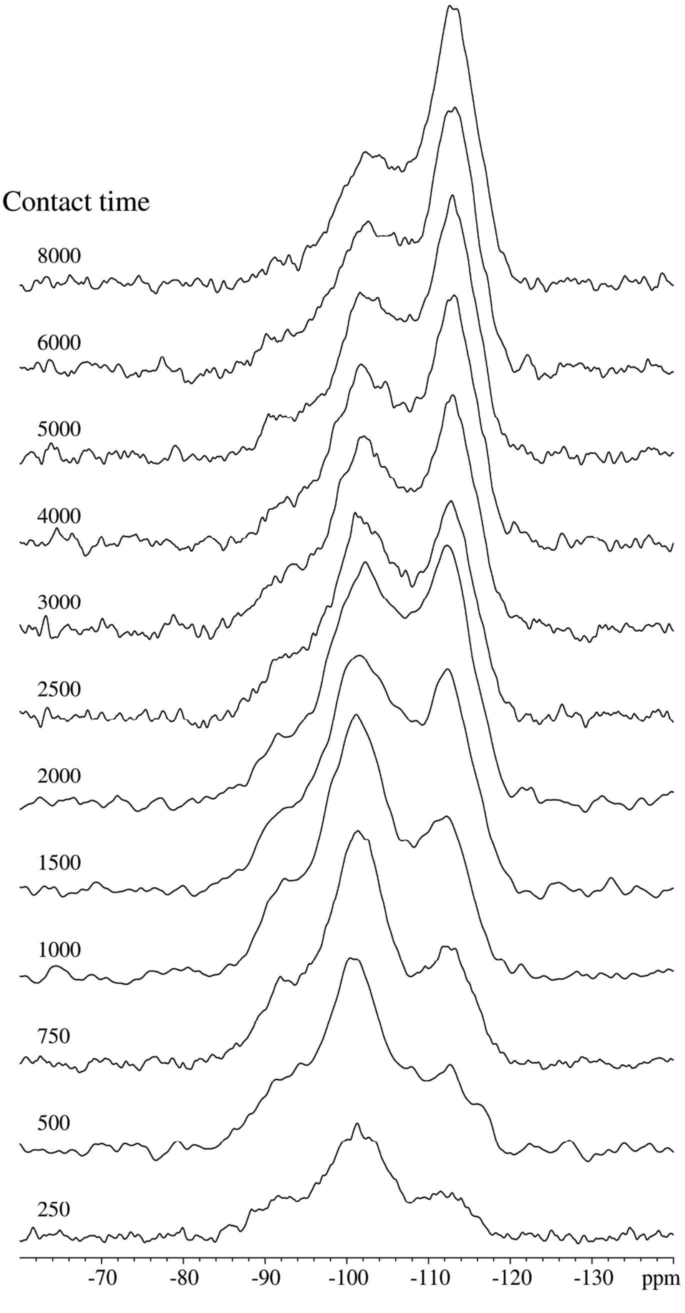
Contact time
8000
6000
5000
4000
3000
2500
2000
1500
1000
750
500
250
-70
-80
-90
-100
-110
-120
-130
ppm

Figure 7

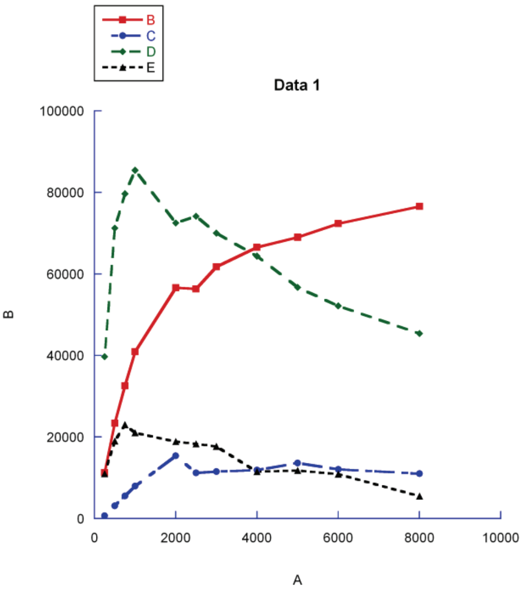

Figure 8

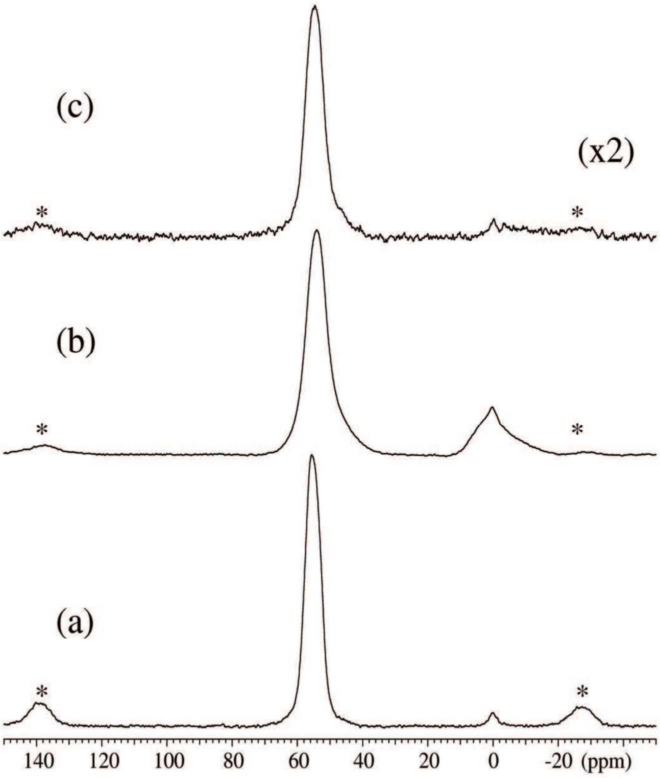

Figure 9

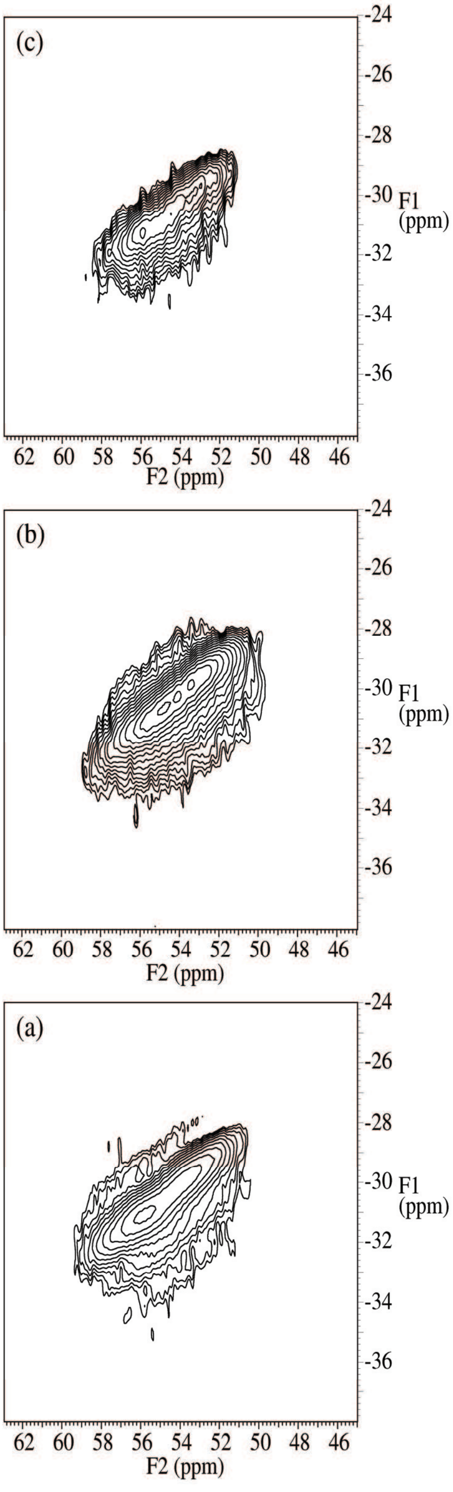

Figure 10.

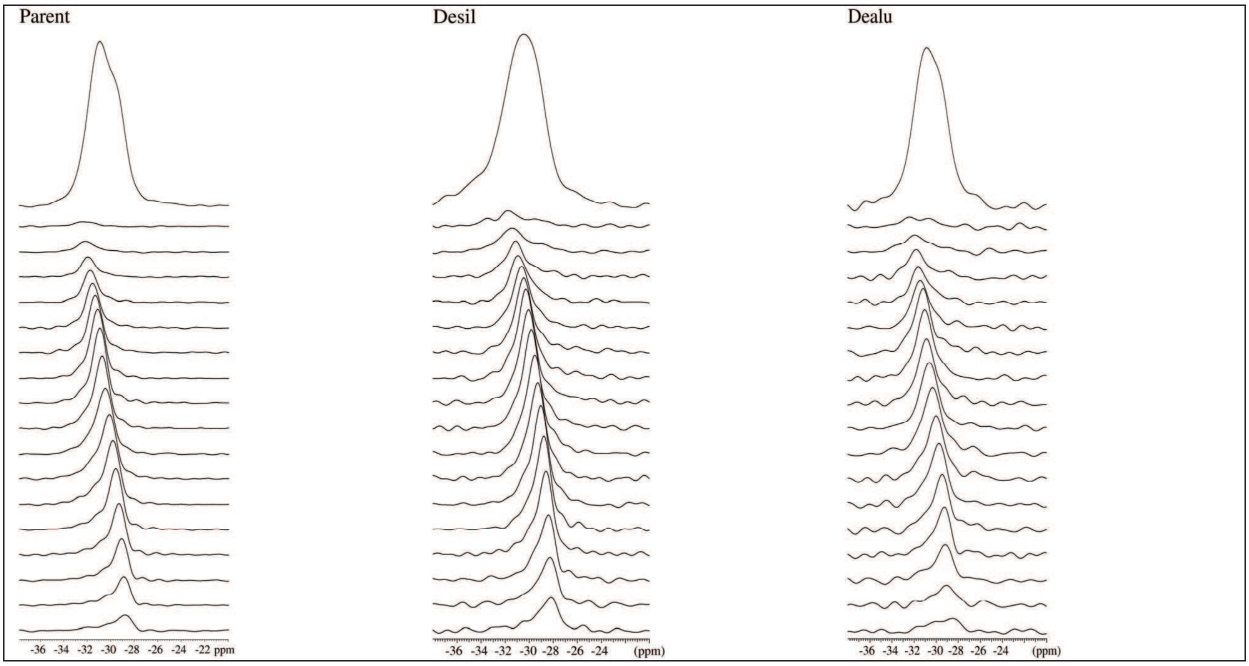

Figure 11.

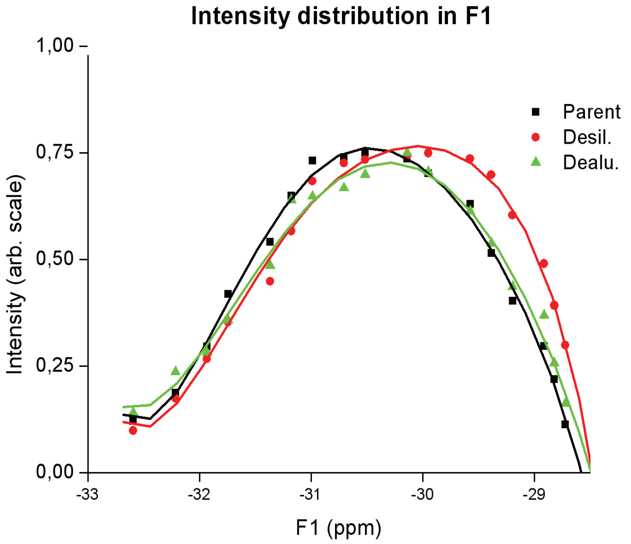

Figure 12.

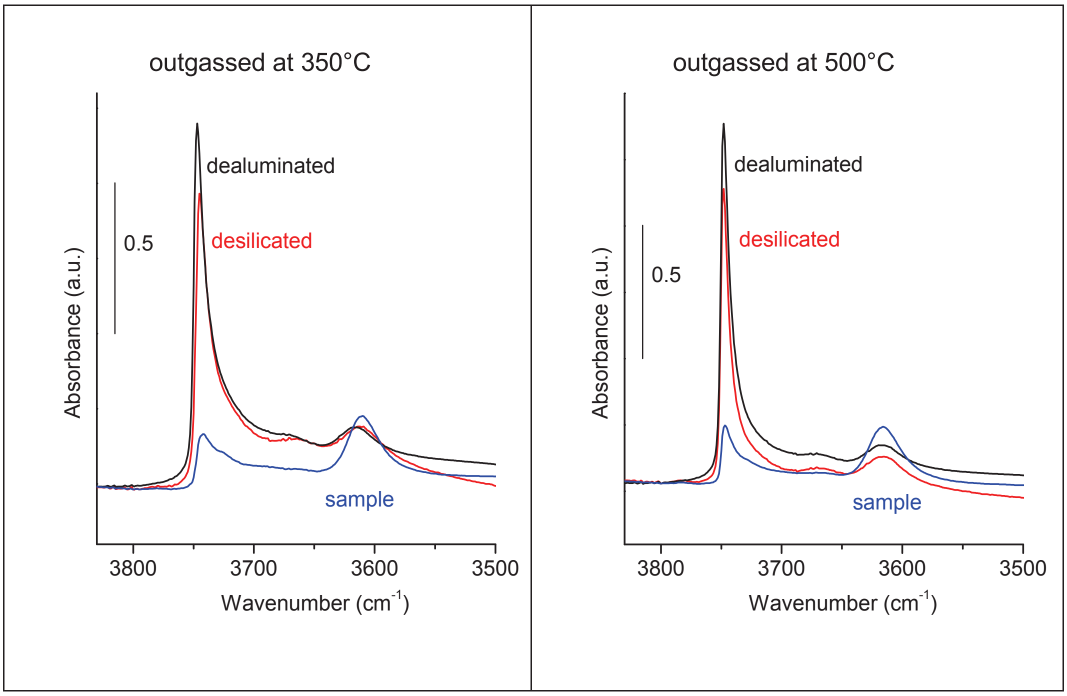
outgassed at 350°C
Absorbance (a.u.)
0.5
dealuminated
desilicated
sample
3800
3700
3600
3500
Wavenumber (cm^{-1})
outgassed at 500°C
Absorbance (a.u.)
0.5
dealuminated
desilicated
sample
3800
3700
3600
3500
Wavenumber (cm^{-1})

Figure 13.

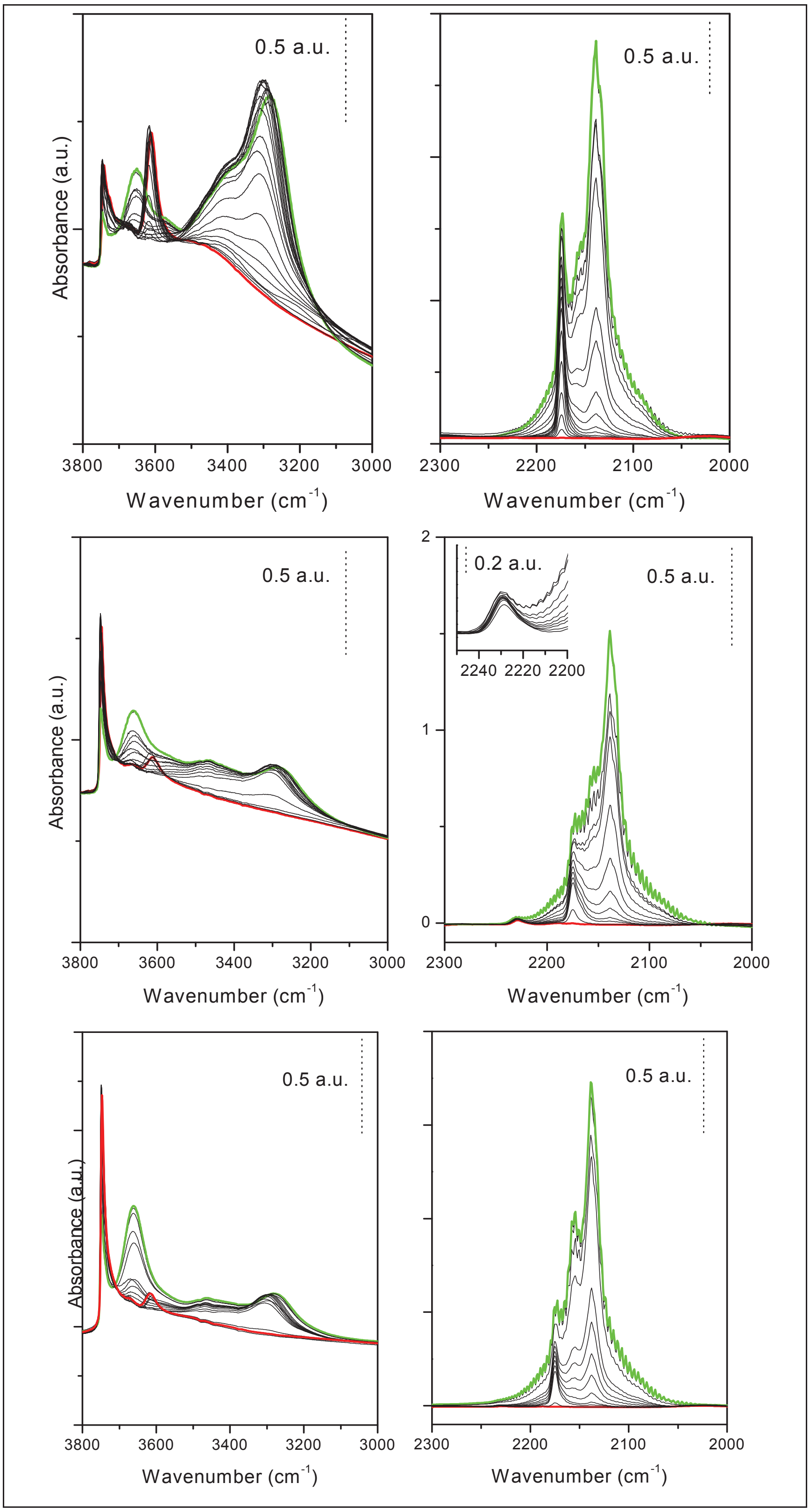
0.5 a.u.
Absorbance (a.u.)
3800
3600
3400
3200
3000
Wavenumber (cm^{-1})
0.5 a.u.
2300
2200
2100
2000
Wavenumber (cm^{-1})
0.5 a.u.
Absorbance (a.u.)
3800
3600
3400
3200
3000
Wavenumber (cm^{-1})
2
1
0
0.2 a.u.
2240
2220
2200
0.5 a.u.
2300
2200
2100
2000
Wavenumber (cm^{-1})
0.5 a.u.
Absorbance (a.u.)
3800
3600
3400
3200
3000
Wavenumber (cm^{-1})
0.5 a.u.
2300
2200
2100
2000
Wavenumber (cm^{-1})

Figure 14.

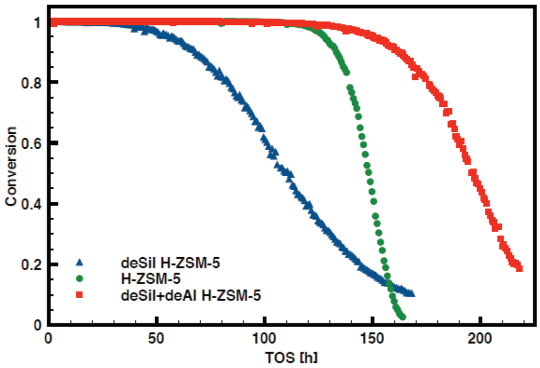

Conversion
1
0.8
0.6
0.4
0.2
0
0
50
100
150
200
TOS [h]
deSil H-ZSM-5
H-ZSM-5
deSil+deAl H-ZSM-5

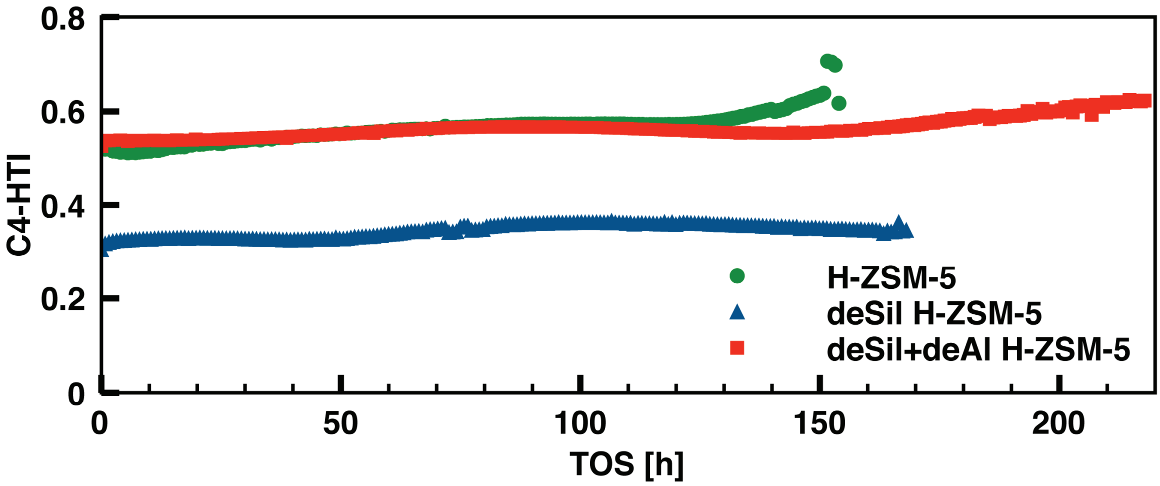

C4-HTI
0.8
0.6
0.4
0.2
0
0
50
100
150
200
TOS [h]
H-ZSM-5
deSil H-ZSM-5
deSil+deAl H-ZSM-5

Conversion of methanol to hydrocarbons over conventional and mesoporous H-ZSM-5 and H-Ga-MFI: Major differences in deactivation behavior

Uffe V. Mentzel*[,a,b], Karen T. Højholt[a,b,c], Martin S. Holm[a,b,c], Rasmus Fehrmann[a], Pablo Beato[c]

[a]Centre for Catalysis and Sustainable Chemistry, Department of Chemistry, Technical University of Denmark, Anker Engelundsvej 1, DK-2800 Kgs. Lyngby, Denmark.

[b]Center for Green and Sustainable Chemistry, Department of Chemistry, Technical University of Denmark, Anker Engelundsvej 1, DK-2800 Kgs. Lyngby, Denmark.

[c]Haldor Topsøe A/S, Nymøllevej 55, DK-2800 Kgs. Lyngby, Denmark.

uvm@kemi.dtu.dk

*Corresponding author

Abstract

Methanol has been converted to hydrocarbons over conventional and mesoporous H-ZSM-5 and H-Ga-MFI. The gallium based zeotypes are analogous to H-ZSM-5, but the Brønsted acidity is introduced by framework incorporation of gallium rather than aluminum, which leads to lower intrinsic acid strength. The catalyst lifetime is higher for the H-ZSM-5 based catalysts, but upon full deactivation the gallium zeotypes only contain very small amounts of coke. For instance, the conventional H-ZSM-5 contains 12.4 % carbon upon deactivation, while the mesoporous H-Ga-MFI contains as little as 0.2 %. This remarkable difference in coke formation is investigated further through catalytic experiments and IR measurements, and it is concluded that the mesoporous H-Ga-MFI is not deactivated by coke formation but by steaming (hydrolysis) of the Ga-O bonds in the zeolite structure.

Keywords

Zeolite, gallium, methanol-to-hydrocarbons, deactivation, regeneration

1. Introduction

In recent years there has been an increasing political and scientific focus on the depletion of world-wide oil deposits and the environmental impact of the massive usage of fossil resources. Development of alternative technologies is essential in order to meet the demands of the growing world population. The methanol-to-hydrocarbons (MTH) reaction [1] offers a plausible pathway for production of fuel grade hydrocarbons from alternative sources. Methanol is produced in large scale today, preferentially from natural gas, but it can also be produced from biomass, which could lead to a more environmentally friendly overall process.

In the MTH reaction an acidic zeolite catalyst is employed to produce hydrocarbons, primarily alkanes, alkenes, and aromatics. The product selectivity is highly dependent on the specific characteristics of the employed zeolite e.g. pore structure, acid strength, acid density etc., and the selectivity can thus be shifted towards production of alkenes (the methanol-to-olefins (MTO) process) or towards heavier compounds, such as aromatics (the methanol-to-gasoline (MTG) process). The MTG reaction was commercialized in the 1980's in New Zealand by Mobil Oil, but the gasoline production was shut down due to the situation in the global oil market [1]. The MTO process has been commercialized by UOP, while Lurgi has developed a more specialized MTP (methanol-to-propene) process and the construction of a plant with a capacity of 100,000 ton pr. year in the Middle East has been announced [2].

During the conversion of methanol, the zeolite deactivates due to formation of carbonaceous deposits (coke) on the catalyst, which must be removed by combustion in order to re-activate the catalyst. Prolongation of the catalyst lifetime between regeneration is desirable and several approaches to reach this goal are pursued, most of them dealing with optimization of the catalyst.

In a zeolite catalyst, the acidic sites are created by incorporation of a trivalent metal into the microporous framework consisting of tetravalent silicon atoms bridged by oxygen atom. In H-ZSM-5, which is the most widely used zeolite catalyst, this trivalent metal is aluminum, but other elements such as boron, gallium, or iron can also be employed [3, 4], leading to zeotype materials. In this work we focus on the H-Ga-MFI zeotype, which is analogous to H-ZSM-5, but with gallium atoms incorporated in the zeolite framework instead of aluminum. This decreases the intrinsic acidity of the individual active sites in the zeolite [5] without compromising the zeolite structure significantly [6]. Several reports exists on conversion of methanol to hydrocarbons over H-Ga-MFI zeotypes [7, 8, 9, 10], and typically a higher selectivity towards alkenes is observed compared to H-ZSM-5 due to the lower acid strength of the Brønsted sites leading to less secondary reactions converting the alkenes to aromatics [10]. Nevertheless, in some cases (especially at high gallium loadings), higher selectivity towards aromatics than for H-ZSM-5 is observed, which is ascribed to dehydrogenation reactions due to the presence of extra framework gallium species [5, 9]. During methanol conversion, the rate of formation of coke is reported to be somewhat lower for H-Ga-MFI than for H-ZSM-5, most likely as a consequence of the lower acidity of the Brønsted sites [5].

The diffusion properties of a zeolite crystal are very important, since reactants have to diffuse into the micropores to react at the active sites, and products have to leave the crystal through the micropores. One way to improve the diffusion properties of a zeolite crystal is to create mesopores in the range of 2-50 nm throughout the crystal. This means that reactants gain much easier access to the micropores in the interior of the zeolite crystal, thus improving the effectiveness of the catalyst by diminishing the transport limitations imposed by the micropores [12]. Mesoporosity can be introduced to the zeolite in a range of different ways, e.g. growing the zeolite crystals around carbon nanoparticles and subsequently combust the carbon to leave mesopores (known as carbon templating [13]) or post synthesis base treatment of the zeolite to create mesopores by removal of silicon atoms from the zeolite framework (known as desilication [14]). Mesoporous H-ZSM-5 has been used to catalyze the MTH reaction in work from several research groups, and the main attribute of the mesoporous zeolites is a prolongation of the catalyst lifetime compared to their conventional counterparts [15, 16, 17].

In this work we are studying the conversion of methanol over conventional and mesoporous H-ZSM-5 zeolites and H-Ga-MFI zeotypes. The catalysts are evaluated in terms of their product selectivity, catalyst lifetime, while special emphasis is put on the formation of coke during the reaction. The mesoporous materials in this work are synthesized via carbon templating.

2. Experimental

All reagents were of reagent grade and used without any further purification. Sodium hydroxide (NaOH, 99 wt%, Riedel-de Häen), tetrapropylammonium hydroxide (TPAOH, 40 wt%, AppliChem), aluminum isopropoxide ($C_9H_{21}O_3Al$, 98 wt%, Aldrich), tetraethylorthosilicate (TEOS, 98 wt%, Aldrich), tetrahydrofuran (THF, 99 wt%, Aldrich), Carbon Black Pearls (BP-2000, average diameter of 12 nm, Carbot Corporation), ethanol (EtOH, 99.9 wt%, Kemethyl A/S), ammonium nitrate (NH_4NO_3, 99.5 wt%, Merck), gallium nitrate hydrate ($Ga(NO_3)_3{\cdot}xH_2O$, 99.9 wt%, Aldrich), methanol (> 99.9 % Aldrich Chromasolv®).

2.1 Catalyst preparation

2.1.1 Conventional ZSM-5

The conventional ZSM-5 was a commercial sample kindly provided by Zeolyst International in its ammonia form (CBV 8014). Prior to use, the zeolite was calcined at 550 °C for 4 h to obtain the proton form.

2.1.2 Mesoporous ZSM-5

The synthesis was performed in accordance with previously published procedures [18]. BP-2000 (14 g) was dried at 110 °C overnight. Aluminum isopropoxide (0.53 g) was quickly mixed with 45 ml THF in a beaker and impregnated onto the carbon, which was left overnight at rt. In another beaker, 28 g of 40 wt% TPAOH, 3.6 g of H_2O, and 0.5 g of NaOH were mixed and stirred until a clear solution was obtained, after which 21 g EtOH was added during stirring. The carbon was impregnated with the obtained solution to incipient wetness. After evaporation of the EtOH at room temperature overnight, the carbon particles were impregnated with 27.09 g TEOS and then left to hydrolyse overnight. The impregnated carbon was transferred to a Teflon beaker which was placed in a stainless steel autoclave containing 1 cm of water to produce saturated steam. The autoclave was heated slowly to 180 °C and kept at this temperature for 72 h. Afterwards the autoclave was cooled to rt., the black product was suspended in water, filtered by suction and washed repeatedly with water until pH of the washing water was neutral. Then the product was dried at 110 °C for 10 h and the carbon black was removed by controlled combustion in air in a muffle furnace at 550 °C for 20 h. The mesoporous Na-ZSM-5 was obtained as a white solid.

2.1.3 Conventional Ga-MFI

2.108 g NaOH was dissolved in 68 g H_2O and 26.52 g TPAOH (40 wt%) was added. In another beaker 1.674 g $Ga(NO_3)_3{\cdot}xH_2O$ was dissolved in 17 g H_2O. The two obtained solutions were simultaneously added dropwise to 68 g TEOS with stirring and left for 2 h with stirring. After approximately 30 min. the mixture turned into a white thin gel. The gel was transferred to a Teflon lined autoclave, placed in an oven and heated to 180 °C for 72 h. After cooling, the gray product was filtered off, washed with water, and dried overnight at rt. The product was calcined at 550 °C for 10 h which afforded the conventional Na-Ga-MFI as a white solid.

2.1.4 Mesoporous Ga-MFI

BP-2000 (15.6 g) was dried at 110°C overnight. $Ga(NO_3)_3 \cdot xH_2O$ (0.667 g) and NaOH (0.56 g) were dissolved in 4.03 g H_2O. When a homogeneously solution was obtained, 31.08 g TPAOH (40 wt%) and 23.3 g EtOH were added. Using incipient wetness, the solution was impregnated onto the carbon and left overnight at rt. After evaporation of the EtOH at rt. overnight, the carbon particles were impregnated with 30.2 g TEOS and left to hydrolyse overnight. The impregnated carbon was transferred to a Teflon beaker which was placed in a stainless steel autoclave with 1 cm water to produce saturated steam. The autoclave was heated slowly to 180°C and kept at this temperature for 72 h. After cooling, the black product was suspended in water, filtered by suction and washed repeatedly with water until pH of the washing water was neutral. Then the product was dried at 110 °C for 10 h and the carbon black was removed by controlled combustion in air in a muffle furnace at 550 °C for 20 h. In this way mesoporous Na-Ga-MFI was obtained as a white solid.

2.1.5 Ion exchange

The three synthesized zeolite/zeotype materials contain sodium as the charge-compensating cation after synthesis. The proton form of each catalyst was obtained using the following procedure: Two consecutive ion exchanges were performed using 1M NH_4NO_3 at 80 °C in ratio 1:30 between mass of Na-zeolite or Na-zeotype (g) and volume of NH_4NO_3 solution (ml). After each ion exchange, the NH_4-form of the zeolite/zeotype was filtered off, washed with water, and dried in air. Finally, the proton form was obtained by heating the NH_4-ZSM-5 or NH_4-Ga-MFI in air to 450 °C for 4 h, whereby NH_3 desorbed from the acidic sites leaving protons as charge-compensating cations.

2.2 Catalytic tests

The catalytic reactions were performed in a fixed bed reactor charged with 300 mg catalyst, which was pretreated in a flow of helium at the reaction temperature for 30 min. prior to the reaction. The reaction was performed at 370 °C (measured inside the reactor, just below the catalyst bed) and 1 bar, and methanol (WHSV = 7.9 h^{-1}) was introduced via an HPLC pump and evaporated before reaching the reactor. Helium was used as a carrier gas, with a flow of 40 mL/min, and the products from the reaction were analyzed by on-line GC (HP6890) equipped a Varian CP-PoraPLOT Q-HT capillary column and a flame ionization detector. When calculating the conversion, methanol and DME are considered reactants and response factors of 0.81 (methanol) and 0.63 (DME) are used, while a response factor of 1 is used for all hydrocarbon compounds.

2.3 Temperature programmed oxidation (TPO) and catalyst regeneration

TPO analyses were performed on 100 mg of spent catalyst which was heated in a flow of 5 % O_2 in helium (20 mL/min) with a heating rate of 2.75 °C/min to 700 °C. The final temperature was maintained for 2 h to ensure complete combustion of carbonaceous species. The concentrations of CO and CO_2 in the outlet were monitored continuously by a BINOS detector.

Regeneration experiments were conducted by heating the deactivated catalyst in a flow of 5 % O_2 in helium (20 mL/min) with a heating rate of 2.75 °C/min to 550 °C. The final temperature was maintained for 4 h to ensure complete combustion of carbonaceous species.

2.4 Characterization methods

All characterizations were made after ion exchange and calcinations. To identify and verify the crystal structure of the products, powder-XRD patterns were recorded using a Philips Diffractometer with Cu Kα radiation in the 2θ interval 5-70°. The elemental analysis was performed by Inductively Coupled Plasma Optical Emission Spectroscopy (ICP-OES) and used to determine the exact amount of Si, Ga and Al in the prepared zeolites and zeotypes.

Surface area and pore volume were determined by nitrogen adsorption and desorption measurements at liquid nitrogen temperature on a Micromeritics ASAP 2020 instrument. The samples were outgassed in vacuum at 573 K for 16 h prior to measurements. The total surface area was calculated according to the BET method, the micropore volumes were determined by the t-plot method and the mesopore volume was determined by the BJH method.

The crystal size and morphology of the zeolites and zeotypes were examined by scanning electron microscopy (SEM) on a Philips XL-30 FEG. The calcined samples were placed on a carbon film and Ag was evaporated onto the sample for approximately 20 minutes to achieve sufficient conductivity.

Temperature programmed desorption of ammonia (NH_3-TPD) was performed on a Micromeritics Autochem 2920. Prior to adsorption of ammonia, the sample was heated to 550 °C in a flow of helium. Desorption of ammonia was performed using a heating ramp of 15 °C/min.

3. Results and discussion

3.1 Catalyst Characterization

All catalysts have been thoroughly characterized concerning their crystallinity, morphology, acidity, elemental composition, surface area, and pore volume. According to X-ray diffraction (see supporting information), all four catalysts have crystalline MFI structure and no traces of amorphous material are detectable. Surface areas and micro- and mesopore volumes are shown in Table 1 alongside the elemental compositions obtained from ICP-OES analyses. The BET areas and micropore volumes are within the expected values for MFI zeolites, even though the BET area for the conventional H-Ga-MFI is somewhat lower than the other samples. The elemental compositions reveal that the gallium based zeotypes contain less trivalent metal than their H-ZSM-5 based counterparts.

Table 1: BET surface areas and micro- and mesopores volumes obtained from physisorption of nitrogen and elemental composition (Si/Al or Si/Ga ratios) obtained from ICP-OES analysis

	BET surface area (m^2/g)	V_{micro} (cm^3/g)	V_{meso} (cm^3/g)	Elemental comp. (Si/Al or Si/Ga)
H-ZSM-5	428	0.17	0.19	37
H-ZSM-5 meso	487	0.19	0.55	40
H-Ga-MFI	285	0.13	0.11	66
H-Ga-MFI meso	415	0.18	0.48	62

Ammonia TPD of the different catalysts is shown in Figure 1. The high temperature peak (around 300 °C) originates from the strong Brønsted sites, while the low temperature peak (around 160 °C) is usually ascribed to adsorption of multiple ammonia molecules on an acidic site [19], and is thus not of interest. As expected [5], the Brønsted peak for the gallium containing zeolites is shifted to lower temperature, due to the lower acidity of the active sites.

In literature, there has been some discussion on whether or not it is possible to observe differences in acid strength from NH_3-TPD experiments [20], since the specific experimental conditions e.g. flow rate, type/shape of sample bed, and temperature ramp rate have a large influence on the results. The employed amount of sample, the acid density of the sample, and nature of the zeolite structure are also able to shift the observed maximum temperature of the peak. Nevertheless, we observe a distinct shift to lower temperatures for both gallium containing catalysts, when the NH_3-TPD is performed at the same conditions for all the samples.

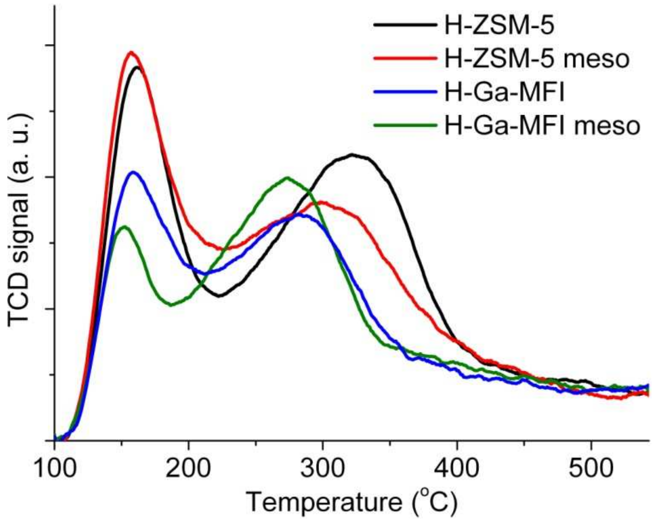

Figure 1: Temperature programmed desorption (TPD) of ammonia for H-ZSM-5, H-ZSM-5 meso, H-Ga-MFI, and H-Ga-MFI meso

To investigate the morphology of the different samples, SEM micrographs have been obtained. The particle sizes of the conventional H-ZSM-5 are in the range of 0.5-2 µm, showing no preferential shape. The mesoporous H-ZSM-5 zeolite (Figure 2b) also consists of particles of approximately 0.5-2 µm in size, but they have a sponge like appearance which is characteristic for mesoporous zeolites [21, 22]. The conventional H-Ga-MFI material (Figure 2c) consists primarily of smaller crystals of around 0.5-1 µm. Most of the crystals have the coffin shape morphology but also intergrown particles and particles with undefined shapes are present. The mesoporous H-Ga-MFI sample (Figure 2d) consists mainly of very small particles with some agglomerates also present.

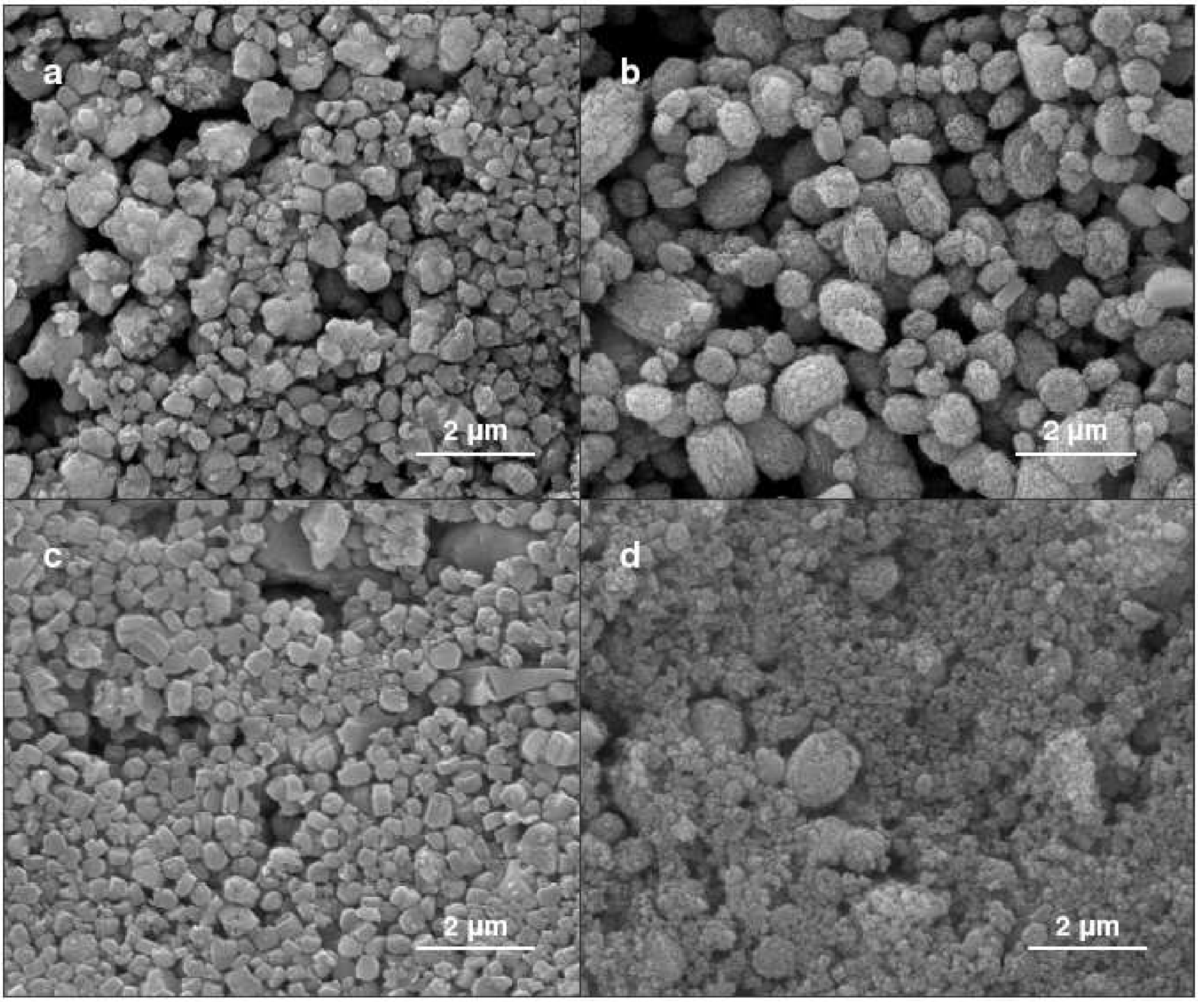

Figure 2: Representative SEM micrographs of a) conv H-ZSM-5, b) meso H-ZSM-5, c) conv H-Ga-MFI, and d) meso H-Ga-MFI

3.2 Catalytic experiments

The mechanism for conversion of methanol to hydrocarbons over zeolite catalysts is quite complex and has been extensively discussed in literature [1, 2], and the so-called "hydrocarbon pool mechanism" [23, 24, 25] has gained general acceptance. In this mechanism, methanol is converted in an indirect manner, via methylation of different hydrocarbon species inside the zeolite. These species are mainly methylbenzenes and alkenes [24] which crack or split off smaller compounds during molecular rearrangements.

When methanol initially reaches the catalyst bed, there is no hydrocarbon pool present, but within a very short time an active hydrocarbon pool is created and full conversion of methanol is achieved. With time on stream, the catalyst deactivates due to coking, and the active hydrocarbon pool moves downstream leaving deactivated catalyst behind. This is known as the "cigar burn model", the burning tobacco being the active hydrocarbon pool and the ash being the deactivated catalyst [26].

As a consequence of this reaction progress, the initial conversion of methanol is 100 %, which is maintained until most of the catalyst bed is deactivated and the conversion drops rapidly after breakthrough of methanol (and DME) [27, 28]. Conversion vs. time on stream for the reaction of methanol over the four different catalysts is shown in Figure 3. The gallium containing zeotypes exhibit shorter lifetime than H-ZSM-5, in particular the conventional H-Ga-MFI deactivates very fast. The mesoporous H-Ga-MFI deactivates much slower than the conventional, and has a lifetime which is close to the conventional H-ZSM-5. For the mesoporous H-ZSM-5, the breakthrough of methanol is observed slightly earlier than for conventional H-ZSM-5, but the decline in conversion is slower resulting in a somewhat higher conversion capacity. This less steep drop in conversion is also observed for mesoporous H-Ga-MFI.

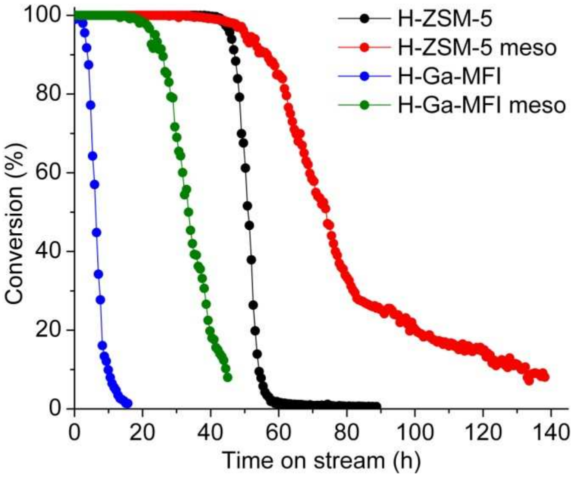

Figure 3: Conversion vs. time on stream for conversion of methanol over H-ZSM-5, H-ZSM-5 meso, H-Ga-MFI, and H-Ga-MFI meso (T = 370 °C, P = 1 bar)

Figure 4 shows the yield of aromatics vs. time on stream. Aromatics are produced from cyclization and hydrogen transfer reactions of alkenes, which also lead to the formation of alkanes [15, 29]. The gallium based zeotypes have a distinct lower selectivity towards aromatics than H-ZSM-5, probably due to a lower hydrogen transfer activity which is related to the lower acid strength of the catalysts. For all the catalysts, the production of aromatics decline with time on stream due to gradual loss of active catalyst available for the cyclization and hydrogen transfer reactions.

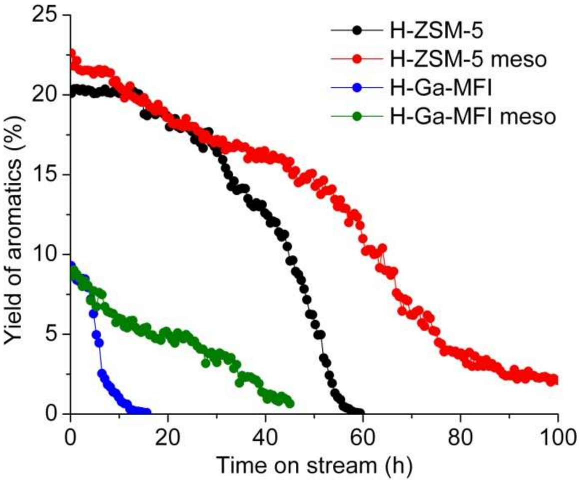

Figure 4: Yield of aromatics vs. time on stream (left) and C_4-HTI vs. conversion (right) for conversion of methanol over H-ZSM-5, H-ZSM-5 meso, H-Ga-MFI, and H-Ga-MFI meso (T = 370 °C, P = 1 bar)

Detailed initial product yields of aliphatics and aromatics for conversion of methanol are shown in Figure 5. Apart from the higher amount of aromatics produced from the two H-ZSM-5 based zeolites, the selectivities for the different catalysts are quite similar, which is reasonable since they all have MFI topology. Interestingly, H-Ga-MFI produces large amounts of propene and especially ethene, while aromatics are present at very low concentrations. Since ethene is primarily produced from decomposition of the lower methylbenzenes, i.e. xylenes and trimethylbenzenes [24], the observed selectivities are explained be a catalyst that is starting to deactivate. The catalyst is simply not active enough to convert the ethene that is split off from the methylbenzenes.

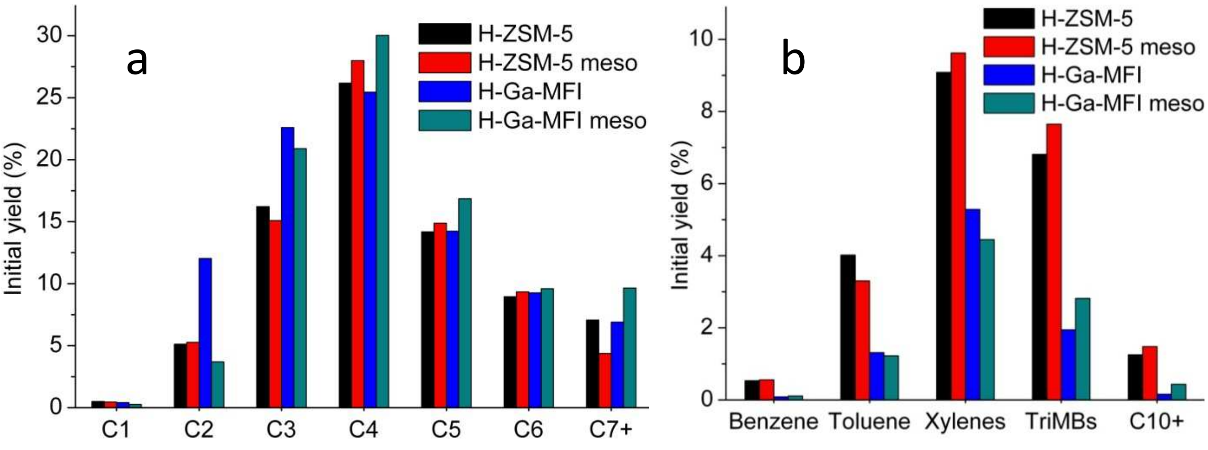

Figure 5: Initial product yields of aliphatics (a) and aromatics (b) for conversion of methanol over H-ZSM-5, H-ZSM-5 meso, H-Ga-MFI, and H-Ga-MFI meso (T = 370 °C, P = 1 bar)

The mesoporous zeolites produce slightly larger amounts of large aromatic compounds than their conventional counterparts, which has been observed in other studies as well [15], and can be explained as a direct effect of the mesoporosity leading to a shorter diffusion path for the larger compounds.

The coke deposition on the different catalysts has been investigated through TPO analyses of the spent catalysts and the resulting carbon contents in the catalysts upon full deactivation during conversion of methanol are shown in Figure 6. Generally, the H-ZSM-5 based zeolites contain much more coke than the gallium based zeotypes. H-Ga-MFI contains only 1 % carbon, while mesoporous H-Ga-MFI contains as little as 0.2 % carbon even though the catalysts are fully deactivated.

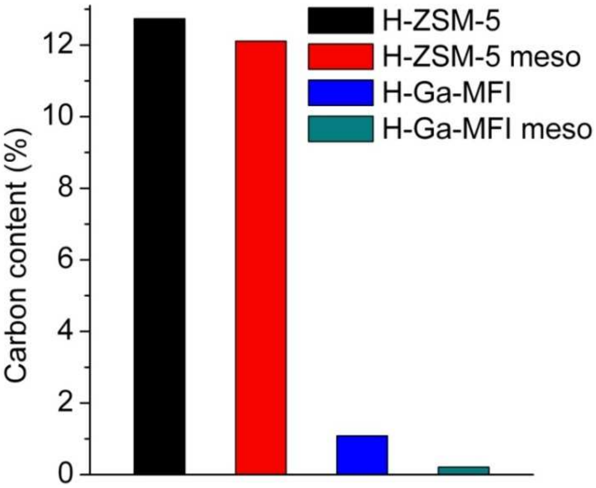

Figure 6: Carbon contents in spent catalysts upon conversion of methanol over H-ZSM-5, H-ZSM-5 meso, H-Ga-MFI, and H-Ga-MFI meso (T = 370 °C and P = 1 bar)

For better comparison of the rate of coke formation, the ratios between the amount of carbon converted and the amount of carbon deposited on the catalyst as coke during the entire catalyst lifetime are shown in Figure 7. A combination of reasonable catalyst lifetime and a very small amount of deposited coke, leads to a remarkably high value for the mesoporous H-Ga-MFI. This catalyst is able to convert over 20 times as much carbon (in the form of methanol) pr. carbon atom deposited than any of the other catalysts. As mentioned in the introduction, H-Ga-MFI is reported to form coke at a slower rate than H-ZSM-5 during methanol conversion, but carbon contents above 10 % are measured at deactivation [5]. This is in stark contrast to what is observed for the gallium containing samples presented here.

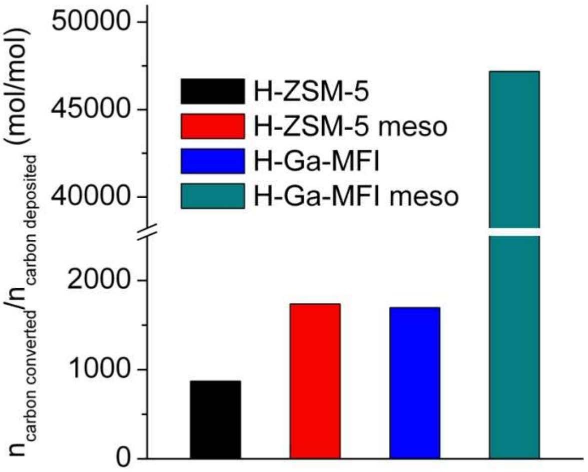

Figure 7: The molar ratios between the amount of carbon converted and the amount of carbon deposited as coke on the catalyst during the entire lifetime of the catalyst for conversion of methanol over H-ZSM-5, H-ZSM-5 meso, H-Ga-MFI, and H-Ga-MFI meso (T = 370 °C, P = 1 bar)

As mentioned, the selectivity towards aromatics is somewhat lower for the gallium containing zeotypes, but it is not negligible, since both catalysts initially produce around 10 % aromatics. Especially in the case of mesoporous H-Ga-MFI, it is thus possible to produce significant amounts of aromatics, while the catalyst is only subjected to trace amounts of coke.

Despite the fact that the spent mesoporous H-Ga-MFI only contains a very small amount of coke, it is still completely deactivated. It is clear that the usually assumed deactivation mechanism of MFI, which is explained by the formation of external coke, cannot be the reason for the observed activity loss, since large amounts of external coke would be necessary to impede the diffusion of reactants into the pores of the catalyst. This means, that the catalyst is either very sensitive towards the presence of coke, i.e. a very small amount of coke is enough to deactivate it, or it is deactivated in another way than coke deposition.

To investigate the mode of deactivation further, spent catalyst samples of conventional H-ZSM-5 and mesoporous H-Ga-MFI were regenerated by combustion of coke and subjected to methanol again, see Figure 8. In the case of H-ZSM-5, the catalyst is fully regenerated and shows a similar lifetime to the fresh catalyst. For the mesoporous H-Ga-MFI, the picture is completely different, and combustion of coke does not lead to reactivation of the catalyst. It is still almost completely inactive in the conversion of methanol. This confirms that the catalyst has not deactivated due to coke formation.

The most straightforward explanation would be that steaming of the gallium sites during methanol conversion is responsible for the deactivation of the catalyst. During steaming, a combination of water presence and relatively high temperature causes the gallium-oxygen bonds in the zeolite to hydrolyze leading to (partial) loss of gallium from the framework and thereby loss of catalytic activity. For H-ZSM-5 this process requires higher temperatures to occur [21], but gallium might be more vulnerable than aluminum in this context. A control experiment where the mesoporous H-Ga-MFI was subjected to water vapor (in a concentration corresponding to what would be expected from methanol dehydration) for 48 h at the reaction temperature (370 °C) and subsequently tested in methanol conversion has been performed. The catalyst was not active for methanol conversion upon this treatment which confirms that steaming is a plausible explanation for the loss of activity.

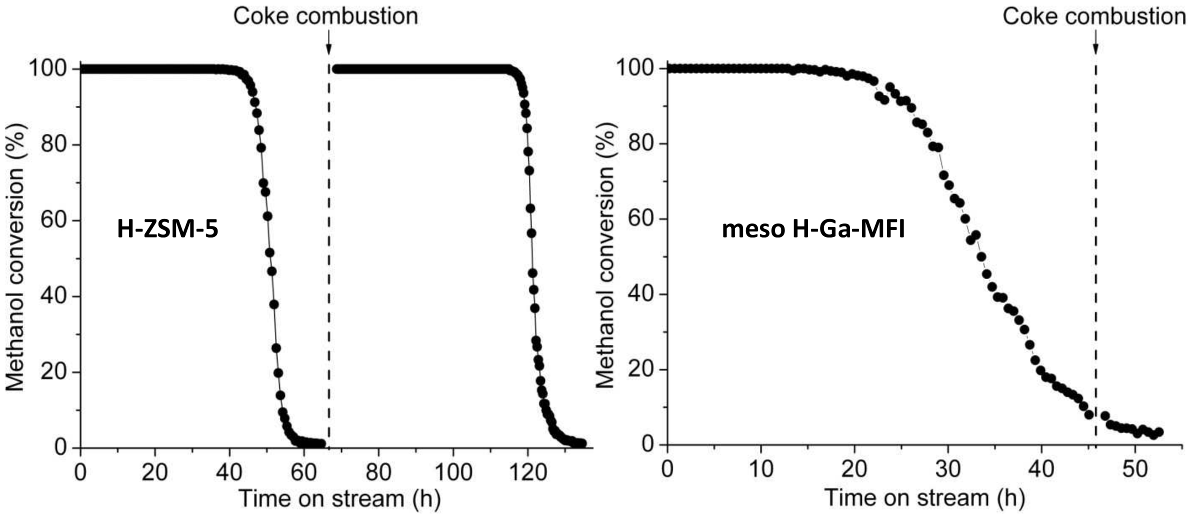

Figure 8: Conversion of methanol over fresh H-ZSM-5 and mesoporous H-Ga-MFI followed by coke combustion and subsequent methanol conversion

Areán *et al.* have investigated the thermal stability of the Si-O-Ga bonds in the MFI structure in the absence of water [31]. They found that in samples treated at high temperature, the gallium atoms show a tendency to leave the framework partially or completely and this phenomenon is particular relevant for temperatures above 900 K and low Si/Ga ratios. Furthermore, they reported that thermal degalliation of samples with high Si/Ga ratios (>50) is negligible. This implies that a relatively high gallium concentration is needed to render the zeolites framework unstable towards thermal treatment in the 800-900 K range. They also stated that the presence of small amounts of water vapor can strongly favor the process, which is highly relevant in connection with the deactivation observed in the present experiments.

To investigate the possible changes of the active sites of the mesoporous H-Ga-MFI during the catalytic test FT-IR experiments have been conducted. As a reference, the mesoporous H-Ga-MFI was steamed at 370 °C for 48 h. The spectra for a fresh, a regenerated, and a steamed sample of mesoporous H-Ga-MFI are given in Figure 9. In order to compare the OH groups, the obtained spectra are normalized to the overtones of the framework vibrations in the 2200-1600 cm^{-1} region.

The spectra of the three samples are similar to those reported in literature [31, 32, 33] as they all show the characteristic O-H band of the Si(OH)Ga-bridged Brønsted groups at 3618 cm^{-1} and external silanol groups at 3746 cm^{-1}. In addition, the fresh sample show a broad band at 3400 cm^{-1} which is ascribed to silanol nests or defects primarily located at the surface. The spectra of the regenerated and steamed samples resemble each other. One could argue that possible structural changes which lead to deactivation could occur during the thermal regeneration and not during the conversion of methanol. But since the spectra for the regenerated and steamed samples are practically identical, the differences in OH-bands from the fresh sample must originate from steaming and not from the thermal regeneration. In addition, Areán *et al.* have shown that gallium zeotypes with high Si/Ga ratios (>50) are not significantly affected by high thermal treatment alone (without water present) [31].

Upon methanol conversion, the intensity of the Brønsted acid band at 3618 cm^{-1} is decreased significantly. The decrease in the density of Brønsted acid sites must be due to hydrolysis and possible dehydration during the reaction which will lead to migration of the gallium atoms into (partially) extra framework positions and ultimately Ga_2O_3 clusters. In the inset in Figure 9 the intensity of the bands at 3746 cm^{-1} is enlarged. It appears that the regenerated and steamed samples contain a higher amount of terminal silanols than the fresh sample. This might be explained by the disintegration of the agglomerates into small primary particles which were initially connected via hydrogen bridges as apparent from the broad band at 3400 cm^{-1}, resulting in non-interacting terminal silanol groups.

In order to verify if the zeolite structure is affected by conversion of methanol and steaming, the regenerated and steamed samples were analyzed by X-ray diffraction (see supporting information). This showed that the structure of the zeolite framework is intact; indicating that changes in catalytic activity is not due to fragmentation of the zeolite framework, but rather local changes around the active sites.

In summary, the deactivation of the mesoporous H-Ga-MFI zeotype appears to be due to loss of active Brønsted acid sites which occurs due to steaming of Si-OH-Ga bonds. In this way, extra framework gallium is produced leaving the catalyst inactive in the conversion of methanol.

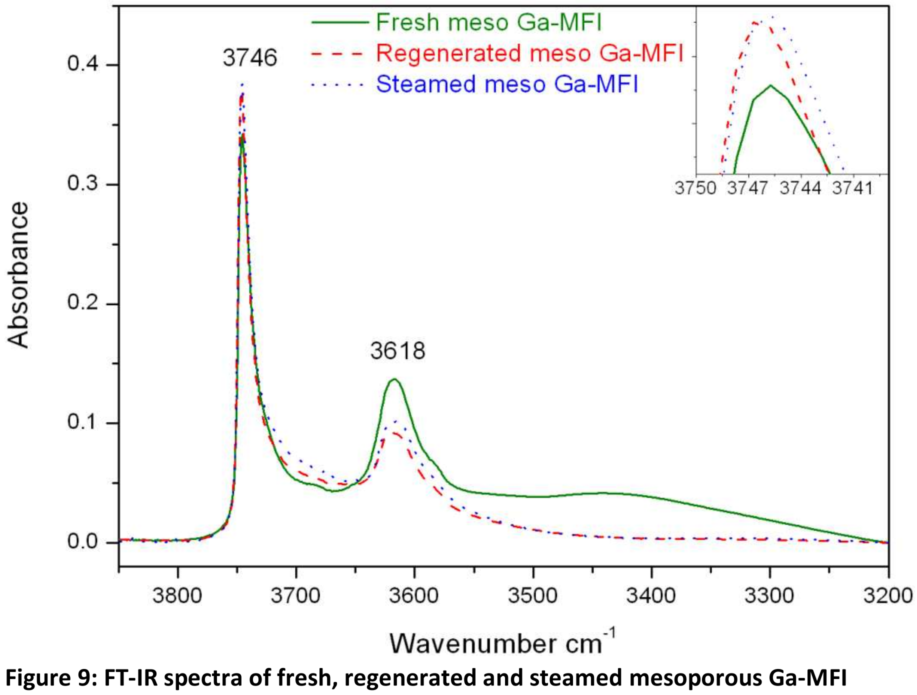

Figure 9: FT-IR spectra of fresh, regenerated and steamed mesoporous Ga-MFI

4. Conclusions

In this work, conventional and mesoporous H-ZSM-5 and H-Ga-MFI have been thoroughly characterized and employed in the conversion of methanol to hydrocarbons.

A remarkable difference in the tendency towards formation of coke during methanol conversion for H-ZSM-5 zeolites compared to H-Ga-ZSM-5 zeotypes is observed. The mesoporous H-Ga-MFI zeolite presented here only contains 0.2 % coke upon deactivation and is able to convert 20 times the amount of methanol pr. carbon atom deposited as coke than a conventional H-ZSM-5 zeolite. Even though the mesoporous H-Ga-MFI only forms insignificant amounts of coke, it is still completely deactivated upon conversion of methanol. Regeneration and steaming experiments indicated that the mesoporous H-Ga-MFI might be subjected to deactivation due to steaming of the Ga-O bonds in the structure during the conversion of methanol leading to loss of gallium from the zeolite framework. This was supported by IR measurements on a fresh, a regenerated (coke combustion upon methanol conversion), and a steamed (at reaction conditions) H-Ga-MFI sample, which showed a similar decrease in the Brønsted band for the steamed and regenerated sample compared to the fresh.

5. References

1. Stöcker, M., Microporous Mesoporous Mater. **1999**, *29*, 3
2. Mokrani, T., Scurell, M., *Catal. Rev.* **2009**, *51*, 1
3. Centi, G.; Parathoner, S.; Arrigo, R.; Giordano, G.; Katovic, A.; Pedulà, V., *Appl. Catal. A* **2006**, *307*, 30
4. Palin, L.; Lamberti, C.; Kvick, Å.; Tesla, F.; Aiello, R.; Milanesio, M.; Viterbo, D., *J. Phys. Chem. B* **2003**, *107*, 4034
5. Handreck, G. P.; Smith, T. D., *J. Catal.* **1990**, *123*, 513
6. Kosslick, H.; Tuan, V. A.; Parlitz, B.; Fricke, R.; Peuker, C.; Storek, W., *J. Chem. Soc. Faraday Trans.* **1993**, *89*, 1131
7. Fricke, R.; Kosslick, H.; Lischke, G.; Richter, M., *Chem. Rev.* **2000**, *100*, 2303
8. Lalik, E.; Liu, X.; Klinowski, J., *J. Phys. Chem.* **1992**, *96*, 805
9. Choudhary, V. R.; Kinage, A. K., *Zeolites* **1995**, *15*, 732
10. Romannikov, V. N.; Chumachenko, L. S.; Mastikhin, V. M.; Ione, K. G., *React. Kinet. Catal. Lett.* **1985**, *29*, 85
11. Mentzel, U. V.; Rovik, A. K.; Christensen, C. H., *Catal. Lett.* **2009**, *127*, 44
12. Pérez-Ramirez, J.; Christensen, C. H.; Egeblad, K.; Christensen, C. H.; Groen, J. C., *Chem. Soc. Rev.* **2008**, *37*, 2530
13. Jacobsen, C. J. H.; Madsen, C.; Janssens, T. V. W., Jakobsen, H. J.; Skibsted, J., *Microporous Mesoporous Mater.* **2000**, *39*, 393
14. Groen, J. C.; Jansen, J. C.; Moulijn, J. A.; Pérez-Ramirez, J., *J. Phys. Chem.* **2004**, *108*, 13062
15. Bjørgen, M.; Joensen, F.; Holm, M. S.; Olsbye, U.; Lillerud, K. P.; Svelle, S., *Appl. Catal. A* **2008**, *345*, 43
16. Sun, C.; Du, J.; Liu, J.; Yang, Y.; Ren, N.; Shen, W.; Xu, Hualong, Tang, Y., *Chem. Commun.* **2010**, *46*, 2671

17. Kim, J.; Choi, M.; Ryoo, R., *J. Catal.* **2010**, *269*, 219
18. Jacobsen, C. J. H.; Madsen, C.; Houzvicka, J.; Schmidt, I.; Carlsson, A., *J. Am. Chem. Soc.* **2000**, *122*, 7116
19. Lónyi, F.; Valyon, J., *Microporous Mesoporous Mater.* **2001**, *47*, 293
20. Parillo, D. J.; Lee, C.; Gorte, R. J.; White, D.; Farneth, W. E., *J. Phys. Chem.* **1995**, *99*, 8745
21. Zhu, K.; Egeblad, K.; Christensen, C. H., *Eur. J. Inorg. Chem.* **2007**, *25*, 3955
22. Svelle, S.; Sommer, L.; Barbera, K.; Vennestrøm, P. N. R.; Olsbye, U.; Lillerud, K.-P.; Bordiga, S.; Pan, Y.-H.; Beato, P., *Catal. Today*, **2011**, *168*, 38
23. Haw, J. F.; Song, W.; Marcus, D. M.; Nicholas, J. B., *Acc. Chem. Res.* **2003**, *36*, 317
24. Bjørgen, M.; Svelle, S.; Joensen, F.; Nerlov, J.; Kolboe, S.; Bonino, F.; Palumbo, L.; Bordiga, S.; Olsbye, U., *J. Catal.* **2007**, *249*, 195
25. Dahl, I. M.; Kolboe, S., *Catal. Lett.* **1993**, *20*, 329
26. Haw, J. F.; Marcus, D. M., *Top. Catal.* **2005**, *34*, 41
27. Janssens, T. V. W., *J. Catal.* **2009**, *264*, 130
28. Mentzel, U. V.; Holm, M. S., *Appl. Catal. A* **2011**, *296*, 59
29. Mentzel, U. V.; Shunmugavel, S.; Hruby, S. L.; Christensen, C. H.; Holm, M. S., *J. Am. Chem. Soc.* **2009**, *131*, 17009
30. Triantafillidis, C. A.; Vlessidis, A. G.; Nalbandian, L.; Evmiridis, N. P., *Micrporous Mesoporous Mater.* **2001**, *47*, 369
31. Areán, C. O.; Palomino, G. T.; Geobaldo, F.; Zechina, A., *J. Phys. Chem.* **1996**, *100*, 6678
32. Khodakov, A. Y.; Kustov, L. M.; Bondarenko, T. N.; Dergachev, A. A.; Kazansky, V. B.; Minachev, M. K.; Borbely, G. Beyer, H. K., *Zeolites* **1990**, *10*, 603
33. Mirsojew, I.; Ernst, S.; Weitkamp, J.; Knözinger, H., *Catal. Lett.* **1994**, *24*, 235

Journal Name

Dynamic Article Links ►

Cite this: DOI: 10.1039/c0xx00000x

www.rsc.org/xxxxxx

ARTICLE TYPE

Tight bifunctional hierarchical catalyst

Karen T. Højholt,[a,b] **Peter N. R. Vennestrøm**[a,c] **and Pablo Beato***[a]

Received (in XXX, XXX) Xth XXXXXXXXX 200X, Accepted Xth XXXXXXXXX 200X
DOI: 10.1039/b000000x

A new concept to prepare tight bifunctional catalyst has been developed, by anchoring CoMo$_6$ clusters on hierarchical ZSM-5 zeolites for simultaneous use in HDS and hydrocracking catalysis. The prepared material displays a significant improved activity in HDS catalysis compared to the impregnated counterpart.

Conventional microporous zeolites have for several years been known as excellent hydrocracking catalyst due to the presence of intrinsic acid sites.[1-4] Environmental regulations demand that sulfur and other contaminants have to be removed which is usually done prior to refinery processes as the sulfur has a severe impact on the catalysts, the equipment, and the quality of the final products.[5] Hydrodesulfurisation (HDS) using a sulfided Co/Mo catalyst at high temperature and high pressure is widely employed by the refineries to produce low-sulfur gasoline and diesel fuel.[6]

Over the years several support materials have thoroughly been investigated and typical support materials in industry are alumina and silica-alumina, while pure silica, zeolites, kieselguhr and magnesia are so far only explored in research.[6] Here, we present a new tight bifunctional catalyst in the sense, that it is applicable for simultaneous use in two reactions namely in HDS and hydrocracking. The intention is to position the active CoMo species close to the Brønsted acid sites inherrent in the zeolite framework whereby the hydrogenation and cracking activity are in tight association.

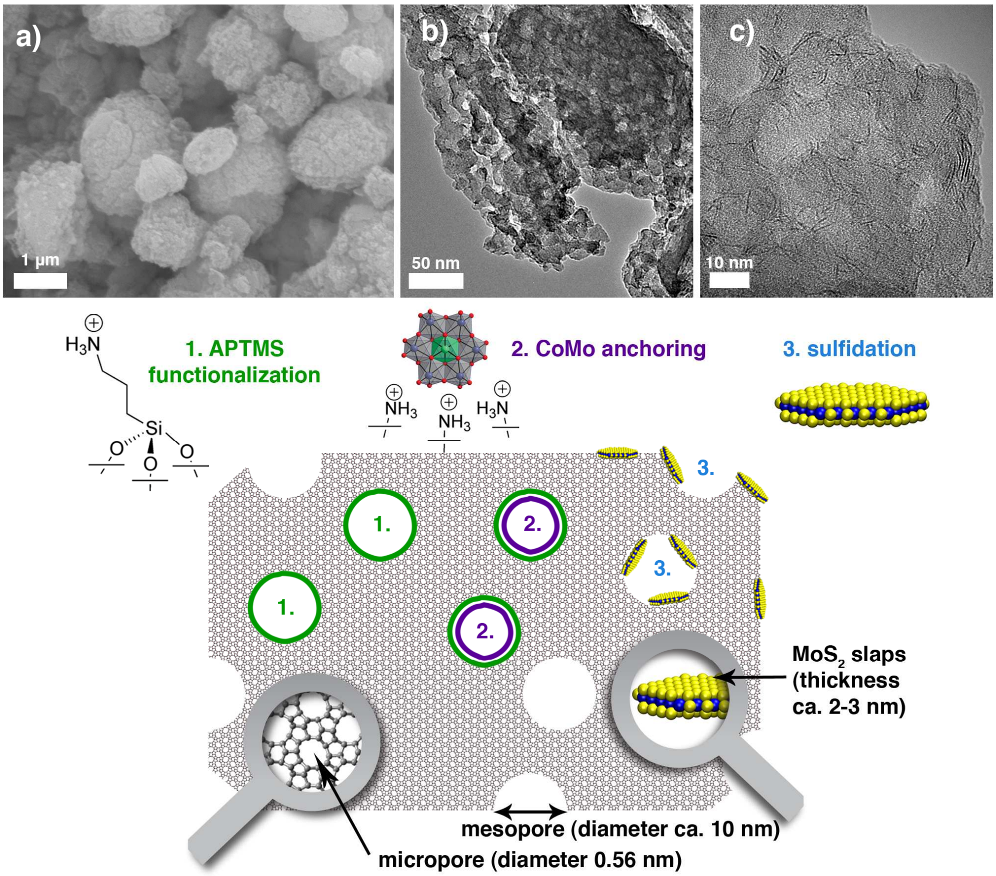

Fig. 1 Schematic illustration of the functionalisation and anchoring of CoMo on hierarchical ZSM-5 together with representative a) SEM image of the parent hierarchical ZSM-5, b) and c) TEM images of the spent catalyst

Usually the Co/Mo phase is impregnated onto the support material. In this work the catalyst is prepared by anchoring $CoMo_6$ clusters onto a mesoporous ZSM-5 zeolite in order to improve the dispersion of the active HDS phase. Using a conventional zeolite as support material it is not possible to place the $CoMo_6$ species close to the acid sites inside the zeolite crystals as the solely microporous structure makes the incorporation of $CoMo_6$ only possible on the external surface of the crystals. Instead, hierarchical zeolites feature in addition to the intrinsic micropore system an auxiliary pore system consisting of larger pores that intersect the micropores. Zeolites containing both micropores and mesopores combine the shape selectivity, hydrothermal stability and possibility for high acidity typical of conventional zeolites with highly efficient transport of reactants and products due to mesopores. The mesopores extend into the microporous crystalline zeolite framework (as shown in Fig. 1) and will be terminated by silanol groups at the meospore wall. These silanol groups makes it possible to functionalise the surface with *e.g.* alkoxysilanes which can be used as linker molecule.[7, 8] Due to the large mesopore surface area the amount of silanol groups is relatively high compared with that on the external surface of conventional zeolite crystals.

The tight bifunctional catalyst is prepared by using (3-aminopropyl)trimethoxysilane (APTMS) as linker molecule to functionalise the mesopores of the zeolite as illustrated in Fig. 1. The mesoporous zeolite was obtained via desilication of a commercial ZSM-5 sample with NaOH solution..After modifying the surface with APTMS the material is treated with hydrochloric acid to convert the amine groups into the corresponding hydrochloric salt. Hereafter, it is possible to attach a mixed cobalt and molybdenum containing Anderson ion, $[H_6CoMo_6O_{24}]^{3-}$ to the surface by ion exchange. The Anderson ion is chosen as metal sources to enhance the probability to form the active Co-Mo-S phase after sulfidation as the promoter metal is introduced directly with the catalytically active metal. To investigate if the anchoring improves the catalytic activity, a reference material was prepared via impregnation of two aqueous solutions of $(NH_4)_6Mo_7O_{24}\cdot 4H_2O$ and $Co(H_2O)_6(NO_3)_2$, onto the parent mesoporous ZSM-5.

X-ray powder diffraction (XRPD) shows that the support material consists of crystalline MFI-structured material, while N_2 physisorption proved the presence of mesoporous with a external surface area of 221 m^2/g and a micropore surface area of 300 m^2/g The XRD pattern, the isotherm and corresponding pore size distribution are given in the supporting information to this communication. From the scanning electron micrographs of the mesoporous zeolite, see *e.g.* Fig. 1a, the particles appear sponge-like, as is typical for mesoporous zeolites, and are in the range of ~0.5-3 μm. Some particles seem to be fragmented, probably as a result of the desilication. The carbon content after functionalisation was 9.82 wt. %, determined by elemental analysis, corresponding to 2.7 mmol APTMS/g zeolite. This is rather high compared to previous results[7] which is most likely due to larger mesopores and higher external surface area.

As numerous authors have verified the intrinsic properties of ZSM-5 zeolite as excellent hydrocracking catalyst [9-11], we have chosen to focus on the catalytic activity in HDS. The results of the model activity test results are given in Table 1,together with the cobalt and molybdenum contents determined by elemental analysis after calcination.

Table 1: Cobalt and molybdenum contents [a] and model activity test results.

Catalyst	Co [wt%]	Mo [wt%]	k(HDS) $[h^{-1}]$
$CoMo_6$-ZSM-5 (anchored)	0.97	10.1	32.4
Co+Mo-ZSM-5 (impregnated)	0.88	9.4	19.3

[a] determined by elemental analysis after calcination at 500 ºC for 3 hours

Table 1 reveals that despite the fact that the anchored and the impreganted reference material contain very similar amounts of metals, a significantly higher HDS activity is observed for the tight bifunctional catalyst.

After catalytic testing, the anchored version was characterised using transmission electron microscopy (TEM). The pronounced contrast differences and the sponge-like appearance seen in Fig. 1b, reveal the mesoporous nature of the zeolite support material, which is further supported by N_2-physisorption (supporting information). Throughout the sample well dispersed MoS_2 slabs are visible both as single and double sheets around 2-3 nm thick, see Fig. 1c. The MoS_2 slabs are located in the mesopores and interparticle voids since they are too large to fit into the micropore system of the zeolite. In selected areas small round particles around 1 nm are also visible, see supporting information. XRPD of the spent catalyst was used to investigate if these particles are related to cobalt or mixed Co/Mo sulfide phases. However, only crystalline ZSM-5 together with an undefined amorphous phase was detected. Further evaluation of the nanoparticles is under preparation, *i.e.* using selected area electron diffraction methods.

In conclusion a new approach for preparing tight bifunctional HDS catalysts was successfully accomplished by ion-exchange $CoMo_6$ polyoxometallate ions onto the functionalised mesopore surface of a ZSM-5. By this approach the HDS activity of the tight bifuctional catalyst displayed a significant higher activity compared to the impregnated counterpart. The difference in HDS activity is attributed to an improved dispersion of the metals throughout the zeolite support, which is supported by the TEM images as illustrated in Fig. 1c and supporting information. The presented concept for the preparation of tight bifunctional catalysts combines the intrinsic properties of the zeolites *i.e.* acidity and size-selectivity with the possibility to anchor catalytically active metal clusters in close vicinity of these acid sites to create a novel type of bifunctional zeolite catalyst..

Notes and references

[a] *Haldor Topsøe A/S, Nymøllevej 55, DK-2800 Lyngby, Denmark, E-mail: pabb@topsoe.dk Fax: + 45 45 27 29 99, Tel: + 45 45 27 26 81*
[b] *Centre for Catalysis and Sustainable Chemistry, Technical University of Denmark, Kemitorvet, DK-2800 Lyngby, Denmark*
[c] *Instituto de Tecnología Química, UPV, Av. Naranjos s/n, E-46022 Valencia, Spain*

† Electronic Supplementary Information (ESI) available: [details of any supplementary information available should be included here]. See DOI: 10.1039/b000000x/

1 J.W. Ward, *Fuel Process. Technol.*, 1993, **35**, 55
2 C. Martinez, A. Corma, *Coordin. Chem. Rev.*, 2011, **255**, 1558
3 M.A. Ali, T. Tatsumi, T. Masuda, *Appl. Catal. A: Gen.*, 2002, **233**, 77

4 A. Hassan, S. Ahmed, M.A. Ali, T. Inui, *Appl. Catal. A: Gen.*, 2001, **220**, 59

5 US EPA, Diesel Fuel Quality: Advance Notice of Proposed Rulemaking, EPA 420-F-99-011, Office of Mobile Sources, May, 1999

6 H. Topsøe, B.S. Clausen, F.E. Massoth, *Hydrotreating Catalysis – Science and Technology,* Springer-Verlag Berlin Heidelberg, New York, 1996

7 D.-H. Lee, M. Choi, B.-W. Yoo, R. Ryoo, *Chem. Commun.*, 2009, 74

8 S. Michell, J. Perez-Ramirez, *Catal. Today*, 2011, **168**, 28

9 M.J.B. Souza, F.A.N. Fernandes, A.M.G. Pedrosa, A.S. Araujo, *Fuel Process Technol.*, 2008, **89**, 819

10 W. Vermeiren, J.-P. Gilson, *Top. Catal.*, 2009, **52**, 1131

11 M.S. Rigutto, R. Van Veen, L. Huve, *Stud. Surf. Sci. Catal.*, 2007, **168**, 855

Supporting information for:

Tight bifunctional hierarchical catalyst

Karen T. Højholt, Peter N. R. Vennestrøm and Pablo Beato

1. Experimental

All reagents were of reagent grade and used without any further purification: Sodium molybdate dihydrate ($Na_2MoO_4 \cdot 2H_2O$, ≥99.5 wt%, Sigma-Aldrich), nitric acid (HNO_3, 65 wt%, Sigma-Aldrich), cobalt(II) sulfate heptahydrate ($CoSO_4 \cdot 7H_2O$, 99 wt%, Sigma-Aldrich), sodium peroxodisulfate ($Na_2S_2O_8$, ≥99 wt%, Aldrich), sodium hydroxide (NaOH, 99 wt%, Riedel-de Häen), ammonium nitrate (NH_4NO_3, 99.5 wt%, Merck), ammonia (NH_3, 25 wt%, Fluka), toluene (C_7H_8, 99.7 wt%, Fluka), (3-aminopropyl)trimethoxysilane (APTMS, 97 wt%, Aldrich), hydrochloric acid (HCl, 37 wt%, Sigma-Aldrich).

1.1 Synthesis of $Na_3[Co(OH)_6Mo_6O_{18}] \cdot 8H_2O$

$Na_3[Co(OH)_6Mo_6O_{18}]$ was synthesised according to Nolan *et al.*[1] using the following procedure: First, 30.26 g $Na_2MoO_4 \cdot 2H_2O$ was dissolved in 50 ml H_2O and acidified to pH 4.51 with HNO_3 (65 wt%). In another beaker 5.75 g $CoSO_4 \cdot 7\ H_2O$ was dissolved in 10 ml H_2O and then added to the molybdate solution under stirring. A solution of 7.53 g $Na_2S_2O_8$ dissolved in 8.8 ml H_2O was then added to the Co/Mo mixture as an oxidising agent. The obtained solution was heated to reflux until a dark turquoise solid precipitated. Upon further refluxing, the precipitate was redissolved and the original red colour of the solution returned. Following this, the solution gradually turned dark green, a color change indicating oxidation of the cobalt (II) to cobalt (III). Boiling was continued until evolution of oxygen ceased, by which time the solution became permanently dark turquoise. Finally the hot solution was filtered and the filtrate was left to precipitate dark green crystals upon cooling and consecutive evaporation of the solvent. The product is referred to as $CoMo_6$.

1.2 Synthesis of mesoporous ZSM-5

Hierarchical ZSM-5 was prepared by desilication of a commercially available ZSM-5 zeolite using a 0.3 M NaOH solution in the ratio 33 ml per gram zeolite materal for 30 min at 70 ºC. The selective silicon leaching was stopped by quenching the solution on ice, and then washed three times with water by centrifugation. The desilicated ZSM-5 was dried over night at room temperature before further treatment. To obtain the ammonium form of the desilicated samples two consecutive ion exchanges were carried out using a 1.7 M NH_4NO_3/0.94 M NH_3 buffer solution with 10 ml solution per gram zeolite, at 80 ºC under stirring for 2 hours. After each exchange, the NH_4-form of the zeolite was isolated by filtration, washed with water and dried in air at 110 ºC. After the last ion exchange, the H-form of the desilicated zeolite was finally obtained by calcining the NH_4-form in air to 550ºC for 3 h.

1.3 Anchoring $CoMo_6$ on mesoporous ZSM-5

The $CoMo_6$ clusters were anchored onto the mesopore surface of hierarchical ZSM-5 by first functionalising the surface with (3-aminopropyl)trimethoxysilane (APTMS): 4 g of mesoporous ZSM-5 were suspended in 160 ml toluene and heated to 65 ºC, followed by the addition of 11 g APTMS. The suspension was stirred overnight, filtered and the obtained product washed with toluene and dried at room temperature. 2 g of functionalised mesoporous ZSM-5 were stirred over night in 150 ml 3 M HCl, filtered and left for drying at room temperature. The $CoMo_6$ Anderson ion was finally attached to the mesoporous ZSM-5 zeolite by ion-exchange. The mesoporous ZSM-5 was added to a solution of 0.323 g $Na_3[Co(OH)_6Mo_6O_{18}]$ in 60 ml H_2O (pH 4.2 adjusted with HNO_3, 65 wt%). After stirring for 12 hours, the solid was filtered of, washed with water and dried at room temperature. The product was named “$CoMo_6$-ZSM-5 (anchored)”.

1.4 Preparation of reference material

The impreganted reference catalyst was prepared via successive incipient wetness impregnation of the mesoporous ZSM-5 (0.518 g) with aqueous solutions of 2.923g $(NH_4)Mo_7O_{24}\cdot 4H_2O$ (AHM) and 0.7844g $Co(H_2O)_6(NO_3)_2$ in 25ml water. After drying overnight at room temperature, the sample was calcined at 500 ºC for 3 hours.

1.5 Model activity test

Catalytic testing was performed in a fixed bed reactor charged with 300 mg catalyst in the fraction 600-850 μm. To achieve a steady flow the catalyst was mixed with Ballotini glass balls (150-250 μm) until a final volume of 1 ml was obtained. Prior to catalytic test the catalyst was sulfidized in a flow of 2.5 % dimethyldisulfide (DMDS) dissolved in *n*-heptane at 350 ºC and 50 bar for 4 hours. Helium was used as a carrier gas with a flow of 250 Nml/min.

After 4 hours of sulfidation the feed was changed to a model oil feed containing 3 % dibenzothiophene (DBT), 0.5 % indole, 1 % naphtalene, 2.5 % dimethyldisulfide (DMDS), 0.5 % *n*-nonane, the rest being *n*-heptan solvent.. The catalytic reaction was also performed at 350 ºC, 50 bar using helium as a carrier gas with a flow of 250 Nml/min. The employed feed rate of oil was 0.3 ml/min and the total WHSV was 68 h^{-1}. The products from the reaction were analysed by an on-line GC equipped with a FID using n-nonane as an internal standard. The reaction was allowed to stabilize over 4 hours in order to obtain steady state conditions after changing to the oil feed prior to catalytic measurements. Afterwards eight GC analyses of the product stream were made with 1 hour intervals.

The activity was determined as a pseudo first order rate constant, k which is calculated on the basis of the 8 measured conversions of DBT. The rate constant *k* was calculated using the equation for the first order rate law (Eq. 6.1) and the correlation between residence time *t* and *WHSV*:

$$ln\left(\frac{[DBT]}{[DBT]_0}\right) = -kt \Leftrightarrow ln\left(\frac{[DBT]_0 - conv.\cdot [DBT]_0}{[DBT]_0}\right) = -kt \Leftrightarrow ln(1-conv.) = -kt$$

where [*DBT*] is the concentration of DBT at time *t*, $[DBT]_0$ is the concentration of DBT at time $t = 0$ and *conv.* is the fractional conversion of DBT.

At steady state conditions the catalyst produces a product stream of steady composition. The time t in the first order kinetic equation is therefore the residence time of the feed in the reactor. This residence time is equal to the reciprocal Weight Hourly Space Velocity (WHSV) defined as:

$$WHSV = \frac{flow \times feed\ density}{catalyst\ mass}$$

and thus get:

$$k = -WHSV \cdot ln(1-conv.)$$

2. Characterisations

2.1 XRPD

The obtained XRPD pattern for the $CoMo_6$ precursor compound is shown in Figure 1 together with the XRPD patterns for ZSM-5 before and after desilication.

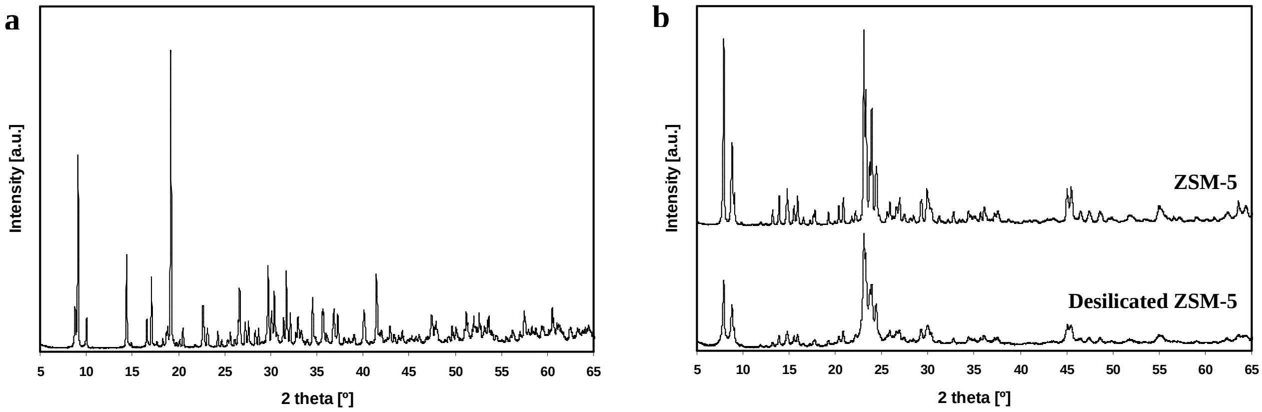

Figure S1: XRPD patterns of a) $Na_3[Co(OH)_6Mo_6O_{18}]\cdot 8H_2O$ and b) ZSM-5 before and after desilication

As seen in Figure S1a the prepared $Na_3[Co(OH)_6Mo_6O_{18}]\cdot 8H_2O$ is a crystalline material with the desired phase[1]. The XRPD patterns for ZSM-5 before and after desilicated (Figure 1b) show that the MFI structure is preserved after the formation of mesopores[2].

2.2 SEM

Figure S2 gives representative SEM images of the parent and desilicated ZSM-5 samples.

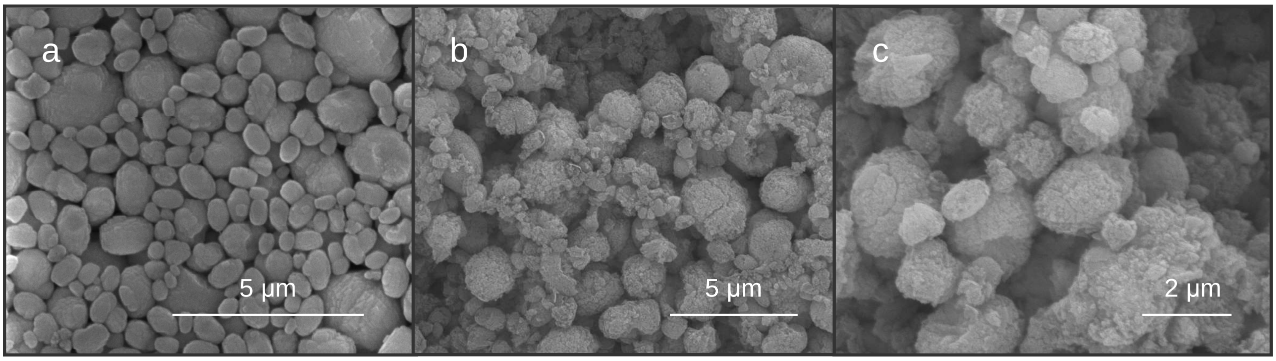

Figure S2:Representative SEM images of ZSM-5 before (a) and after desilication (b, c)

The parent ZSM-5 sample consists of particles in the range of ~ 0.5-3 µm, Figure 2, and the shape is more oval-like than the typical coffin-shaped zeolites. From the SEM images of the desilicated sample the particles appear sponge-like, typically for mesoporous zeolites, but retain more or less their original size. Some particles are fragmented, probably as a result of the desilication.

2.3 N_2 Physisorption

The pore volumes and surface areas calculated from the N_2 physisorption measurements are listed in Table S1. Figure 3 shows the physisorption isotherms given by the parent and desilicated ZSM-5 samples and the pore size distributions derived from the desorption isotherm.

Table 6.1: Surface areas and pore volumes of the parent and desilicated zeolite samples

	Surface area[a] [m^2/g]	External surface area[b] [m^2/g]	Micropore surface area [m^2/g]	Micropore volume[b] [cm^3/g]	Total pore volume[c] [cm^3/g]
Parent ZSM-5	430	48	382	0.17	0.26
Desilicated ZSM-5	521	221	300	0.13	1.07

[a] Calculated using the BET method, [b] determined using the t-plot method and [c] volume adsorbed at P/P_0=0.99

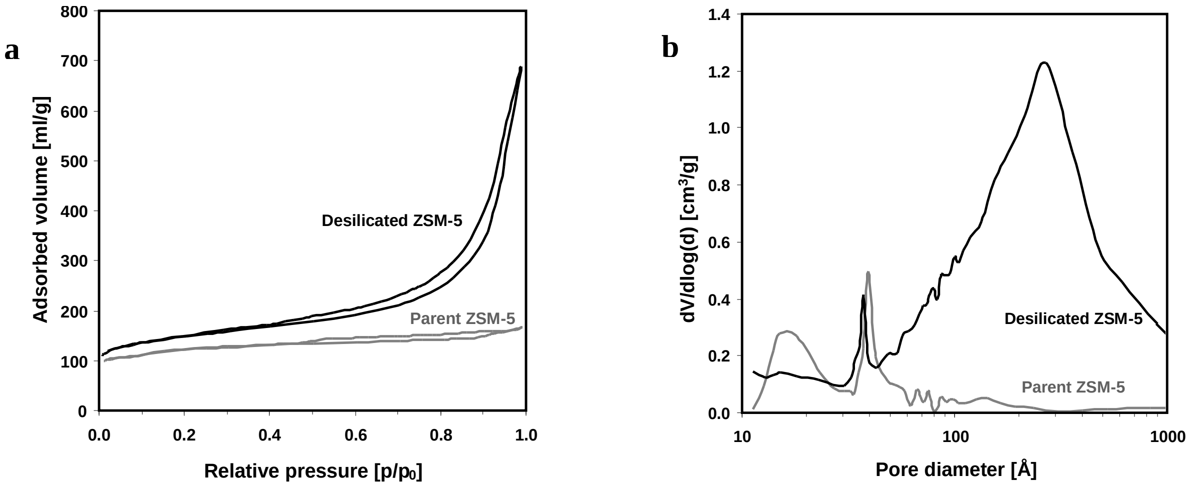

Figure S3 N_2 adsorption-desorption isotherms (a) and corresponding pore size distribution (b) of the parent and desilicated ZSM-5 zeolites. The pore size distributions are obtained from the desorption branch of the isotherm using the BJH method

The isotherm from the desilicated sample in Figure S3a exhibits a hysteresis typical for mesoporous materials. The sample can therefore be classified as a hierarchical zeolite. Contrary, the isotherm of the parent sample does not contain any significant amount of hysteresis and displays an isotherm typical for solely microporous materials. Figure S3b shows the pore size distributions, including the artefacts at 2 and 4 nm due to the well known quasi-phase transition of N_2 and forced closure of the hysteresis loop, respectively. For the desilicated sample pore size distribution is spread over the mesopore and macropore region, centred at 27 nm. Table S1 quantitatively reveals the large increase in total pore volume and external surface area upon the desilication treatment calculated from the isotherms. It is noteworthy to mention that the large increase in mesopore volume and external surface area only occurs at a small expense of the micropore volume and surface area. This indicates that most of the intrinsic properties of the ZSM-5 zeolite are preserved after the treatment.

2.4 TEM

After sulfidation and catalytic testing the anchored version was characterised using TEM. In general it was difficult to conduct TEM especially at high magnifications due to the electron beam sensitivity of the zeolite framework. Representative TEM images are given in Figure S4.

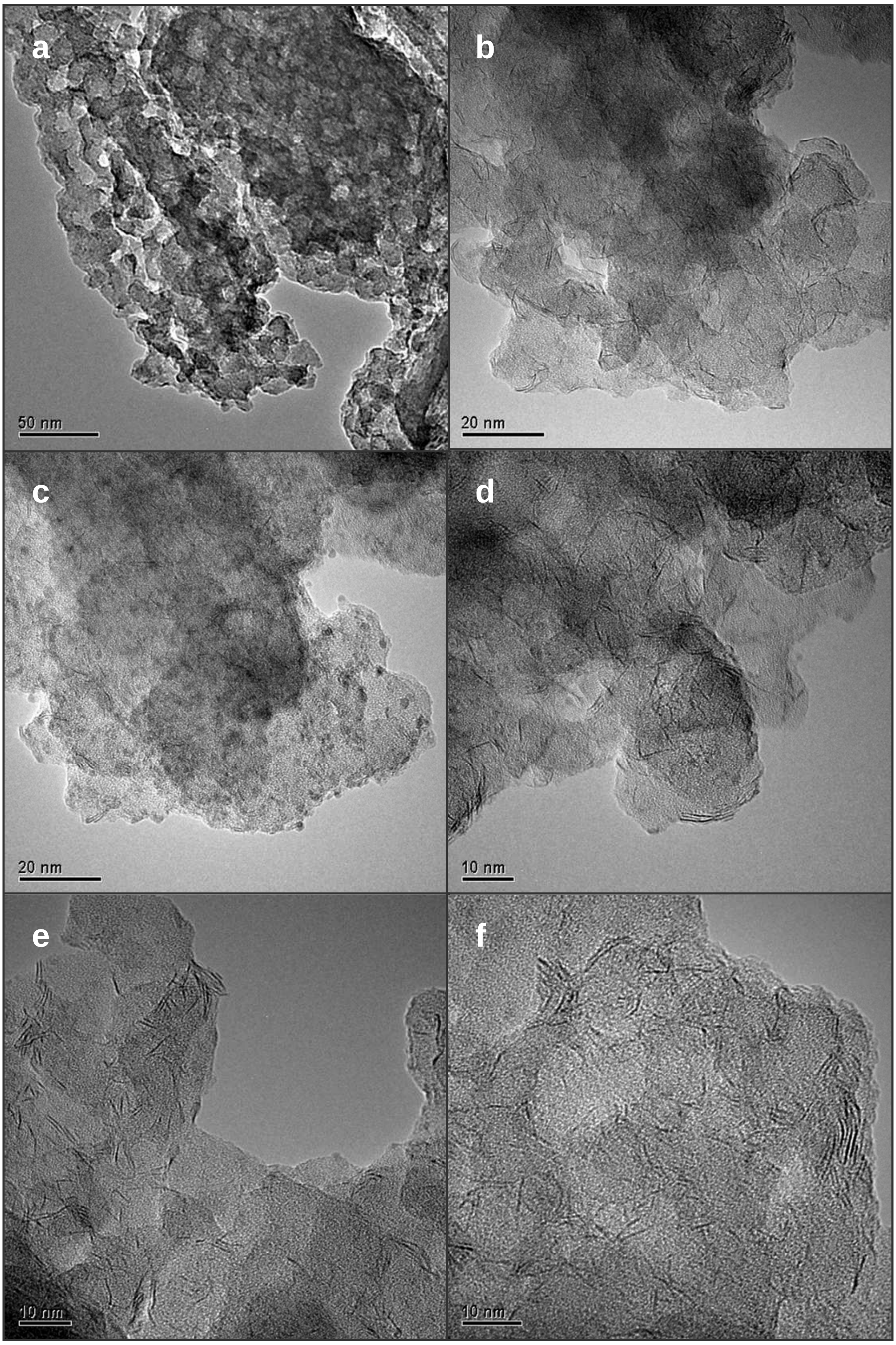

Figure S4: Representative TEM images of the spent catalyst whose precursor contained anchored $CoMo_6$ clusters

The mesoporous nature of the zeolite can clearly be recognised by the pronounced contrast differences shown in Figure S4a. Throughout the sample, MoS_2 slabs are present both as single and double sheets. The MoS_2 slabs are primarily located in the mesopores since they are too large to fit into the micropore system of the zeolite. The MoS_2 slabs are estimated to 2-3 nm. To further explore the location of the MoS_2 inside the zeolite particles TEM tomography is planned as future work.

In selected areas small round particles of homogeneous size distribution at around 1 nm were observed, especially apparent in Figure S4c and d. XRPD of the spent catalyst did only detect crystalline ZSM-5 together with an undefined amorphous phase. This could be due to the very small particles size of both the undefined particles and MoS_2 slabs. Most likely the small particles are due to non or only partially sulfided CoMo phase.

---

[1] A.L. Nolan, C.C. Allen, R.C. Burns, D.C. Craig, G.A. Lawrance, *Aust. J. Chem.*, 1998, **51**, 825

[2] Website of the International Zeolite Association: http://www.iza-structure.org/databases/ (1st of June 2011)

Top Catal
DOI 10.1007/s11244-011-9722-x

ORIGINAL PAPER

Size-Selective Oxidation of Aldehydes with Zeolite Encapsulated Gold Nanoparticles

Karen T. Højholt · Anders B. Laursen · Søren Kegnæs · Claus H. Christensen

Abstract Here, we report a synthesis and catalytic study of hybrid materials comprised of 1–3 nm sinter-stable Au nanoparticles in MFI-type zeolites. An optional post-treatment in aqua regia effectively remove Au from the external surfaces. The size-selective aerobic aldehyde oxidation verifies that the active Au is accessible only through the zeolite micropores.

Keywords Catalysis · Gold · Zeolite · Aerobic oxidation · Size-selectivity

1 Introduction

Supported gold nanoparticles with a diameter of less than 10 nm are highly active oxidation catalysts for many reactions [1]. However, these catalysts frequently deactivate as the average size of the supported metal nanoparticles increases due to sintering [2–5]. Several methods have been developed to produce sinter-stable nanoparticle catalyst, including encasing the metal nanoparticles in a protective shell or in a mesoporous silica matrix [6–9]. Generally all of these materials are non-selective in their catalytic activity. One option for enhancing selectivity is encapsulating the nanoparticles in a zeolite matrix. Zeolites have an inherent micropore system of molecular dimensions, which allows for shape-selective catalysis. Furthermore, zeolites are often materials with a high thermal stability and remarkably high surface areas. These properties also make zeolites particularly useful as the catalyst in several applications, and this use of zeolites has indeed received significant attention [10, 11]. Therefore, hybrid materials consisting of nanoparticles, which are only accessible via the micropore system of zeolites are interesting as they will combine the benefits of sinter-stable nanoparticles with the shape-selective properties of zeolites. Several authors [12–15] have entrapped metal nanoparticles in the cages of zeolite crystals using post treatment methods. This type of hybrid material though, is restricted to zeolites the structure of which contains cages.

Recently, we have reported the synthesis of immobilized Au nanoparticles in silicalite-1 type crystals [16]. It was demonstrated that Au nanoparticles are primarily encapsulated in the zeolite crystals but are also present as larger agglomerates on the external surface of the zeolite. By calcination experiments both ex situ and in situ it was shown that the encapsulated Au nanoparticles are highly stable towards sintering up to a temperature of 500 °C.

Here, we present a new and improved 2-step synthesis route to encapsulate Au metal nanoparticles in ZSM-5 zeolite crystals. Besides being a 2-step synthesis, this new

K. T. Højholt · A. B. Laursen (✉)
Haldor Topsøe A/S, Nymøllevej 55, 2800 Kgs,
Lyngby, Denmark
e-mail: a.b.laursen@fysik.dtu.dk

K. T. Højholt
e-mail: kntl@topsoe.dk

K. T. Højholt · S. Kegnæs
Department of Chemistry, Technical University of Denmark,
Center for Catalysis and Sustainable Chemistry, 2800 Kgs,
Lyngby, Denmark
e-mail: skk@kemi.dtu.dk

A. B. Laursen
Department of Chemical Engineering & Department of Physics,
Center for Individual Nanoparticle Functionality, Technical
University of Denmark, 2800 Kgs, Lyngby, Denmark

C. H. Christensen
LORC (Lindoe Offshore Renewables Center),
Kystvejen 100, 5330 Munkebo, Denmark
e-mail: chc@lorc.dk

synthesis allows Al to be introduced in the zeolite structure, which allows for tuning the acidic and hydrophobic properties of the zeolite matrix. Furthermore, we present a comprehensive characterization study using BET/N_2-physisorption, inductively coupled ion-plasma optical emission spectroscopy (ICP-OES), powder X-ray diffraction (XRPD), scanning and transmission electron microscopy (SEM and TEM). Our new hybrid material is then compared to the previous synthesized hybrid material in the aerobic oxidation of benzaldehyde and 3,5-dimethylbenzaldehyde see Scheme 1. Hereby, we demonstrate that the presence of embedded Au nanoparticles in the zeolite crystals enhance the selectivity towards the sterically less hindered methylbenzoate for both hybrid materials, thus verifying that the Au metal nanoparticles are truly encapsulated.

To investigate the role of the Au present on the surface of the catalyst, these are removed by a treatment with aqua regia. All four catalysts from the two synthesis strategies, including the Au leaching, are shown in Scheme 2.

The first material termed I-Au@MFI is made as previously described [16] by first immobilizing Au nanoparticles in amorphous silica followed by a hydrothermal synthesis to produce encapsulated Au nanoparticles in crystalline silicalite-1 crystals. During the optional acid leaching the organic template is kept in the micropores of the silicalite-1 crystals, as a filling agent to prevent the aqua regia in dissolving the embedded Au nanoparticles. The effectiveness of this technique, in preventing solvent penetration of the micropore system, has also previously been reported for the constrained desilication of ZSM-5 crystals [17]. The acid leached product is termed II-Au@MFI. In the new 2-step synthesis the first step is to immobilize Au nanoclusters in amorphous silica followed by a hydrothermal synthesis creating silicalite-1 seeds with a higher Au content than the previous product (I-Au@MFI). The resulting silicalite-1 seeds is suspended in a ZSM-5 growth medium containing aluminium and synthesised into the product termed III-Au@MFI. After the optional acid leaching the product is termed IV-Au@MFI.

All the synthesised materials were characterized using XRPD, ICP-OES, N_2 physisorption, SEM and TEM. Furthermore, the catalytic ability of the catalyst materials are tested in the aerobic oxidation of benzaldehyde and 3,5-dimethylbenzaldehyde in methanol to the corresponding methyl esters at room temperature and under atmospheric pressure.

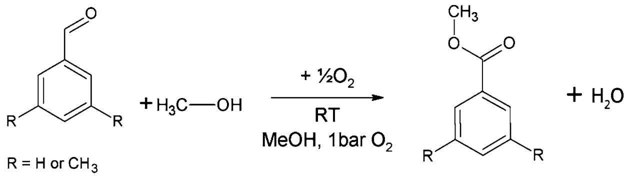

Scheme 1 Reaction scheme for the catalytic test reaction using two different reagent: R = H the stericly unhindered benzaldehyde and R = CH_3 the stericly hindered 3,5-dimethylbenzaldehyde

2 Experimental

2.1 Synthesis and Catalysts Preparation

All chemicals were used as-received without further purification.

2.1.1 *Synthesis of I-Au@MFI*

The catalyst was prepared as described in our previous study [16].

2.1.2 *Synthesis of III-Au@MFI*

The gold nanoclusters were prepared as described by Wu et al. [18] equimolarly exchanging the phenylethylthiol for 3-mercaptopropyltrimethoxysilane (MPTMS, Sigma-Aldrich, 95%). 25 mL of the resulting colloidal suspension was diluted with 500 mL THF (Sigma-Aldrich >99%), and 5.25 mL NH_4OH (Merck 25% NH_3) in an Erlenmeyer flask. After stirring (600 rpm) for 15 min 0.39 mL tetraethyl orthosilicate, TEOS (Sigma-Aldrich, 98%) was added and stirred for 8 h. Four additions of TEOS were made at 8 h intervals. The solid precursor product was recovered by evaporation of the solvents at 100 °C overnight. In a beaker 119 g deionized water was mixed with 19 g ethanol, 0.16 g NaOH, and 2.79 g TPAOH (AppliChem, 40 wt%). After obtaining a homogeneous solution 1.23 g precursor was suspended in this and then stirred for 15 min. The suspension was transferred to a 160 mL Teflon lined autoclave, sealed and heated to 100 °C for 5 days. After quenching the autoclave to room temperature the zeolite seeds was recovered by centrifugation at 9,000 rpm for 30 min and decanting off the mother liquid. The solid was washed five times by suspending it in water, centrifuging, and decanting off the mother liquid. Finally, the zeolite seeds were dried at 100 °C overnight. A ZSM-5 growth medium was prepared, by a procedure modified from literature [19], by dissolving 0.079 g NaOH, 0.098 g anhydrous $NaAlO_2$ (Riedel-de Häen, 29.3% Al) in 7.9 mL deionized water under stirring (600 rpm). Silica was added in small portions until 0.876 g SiO_2 gel (SiO_2 gel 100, 0.063–0.2 mm, Merck) had been added. The resulting suspension was mixed by shaking vigorously for 1 h. Then, 0.126 g zeolite seeds were added and shaken another hour. The final catalyst was obtained by sealing the suspension in a 160 mL Teflon lined autoclave and heating it to 180 °C

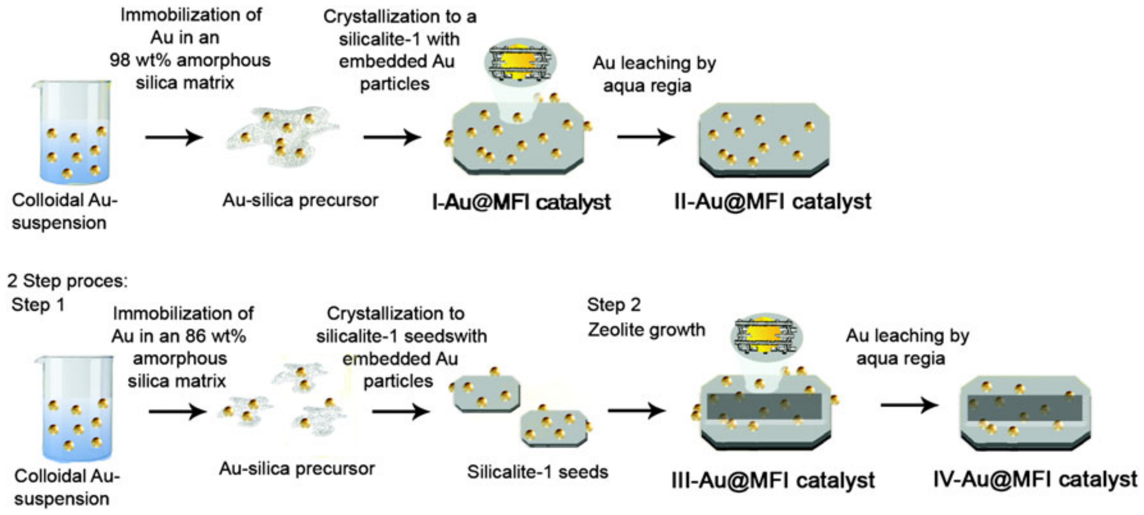

Scheme 2 Synthesis scheme for the four catalysts. The *upper one* is the first strategy and the *lower one* is the 2-step synthesis

for 40 h. After quenching the autoclave to room temperature the zeolite crystals were recovered by filtration on a cellulose filter in a Buchner funnel under suction. Finally, the solid product was washed in deionized water until a pH of 7 was reached. The final product was obtained by drying at 100 °C for 16 h.

2.1.3 Synthesis of II-Au@MFI and IV-Au@MFI

In a typical synthesis 0.4 g un-calcined product of the I-Au@MFI and III-Au@MFI synthesis, respectively, was transferred to a sintered glass frit filter (#4) and washed in 5 mL deionized water under suction. The solid was then washed in 25 mL aqua regia in portions of four each separated by washing in 5 mL deionized water. Finally, the acid was removed by washing in 200 mL deionized water.

2.1.4 Calcination

All four prepared Au@MFI samples are ground in a mortar and calcined in air by heating in a muffle oven. The samples are heated in a ceramic crucible to 550 °C at a ramp of 2 °C/min. The samples are held at this temperature for 3 h to ensure complete decomposition of the organic templates, after which it is allowed to cool naturally to room temperature.

2.2 Characterizations Methods

To identify and verify the crystal structure of the products, XRPD patterns were recorded using a Philips PANalytical X'PERT powder diffractometer with Cu Kα radiation in the 2θ interval 5–70°. The elemental analysis were preformed by ICP-OES and used to determine the exact amount of Au in the Au@MFI samples.

The surface area and the pore volume were determined by nitrogen adsorption and desorption measurements at liquid nitrogen temperature on a Micromeritics ASAP 2020. The samples were outgassed in vacuum at 473 K for 6 h prior to measurements. The total surface area was calculated according to the BET method and the micropore volumes were determined by the *t*-plot method [20].

The crystal size, morphology of the zeolite, and amount of highly reflecting Au of the Au@MFI samples were examined by scanning electron microscopy (SEM) on a Phillips XL20 FEG using a backscatter detector. The samples were placed on a carbon film and 20 nm Pt/Pd was evaporated onto the sample to achieve sufficient conductivity.

To investigate the size of the Au particles and the effect of the acid leaching sample I-Au@MFI and II-Au@MFI were examined by transmission electron microscopy (TEM) on a Titan 80–300 SuperTwin electronmicroscope operated at 300 kV. The samples were measured after calcination and then placed on a Cu-grid with a lacey carbon film.

2.3 Catalytic Aerobic Oxidation of Aldehydes

All reagents used were of reagent grade and used without further purification: Benzaldehyde (C_7H_6O, 99%, Sigma-Aldrich), 3,5-dimethylbenzaldehyde ($C_9H_{10}O$, 97%, Sigma-Aldrich), methanol (CH_3OH, 99%, Sigma-Aldrich), 30 wt% sodium methoxide solution (Sigma-Aldrich), anisol (C_7H_8O, 99% Sigma-Aldrich).

In a typical experiment, a mixture of 0.5 mmol aldehyde (benzaldehyde or 3,5-dimethylbenzaldehyde), 60 mmol methanol and 0.1 mmol sodium methoxide were charged into a 10 mL two-neck round-bottom flask equipped with a condenser and a septum together with a Au@MFI catalyst (0.1 mol% Au). The reactor system was connected to an O_2 cylinder and flushed with O_2. The reaction mixture was mixed with magnetic stirring and small samples were taken at selected times, filtered directly through a syringe filter and analysed by GC and GC–MS. The GC column Agilent Technologies Inc. HP-5 was used. The amounts of substrates and products were quantified using anisol as internal standard.

3 Results and Discussion

3.1 Characterization of the Au Zeolite Hybrid Materials

The XRPD patterns for the four Au@MFI catalysts are all shown in Fig. 1. All patterns are recorded after the zeolite synthesis and prior to combustion of the organic template. From Fig. 1 it is clearly seen that all samples contain highly crystalline material with the MFI structure [21] along with Au particles [22].

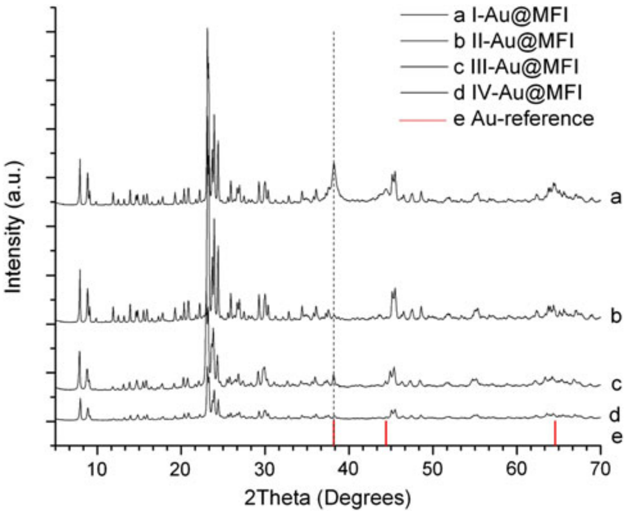

Fig. 1 XRPD patterns of **a** I-Au@MFI, **b** II-Au@MFI, **c** III-Au@MFI and **d** IV-Au@MFI. A reference pattern [22] **e** for bulk Au is shown as *bars* below the experimental patterns. All patterns are recorded before combustion of the organic template

The average diameter of the Au particles in the [111] crystal direction is estimated by the Debye–Scherrer equation and listed in Table 1. In Table 1 is also given the Au content determined from elementary analysis, ICP-OES, and the results from N_2 physisorption measurements are also given.

Comparing the average Au particle size before and after calcination yields the same trend for both sets of preparation methods. The overall trend is that the Au [111] sizes increase significantly for all samples. However, the most significant increase is for the two parent samples: I-Au@MFI (a factor of ~5.1) and III-Au@MFI (a factor of >1.6). It is assumed that this is due to the larger amount of Au particles on the surface of the parent samples, which may sinter freely, compared to the two washed samples, II-Au@MFI (a factor of ~1.5) and IV-Au@MFI (a factor of ~1.3). However, it could not be ruled out that the effect originates from the lower gold loading of the leached samples, i.e., nanoparticle dispersion. It is anticipated that the acid leaching decreases the average Au particle size since all the small Au particles should primarily be embedded in the zeolite and therefore inaccessible to the acid. This appears to be invalid in going from sample I-Au@MFI to II-Au@MFI. Here, the average diameter has increased from 18 to 28 nm prior to calcination. This could be due to the presence of small gold particles on the surface that would be removed first during the acid leaching leaving behind the larger Au particles resulting in an increase in the relative amount of larger particles. Opposed to this sample III-Au@MFI shows a small but net decrease in average diameter in going from sample III-Au@MFI to sample IV-Au@MFI. The Au content determined from ICP-OES analysis show that a significant amount of Au is lost during the acid leaching. However, the amounts of Au lost from the two acid leached samples are comparable, i.e., ca. 20%. Comparing the two parent samples, I-Au@MFI and III-Au@MFI, there is a considerable difference in the amount of Au demonstrating that the second synthesis routes gives a product containing an increased amount of Au.

Table 1 The average Au particle size before and after calcinations, Au content measured by ICP-OES and N_2 physisorption data. Au content and N_2 physisorption measurements are recorded after the combustion of the organic template

Material	Au size before/after calcination (nm)[a]	Au content (wt%)	Surface area (m^2/g)[b]	Micropore volume (cm^3/g)[c]	Zeolite size (μm)[d]
I-Au@MFI	18/92	1.37	306 [16]	0.096 [16]	2
II-Au@MFI	28/41	0.25	329	0.112	2
III-Au@MFI	64/ >100	3.34	245	0.105	10
IV-Au@MFI	49/63	0.65	269	0.093	10

[a] Estimated by Scherrer Equation D[111][b]Calculated by BET[c]Calculated by *t*-plot method[d]Estimated from SEM

This is believed to be due to a loss of either Au (I-Au@MFI) or zeolite precursor (III-Au@MFI) during the synthesis or a combination; this could not be verified from the available data.

In Table 1 the BET surface areas and micropore volumes of the four Au@MFI sample are given. The surface area for I-Au@MFI and II-Au@MFI lie in the range of previous results for conventional MFI samples around 300 m^2/g [23, 24]. The surface areas for III-Au@MFI and IV-Au@MFI are lower than for the former, which the authors speculate might be due to either crystal size, micropore blockage by the incorporated Au nanoparticles or extra framework alumina, or a very small amount of amorphous material. The latter, however, seems contradicted as the XRPD pattern shows only crystalline zeolite and gold. The micropore volumes for all four Au@MFI lie in the range of previous results [23, 24]. The surface area and micropore volume for the four Au@MFI samples illustrate that in spite of the incorporation of gold particles in the materials they are expected to perform like a conventional zeolite in respect to size-selectivity.

The SEM images of the four Au@MFI samples are shown in Fig. 2 and the images are recorded using the backscatter detector. By using the backscatter detector the Au particles, which are highly reflecting particles, will appear as bright spots.

Comparing sample I-Au@MFI and II-Au@MFI (Fig. 2a, b) there is a clear reduction in the amount of Au particles on the MFI crystal surfaces after the acid leaching in Fig. 2b. Note that only two larger Au particles are still observed after the treatment and that all smaller particles have disappeared from view. This observation indicates that the dissolution strategy has worked as intended. It should be emphasized that the resolution of the SEM images does not allow for detection of the small Au particles dominating this sample and the conclusions are only based on the larger particle agglomerates. From the SEM images of sample I-Au@MFI and II-Au@MFI it can be observed that a homogeneous distribution exists concerning the size of the MFI crystals of around 2 μm (Fig. 2a, b). From the SEM images it can also be seen that the crystals are primarily the typical coffin-shaped morphology for MFI-zeolites [23, 24]. Some twinned and some highly inter-grown crystals are also observed for the two samples. The acid treatment has not had a detectable influence on the morphology of the zeolites. Figure 2c, d show the 2-step synthesis strategy before and after acid leaching (sample III-Au@MFI and IV-Au@MFI). Comparing the two images one can observe a smaller amount of the high reflecting Au particle agglomerates on the crystal surface of the acid leached sample. The size and morphology of the zeolite does not change during the acid leaching. The MFI crystals are significantly larger for the 2-step synthesis compared to the first. The crystals are around 10 μm and have less distinct and less smooth morphologies than the previous, although the overall morphology is still coffin

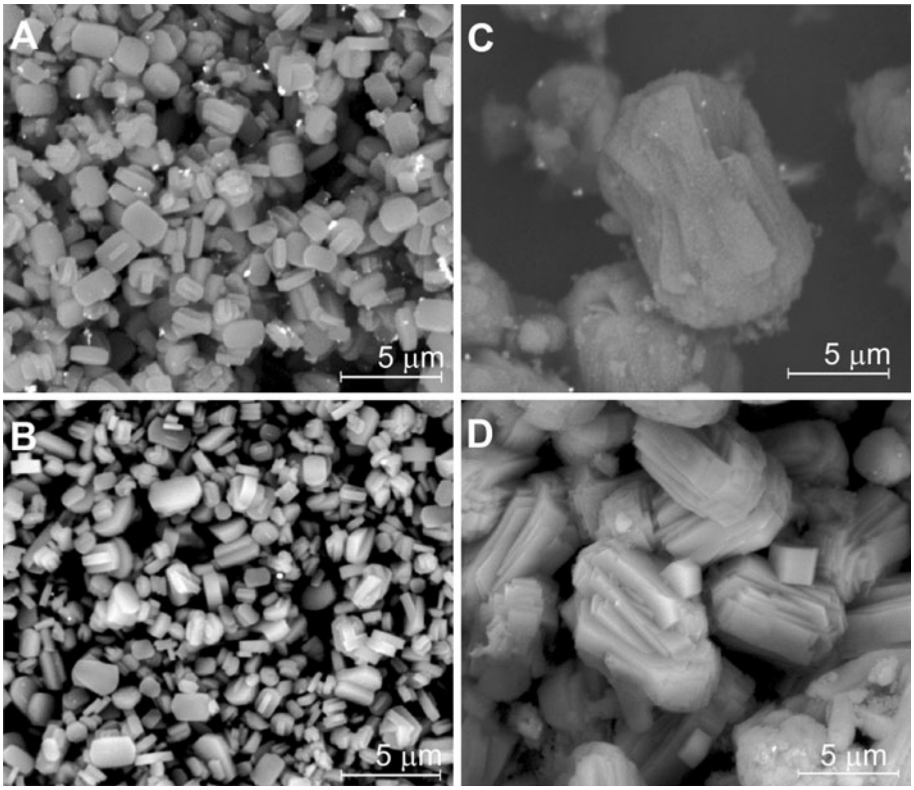

Fig. 2 SEM images of **a** I-Au@MFI, **b** II-Au@MFI, **c** III-Au@MFI, and **d** IV-Au@MFI. The images are recorded using the backscatter detector and after combustion of the template

shaped-like. The differences in size and morphology are ascribed to the difference in synthesis procedures. The ratio of silica to aluminium in the zeolite is estimated by EDS measurement to be 14 prior to acid treatment and 21 after. This shows that the 2-step synthesis results in a zeolite which may be made acidic by ion-exchange making it a potentially bi-functional catalyst and that the acid treatment dealuminates the sample slightly. In summary the silicalite-1 zeolites (I- and II-Au@MFI) are apparently unaffected by the aqua regia in terms of both morphology and crystallinity as seen from SEM and XRPD, respectively. The Al-containing zeolites (III- and IV-Au@MFI) lose a significant amount of Al, the morphology remains unchanged, and the crystallinity is only slightly decreased by the aqua regia treatment. As the catalytic activity of Au is governed by the presence of catalytic amounts of base [25], it is not relevant to test an acid form of the catalysts, as reaction with the base would result in the Na-form and a loss of activity. The Al-containing catalysts (III- and IV-Au@MFI) still contain some Lewis acidity in the tested Na-form; however, this is not expected to affect the activity.

To investigate the size of the Au particles, and whether the Au particles are on the external surface of the MFI crystals after the acid leaching, TEM is used. The larger MFI crystals of samples III- and IV-Au@MFI make a TEM investigation impossible thus only the TEM investigation of I- and II-Au@MFI are shown here. In Fig. 3 representative TEM images of samples I- and II-Au@MFI are shown. In these images the gold particles are seen as dark particles both in profile view, i.e., on the edge of the zeolite crystal perimeter and in the plane view, i.e., on the centre of the zeolite crystals.

In Fig. 3a the smaller particles (1–3 nm) are concentrated in the centre of the plane view but are also present in the profile view together with larger agglomerated particles (>20 nm). These particles are all much larger than the cages present in the MFI zeolite, indicating that the framework have been disrupted to accommodate the Au particles. It is well known that only small Au particles are active in catalysis [1, 26, 27]. Therefore, the small particles on the outer surface of the zeolite will result in unselective catalytic activity. These particles are thus the most important to remove by the acid treatment. A representative TEM image of the acid leached sample II-Au@MFI is shown in Fig. 3b. It is seen that all the particles, in the profile view, have been removed leaving the small particles in the plane view intact. Throughout the sample all the small Au particles on the external surface appears to be removed while few large particles remain. From this it is concluded that if all the small particles had been accessible to the acid treatment no small particles would be left. We have previously determined by TEM tomography that most of the Au particles in the plane view of sample I-Au@MFI are embedded in the MFI crystal [16]. Hence, it seems likely that the small Au particles left by the acid treatment are also the ones incorporated into the zeolite. The strategy of removing the small particles on the outer surface by leaving the template molecule in the pores while washing with aqua regia has been effective. It is worth noting that from the presented data the selectivity of the acid treatment has only been qualitatively demonstrated and is not expected to be completely selective. The novel discovery of this work is, however, that the acid treatment is selective and this opens the possibility to remove all Au from the surfaces leaving only the catalytic active particles. These results are consistent with the assumptions made previously in the XRPD investigation, i.e., that the average Au diameter increases on acid leaching due to the faster dissolution of the small Au particles on the external surface.

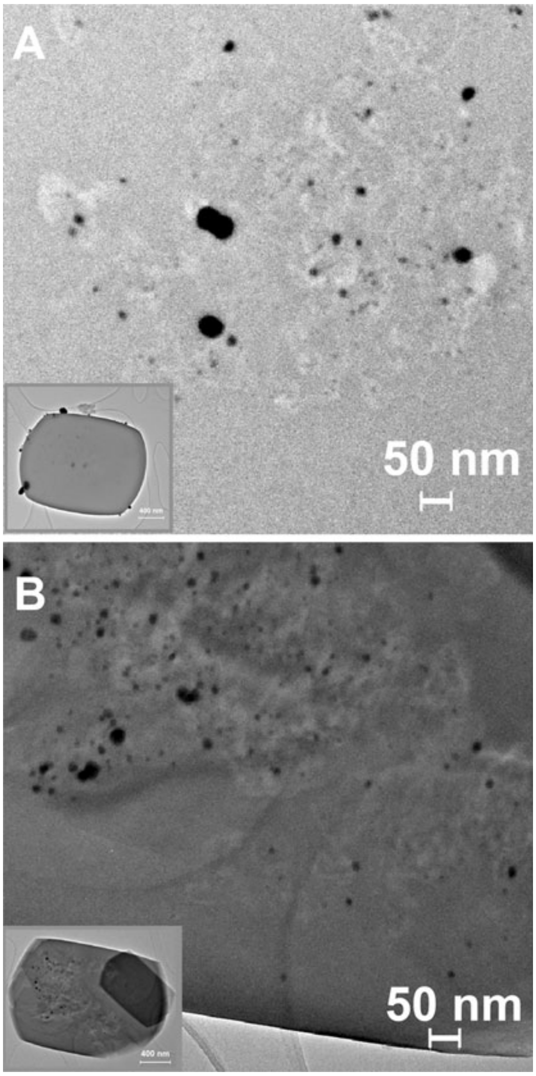

Fig. 3 A magnified TEM image of **a** I-Au@MFI and **b** II-Au@MFI. The *scale bars* in the images are 50 nm and in the *inset* they are 400 nm

Furthermore in the TEM images small areas of lower contrast are observed surrounding the Au particles. This is attributed to areas of mesoporosity arising when the Au nanoparticles are incorporated in the framework accompanied by disruption of the crystal structure. Note that this porosity does not show in the physisorption and hence it must be of insignificant concentration.

3.2 Catalytic Experiments

It is well known that Au nanoparticles can oxidise aldehydes to esters [25, 28]. The four Au@MFI catalysts are tested in the size-selective oxidation of benzaldehyde and 3,5-dimethylbenzaldehyde, see Scheme 3.

The benzaldehyde molecules should be able to diffuse into the zeolite crystals and be oxidized by the embedded gold particles. Whereas, the more bulky 3,5-dimethylbenzaldehyde molecules can only be oxidized by gold nanoparticles located on the outside of the zeolite crystals. The activity measurements are illustrated in Fig. 4 as yield of methyl esters as a function of time.

In Fig. 4a the catalytic activity for I-Au@MFI and II-Au@MFI in the oxidation of both benzaldehyde and 3,5-dimethylbenzaldehyde is shown. It is seen that both I-Au@MFI and II-Au@MFI are able to catalyse the oxidation of benzaldehyde giving yield of 97 and 94%, respectively, after 72 h at full conversion (>99%). The major by-product is benzoic acid in <6% yield, as previously observed in literature [28]. In the case of 3,5-dimethylbenzaldehyde the activities are much lower for the two catalysts resulting in yields of <3% with conversion <5% after 72 h. In Fig. 4b the catalytic activities of III-Au@MFI and IV-Au@MFI are shown. It shows that III-Au@MFI and VI-Au@MFI have the same selectivity in the oxidation of benzaldehyde and 3,5-dimethylbenzaldehyde as I-Au@MFI and II-Au@MFI. However, the yields and conversions are a little lower for the methyl benzoate but comparable for the methyl 3,5-dimethylbenzoate.

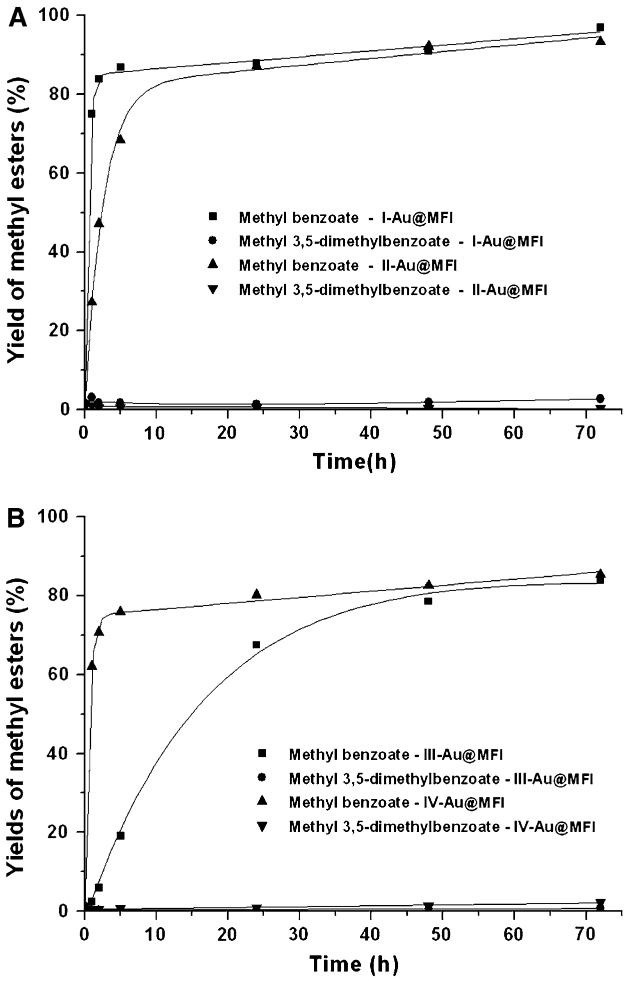

Fig. 4 Yields as a function of time for **a** I-Au@MFI and II-Au@MFI and **b** III-Au@MFI and IV-Au@MFI. The catalytic tests were carried out in an open flask at room temperature, atmospheric pressure and with the following ratios: Aldehyde: 5; CH_3OH: 600; $NaOCH_3$: 1 and with 0.1 mol% Au@MFI

The catalytic result proves that the embedded gold nanoparticles are accessible and catalytic active through zeolite micropores since it is possible to oxidise benzaldehyde. Furthermore, as it is not possible to oxidise the more bulky 3,5-dimethylbenzaldehyde, it is only the embedded gold particles, which are catalytically active. Regarding the washing of the catalysts with aqua regia, it was expected that the catalytic activity in the oxidation of 3,5-dimethylbenzaldehyde would decrease when removing the Au particles on the surface. However, at these conversions no clear change in the catalytic activities was observed. As a reference catalyst Au on TiO_2 (Mintek,

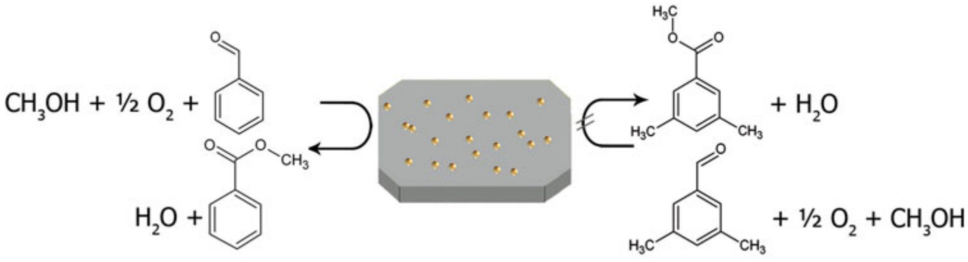

Scheme 3 Schematic drawing of the size-selectivity in the benzaldehyde and 3,5-dimethylbenzaldehyde oxidation reaction

1 wt%) was tested. It showed no shape-selectivity and was highly cable of oxidising both benzaldehyde and 3,5-dimethylbenzaldehyde. The small difference in activity and selectivity for the catalysts before and after acid leaching can be ascribed to sintering of the small Au nanoparticles on the external surface of the zeolite crystals during calcinations. Meaning that after calcination very few active particles remain on the surface of the parent samples. The effect of the average Au nanoparticles size determined from XRPD (Table 1) could not be correlated to the catalyst activity. The authors speculate that this is due to the broad particle distribution, which makes it impossible to determine the amount or average size of the active Au nanoparticles, i.e., with a diameter of less than 10 nm [1, 26, 27]. The catalytic results also show that the Au nanoparticles are active even after calcinations at 550 °C hereby verifying that the Au nanoparticles are sinter-stable when encapsulated.

4 Conclusions

In conclusion we have studied the catalytic activities of hybrid materials comprising sinter-stable Au nanoparticles accessible only through zeolite micropores. We have shown two different synthesis strategies to prepare MFI type zeolite crystals, which contain embedded Au nanoparticles in the range of 1-3 nm. Aluminium was successfully introduced in the zeolite matrix yielding opportunities to tune the material properties. Furthermore, the effect of post aqua regia treatment to remove Au agglomerates on the external surface of the MFI type zeolite has been studied. By TEM it was shown that all the small Au nanoparticles on the external surface of the hybrid material were removed by acid leaching. No significant change in activity for catalysts III- and IV-Au@MFI, which have some Lewis acid sites due to the presence of Al, was observed. This is in line with the expectations as the aerobic oxidations using gold rely on a catalytic amount of base. Future work will include the utilization of the bi-functionality of catalysts III- and IV-Au@MFI, for a reaction requiring both acidic and oxidative properties.

Moreover, the hybrid materials were tested in the aerobic oxidation of benzaldehyde and 3,5-dimethylbenzaldehyde in methanol to the corresponding methyl esters. The reactions were conducted at room temperature and under atmospheric pressure. The materials were active as substrate-size selective oxidation catalysts for in the aerobic oxidations. We have shown that it is not possible to oxidize 3,5-dimethylbenzaldehyde whereas benzaldehyde is readily oxidized to the methylester very selectively, thus showing that the encapsulated Au nanoparticles are only accessible through the zeolite micropores.

Acknowledgments The Centre for Catalysis and Sustainable Chemistry is sponsored by the Danish National Research Foundation. We gratefully acknowledge the assistance of Eva Charlotte Bendixen and Aino Nielsen at Haldor Topsøe A/S for obtaining the TEM and SEM images, respectively.

References

1. Haruta M (2003) Chem Rec 3:75
2. Haruta M, Yamada N, Kobayashi T, Iilima S (1997) J Catal 115:301
3. Valden M, Lai X, Goodman DW (1998) Science 281:1674
4. Bartholomew CH (1997) Stud Surf Sci Catal 111:585
5. Haruta M (1997) Catal Today 36:153
6. Arnal PM, Comotti M, Schüth F (2006) Angew Chem Int Ed 45:8224
7. Ren N, Yang Y-H, Shen J, Zhang Y-H, Xu H-L, Gao Z, Tang Y (2007) J Catal 251:182
8. Joo SH, Park JY, Tsung C-K, Yamada Y, Yang P (2009) Nature Mater 8:126
9. Beakley LW, Yost SE, Cheng R, Chandler BD (2005) Appl Catal A 292:124
10. Corma A (1995) Chem Rev 95:559
11. Corma A (1997) Chem Rev 97:2373
12. Fierro-Gonzalez JC, Hao Y, Gates BC (2007) J Phys Chem C 111:6645
13. Kuge K, Calzaferri G (2003) Microporous Mesoporous Mater 66:15
14. Guillemot D, Polisset-Thfoin M, Fraissard J (1996) Catal Lett 41:143
15. Liu X, Dilger H, Eichel RA, Kunstmann J, Roduner E (2006) J Phys Chem B 110:2013
16. Laursen AB, Højholt KT, Simonsen SB, Lundegaard LF, Helveg S, Schüth F, Paul M, Grunwaldt J-D, Kegnæs S, Christensen CH, Egeblad K (2010) Angew Chem Int Ed 49:3504
17. Pérez-Ramírez J, Abelló S, Bonilla A, Groen JC (2009) Adv Funct Mater 19:164
18. Wu Z, Suhan J, Jin R (2009) J Mater Chem 19:622
19. Lechert H, Kleinwort R (2001) High-Alumina ZSM-5. In: Robson H, Lillerud KP (eds) Verified syntheses of zeolitic materials, 2nd revised edn. Elsevier Science BV, Amsterdam. http://www.iza-online.org/synthesis/Recipes/High-Alumina%20ZSM-5.html
20. Lippens JH, de Boer J (1965) J Catal 4:319
21. Baerlocher CH, McCusker LB (2007) IZA database of zeolite structures. http://www.iza-structure.org/databases/
22. Hanawalt et al. (1938) Anal Chem 10: 475 (ICSD XRPD pattern for Au, reference PDF# 00-001-1172)
23. Kustova MY, Rasmussen SB, Kustov AL, Christensen CH (2006) Appl Catal B 67:60
24. Egeblad K, Kustova M, Klitgaard SK, Zhu K, Christensen CH (2007) Microporous Mesoporous Mater 101:214
25. Marsden C, Taarning E, Hansen D, Johansen L, Klitgaard SK, Egeblad K, Christensen CH (2008) Green Chem 10:168
26. Wolf A, Schüth F (2002) Appl Catal A 226:1
27. Haider P, Kimmerle B, Krumeich F, Kleist W, Grunwaldt J-D, Baiker A (2008) Catal Lett 125:169
28. Klitgaard SK, DeLaRiva AT, Helveg S, Werchmeister RM, Christensen CH (2008) Catal Lett 126:213

Hybrid Materials

DOI: 10.1002/anie.200906977

Substrate Size-Selective Catalysis with Zeolite-Encapsulated Gold Nanoparticles**

Anders B. Laursen, Karen T. Højholt, Lars F. Lundegaard, Søren B. Simonsen, Stig Helveg, Ferdi Schüth, Michael Paul, Jan-Dierk Grunwaldt, Søren Kegnæs, Claus H. Christensen, and Kresten Egeblad**

Over the years, many strategies have been developed to address the problem of sintering of nanoparticle catalysts,[1] including encapsulating metal nanoparticles in protective shells,[2–4] and trapping nanoparticles in the cavities of certain zeolites in post-synthesis steps.[5–8] In general, materials that contain metal nanoparticles that are only accessible via zeolite micropores are intriguing, specifically, but not exclusively, for catalytic applications. The encapsulation of carbon nanoparticles during zeolite crystallization is a well-known approach for making carbon–zeolite composites that afford mesoporous zeolites after combustion.[9–11] Herein, we show that metal nanoparticles can also be encapsulated during zeolite crystallization, as exemplified by silicalite-1 crystals that are embedded with circa 1–2 nm-sized gold nanoparticles that remain stable and catalytically active after calcination in air at 550 °C. Moreover, we show that the encapsulated gold nanoparticles are only are accessible through the micropores of the zeolite, which makes this material a substrate-size selective oxidation catalyst.

Currently, more than 175 different zeolite structures have been reported,[12] and these can be tuned according to the desired acidity and/or redox properties. Expanding the scope from pure zeolites to hybrid materials, by combining the properties of zeolites with other components, significantly widens the field of zeolite materials design. Aside from post-treatment methods, two types of approaches have been pursued for preparing hybrid zeolite–nanoparticle materials. The first type of approach involves crystallization of the zeolite from a gel that contains metal ions that are immobilized in the zeolite during crystallization.[13–14] With this kind of approach, it is very difficult to control the properties of the non-zeolite component in terms of, for example, particle size. The other type of approach is to first synthesize the non-zeolite component and subsequently encapsulate this in the individual zeolite crystals during crystallization. Indeed, this strategy is also well-known and an entire family of materials, known as mesoporous or hierarchical zeolite crystals, are based on the embedding of carbon nanoparticles, nanofibers, nanotubes, or other nanostructures during zeolite crystallization (and subsequent combustion) in a process known as carbon templating.[9–11,15,16] Concerning the embedding of metal nanoparticles in zeolites, Hashimoto et al. reported a top down approach that features downsizing gold flakes to approximately 40 nm particles by laser ablation, and subsequent encapsulation of these particles during crystallization.[17] A reduction in particle size by one order of magnitude is necessary for an efficient use of costly noble metals in catalytic applications. However, a reduction of the particle size enhances the tendency for sintering, owing to the increase in surface free energy. To mitigate this problem, we report herein a bottom-up approach for the preparation of hybrid zeolite-nanoparticle materials that contain small metal nanoparticles, dispersed throughout the zeolite crystals. This synthetic approach comprises three steps (Figure 1): First, a metal nanoparticle colloid is prepared with suitable anchor points for the generation of a silica shell. Second, the particles are encapsulated in an amorphous silica matrix. Third, the silica nanoparticle precursor is subjected to hydrothermal conditions in order for zeolite crystallization to take place. Using this approach, we successfully prepared a material that consisted predominantly of circa 1–2 nm sized gold particles that were embedded in silicalite-1 crystals. X-ray diffraction revealed that the material contained exclusively gold as well as MFI-structured material (generalized silicalite-1 crystal structure type).

Figure 2 shows scanning electron microscopy (SEM) and transmission electron microscopy (TEM) images of the hybrid material that consists of gold nanoparticles embedded in silicalite-1 crystals. The SEM image reveals that the material is mainly composed of circa 1–2 μm long coffin-shaped crystals, with a minor fraction of intergrown coffin-

---

[*] A. B. Laursen, K. T. Højholt, L. F. Lundegaard, S. B. Simonsen, S. Helveg, Prof. C. H. Christensen, K. Egeblad
Haldor Topsøe A/S
Nymøllevej 55, 2800 Kgs. Lyngby (Denmark)
E-mail: chc@topsoe.dk
kreg@topsoe.dk

A. B. Laursen, Prof. J.-D. Grunwaldt
DTU Chemical Engineering
Technical University of Denmark
2800 Kgs. Lyngby (Denmark)

K. T. Højholt, S. Kegnæs, Prof. C. H. Christensen, K. Egeblad
Center for Sustainable and Green Chemistry
Technical University of Denmark
2800 Kgs. Lyngby (Denmark)

Prof. Dr. F. Schüth, M. Paul
Max-Planck-Institut für Kohlenforschung
45470 Mülheim (Germany)

[**] We gratefully acknowledge the participation of the CTCI Foundation, Taiwan, in the establishment of the in situ electron microscopy facility at Haldor Topsøe A/S and the Catalysis for Sustainable Energy Initiative, Technical University of Denmark.

Supporting information for this article, including experimental procedures and TEM movies, is available on the WWW under http://dx.doi.org/10.1002/anie.200906977.

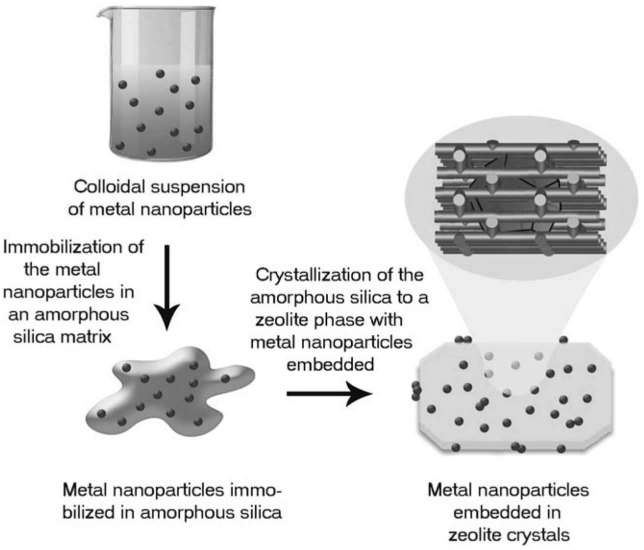

Figure 1. Schematic illustration of the encapsulation of gold nanoparticles in zeolite crystals.

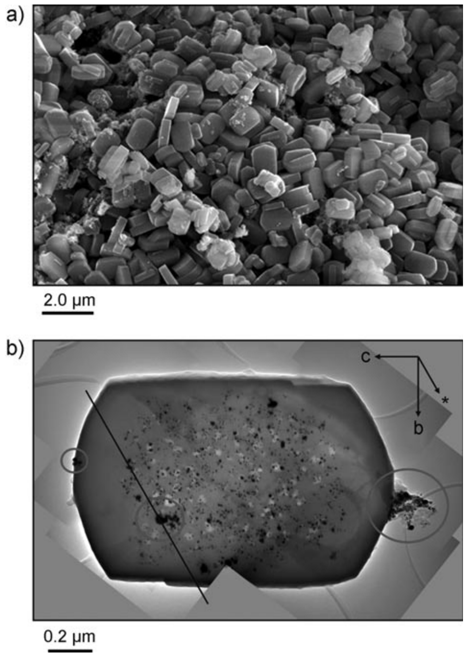

Figure 2. SEM and TEM micrographs of the composite zeolite sample. a) SEM micrograph showing the coffin-shaped crystallites, characteristic for silicalite-1. b) Mosaic composed of 10 TEM bright-field micrographs that shows a representative crystallite as seen along the [1 0 0] zone axis. The crystal lattice is indexed based on the standard *Pnma* space group setting. The black areas represent high density regions, and therefore correspond to the gold particles. Voids are observed as light regions within the zeolite crystal. Circles mark gold particles that are either obviously on the surfaces or are later shown to be on the surface of the crystallite (cf. Figure 3).

shaped crystals and irregularly shaped crystals (Figure 2a). The coffin-shaped and intergrown coffin-shaped crystal morphologies are commonly observed for MFI-structured zeolite materials. The mosaic TEM image reveals an overall uniform contrast over the entire crystal, superimposed by areas of darker and brighter contrast (Figure 2b). The variable contrast is attributed to variable mass-thickness over the crystal: the darker areas correspond to gold particles and the brighter areas correspond to voids in the crystal. The very small voids are consistent with small mesoporosity, measured by N_2 physisorption (see the Supporting Information). Gold particles that are observed in plan view in the crystal are approximately 1–2 nm in diameter, whereas those imaged in the profile view at the crystal edges are significantly larger and more agglomerated. The voids appear to be concentrated in the center of the crystal, around the gold particles. Similar observations, that the formation of metal nanoparticles induce secondary pore formation in zeolites, have been reported previously, for instance for platinum nanoparticles in zeolite NaX.[18] As a TEM image is a two-dimensional projection of the specimen, it is not possible to determine whether the small particles are located on the crystal surfaces or inside the zeolite crystal. To determine the relative positions of the gold nanocrystals with respect to the zeolite crystal, three-dimensional imaging was pursued by means of bright field TEM tomography.[19–21]

The reconstructed tomogram shows all of the characteristic features that were observed in the TEM images apart from the smallest gold particles; this is a result of the blurring effect caused by the weighted back-projection algorithm. From the tomogram sections, shown in Figure 3, it is clear that significant amounts of gold are located inside the zeolite crystal. Investigation of all of the tomogram sections shows that all of the gold particles shown in Figure 2b (except those marked by the circles) are encapsulated within the zeolite crystal.

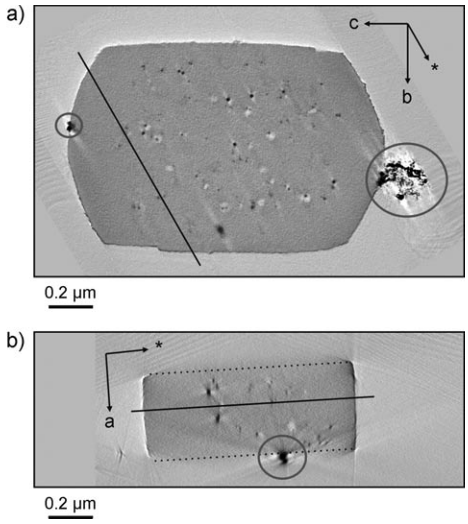

Figure 3. Sections through tomogram reconstruction. Images in a) and b) are tomogram sections approximately perpendicular to and parallel to the [1 0 0] zone axis, respectively. The full lines in each section correspond to the intersection of the other tomogram section. The missing wedge of the tilt series parallel to the [1 0 0] zone axis results in low contrast on crystal surfaces normal to this direction. Dotted lines have been added to clearly show the position of the {1 0 0} surfaces in b). Red circles mark gold particles on the surface of the zeolite crystal (compare to Figure 2).

To address if the zeolite encapsulation stabilizes the gold nanocrystals, TEM images were recorded before and after calcination (550 °C in air, 3 hours; Figure 4 a,b). Before calcination, the majority of the gold particles were generally circa 1 nm in diameter (Figure 4 a). However, after calcination, the particles imaged in profile view at the edges are larger and more rounded in shape (Figure 4 b), whereas the majority of the particles imaged in the plane view in the crystal remain unaltered in size. This observation indicates that the gold particles that are embedded within the zeolite crystals have an enhanced stability towards sintering, despite the smaller gold particle size. Therefore, this synthesis affords a gold–silicalite-1 hybrid material with an enhanced sintering stability of the metal nanoparticles.

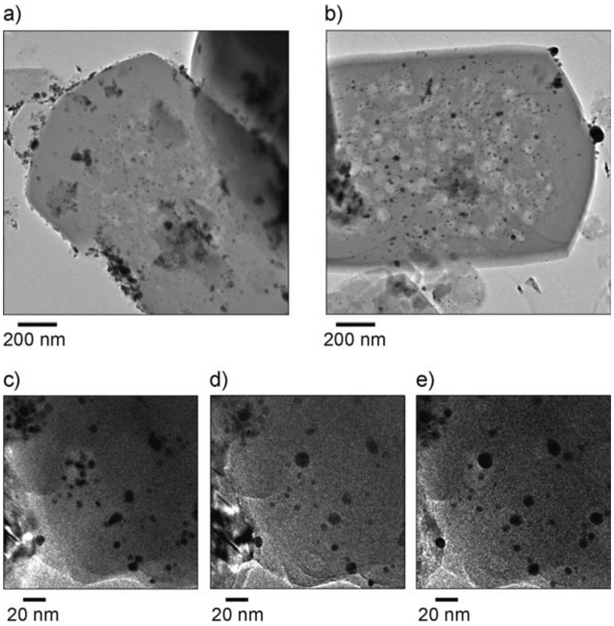

Figure 4. TEM images a) before and b) after calcination (550 °C, 3 h). In situ TEM images obtained under an O_2 atmosphere at c) 25, d) 300, and e) 500 °C.

The enhanced stabilization of the gold nanoparticles is further corroborated by a series of in situ TEM images (Figure 4 c–e) that were obtained during exposure of the material to an O_2 atmosphere at temperatures from 25–500 °C. At 25 °C, the sample area contains gold particles of different sizes (Figure 4 c). By heating to 300 °C, and further up to 500 °C, the larger gold particles preferentially sinter whilst the smallest particles are stable. This could be regarded as unexpected, as the sintering rate of nanoparticles usually scales inversely with their size. However, in this material, the small nanoparticles are less prone to sintering because they are fixed within the zeolite crystal. Given the information obtained from Figure 4 a–b, the in situ observation is fully consistent with the finding that particle embedment in the zeolite improves their stability towards sintering.

In order to verify that the encapsulated gold nanoparticles are accessible for catalysis, we investigated the aerobic oxidation of a mixture of benzaldehyde and 3,5-di-*tert*-butylbenzaldehyde in methanol into their corresponding methyl esters. The reaction was conducted at room temperature under atmospheric pressure.[22,23] The results of these experiments, together with reference experiments carried out using a Au/TiO_2 catalyst, are shown in Figure 5. Both substrates are oxidized using the Au/TiO_2 catalyst, whereas only benzaldehyde is oxidized in appreciable amounts using the gold–silicalite-1 catalyst. This observation is attributed to the different size of the substrates; 3,5-di-*tert*-butylbenzaldehyde is much more bulky than the unsubstituted benzaldehyde, and is therefore not able to diffuse into the zeolite interior where the catalytically active gold nanoparticles are located.

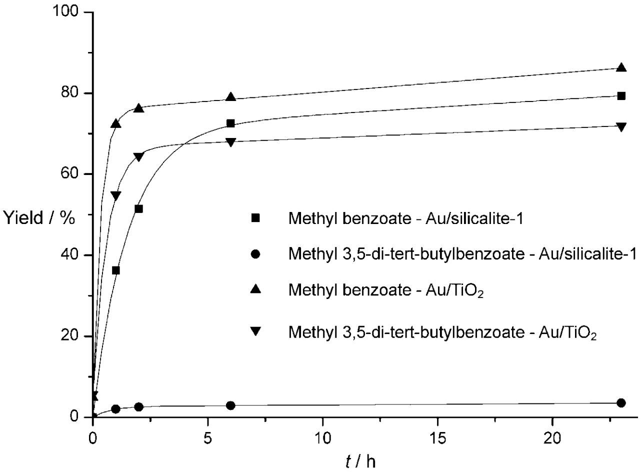

Figure 5. Gold-catalyzed oxidation of a mixture of benzaldehyde and 3,5-di-*tert*-butylbenzaldehyde in methanol to form the methyl esters.

In summary, we have developed an approach for the preparation of hybrid materials that are comprised of 1–2 nm sized gold nanoparticles that are embedded in silicalite-1 crystals. We have shown by three-dimensional TEM tomography that some gold particles are embedded within the zeolite and some are on the external surface of the zeolite crystals. Moreover, calcination experiments, followed by both ex situ and in situ TEM, indicate that the nanoparticles embedded within the zeolite crystals are highly stable towards sintering, whereas the particles located on the outer surface of the zeolite tend to sinter. Furthermore, we have shown that the encapsulated gold nanoparticles are only accessible through the zeolite micropores as it is not possible to oxidize 3,5-di-*tert*-butylbenzaldehyde whereas benzaldehyde is readily oxidized. Therefore, hybrid materials such as these might find application as sinter-stable nanoparticle catalysts or in other areas of materials science.

Received: December 11, 2009
Revised: January 19, 2010

Keywords: gold · mesoporous materials · nanoparticles · oxidation · zeolites

---

[1] C. H. Christensen, J. K. Nørskov, *Science* **2010**, *327*, 278 – 279.
[2] P. M. Arnal, M. Comotti, F. Schüth, *Angew. Chem.* **2006**, *118*, 8404 – 8407; *Angew. Chem. Int. Ed.* **2006**, *45*, 8224 – 8227.
[3] S. H. Joo, J. Y. Park, C.-K. Tsung, Y. Yamada, P. Yang, G. A. Somorjai, *Nat. Mater.* **2009**, *8*, 126 – 131.
[4] N. Ren, Y.-H. Yang, J. Shen, Y. Zhang, H.-L. Xu, Z. Gao, Y. Tang, *J. Catal.* **2007**, *251*, 182 – 188.
[5] J. C. Fierro-Gonzalez, Y. Hao, B. C. Gates, *J. Phys. Chem. C* **2007**, *111*, 6645 – 6651.
[6] L. F. Nazar, G. A. Ozin, F. Hugues, J. Godber, D. Rancourt, *Angew. Chem.* **1983**, *95*, 645 – 646; *Angew. Chem. Int. Ed. Engl.* **1983**, *22*, 624 – 625; Supplement: L. F. Nazar, G. A. Ozin, F. Hugues, J. Godber, D. Rancourt, *Angew. Chem.* **1983**, *95*, 898 – 919; *Angew. Chem. Int. Ed. Engl.* **1983**, *22*, 898 – 919.
[7] G. Lu, T. Hoffer, L. Guczi, *Catal. Lett.* **1992**, *14*, 207 – 220.
[8] X. S. Zhao, G. Lu, G. J. Millar, *J. Porous Mater.* **1996**, *3*, 61 – 66.
[9] C. J. H. Jacobsen, C. Madsen, J. Jindrich, I. Schmidt, A. Carlsson, *J. Am. Chem. Soc.* **2000**, *122*, 7116 – 7117.
[10] I. Schmidt, A. Boisen, E. Gustavsson, K. Ståhl, S. Pehrson, S. Dahl, A. Carsson, C. J. H. Jacobsen, *Chem. Mater.* **2001**, *13*, 4416 – 4418.
[11] K. Egeblad, C. H. Christensen, M. Kustova, C. H. Christensen, *Chem. Mater.* **2008**, *20*, 946 – 960.
[12] C. Baerlocher, L. B. McCusker, D. H. Olson, *Atlas of Zeolite Framework Types*, Elsevier, Amsterdam, **2007**.
[13] P. B. Weisz, V. J. Frilette, R. W. Maatman, E. B. Mower, *J. Catal.* **1962**, *1*, 307 – 312.
[14] H. Yang, H. Chen, J. Chen, O. Omotoso, Z. Ring, *J. Catal.* **2006**, *243*, 36 – 42.
[15] Z. Pavlackova, G. Kosova, N. Zilkova, A. Zukal, J. Cejka, *Stud. Surf. Sci. Catal.* **2006**, *162*, 905 – 912.
[16] A. H. Janssen, I. Schmidt, C. J. H. Jacobsen, A. J. Koster, K. P. De Jong, *Microporous Mesoporous Mater.* **2003**, *65*, 69 – 75.
[17] S. Hashimoto, T. Uwada, H. Masuhara, T. Asahi, *J. Phys. Chem. C* **2008**, *112*, 15089 – 15093.
[18] J. Rathousky, A. Zukal, N. Jaeger, G. Schulz-Ekloff, *Nanostruct. Mater.* **1992**, *1*, 355 – 360.
[19] H. Friedrich, P. E. de Jongh, A. R. Verkleij, K. P. De Jong, *Chem. Rev.* **2009**, *109*, 1613 – 1629.
[20] P. A. Midgley in *Handbook of Microscopy for Nanotechnology* (Eds.: N. Yao, L. Z. Wang), Kluwer Academic Publishers, Dordrecht, **2005**, pp. 601 – 628.
[21] P. A. Midgley, R. E. Dunin-Borkowski, *Nat. Mater.* **2009**, *8*, 271 – 280.
[22] C. Marsden, E. Taarning, D. Hansen, L. Johansen, S. K. Klitgaard, K. Egeblad, C. H. Christensen, *Green Chem.* **2008**, *10*, 168 – 170.
[23] S. K. Klitgaard, A. T. DeLaRiva, S. Helveg, R. M. Werchmeister, C. H. Christensen, *Catal. Lett.* **2008**, *126*, 213 – 217.

Angewandte Chemie
Eine Zeitschrift der Gesellschaft Deutscher Chemiker

Supporting Information

69451 Weinheim, Germany

Substrate Size-Selective Catalysis with Zeolite-Encapsulated Gold Nanoparticles**

Anders B. Laursen, Karen T. Højholt, Lars F. Lundegaard, Søren B. Simonsen, Stig Helveg, Ferdi Schüth, Michael Paul, Jan-Dierk Grunwaldt, Søren Kegnæs, Claus H. Christensen, and Kresten Egeblad**

anie_200906977_sm_miscellaneous_information.pdf
anie_200906977_sm_insitu.avi
anie_200906977_sm_tilt.mpg
anie_200906977_sm_tomo.mpg

Supporting information

Supporting information

Synthesis of the Au-silica precursor material and the hybrid Au-Silicate-1 Material

Following the procedure described by Haider et al.[1] we prepared 1 L Au colloid suspension with Au nanoparticles in the size range 1-2 nm (measured by TEM) starting from $HAuCl_4 \cdot 3H_2O$ (Sigma-Aldrich, 99.9+%), tetrakis(hydroxymethyl)phosphonium chloride (THPC, Sigma-Aldrich 98%) and NaOH. The Au colloid was then immobilized in an amorphous silica matrix following a procedure close to that described by Liz Marzan et al.[2] First, 70 mL (1 mmol L^{-1} in deionized water) 3-mercaptopropyltrimethoxysilane (MPTMS, Sigma-Aldrich, 95%) was added to 1 L of the Au colloid and the resulting mixture was stirred for 30 min. Then, 500 mL diluted water glass (Riedel-de Haën, 27% SiO_2) (diluted with water to 0.16 wt% SiO_2) was added and the mixture was stirred for 24 h. The aqueous reaction mixture was then diluted with a 4-fold volume excess of ethanol (absolute) and 1 mL NH_3 (Fluka, 25 wt%) was added. Then, 9.82 mL tetraethylorthosilicate (TEOS, Sigma-Aldrich, 98 %) was added under stirring in portions of 0.27 mL approximately every 8th hour. After addition of the TEOS the reaction mixture was allowed to settle overnight before the solid product was separated from the mother liquor by decantation, washed 8 times by centrifugation (15 min at 9000 rpm) and dried at 100 °C for 16 h. (Molar ratio of Au/Si = 0.096 measured by SEM-EDS)

The Au-silica material was transformed into the Au-silicalite-1 material using a procedure close to that reported by Botella et al.[3] To a mixture of 0.11 g NaOH, 2.9 g tetrapropylammonium hydroxide (AppliChem, 40 wt%), 23 g ethanol and 90 g deionised water was added 0.76 g of the Au-silica material and the resulting mixture was stirred for 15 min. Then, the reaction mixture was transferred to a Teflon-lined autoclave which was heated to 100 °C for 72 h. After quenching to room temperature, the solid product was recovered by filtration, washed with deionized water and dried at 100 °C for 16 h before it was calcined in air at 550 °C for 3 h in a muffle furnace.

Before calcinations 0.25 g product is obtained. (Yield = 32.9 %, Molar ratio of Au/Si = 0.037 as measured by SEM-EDS)

Sample characterization

For scanning electron microscopy (SEM) the samples were prepared by applying the solid directly onto carbon tape followed by sputter coating using a Pt/Pd alloy. The secondary electron micrographs were recorded on a Philips XL-30 FEG instrument.

Transmission electron microscopy (TEM) was performed using from Philips/FEI Company a CM200-FEG UltraTwin electron microscope, operated at 200 kV with an information limit of ca. 0.14 nm, and an image aberration-corrected Titan 80-300 SuperTwin electron microscope, operated at 300 kV with an information limit of ca. 0.10 nm. TEM images were acquired using a bottom-mounted 1k x 1k (CM200) and 2k x 2k (Titan) CCD cameras at magnifications corresponding to pixel sizes of 0.67 nm (individual images in Figure 2b) and 0.71 nm (Figure 3a-b), respectively. TEM tomography was performed using the CM200 electron microscope. 151 TEM images were collected manually in steps of one degree tilt with respect to the specimen holder axis and at a magnification corresponding to a pixel size of 1.9 nm. Images of the tilt series were aligned relative to a common origin using the gold particles in the zeolite as fiducial markers and the electron tomogram was reconstructured using all the images via weighted backprojection using the IMOD program suite. The supplementary information contains two movies showing the tilted image series after alignment and a sliced images through the electron tomogram. An in situ transmission electron microscopy experiment was carried out using a CM300 FEG SuperTwin environmental transmission electron microscope (Philips/FEI Company), operated at 300 kV with an information limit of ca. 0.14 nm, facilitating time-lapsed image series to be recorded of specimens during exposure to reactive gasses at elevated temperatures.[4] Part of the Au-silicalite-1 sample was dispersed in dry state onto a stainless steel grid which was inserted into the microscope using a Gatan heating holder (model 628). The specimen was exposed to 2 mbar O_2 with a nominel purity of 99.998% and heated at 30 °C/min from room temperature to successively elevated temperatures of 200 °C, 300 °C, 400 °C and 500 °C, respectively. After 15 min at each temperature, a TEM image of the same area was recorded using a 1k x 1k Tietz Fastscan F-114 CCD camera with a pixel size of 0.18 nm. The electron beam was switched off in the intervening time between successive images to minimize effects of the electron beam.

Nitrogen physisorption

To determine the surface area, micropore volumen and the extent of mesoporosity observed as voids in TEM N_2 physisorption measurements were preformed. The measurement was preformed on a Micromeritics ASAP 2020 instrument at liquid nitrogen temperature. The samples were outgassed in vacuum at 573 K for 16 h prior to measurements. In Table 1, the BET surface areas and micro- and mesopore volumes of the Au embedded in silicalite-1 crystals. The total surface area was calculated according to the BET method, the micropore volumes were determined by the t-plot method and the mesopore volume was determined by the BJH method.

Table 1: Surface area, micro- and mesopore volumen for the silicalite-1 with embedded Au nanoparticles calculated according to ^{a} the-plot method, ^{b} the BJH-method (adsorption), ^{c} the BET method and ^{d} the BJH adsorption adsorption branch.

	V_{micro} $(cm^3/g)^a$	V_{meso} $(cm^3/g)^b$	S_{BET} $(m^2/g)^c$	S_{Meso} $(m^2/g)^d$
Au/Silicalite-1	0.096	0.07	305.5	72.1

The surface area and micropore volume lie in the range of previously results. [5,6] The mesopore volume is rather low compared to mesoporous zeolites[5,6] and can therefore be due to intercrystalline porosity. In Figure 1 the Nitrogen adsorption/desorption isotherms are shown.

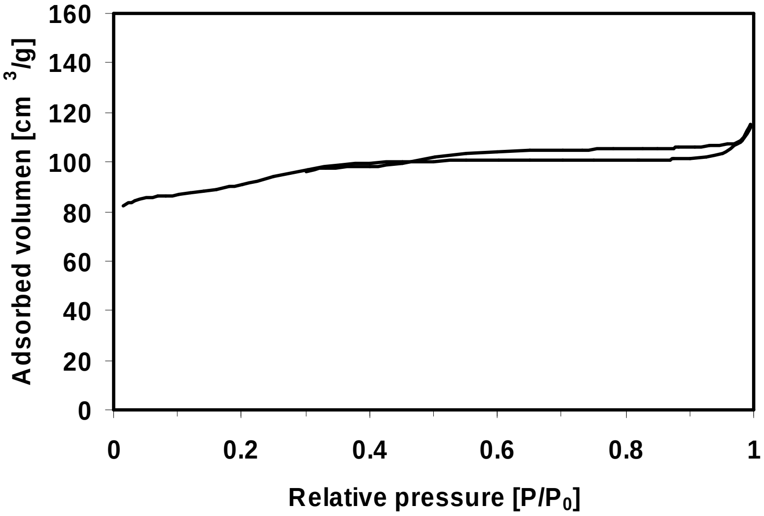

Figure 1: Nitrogen adsorption/desorption isotherms for the silicalite-1 with embedded Au nanoparticles.

The isotherm exhibits a modest hysteresis loop indicating that the sample contains very little mesoporosity.

The physisorption clearly demonstrate that the encapsulating material is primarily a microporous zeolite, with no significant amount of mesoporosity. The difference in density observed in TEM is indicated to be present in relatively small amount that it is unimportant to the properties of the material.

TEM movies

The following TEM movies are found in separate files: A movie composed of TEM images recorded at different tilt angles (tilt.mpg); a 3D TEM tomography movie (tomo.mpg); and an in situ TEM movie (insitu.avi) presenting a time-lapsed image series recorded during exposure to 2 mbar oxygen at room temperature to successively elevated temperatures of 200 °C 300 °C, 400 °C and 500 °C, respectively.

Catalytic tests

All reagents used were reagent grade and used without further purification: benzaldehyde (C_7H_6O, 99 %, Sigma-Aldrich), 3,5-di-tert-butylbenzaldehyde ($C_{15}H_{22}O$, 97%, Sigma-Aldrich) methanol (CH_3OH, 99 %, Sigma-Aldrich), 25 wt% sodium methoxide solution (Sigma-Aldrich), anisol (C_7H_8O, 99% Sigma-Aldrich).

In a typical experiment, a mixture of benzaldehyde (0.5 mmol) and 3,5-di-tert-butylbenzaldehyde in a 1:1 mol ratio was added to a solution of methanol (60 mmol) and sodium methoxide (0.2 mmol). The final solution was charged to a 10 ml two two-neck round-bottom flask equipped with a condenser and a septum together with the catalyst, the gold nanoparticles embedded in zeolite crystals (0.2 mol% Au). The reactor system was connected to an O_2 cylinder and it was flushed with O_2. The reaction mixture was mixed with magnetic stirring and small samples were taken at selected times, filtered directly through a syringe filter and analysed by GC and GC-MS. A HP-5 column from Agilent Technologies Inc. was used. The amounts of substrates and products were quantified using anisol as internal standard.

For the oxidation reactions a referent catalyst was used. The used referent catalyst was gold supported on titanium dioxide, 1% Au/TiO_2 supplied by Mintek.

References

[1] P. Haider, B. Kimmerle, F. Krumeich, W. Kleist, J.-D. Grunwaldt, A. Baiker, *Catal. Lett.* **2008**, *125*, 169-176

[2] L. M. Liz-Marzán, M. Giersig, P. Mulvaney, *Langmuir* **1996**, *12*, 4329-4335

[3] P. Botella, A. Corma, M. T. Navarro, *Chem. Mater.* **2007**, *19*, 1979-1983

[4] P. L. Hansen, S. Helveg, A. K. Datye, *Adv. Catal.* **2006**, *50*, 77- 95

[5] M.Y. Kustova, S.B. Rasmussen, A.L. Kustova, C.H. Christensen, *Appl. Catal. B.* **2006**, 67, 60-67

[6] K. Zhu, K. Egeblad, C. H. Christensen, *Eur. J. Inorg. Chem.* **2007**, *25*, 3955-3960

Applied Catalysis A: General 348 (2008) 257–265

Contents lists available at ScienceDirect

Applied Catalysis A: General

journal homepage: www.elsevier.com/locate/apcata

Synthesis and characterization of conventional and mesoporous Ga-MFI for ethane dehydrogenation

Karen Thrane Leth [a], Anne Krogh Rovik [a], Martin Spangsberg Holm [a], Michael Brorson [b], Hans J. Jakobsen [c], Jørgen Skibsted [c], Claus Hviid Christensen [a,*]

[a] *Center for Sustainable and Green Chemistry, Department of Chemistry, Technical University of Denmark, DK-2800 Kgs. Lyngby, Denmark*
[b] *Haldor Topsøe A/S, Nymøllevej 55, DK-2800 Kgs. Lyngby, Denmark*
[c] *Instrument Centre for Solid-State NMR Spectroscopy and Interdisciplinary Nanoscience Center (iNANO), Department of Chemistry, University of Aarhus, DK-8000 Aarhus, Denmark*

ARTICLE INFO

Article history:
Received 25 May 2008
Received in revised form 6 July 2008
Accepted 8 July 2008
Available online 15 July 2008

Keywords:
Ga-MFI zeolites
Mesoporous
Ethane dehydrogenation
Aromatization
^{71}Ga MAS NMR

ABSTRACT

Gallium was for the first time incorporated into the crystal structure of a mesoporous MFI zeolite. As a reference material, a well-defined conventional MFI zeolite with gallium incorporated was also synthesized. The materials were characterized by XRPD, NH_3-TPD, elemental analysis, N_2 physisorption measurements, SEM, FT-IR as well as ^{29}Si and ^{71}Ga MAS NMR spectroscopy. The Ga contents correspond to molar ratios of Si/Ga = 43 and 38 for the conventional and mesoporous Ga-MFI, respectively. The different types of analysis show that two almost identical zeolites were synthesized, the main difference being the morphology of the crystals. The catalytic properties of the samples were tested in ethane dehydrogenation at 823 K and at atmospheric pressure. The two Ga-MFI samples differ greatly in conversion of ethane, as a result of their difference in porosity, and it is found that the conversion is significantly improved by introducing mesopores into the structure. The major product is ethene for the conventional Ga-MFI, but there are significant amounts of benzene and toluene by-products for the mesoporous Ga-MFI. The ^{71}Ga isotropic chemical shift and second-order quadrupolar effect parameter is reported for tetrahedral Ga incorporated in the MFI structure and it is shown that absorbed water molecules have an important impact on the ^{71}Ga electric field gradients and thereby on the quantitative evaluation of the ^{71}Ga MAS NMR intensities.

1. Introduction

Zeolites have for a long time been recognized to be stable and efficient heterogeneous catalysts and accordingly they are some of the most widely used catalysts in industry [1]. Zeolites are microporous materials with a well-defined crystal structure; however, the small dimensions of the micropores can cause problems in some applications because it can impose diffusion limitations on the reaction rate [2]. This limitation may be overcome by reducing the size of the zeolite crystals and thereby shortening the diffusion path [3–6]. An alternative approach is to introduce relatively large extra pores in the zeolites [7–9] which resulted in the discovery of the mesoporous molecular sieves that contains pores in the range of 2–50 nm [10–12]. Mesopores can be introduced in the individual microporous zeolite crystals by post-treatments such as dealumination [13] and desilication [14], however, in some cases this is not the preferred procedure because it leads to partial destruction of the zeolite crystals. Another way to introduce the mesopores into the microporous structure was invented by Jacobsen et al. [15], who obtained mesopores by growing the zeolite crystals in a mixture where the crystals partially encapsulate a carbon material. This carbon material is removed by combustion after complete crystallization of the zeolite. This proven route of preparation of mesoporous zeolites has the advantages of controlling the ratio between silicon and other incorporated metals and at the same time preventing destruction of the zeolite crystals. Today, several routes are available to synthesise zeolites with additional mesopores [16–18].

Even though mesoporous zeolites have the advantage of better transport for reactants and products to and from the active sites, they still have a very limited range of applications in industry [2]. In reactions such as direct NO-decomposition and dehydrogenation of light alkanes, mesoporous zeolites display a significantly higher degree of conversion than conventional zeolites [19–21] and it is interesting to examine if this is also the case for

---

[*] Corresponding author.
E-mail address: chc@topsoe.dk (C.H. Christensen).

0926-860X/$ – see front matter © 2008 Elsevier B.V. All rights reserved.
doi:10.1016/j.apcata.2008.07.003

dehydrogenation and aromatization of light alkanes. Aromatization of lower alkanes has a great commercial interest. First of all, aromatics such as benzene, toluene and xylenes (BTX) have high octane numbers and are therefore key components of gasoline. BTX is also an important source of petrochemicals. Secondly, ethane exists as an abundant feedstock because it is a main constituent of natural gas, accompanying gasses and waste effluents of petrochemical processes [22,23]. The transformation of light alkanes into aromatics has been extensively investigated for MFI zeolite catalysts modified by different kinds of metals [22]. The focus has mainly been on the higher alkanes because they, due to thermodynamics, are much easier to convert into aromatics than methane and ethane [22]. One of the most promising metals for this kind of catalytic reaction is gallium [22], which can be introduced into zeolites in various ways: incorporation into the framework, impregnation, ion exchange, and by physical mixing of MFI-zeolites and Ga_2O_3. When gallium is incorporated into the crystal framework, the general perception is that the catalyst is more stable than in cases where Ga is impregnated or ion exchanged [22]. Another advantage of incorporating Ga is that the Ga species may be uniformly distributed over all the tetrahedral silicon framework sites in the zeolite structure and thereby not only onto the surfaces of the zeolite or in the outer part of the channels [24].

In this work, we have synthesized a conventional and a mesoporous MFI type zeolite with almost the same amount of Ga incorporated into the structure. The samples were characterized thoroughly and their catalytic properties were investigated for the conversion of ethane. The influence of the mesoporosity introduced into the zeolite structure on the catalytic activity and selectivity in ethane conversion was determined. The results from the activity measurements show that both types of catalysts are very stable and that the introduction of mesoporosity gives a significantly higher degree of conversion and a higher selectivity towards aromatics.

2. Experimental and methods

2.1. Catalysts preparation

2.1.1. Synthesis of conventional H–Ga-MFI

0.45 g NaOH, dissolved in 22.5 g water, was mixed with 7.5 g silica gel and stirred for 1 h. In one beaker 0.35 g NaOH was dissolved in 22.5 g water and in another beaker 0.914 g $Ga(NO_3)_3 \cdot xH_2O$ was dissolved in 17.3 g water. The two solutions were simultaneously added dropwise to 10.16 g tetrapropyl ammonium hydroxide (TPAOH). This mixture thus obtained was added dropwise to the silica gel solution. This procedure gives the following composition of the synthesis gel: $SiO_2 \cdot 0.08Na_2O \cdot 0.08TPA_2O \cdot 27.7H_2O \cdot 0.057Ga_2O_3$. After 3 h of stirring, the homogeneous gel obtained was transferred to a stainless steel autoclave and heated to 453 K for 36 h. After cooling the autoclave to room temperature the white product was isolated by suction filtration and washed several times with water. The product was dried at 333 K for 30 min and finally the organic template was removed by calcination in a muffle furnace at 823 K for 20 h. The acidic H-form of the zeolite was produced by two consecutive ion exchanges with 1 M NH_4NO_3 in the ratio 1:30 between mass of sample (g) and volume of NH_4NO_3 (ml). The ion exchanges were performed at 353 K with stirring for 3 h. After each ion exchange, the NH_4-form of the zeolite was filtered off, washed with water, and dried in air. Finally, the H–Ga-MFI was obtained by heating the NH_4–Ga-MFI in air to 723 K for 4 h.

2.1.2. Synthesis of mesoporous H–Ga-MFI

The preparation of the mesoporous Na–Ga-MFI was performed according to the procedure reported by Jacobsen et al. [15]. Gallium oxide was prepared by precipitation from a solution of 4.95 g $Ga(NO_3)_3 \cdot xH_2O$ dissolved in water by means of aqueous ammonia (25%) in excess (~15 ml). The precipitate was washed twice with water and then dissolved together with 1.04 g NaOH in 6.45 g water. 25 g of carbon black (Black Pearls 2000, BP-2000, supplied by Carbot Corp.) was dried overnight at 383 K. 43.01 g TPAOH was mixed with the prepared gallium solution and stirred until a clear solution was obtained. 37.88 g ethanol was added and the stirring was continued until the solution was homogeneous. The carbon was impregnated with this solution by the incipient wetness technique and the mixture was left overnight at room temperature for the ethanol to evaporate. After evaporation the carbon was impregnated again by this method with 48.38 g tetraethylorthosilicate (TEOS) and left to hydrolyze at room temperature overnight. The final composition of the impregnated mixture was: $SiO_2 \cdot 0.56Na_2O \cdot 0.18TPA_2O \cdot 1.54H_2O \cdot 0.042Ga_2O_3 \cdot 3.54EtOH$. After hydrolysis, the impregnated carbon black was transferred to a Teflon beaker which was placed in a stainless steel autoclave containing 100 ml of water to produce saturated steam. The autoclave was heated to 453 K and left for 72 h. After cooling the autoclave to room temperature, the black product was suspended in water, filtered and rinsed thoroughly with water several times using 1 l of water. The product was dried at 383 K for 10 h and the carbon was removed by combustion in air in a muffle furnace at 823 K for 12 h. To obtain the acidic H-form of the mesoporous Ga-MFI, two consecutive ion exchanges were performed using the same procedure as for the conventional H–Ga-MFI (Section 2.1.1).

2.2. Characterization

To identify and verify the crystal structure of the products, powder-XRD patterns were recorded using a Phillips powder diffractometer with Cu Kα radiation in the 2θ interval 5–50°. The elemental analysis was performed by ICP and used to determine the exact amount of Ga in the Ga-MFI type zeolites.

The surface area, pore volume, and the adsorption isotherms were determined by nitrogen adsorption and desorption measurements at liquid nitrogen temperature on a Micromeritics ASAP 2020. The samples were out gassed in vacuum at 473 K for 6 h prior to measurements. The total surface area was calculated according to the BET method, the micropore volumes were determined by the t-plot method and the mesopore volume was determined by the BJH method. The acidity was determined by ammonia temperature programmed desorption (NH_3-TPD), using the following procedure: 150 mg of the sample was loaded into a quartz tube reactor at room temperature and kept in a flow of dry NH_3 for 30 min (100 ml/min, 1% NH_3/N_2). Prior to the NH_3 desorption measurement, the sample was heated to 373 K in a dry nitrogen flow (100 ml/min) and kept at this temperature for 90 min to remove physically adsorbed ammonia. Subsequently, the sample was cooled to room temperature and the temperature was raised at a rate of 5 °C/min to 923 K. The rate of NH_3 desorption was monitored by a computer-interfaced UV–vis spectrometer using the characteristic ammonia band at 201.2 nm. The ammonia concentration was calculated on the basis of the intensity for the ammonia band, employing a calibration curve. The total amount of desorbed NH_3 was calculated from the area under the TPD curve.

The crystal size and morphology of the zeolites were examined by scanning electron microscopy (SEM) on a Phillips XL20 FEG. The calcined zeolite samples were placed on a carbon film and Pt was evaporated onto the sample for approximately 20 min to achieve sufficient conductivity.

The ^{29}Si MAS NMR spectra were recorded on a Varian Unity INOVA-400 spectrometer employing a homebuilt CP/MAS NMR probe for 7 mm o.d. rotors, a spinning speed of 6.0 kHz, and single-pulse excitation (~45° flip angle for $\gamma B_1/2\pi \approx 40$ kHz). To investigate second-order quadrupolar effects, ^{71}Ga MAS NMR spectra were recorded at four different magnetic field strengths (4.7, 7.1, 9.4, and 14.1 T) on Varian Unity-plus-200, Unity INOVA-300, -400, and -600 spectrometers. The experiments employed homebuilt CP/MAS NMR probes for either 4 mm o.d. rotors (14.1 T) or 5 mm o.d. rotors (4.7, 7.1, and 9.4 T), spinning speeds of 10.0–15.0 kHz, single-pulse excitation (a flip angle < 30° for $\gamma B_1/2\pi$ = 50–65 kHz), and typically around 100.000 scans. ^{29}Si and ^{71}Ga chemical shifts are in ppm relative to external samples of neat tetramethylsilane (TMS) and a 1.0 M $Ga(NO_3)_3$ solution, respectively.

FT-IR was carried out on a Bio-Rad spectrometer equipped with a MCT detector. The Ga-MFI zeolite was pressed into a self supporting wafer and mounted in a homebuilt Pyrex cell allowing sample cooling with liquid N_2 and equipped with NaCl windows. Samples were pre-treated by out gassing for approximately 4 h at 673 K reaching a background pressure of $<5 \times 10^{-5}$ Torr. Spectra of the respective zeolites in transmission mode were obtained from 64 to 500 scans at a resolution of 2 cm^{-1}. Carbon monoxide was subsequently used as a probe molecule in order to investigate the acidic properties of the synthesized zeolites. The samples were cooled with liquid nitrogen and dosed with CO to an equilibrium pressure of 50 Torr. The adsorption series generated corresponds to a gradual evacuation thus removing the adsorbed CO in an order dictated by the interaction strength CO and adsorption site in-between.

2.3. Catalytic activity and stability

Prior to the catalytic tests, the Ga-MFI samples were pelletized, crushed, and sieved to ensure a uniform particle size of 212–355 μm. The particles were subsequently diluted by mixing with an equal amount of quartz (400 mg) of the same sieve fraction. Tests were performed in a quartz tube plug flow reactor (3.7 mm in diameter) where the height of the catalyst bed was around 50 mm. The catalysts were pre-treated for 1 h in a stream of Ar (675 ml (SATP)/h) at 823 K. SATP is standard ambient temperature and pressure, which is 298 K at 1 bar.

The catalytic tests were carried out at 823 K and atmospheric pressure. An ethane/Ar mixture with a concentration of 9.7% of ethane was introduced at four different flows: 910, 455, 1820 and 225 ml (SATP)/h. After the reactor, 75 ml (SATP)/h of CO_2 was added to the effluent gasses as a standard. All piping and valves after the reactor were heated to 473 K to avoid condensation of any formed aromatics. Temperature programmed oxidation (TPO) was carried out after the catalytic tests in the same setup by flowing a 2% O_2 in Ar (4133 ml/h (SATP) of the O_2/Ar-mix) through the catalyst and increasing the temperature by 0.5 K/min from 473 to 1073 K.

The effluent gasses from the catalytic test and TPO were analyzed by an on-line coupled HP6890A Gas Chromatograph equipped with a HP-PLOT Q column and a HP-PLOT Molesieve column as well as a thermal conductivity detector (TCD) and a flame ionization detector (FID) in series.

3. Results and discussion

3.1. Characterization

The XRPD patterns for the conventional and mesoporous Ga-MFI zeolite are both shown in Fig. 1. Both patterns are recorded after the zeolite synthesis and after combustion of the organic template as well as the auxiliary carbon black material. It is clearly seen that both samples exclusively contain highly crystalline material with the MFI structure [25].

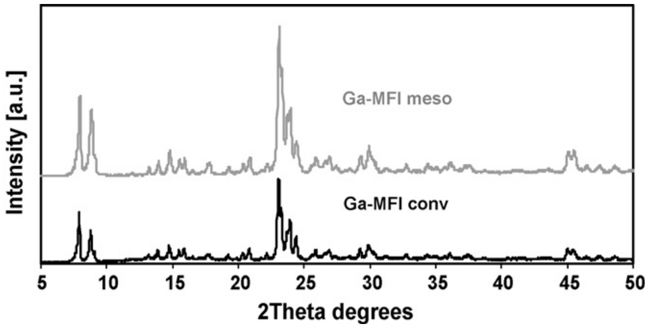

Fig. 1. XRPD patterns of the conventional and mesoporous Ga-MFI zeolite. The patterns are recorded after the combustion of the template and the carbon matrix.

The Ga contents determined from chemical analysis are listed in Table 1 together with the measured acidity from NH_3-TPD. These data show that the two types of Ga-MFI include rather similar amounts of Ga, i.e., 2.36 and 2.76 wt.% Ga for the conventional and the mesoporous Ga-MFI, respectively.

Desorption curves for NH_3 for the conventional and the mesoporous Ga-MFI zeolites are shown in Fig. 2. It seems that they do not have the exact same shape, but the highest peak is for both curves located at 179 °C. There seem to be some disagreement in the literature on how to interpret NH_3 desorption curves for zeolites. Some authors [26] believe that the area under the first peak is due to desorption of physically adsorbed ammonia and must therefore be subtracted from the total area. Other authors [27] is of the opinion that the first peak should be assigned to weakly acidic sites, while the second peak is attributed to strongly acidic sites and both peaks therefore are needed for the determination of the acidity. Both the total area and the total area subtracted the area of the first peak are given for the two Ga-MFI zeolites in Table 1. It is seen that even though the shapes of the curves are not completely identical, the areas are quite similar. Therefore it can be concluded that the zeolites have similar density of acidic sites.

The nitrogen adsorption/desorption isotherms for the conventional and mesoporous Ga-MFI zeolite are given in Fig. 3. The isotherm for the mesoporous Ga-MFI contains a hysteresis loop at a relative pressure higher than $p/p_0 = 0.4$ which is a characteristic feature for mesoporous materials [28]. The mesopore size distribution is obtained from the desorption branch of the

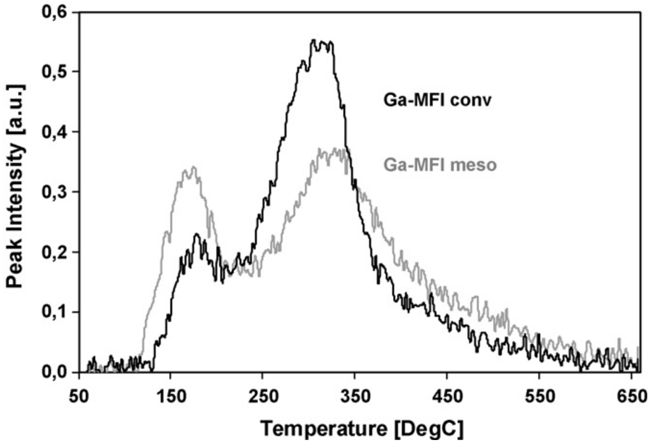

Fig. 2. NH_3 desorption curves for the conventional and the mesoporous Ga-MFI zeolite.

Table 1
Ga contents from elementary analysis and NH_3-TPD data

Zeolite	Conventional/mesoporous	Ga content (wt.%)	NH_3 desorbed, total (μmol/g)	NH_3 desorbed, 2nd peak only (μmol/g)
Ga-MFI	Conventional	2.36	514	431
Ga-MFI	Mesoporous	2.76	533	399

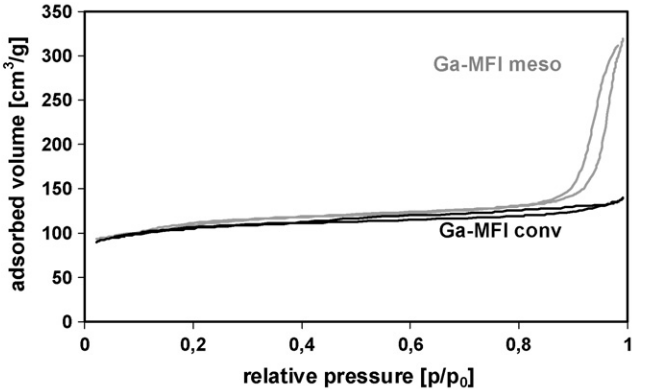

Fig. 3. Nitrogen adsorption and desorption isotherms of conventional Ga-MFI and mesoporous Ga-MFI zeolite.

Table 2
Nitrogen adsorption data of the conventional and the mesoporus Ga-MFI zeolites after combustion of the organic template and the carbon matrix

Zeolite	Conventional/ mesoporous	V_{micro} (cm^3/g)[a]	V_{meso} (cm^3/g)[b]	BET area (m^2/g)[c]
Ga-MFI	Conventional	0.1	0.0	360
Ga-MFI	Mesoporous	0.08	0.37	374

[a] Calculated by t-plot method.
[b] Calculated by BJH method (desorption).
[c] Calculated by BET method.

isotherm using the BJH method. The mesopore size distribution is quite broad, ranging from 10 to 100 nm which is in correlation with previously results for carbon templated zeolites [29,30]. The average mesopore size is approximately 32 nm.

The nitrogen adsorption/desorption isotherm for the conventional Ga-MFI zeolite is not the typical isotherm for microporous materials [28]. There seems to be a small hysteresis loop, which could be due to agglomeration of the zeolite crystals. The surface area for the conventional Ga-MFI is 360 m^2/g and the micropore volume is 0.1 cm^3/g. For the mesoporous Ga-MFI the surface area is 374 m^2/g and the micropore and mesopore volumes are 0.08 and 0.37 cm^3/g, respectively. In Table 2, the BET surface areas and micro and mesopore volumes of the conventional and the mesoporous MFI zeolites are given. All numbers for the BET surface areas and the mesopore volume lie in the range of previous results for conventional and mesoporous Al-MFI (ZSM-5) [19]. The typical micropore volume for highly crystalline MFI type materials lie in the range of 0.09–0.19 cm^3/g [19,29–31], which means the micropore volume for the conventional and mesoporous Ga-MFI are relatively low compared to the typical value.

The SEM images of the conventional and mesoporous Ga-MFI zeolite are shown in Fig. 4. The images are recorded after combustion of the template and the carbon matrix. From the SEM images of the conventional zeolite (Fig. 4a and b) it can be observed that there exists a homogeneous distribution concerning the crystal sizes of the zeolite particles of around 8 μm. From the SEM images, it can also be seen that the particles are highly crystalline. The conventional Ga-MFI crystals do not have the typical coffin-shape, which can be due to the source of silica [32].

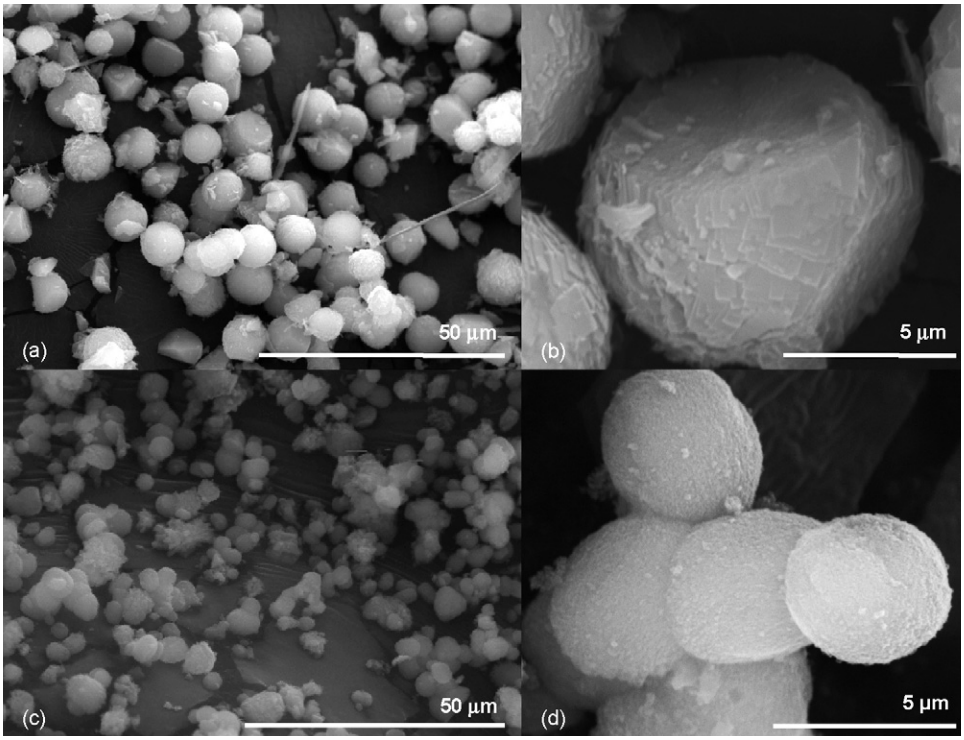

Fig. 4. SEM images of conventional (a and b) and mesoporous (c and d) Ga-MFI crystals. The images are recorded after combustion of the template and the carbon matrix.

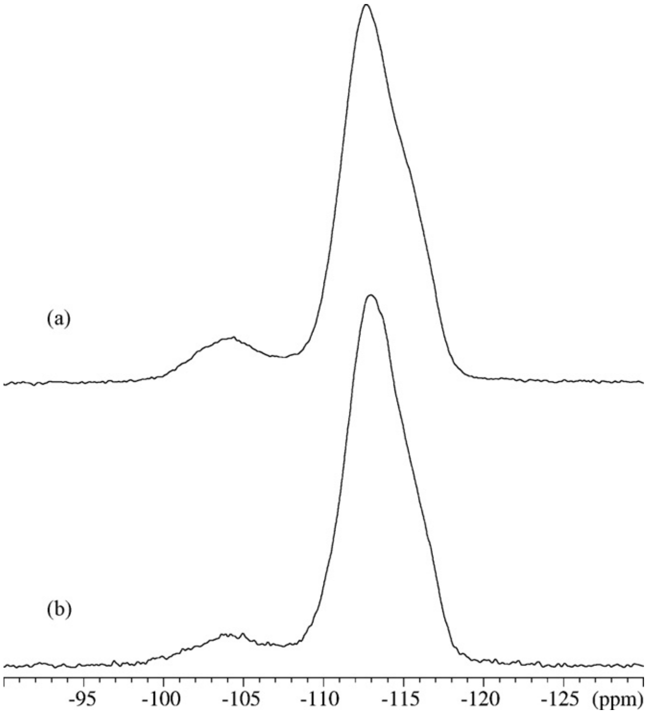

Fig. 5. ^{29}Si MAS NMR spectra of (a) the conventional and (b) the mesoporous Ga-MFI samples obtained at 9.39 T using a spinning speed of 6.0 kHz, a 30-s relaxation delay and 3154 and 2377 scans, respectively.

From the SEM images of the mesoporous Ga-MFI zeolite (Fig. 4c and d) it is seen that the mesoporous zeolites are highly crystalline and that crystals exist in a uniform size of approximately 4 μm.

^{29}Si and ^{71}Ga MAS NMR spectra of the conventional and mesoporous Ga-MFI, recorded after removal of the template molecules and carbon black material, are shown in Figs. 5 and 6, respectively. The ^{29}Si MAS NMR spectra exhibit the same spectral features as reported earlier for Al- as well as Ga-substituted MFI zeolites [33–36] and thereby support the XRPD results, which identifies the structures as MFI. The dominating resonance is observed at -113 ppm with a low-frequency shoulder at -116 ppm, both originating from Si*(OSi)$_4$ sites of the framework structure. The resonance with lower intensity, ranging from -98 to approximately -108 ppm, is ascribed to an overlap of resonances from (GaO)Si*(OSi)$_3$ and (HO)Si*(OSi)$_3$ sites, following the earlier studies of Ga-MFIs [31–33] and the fact that each OH group connected to the SiO$_4$ tetrahedron results in a shift by about 5–8 ppm to higher frequency. The relative ^{29}Si intensity for the (Ga/HO)Si*(OSi)$_3$ type of Si sites (Fig. 5) is slightly higher for the conventional MFI (i.e., I[(Ga/HO)Si*(OSi)$_3$] = 11.7%) as compared to the mesoporous sample (I[(Ga/HO)Si*(OSi)$_3$] = 9.4%). This observation suggests that the conventional MFI includes a larger quantity of Ga incorporated in the framework structure, if the amount of (HO)Si*(OSi)$_3$ sites are very similar for the two samples as indicated by the NH$_3$-TPD data (Table 1 and Fig. 2).

The ^{71}Ga MAS NMR spectra, recorded at the highest magnetic field (Fig. 6a and b), reveal for both samples a Gaussian-like resonance for the central transition ($m = 1/2 \leftrightarrow -1/2$) with a center of gravity at 156 ppm and linewidths of FWHM = 20–25 ppm. This resonance is assigned to tetrahedrally coordinated Ga incorporated in the framework silicate structure (i.e., Ga*(OSi)$_4$ sites), following earlier ^{71}Ga MAS NMR studies of Ga–MFI samples [34,36–40]. However, the centerband intensity for the mesoporous MFI corresponds to only 28% of the observed intensity for the conventional MFI, indicating that the number of Ga incorporated in the framework structure is significantly lower for the mesoporous MFI as compared to the conventionally prepared sample. To investigate this discrepancy, additional experiments were performed at 9.39 T since at this stage no precautions had been made to store or handle the samples under non-humid conditions.

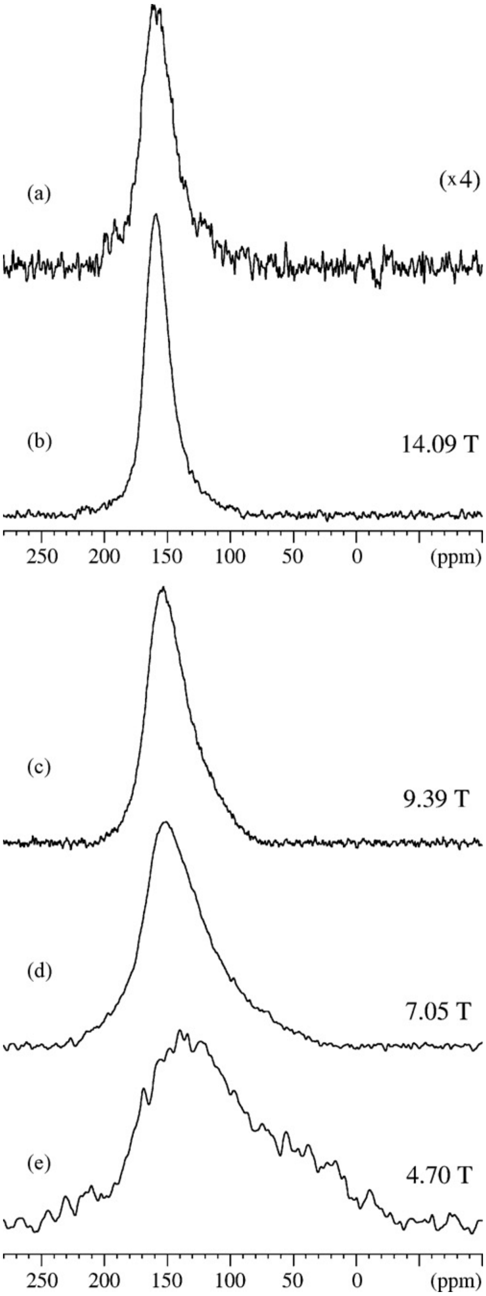

Fig. 6. ^{71}Ga MAS NMR spectra of (a) the mesoporous Ga-MFI and (b–e) the conventional Ga-MFI sample recorded at (a and b) 14.09 T (182.9 MHz), (c) 9.39 T (121.9 MHz), (d) 7.05 T (91.5 MHz), and (e) 4.70 T (61.0 MHz) employing spinning speeds of (c) 10.0 kHz, (d and e) 12.0 kHz, and (a and b) 15.0 kHz.

The initial ^{71}Ga MAS NMR experiments for the two samples at 9.39 T, shown in Fig. 7a for the conventional Ga-MFI, gave a centerband intensity ratio very similar to that obtained at 14.1 T. This could potentially be related to a significant absorption of water for the mesoporous sample, and thus, the experiments were repeated for samples dried at 383 K for 2 h and subsequently handled under non-humid conditions. For both samples, the drying

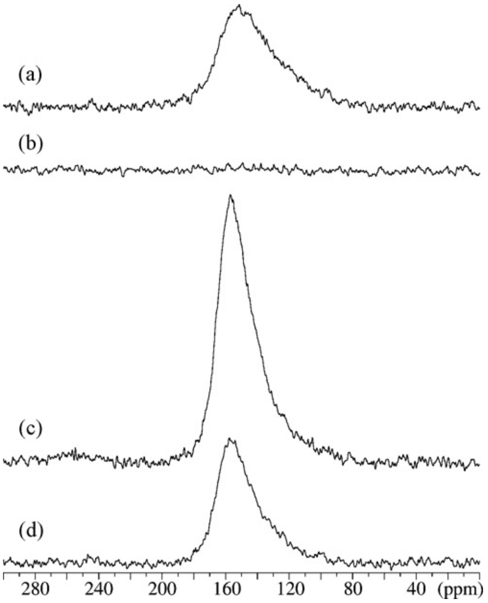

Fig. 7. ^{71}Ga MAS NMR spectra of (a–c) the conventional Ga-MFI and (d) the mesoporous Ga-MFI recorded under identical conditions at 9.39 T using a spinning speed of 12.0 kHz. Spectra before and after drying in air for 2 h at 383 K are shown in parts (a) and (b), respectively, while the spectra in (c) and (d) are obtained for samples re-hydrated overnight in a humid, CO_2-free atmosphere (22 °C, 100% RH). The spectra are shown on the same intensity scale, normalized to the actual sample weights. Thus, the different degree of water absorption for the conventional and mesoporous MFIs should be considered in the evaluation of the intensities in (c) and (d).

procedure completely eliminates observation of the ^{71}Ga signal from Ga in tetrahedral environments as illustrated in Fig. 7b for the conventional MFI. The absence of a ^{71}Ga signal is ascribed to the presence of very strong quadrupole couplings for the framework Ga sites after drying which prevent their observation under the present experimental conditions. Ga species that are unobservable by ^{71}Ga MAS NMR under normal conditions have earlier been described for non-framework Ga sites in zeolitic materials, which exhibit very strong quadrupole couplings, in studies that focus on the quantitative aspects of ^{71}Ga MAS NMR [34,37,40]. However, the spectra in Fig. 7c and d for the conventional and mesoporous MFI demonstrate that the ^{71}Ga MAS NMR signal can be recovered again after storage of the dried samples in a humid (CO_2 free) atmosphere overnight. The weights of the samples before and after curing in the humid atmosphere show that the conventional MFI absorbs 10.3 wt.% H_2O while a significantly larger absorption (23.4 wt.%) is observed for the mesoporous MFI. Thus, an evaluation of the intensities observed in Fig. 7c and d, considering the actual sample amount in the NMR rotor and the different water absorption for the two samples, shows that the ^{71}Ga intensity for the mesoporous MFI equals 58% of the corresponding intensity observed for the conventional MFI. Thus, the amount of Ga incorporated in the mesoporous MFI is only slightly lower as compared to the conventional MFI, in accordance with the indications from the ^{29}Si MAS NMR spectra (Fig. 5). Furthermore, the ^{71}Ga MAS NMR spectra following the drying and re-hydration of the samples (Fig. 7a–c) demonstrate that absorbed water molecules must be located in the vicinity of the framework Ga sites in order to have a considerable impact of the electric field gradients of the ^{71}Ga sites.

Generally, direct comparison of MAS NMR spectra for quadrupolar nuclei requires either spectra recorded at the same magnetic field or a preknowledge of the isotropic chemical shift (δ_{iso}) and quadrupole coupling parameters (i.e., the quadrupole coupling constant (C_Q) and the associated asymmetry parameter (η_Q)) for the individual sites. However, a precise determination of these ^{71}Ga parameters for framework Ga in zeolites is not straightforwardly obtained, considering the second-order quadrupolar shift and the absence of a well-defined second-order quadrupolar lineshape for the central transition that allows extraction of δ_{iso}, C_Q, and η_Q from spectral simulations. A valuable estimate of $\delta_{\mathrm{iso}}(^{71}\mathrm{Ga})$ and the quadrupolar product parameter $P_Q = C_Q(1+\eta_Q^2/3)^{1/2}$ is obtained for the framework Ga in the conventional MFI sample, utilizing the magnetic field dependency of the center of gravity for the central transition ($\delta^{\mathrm{cg}}_{1/2,-1/2}$) given by the following relationship for a spin $I = 3/2$ nucleus [41]:

$$\delta^{\mathrm{cg}}_{1/2,-1/2} = \delta_{\mathrm{iso}} - \frac{1}{40}\left(\frac{P_Q}{\nu_L}\right)^2 \tag{1}$$

Linear regression of the following experimental $\delta^{\mathrm{cg}}_{1/2,-1/2}$ values, 118.9, 138.6, 148.6, and 156.5 ppm measured at 4.70, 7.05, 9.39, and 14.09 T corresponding to the Larmor frequencies 61.0, 91.5, 121.9, and 182.9 MHz (Fig. 6b–e), respectively, as a function of $1/40\nu_L^2$ gives the parameters $\delta_{\mathrm{iso}}(^{71}\mathrm{Ga}) = 159.3$ ppm and $P_Q = 2.48$ MHz with the regression coefficient $R = 0.994$. These data are in accord with the center of gravity, $\delta^{\mathrm{cg}}_{1/2,-1/2} = 155$ ppm at 14.1 T, reported earlier for a Ga-MFI with a similar Ga content [31].

Apart from ^{29}Si MAS NMR and ^{71}Ga MAS NMR also FT-IR was used to determine the amount of Ga incorporated into the zeolite framework. The infrared transmission spectra given in Fig. 8a and b were recorded at room temperature of the conventional and mesoporous Ga-MFI zeolites. Various key components are present in the OH-stretching region. Importantly, the ~3618 cm^{-1} vibration, which is present in both samples, is designated to the

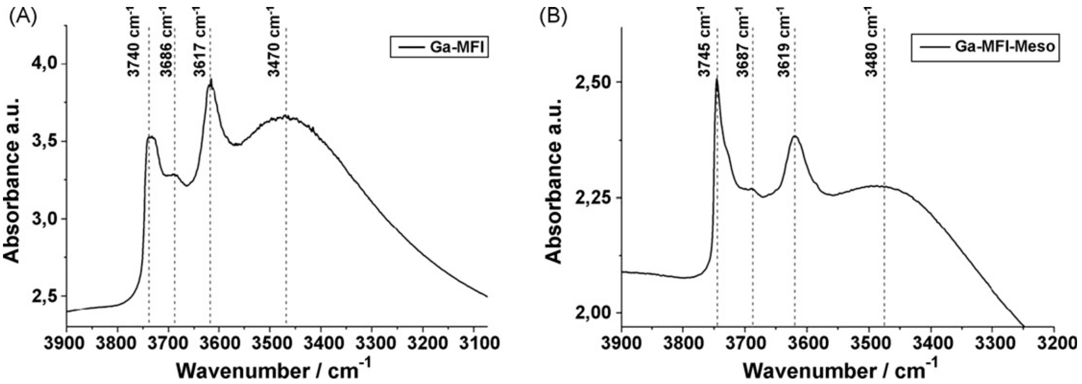

Fig. 8. Infrared transmission spectra of the OH-stretching region of the (a) conventional and (b) mesoporous Ga-MFI zeolites prior to CO adsorption. The spectra are recorded at room temperature.

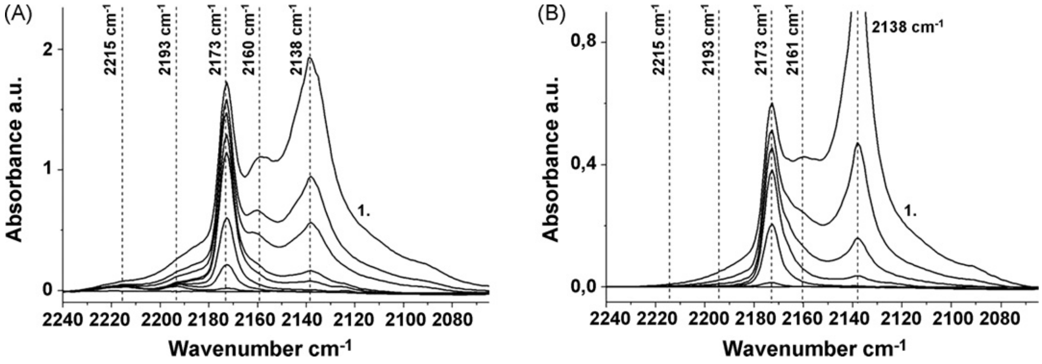

Fig. 9. Infrared transmission difference spectra presenting the CO stretch region during stepwise CO desorption for (a) conventional and (b) mesoporous Ga-MFI zeolites.

Brønsted acidic proton associated with gallium tetrahedrally incorporated into the framework. Distinct peaks commonly ascribed to various silanol groups are also seen. This can be exemplified at 3745 cm^{-1} where a band appears due to the terminal silanols present at the crystal surface. Silanol groups related to crystal defects give rise to the shoulder located at 3727 cm^{-1} as well as the broad band centered at 3475 cm^{-1} commonly mentioned as silanol nests [27]. The silanol nest band may be present in silicalite [42]. However it is discussed [43,44] whether bridging hydroxyls could be involved in hydrogen bonding and contribute to the broad 3475 cm^{-1} band. Importantly this would mask Brønsted acid sites interacting with defects or in other ways perturbed from straightforward IR designation. Recent examples are published on the SSZ-33 and SSZ-35 zeolites [45].

Extra-framework species detectable in the OH stretching region belonging to the GaOOH type and designated to around 3670 cm^{-1} could be coincident with the minor contributions seen for both samples at ~3687 cm^{-1} [46].

The difference plots of the two respective zeolites, obtained by subtraction of the parent spectrum prior to CO adsorption, are presented in Fig. 9a and b. The curve labelled 1 in both cases corresponds to the highest CO loading followed by recordings at the stepwise decreasing CO equilibrium pressure.

As CO interacts with an acidic proton from the zeolite the observed stretching frequency is perturbed and shifts proportional to the interaction strength. In the case of proton interaction this can be interpreted as a measure of acid strength [47,48].

Examining the difference spectrum of the conventional sample in Fig. 9a, two distinct peaks at 2138 and 2173 cm^{-1} are clearly visible. The broad band at 2138 cm^{-1} corresponds to liquid-like CO present at high loadings in the pores of the zeolite. Furthermore, a band shifted to 2173 cm^{-1} arising from CO interacting with the Brønsted protons from framework gallium is identified. If present, CO binds strongly to Lewis acidic sites, which in this material presumably arises from non-framework gallium having different extents of unsaturation. A multi-component band positioned around 2210–2230 cm^{-1} is thus produced and actually modestly seen in the conventional material centered at 2215 cm^{-1} [49]. This CO···Lewis acid adduct typically is more stable than the Brønsted analogue and therefore disappear only after extinction of the 2173 cm^{-1}.

Correspondingly, when analysing the difference spectrum of the mesoporous sample given in Fig. 9b, we observe no sign of any extra-framework gallium species.

To summarize, it may therefore be concluded from FT-IR that the vast majority of gallium present in the materials appear to be incorporated tetrahedral in the zeolitic framework in both samples. The conventional zeolite though simultaneously has a minor contribution from extra-framework gallium in contrast to the mesoporous sample.

Thus, the characterizations of the catalysts reveal two almost identical catalysts where only the morphology differs. Similar overall amounts of Ga are detected by elementary analysis and similar density of acidic sites is detected by NH_3-TPD though the acidic strength is not exactly the same for the two samples. ^{71}Ga MAS NMR allows us to conclude that the amount of Ga incorporated into the MFI framework is slightly lower for the mesoporous MFI compared to the conventional, but the visibility of the Ga is very dependent on the surroundings of the Ga species and therefore strongly influenced by the humidity of the sample. FT-IR measurements demonstrate that the main part of the Ga is incorporated into the zeolite framework in both samples. The overall conclusion on the characterizations is therefore that two almost identical catalysts are synthesized where the morphology is the only major difference.

3.2. Catalytic activity and stability

The activity measurements are illustrated in Fig. 10, where the conversion of ethane is shown as a function of time on stream (TOS).

The flow of ethane/Ar is varied four times: 910 ml (SATP)/h for the first 300 min, 455 ml (SATP)/h for 940 min, 1820 ml (SATP)/h for 180 min, and 225 ml (SATP)/h for 200 min. The conversion on the conventional Ga-MFI is around 0.8% at 910 ml (SATP)/h, rising to 1% at 455 ml (SATP)/h, falling to 0.4% at 1820 ml (SATP)/h, and increasing to 1.3% at 225 ml (SATP)/h. For the mesoporous Ga-MFI,

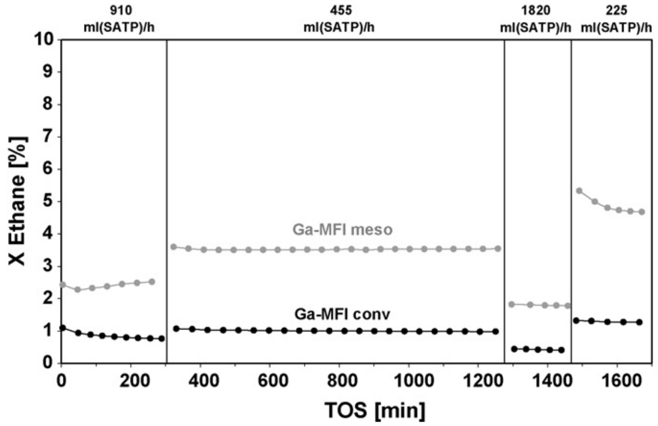

Fig. 10. Conversion of ethane as a function of time on stream (TOS) for the conventional and the mesoporous Ga-MFI zeolites ((●) conventional Ga-MFI and (●) mesoporous Ga-MFI). The catalytic tests were carried out at 823 K, atmospheric pressure and with an ethane/Ar mix with a concentration of 9.7% of ethane. The total ethane/Ar flow was varied four times: 910, 455, 1820 and 225 ml (SATP)/h.

the conversions vary from 2.5% in the first period, to 3.5% in the second period, to 1.8% in the third period, and finally to around 4.7%. The conversions of ethane are generally kept low considering that the conversion at thermodynamic equilibrium is 29% for the ethane dehydrogenation of 9.7% ethane in Ar. Thus, the measurements are not influenced by a close approach to equilibrium. The mesoporous Ga-MFI has the highest conversion of around 4.3% and the conventional Ga-MFI has 1.3% conversion as maximum; both measured at a flow of ethane/Ar at 225 ml (SATP)/h.

In the first period of time on stream, the conversion increases from 2.3 to 2.5% during 300 min for the mesoporous Ga-MFI. In the same period of time, the conventional Ga-MFI has a more constant though slightly decreasing conversion compared to the mesoporous sample. This indicates that the mesoporous Ga-MFI needs to be pre-treated slightly longer than the conventional Ga-MFI before reaching a steady state. The two catalysts were both pre-treated in a flow of Ar for 1 h at 823 K prior to testing. The fact that only the mesoporous Ga-MFI needs a longer pre-treatment could indicate that there is slightly more Ga species in the mesoporous catalyst that is not incorporated into the zeolite structure. All characterization methods used here conclude though that the main difference between the two catalysts is the porosity.

The catalyst is not significantly deactivated during the time of test since very constant conversions for each flow of ethane/Ar are observed. Usually when testing catalytic anaerobic dehydrogenation of ethane large amounts of coke is produced which deactivates the catalysts significantly [20,22]. Here, both the conventional and mesoporous Ga-MFI are apparently not significantly deactivated by coke, which is also confirmed by TPO performed after catalytic testing. TPO shows no detectable CO_2 or CO and therefore no significant coke formation on the catalysts occurred. The high stability of the catalysts also indicates that the Ga species do not migrate out of the framework, which could lead to a reduction of the catalytic activity.

From Fig. 10 it is seen that a relatively low flow of ethane/Ar (that is a relatively long contact time) leads to a relatively high conversion. Since longer residence times lead to higher conversions, the thermodynamic equilibrium is clearly not reached and, as expected, the conversions are therefore strongly influenced by the flow of ethane. It can also be seen that for all four flows of ethane/Ar, the mesoporous Ga-MFI is significantly more active than the conventional zeolite.

Presumably, the catalytic activity in ethane dehydrogenation is different whether the gallium is incorporated into the crystal structure of the zeolite (Brønsted acid) or gallium exists as extra-framework (Lewis acid) [23]. According to NH_3-TPD the conventional and mesoporous Ga-MFI has comparable acidity, but the technique does not differentiate between Brønsted and Lewis acidic sites. FT-IR investigations showed that the majority of gallium in both samples exists tetrahedral in framework. Only the conventional Ga-MFI might contain a very small amount of Lewis acidic sites.

The characterizations of the two catalysts have shown us that the only significant difference between the two Ga-MFI zeolites is the morphology. The reason for the significantly better conversion of ethane by the mesoporous Ga-MFI is most likely related to a difference in morphology. Therefore, introducing mesopores into the otherwise microporous zeolite catalyst leads to an easier access of ethane to the active sites inside the crystal and an easier exit of the products from the catalytic reaction. The fact that this effect is so pronounced is attributed to the conventional Ga-MFI zeolite having a quite large crystal size.

The selectivities for the two Ga-MFI zeolites are shown in Figs. 11 and 12. Both Ga-MFI type zeolites exhibit high selectivity for ethene; around 95% in the first period. Therefore, mainly the dehydrogenation of ethane takes place during the test. Also some methane resulting from the hydrogenolysis of ethane is observed. The methane selectivity is 1.6% for the conventional and around 3.4% for the mesoporous in the first period of time. There is a clear tendency in the product distribution when the flow of ethane is varied. When the ethane flow is lowered the ethene selectivity is decreased for both the conventional and the mesoporous Ga-MFI. At the same time, the selectivities for methane and C_3 are increased on the conventional zeolite whereas the selectivities for methane, C_3, benzene, and toluene are increased on the mesoporous Ga-MFI. The intermediate species in the aromatization of ethane is ethene and therefore low flows (high contact times) leads to lower selectivity for ethene and higher selectivities for C_3, benzene, and toluene.

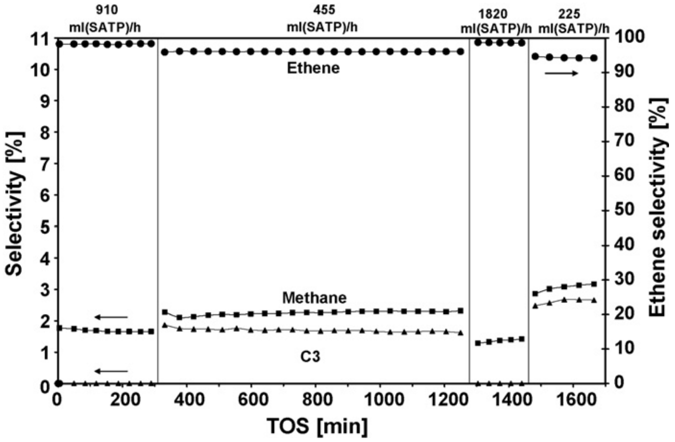

Fig. 11. Selectivity as a function of TOS for the conventional Ga-MFI zeolite ((■) methane, (●) ethane, and (▲) C_3). The catalytic tests were carried out at 823 K, atmospheric pressure and with an ethane/Ar mix with a concentration of 9.7% of ethane. The total ethane/Ar flow was varied four times: 910, 455, 1820, and 225 ml (SATP)/h.

The mesoporous Ga-MFI is the only catalyst that has any detectable selectivity for the aromatics benzene and toluene. Since the acidity and the amount of incorporated Ga is essentially the same for the two catalysts, the differences in selectivity must be attributed to the higher activity which is related to the differences in morphology. The mesopores also lead to an easier exit of the produced aromatics from the interior of the zeolite whereby the

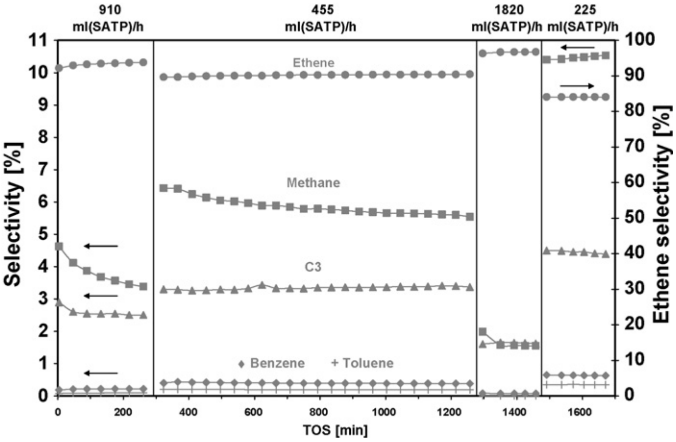

Fig. 12. Selectivity as a function of TOS for the mesoporous Ga-MFI zeolite ((■) methane, (●) ethane, (▲) C_3, (◆) benzene, and (+) toluene). The catalytic tests were carried out at 823 K, atmospheric pressure and with an ethane/Ar mix with a concentration of 9.7% of ethane. The total ethane/Ar flow was varied four times: 910, 455, 1820, and 225 ml (SATP)/h.

selectivity can be shifted towards producing more aromatics. For these reasons, benzene and toluene are produced in the mesoporous zeolite and not at any measurable extent in the conventional zeolite. Although aromatics are detected from conversion over the mesoporous Ga-MFI, it is only very small amounts that are produced (the selectivity is around 0.4% in the first period). This is due to the fact that the conversion of ethane into aromatics is enhanced by acidic sites on the catalyst [22,23,50] and that the Ga-MFI zeolites are not very acidic. The fact that the mesoporous Ga-MFI produces aromatics can also partly explain the higher conversion on the mesoporous Ga-MFI compared to the conventional. The thermodynamic equilibrium conversion is higher when aromatics are formed along with ethene and methane. Producing aromatics on the mesoporous Ga-MFI is therefore also one explanation of why the conversions on the mesoporous Ga-MFI are significantly higher than on the conventional Ga-MFI.

4. Conclusion

A conventional Ga-MFI zeolite and, for the first time, a mesoporous Ga-MFI zeolite were successfully synthesized. The two different MFI samples were characterized by XRPD, NH_3-TPD, elemental analysis, N_2 physisorption measurements, SEM, FT-IR, as well as ^{29}Si and ^{71}Ga MAS NMR. These analyses show that the main difference between the two MFI type zeolites is the morphology of the zeolite crystals. It was shown that water molecules located in the vicinity of the tetrahedral Ga sites result in a considerable modification of the electric field gradients at the ^{71}Ga nuclear sites. This observation has an important impact on the quantification of the ^{71}Ga signal intensities even in high-speed MAS NMR spectra recorded at relatively high magnetic fields (9.39–14.09 T). The introduction of the mesoporosity into the Ga-MFI zeolite leads to a significant improvement of the catalytic activity and selectivity in ethane aromatization. The main product for both Ga-MFI type zeolites is ethene, but the mesoporous Ga-MFI zeolite also produces a small amount of aromatics such as benzene and toluene. The difference in conversion is attributed to the improved accessibility to the active Ga species inside the mesoporous zeolite crystals since the catalysts only differ in the morphology.

References

[1] A. Corma, Chem. Rev. 95 (1995) 559.
[2] M. Hartmann, Angew. Chem. Int. Ed. 43 (2004) 5880.
[3] M.A. Camblor, A. Corma, S. Valencia, Micropor. Mesopor. Mater. 25 (1998) 59.
[4] P.A. Jacobs, E.G. Derouane, J. Weitkamp, J. Chem. Soc., Chem. Commun. (1981) 591.
[5] I. Schmidt, C. Madsen, C.J.H. Jacobsen, Inorg. Chem. 39 (2000) 2279.
[6] L. Tosheva, V.P. Valtchev, Chem. Mater. 17 (2005) 2494.
[7] M.E. Davis, C. Saldarriaga, C. Montes, J. Garces, C. Crowder, Nature 331 (1988) 698.
[8] C.C. Freyhard, M. Tsapatsis, R.F. Lobo, K.J. Balkus, Nature 381 (1996) 295.
[9] A. Corma, M. Diaz-Cabanas, J. Martinez-Triguero, F. Rey, J. Rius, Nature 418 (2002) 514.
[10] C.T. Kresge, M.E. Leonowicz, W.J. Roth, J.C. Vartuli, J.S. Beck, Nature 359 (1992) 710.
[11] T. Yanagissawa, T. Shimizu, K. Kuroda, C. Kato, Bull. Chem. Soc. Jpn. 63 (1990) 988.
[12] D. Zhao, Q. Huo, J. Feng, B. Chmelka, G.D. Stucky, J. Am. Chem. Soc. 120 (1998) 6024.
[13] S. Donk, A.H. Janssen, J.H. Bitter, K.P. de Jong, Catal. Rev. 45 (2003) 297.
[14] M. Ogura, S.H. Shinimiya, J. Tateno, Y. Nara, E. Kikuchi, M. Matsukata, Chem. Lett. (2000) 882.
[15] C.J.H. Jacobsen, C. Madsen, J. Houzvicka, I. Schmidt, A. Carlsson, J. Am. Chem. Soc. 122 (2000) 7116.
[16] S. Mintova, J. Cejka, Stud. Surf. Sci. Catal. 168 (2007) 301.
[17] Y. Tao, H. Kanoh, L. Abrams, K. Kaneko, Chem. Rev. 106 (2006) 896.
[18] K. Egeblad, C.H. Christensen, M. Kustova, C.H. Christensen, Chem. Mater. 20 (2008) 946.
[19] M.Y. Kustova, S.B. Rasmussen, A.L. Kustov, C.H. Christensen, Appl. Catal. B 67 (2006) 60.
[20] A.K. Rovik, A. Hagen, I. Schmidt, S. Dahl, I. Chorkendorff, C.H. Christensen, Catal. Lett. 109 (2006) 153.
[21] C.H. Christensen, K. Johansen, I. Schmidt, C.H. Christensen, J. Am. Chem. Soc. 125 (2003) 13370.
[22] A. Hagen, F. Roessner, Catal. Rev.: Sci. Eng. 42 (2000) 403.
[23] M. Guisnet, N.S. Gnep, Appl. Catal. A 89 (1992) 1.
[24] C.R. Bayense, J.H.C. van Hooff, Appl. Catal. A 79 (1991) 127.
[25] Database of zeolite structures: http://www.iza-structure.org/databases/ (February 12, 2008).
[26] T.J.G. Kofke, R.J. Gorte, G.T. Kokotailo, Appl. Catal. 54 (1989) 177.
[27] R. Fricke, H. Kosslick, G. Lischke, M. Richter, Chem. Rev. 100 (2000) 2303.
[28] K.S.W. Sing, D.H. Everett, R.A. Haul, L. Moscou, R.A. Pierotti, J. Rouquerol, T. Siemieniewska, Pure Appl. Chem. 57 (1985) 603.
[29] K. Egeblad, M. Kustova, S.K. Klitgaard, K. Zhu, C.H. Christensen, Micropor. Mesopor. Mater. 101 (2007) 214.
[30] K. Zhu, K. Egeblad, C.H. Christensen, Eur. J. Inorg. Chem. 25 (2007) 3955.
[31] R. Ghezini, M. Sassi, A. Bengueddash, Micropor. Mesopor. Mater. 113 (2008) 370.
[32] V.R. Choudhary, A.K. Kinage, J. Chem. Technol. Biotechnol. 72 (1998) 176.
[33] For ^{29}Si MAS NMR spectra of Al substituted MFI samples, see C.J.H. Jacobsen, C. Madsen, T.V.W. Janssens, H.J. Jakobsen, J. Skibsted, Micropor. Mesopor. Mater. 39 (2000) 393, and references cited therein.
[34] C.R. Bayense, A.P.M. Kentgens, J.W. de Haan, L.J.M. van de Ven, J.H.C. van Hoof, J. Phys. Chem. 96 (1992) 775.
[35] H. Kosslick, V.A. Tuan, B. Parlitz, R. Fricke, C. Peuker, W. Storek, J. Chem. Soc., Faraday Trans. 89 (1993) 1131.
[36] S.M. Bradley, R.F. Howe, Micropor. Mater. 4 (1995) 131.
[37] A. Diaz, R. Monque, M. Bussolo, Bull. Magn. Reson. 15 (1993) 112.
[38] A. Montes, Z. Gabélica, A. Rodríguez, G. Giannetto, Appl. Catal. A 169 (1998) 87.
[39] D. Ma, Y. Shu, C. Zhang, W. Zhang, X. Han, Y. Xu, X. Bao, J. Mol. Catal. A 168 (2001) 139.
[40] M. García-Sánchez, P.C.M.M. Magusin, E.J.M. Hensen, P.C. Thüne, X. Rozanska, R.A. van Santen, J. Catal. 219 (2003) 352.
[41] A. Samoson, Chem. Phys. Lett. 119 (1985) 29.
[42] A. Zecchina, S. Bordiga, G. Spoto, L. Marchese, J. Phys. Chem. 96 (1992) 4991.
[43] I. Pápai, A. Goursot, F. Fajula, J. Phys. Chem. 98 (1994) 4654.
[44] C. Páze, S. Bordiga, C. Lamberti, M. Salvalaggio, A. Zecchina, J. Phys. Chem. B 101 (1997) 4740.
[45] B. Gil, S.I. Zones, S.-J. Hwang, M. Bejblova, J. Cejka, J. Phys. Chem. C 122 (2008) 2997.
[46] C.O. Arean, G.T. Palomino, F. Geobaldo, A. Zecchina, J. Phys. Chem. 100 (1996) 6678.
[47] S. Bordiga, L. Regli, D. Cocina, C. Lamberti, M. Bjørgen, K.P. Lillerud, J. Phys. Chem. B 109 (2005) 2779.
[48] M. Sigl, S. Ernst, J. Weitkamp, H. Knözinger, Catal. Lett. 45 (1997) 27.
[49] C.O. Areàn, B. Bonelli, G.T. Palomino, A.M.C. Safont, E. Garrone, Phys. Chem. Chem. Phys. 3 (2001) 1223.
[50] G. Caeiro, R.H. Carvalho, X. Wang, M.A.N.D.A. Lemos, F. Lemos, M. Guisnet, F. Ramôa Ribeiro, J. Mol. Catal. A: Chem. 255 (2006) 131.